Open Research Online

Carbon deposition on transition metal- and uranium-oxides

Thesis

For guidance on citations see FAQs.

oro.open.ac.uk

CARBON DEPOSITION ON TRANSITION METAL- AND URANIUM-OXIDES

Keith Richard Hallam

Submitted to the Council for National Academic Awards in partial fulfilment of the requirements for the degree of Ph.D.

Nuclear Electric plc.,
Berkeley Nuclear Laboratories,
Berkeley,
Gloucestershire,
GL13 9PB

November 1991

MISSING PRINT

CARBON DEPOSITION ON TRANSITION METAL- AND URANIUM-OXIDES

Keith Richard Hallam

Submitted to the Council for National Academic Awards in partial fulfilment of the requirements for the degree of Ph.D.

Nuclear Electric plc.,
Berkeley Nuclear Laboratories,
Berkeley,
Gloucestershire,
GL13 9PB

November 1991

CONTENTS

ILLUSTRATIONS

TABLES

ACKNOWLEDGEMENTS

DECLARATION

This thesis is an account of original research performed by the author in Nuclear Electric plc.'s Berkeley Nuclear Laboratories. The work was carried out between September 1986 and March 1990. Where findings of other workers have been used, due reference is given.

SUMMARY

Advanced gas cooled nuclear reactors (AGRs) contain a range of alloys, selected for their physical and chemical performance in the conditions present. Carbon deposition on boiler and fuel pin heat transfer surfaces affects a reactor's efficiency and may necessitate downrating to maintain safety margins. This is believed to arise from decomposition of some of the coolant gas constituents. Deposition minimisation, while maintaining the structural integrity of the reactor, is technologically and economically important. This study has looked at deposition on a range of transition metal spinels, manganese oxides, uranium oxides and single crystal magnetite samples with a view to furthering knowledge of catalytic reactions that may occur within an AGR. In particular, the effect of mixed valency on deposition rates was studied.

The spinels were successfully prepared by solid state reactions between the relevant oxides, oxalates and / or carbonates. A range of elemental and chemical analytical techniques were used to characterise the samples both before and after exposure under controlled gas and radiological conditions. Deposition was induced, to varying extents, on all the samples exposed. No filamentary deposits were observed. The spinels gave quantities of deposition in the order:

$$Fe_xCo_{1-x}Fe_2O_4 > Mn_xCo_{1-x}Fe_2O_4 > Ni_xCo_{1-x}Fe_2O_4$$
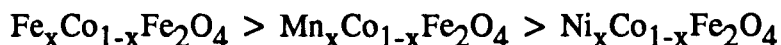
Manganese spinels gave increasing deposition with increasing manganese content at 650°C, but decreasing deposition at 550°C. Iron-cobalt spinels showed no consistent increase or decrease in carbon deposition with changing composition. Nickel rich spinels were unstable in the reaction gas mixture and generated metallic nickel during exposure. At both temperatures, this gave levels of carbon deposition which increased with increasing nickel content of the original oxide. $NiFe_2O_4$ exposed at 550°C fragmented as it catalysed carbon formation.

Manganese oxides converted to MnO during exposure, MnO proving also to be a most effective catalyst. Mn_3O_4, an Mn^{2+} / Mn^{3+} compound where the manganese ions do not form an electron exchanging octahedrally coordinated pair, did not yield large quantities of deposit. The uranium oxides examined converted to the interacting mixed valence U_4O_9, which gave copious carbon deposition. The U^{4+} / U^{6+} non interacting mixed valence α-U_3O_8 gave the least deposition.

Magnetite slices gave laminar carbon deposits, but no filamentary growth. Structured deposit was seen in two cases, including on one face oriented approximately parallel to the [111] plane, the plane previously expected to catalyse deposition most effectively.

ABBREVIATIONS

ADC   Analogue-to-digital convertor

AES   Auger electron spectroscopy

AGR   Advanced gas-cooled reactor

BE   Binding energy

BEI   Backscattered electron image

BNL   Berkeley Nuclear Laboratories

BSE   Backscattered electron

CEGB   Central Electricity Generating Board

CRT   Cathode ray tube

EBIC   Electron beam induced current

EDTA   Ethylenediaminetetraacetate

EDX   Energy dispersive x-ray analysis

EPMA   Electron probe microanalysis

ESCA   Electron spectroscopy for chemical analysis

eV   Electron volt

FAT   Fixed analyser transmission

fcc   Face centred cubic

FET   Field effect transistor

FRR   Fixed retard ratio

FWHM   Full width half maximum

JCPDS   Joint Committee on Powder Diffraction Standards

KAP   Potassium acid phthalate

KE   Kinetic energy

LED	Light emitting diode
LIMA	Laser ionisation mass analysis
SEAM	Scanning electron acoustic microscopy
SEI	Secondary electron image
SEM	Scanning electron microscope / microscopy
SIM	Scanning ion microscopy
SIMS	Secondary ion mass spectrometry
TEM	Transmission electron microscopy
UHV	Ultra-high vacuum
UPS	Ultraviolet photoelectron spectroscopy
vpm	Vapour parts per million
WDX	Wavelength dispersive x-ray analysis
XP	X-ray photoelectron
XPS	X-ray photoelectron spectroscopy
XRD	X-ray diffraction
YAG	Yttrium-aluminium-garnet
Z	Atomic number
ZAF	Atomic number / absorption / fluorescence (correction factors in quantitative energy dispersive x-ray analysis)
ZAF-PB	Atomic number / absorption / fluorescence / peak / background (correction factors in quantitative energy dispersive x-ray analysis for particles or rough surfaces)

1   INTRODUCTION

1.1   Aims and Technological Relevance

Gas-cooled nuclear power stations, in Magnox and advanced gas-cooled reactor (AGR) forms, account for approximately 15% of the total electricity generation in England and Wales[1, 2]. Their continued efficient and safe operation is of major importance to the industry, and the country as a whole.

AGRs were developed from the original Magnox gas-cooled reactor design. Higher steam temperatures, around 565°C, were desired[3], and necessitated the use of ceramic (UO_2) fuel clad in stainless steel. Steel surface temperatures up to 825°C are obtained[3], heating the CO_2 based coolant up to 665°C. The hot coolant is drawn into the boilers by circulating fans, and passes over the fuel element assemblies as it rises through the boilers. There are four boilers, each fed from a distinct quadrant of the core. A portion of the coolant gas is drawn off to have the balance of its constituents returned to the required mix. Species generated in the core are removed, and those consumed are replaced. Figure 1.1.1 shows a cross section through the Hinkley Point B AGR[4].

An AGR contains a variety of steels used in many components, each chosen to operate in a specific environment. As in other situations, oxide films form on the steel surfaces, ideally to form a protective coating, allowing the steel to last for its design life. 18% Cr / 8% Ni steel is used for reheater and superheater pipework inside the boilers[5]. The oxide formed on this alloy when heated in air contains a chromium-rich rhombohedral phase together with either a nickel-chromium spinel or magnetite, Fe_3O_4[6].

The fuel cladding, 20% Cr / 25% Ni / Nb-stabilised steel, in CO_2 at 750 - 850°C, forms a duplex Cr_2O_3/spinel oxide[7]. In CO_2 / 1% CO and 850°C, a silicon rich rhombohedral Cr_2O_3 layer initially forms. Above this, a Cr_2O_3 layer is present, followed by a manganese chromite spinel phase. A carbon rich layer is present between the Cr_2O_3 and $MnCr_2O_4$[8]. Heating fuel can material to 1200°C, well above the normal operating temperature, causes magnetite crystals to form[9]. The Cr_2O_3 layer has not always been observed. Oxidation of fuel can material at 800°C for 15 min in 50 τ of CO_2 gave rise to an initial iron rich oxide and a bulk $MnCr_{2-x}Fe_xO_4$ phase.

Oxides, in particular the outer spinel phases on fuel can material, may detach (spall) from their parent steel surfaces due to thermal cycling of the component, exposing fresh alloy surfaces that may be susceptible to more rapid corrosion until the chromia film reforms[10]. The spalled oxide particles, if carried

round the primary cooling circuit of the reactor and, then, subsequently removed for examination, may reveal their origins by their chemical composition.

AGRs contain some components that, once the reactor has been in operation, cannot be replaced. Their failure, thus, means that the working life of the plant is at an end. One such is the graphite core of the reactor, which acts not only as the moderator for the neutrons, slowing them down sufficiently to allow their ready reaction with the uranium fuel, but also as the structure defining the fuel and control rod channels.

Deposition of carbon has been found on both boiler heat transfer surfaces and fuel cladding when AGRs have been operated under certain conditions. Figure 1.1.2, from Reference 5, shows a clean and a deposited fuel element. The deleterious effect on the heat transfer properties of the materials involved as the coolant gas flows over the surfaces may necessitate the down-rating of the reactor concerned until such time as the deposit and/or fuel elements concerned have been removed. The AGR coolant includes, in addition to the carbon dioxide main constituent, carbon monoxide and methane, from which the carbon in the deposit may originate. Both gases are added in order to counter the radiolytic oxidation of the graphite moderator in the core[5]. Figure 1.1.3 illustrates a so-called coolant window. With pure CO_2 coolants, a plant life, determined as the safe life of the graphite moderator material, before an average of 20% of the mass of graphite has been lost, would be close to 15 years. Additions of up to 2 volume% of CO and 400 vpm of CH_4 can increase this to more than 35 years. However, at such concentrations, there is heavy deposition on the boiler surfaces. Low CO / high CH_4 coolants exceed the plant limit, the limit of the ability of the installed plant to remove water produced in the coolant as it passes through the core. High CO / low CH_4 coolants increase only a little the moderator lifetime. An optimum coolant would both prevent graphite corrosion and keep carbon deposition at a minimum. The stepped line shows the coolant composition path taken for Hinkley Point B power station during its early life, heading towards progressively more potentially depositing coolants in order to locate the deposition boundary for that plant.

The rate and type of carbon deposition may be affected by the surface morphology of the steel substrate. Fuel pins have been shown[11] to acquire different types of carbon deposit. Normally, thin, dense layers are formed. In iron and manganese rich areas of the can material, these may thicken to a few tens of microns in depth. If the CO and/or CH_4 concentration in the coolant gas is increased, thicker, low density layers, made up of plumes of laminar and filamentous carbon, are seen to be formed. This type of deposit is often seen in regions of the core fed by gas returning from the gas composition control plant. This may indicate a catalysing agent

2

originating in the control plant, and nickel has been found associated with some of these thick carbon deposits. It is also possible to form carbon deposits in the gamma cell at BNL. Figure 1.1.4 shows an array of mounds of fibrous carbon deposit formed on a piece of 20% Cr / 25% Ni / Nb-stabilised stainless steel exposed at 550°C for 49 days to a CO_2 / 1% CO / 700 vpm CH_4 gas mixture.

Boiler deposition has been shown to be less dependent on coolant composition[11]. It is seen to occur most heavily on high nickel steels. A fully developed deposit has a dense inner layer, a very fine fibrous outer layer and, occasionally, some thicker and straighter filaments. Hollow filaments have not been identified. These deposits tend not to contain much in the way of potentially catalytic material, such as nickel. The low density, fuel pin deposits have the greatest effect on heat transfer and plant efficiency, though determination of the origins of all the forms of deposit is important for the safe and reliable operation of the AGRs.

As the composition of the steel oxide is likely to be a contributing factor to the rate and type of carbon deposition, this present work has investigated the carbon deposition on a range of oxides. Previous work[6] looked at deposition on chromium-, iron-, manganese- and nickel-based oxides. This work is centred around cobalt-based oxides, together with manganese and uranium oxides, looking at the effect of oxide composition and rapid electron exchange on the deposition.

Solid state reactions were used for the preparation of the cobalt spinel oxides. X-ray diffraction (XRD) was used to characterise both the starting materials and the products by determination of lattice parameters and comparison with literature values, where available. Energy dispersive x-ray (EDX) analysis was used to check the cation ratios in the products.

The samples were exposed to conditions similar to those in an AGR in the Berkeley Nuclear Laboratories gamma irradiation facility. Scanning electron microscopy (SEM), EDX, XRD and x-ray photoelectron spectroscopy (XPS) were used to examine the samples after exposure.

1.2   Coolant Gas Chemistry

Though the actual composition varies depending on a reactor's particular requirements, an AGR coolant is based on carbon dioxide. Additions of around 1% carbon monoxide and 200 - 300 vpm of methane are made. In the absence of radiation, such a gas mixture is stable. However, the radiation in a nuclear reactor causes many reactions to occur. Carbon dioxide can oxidise the graphite moderator material[5]:

$$C + CO_2 \rightarrow 2CO$$
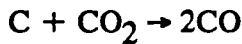
The CO added to the coolant gas is there to reduce the extent of the graphite oxidation reaction. Methane and water assist in this process by giving rise to carbon deposits on the graphite surfaces. This carbon deposition is helpful. On fuel pin or boiler surfaces it is less so.

It is believed that the unwanted carbon deposits originate in the catalytically-assisted thermal decomposition of coolant gases, or the products of reaction of these gases, on metals inside the reactor, either in the form of metallic components of the reactor or in small, metal-rich particles carried around the coolant circuit.

A wide variety of organic species are created within the coolant circuit of an AGR, and a lot of work has been put into building up an understanding of the reactions that occur (see, for instance, References 12 to 24).

It has been shown, by use of isotopically-labelled gases, that the majority of the carbon originates in the methane component of the coolant. A number of pathways for this process have been proposed[22], such as:

$$CO_2 \rightarrow CO_2^+ + e^-;$$
$$CO \rightarrow CO^+ + e^-; \text{ and}$$
$$CO_2^+ + nCO_2 \rightarrow (CO_2)_{n+1}^+$$
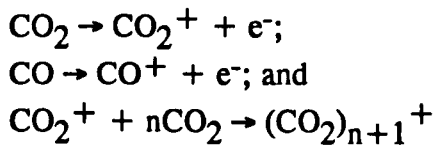
Hydrocarbons present in the coolant may then be attacked by the ion clusters via hydrogen extraction, e.g.:

$$CH_4 + (CO_2)_n^+ \rightarrow \cdot CH_3 + H(CO_2)_n^+; \text{ and}$$
$$2 \cdot CH_3 \rightarrow C_2H_6$$
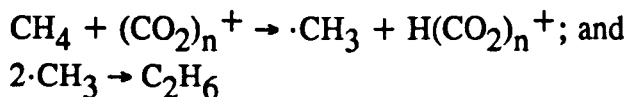
Attack on higher hydrocarbons may lead to the formation of unsaturated hydrocarbons or hydrocarbon radicals:

$$C_2H_6 + (CO_2)_n^+ \rightarrow \cdot C_2H_5 + H(CO_2)_n^+;$$
$$\cdot C_2H_5 \rightarrow C_2H_4 + \cdot H;$$
$$C_2H_4 + (CO_2)_n^+ \rightarrow \cdot C_2H_3 + H(CO_2)_n^+;$$
$$C_2H_4 + \cdot H \rightarrow \cdot C_2H_3 + H_2$$
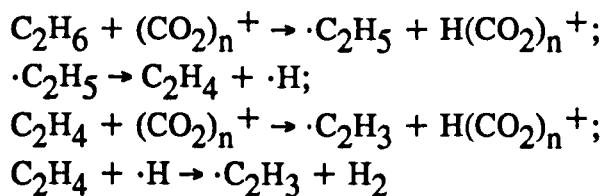
Below 500°C, the destruction of methane produces mainly C_2H_6 and C_3H_8, together with a small amount of carbon monoxide and water:

$$CH_4 + 3CO_2 \rightarrow 4CO + 2H_2O$$

4
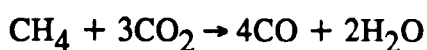
At higher temperatures, C_2H_4 is produced, along with increased quantities of CO and H_2O. Ethane production peaks at temperatures between 550 and 650°C.

1.3   Layout of Thesis

This chapter has explained the background to the present study. Chapter 2 is an investigation of the literature with regard to carbon deposition within nuclear power plant, and other situations where relevant to this study. Chapter 3 describes the various techniques and experimental procedures used for this work. Chapter 4 goes through the preparation of the samples and their characterisation before and after exposure in the gamma cell. Discussion of the results as a whole is presented in Chapter 5.

1.4   References

1. Central Electricity Generating Board, "The CEGB and Nuclear Power - Questions and Answers", Central Electricity Generating Board, (1985).

2. Central Electricity Generating Board, "Central Electricity Generating Board - Annual Report and Accounts 1987/88", Central Electricity Generating Board, (1988).

3. "Hinkley Point B - A Survey of Design and Construction", Nuclear Engineering, *August*, 652 - 653 (1968).

4. Central Electricity Generating Board, "Hinkley Point B Nuclear Power Station Reactor Plant Details Pocket Book", Central Electricity Generating Board, (1982).

5. J. M. Butterfield, C. J. Knights, D. J. Norfolk and D. G. Abbott, "A Longer Moderator Life for Advanced Gas-Cooled Reactors", CEGB Research, *16*, 18 - 33, (1984).

6. J. A. Jutson, "The Deposition of Carbon on Transition Metal Oxide Surfaces", Ph.D. thesis, Council for National Academic Awards, (1989).

7. J. M. Francis and W. H. Whitlow, "Oxidation of a 20%Cr-25%Ni-Nb Austenitic Steel in Carbon Dioxide at 750° and 850°C", Journal of the Iron and Steel Institute, *May*, 468 - 473, (1965).

8. G. C. Allen, R. K. Wild and M. Weiss, "Characterisation of the Oxide-Metal Interface at the Surface of a Stainless Steel", Philosophical Magazine A, *48*, 373 - 386, (1983).

9. T. B. Burgoyne, R. T. Sumerling, W. G. Anderson and N. A. Leech, "The Effect of Oxidation on the Emissivity of the Fuel Cladding of an Advanced Gas-Cooled Reactor during a Temperature Transient", in Institute of Mechanical Engineers, "Heat and Fluid Flow in Nuclear and Process Plant Safety", 181 - 188, (1983).

10. J. E. Antill and A. E. Truswell, "Mechanistic Aspects of the Reactions of Austenitic Stainless Steel with Carbon Dioxide at High Temperatures", proceedings of the British Nuclear Energy Society International Conference on Corrosion of Steels in CO_2, 330 - 337, (1974).

11. D. J. Norfolk, R. F. Skinner, M. A. Treasure and W. J. Stephen, "The Microstructure of Carbon Deposits in Gas-Cooled Nuclear Reactors", Carbon '88 extended abstracts, 31 - 33, (1988).

12. T. Baird, "Electron Microscope Studies of Solids Produced by α-Radiolysis of Carbon Monoxide", Carbon, *9*, 773 - 781, (1971).

13. D. J. Norfolk, "The Effect of Radiation on Gases Adsorbed on Alumina", Radiation Research Revues, *5*, 373 - 489, (1974).

14. D. J. Norfolk and T. Swan, "Radiolysis of Methane Adsorbed on γ-Alumina Part 1 - The Influence of Surface Sites", Central Electricity Generating Board report RD/B/N2855, (1974).

15. D. J. Norfolk, "A Review of the Radiolysis of Methane", Central Electricity Generating Board report RD/B/N3027, (1975).

16. G. C. Allen, D. J. Norfolk and T. Swan, "Electron Spin Resonance Study of the γ-Radiolysis of Methane Adsorbed on γ-Alumina", Journal of Nuclear Materials, *60*, 132 - 136, (1976).

17. D. J. Norfolk and T. Swan, "γ-Radiolysis of Methane Adsorbed on γ-Alumina, Part 1 - Development of Sites Active in Energy Transfer", Journal of the Chemical Society, Faraday Transactions I, *73*, 1454 - 1456, (1977).

18. D. J. Norfolk and T. Swan, "γ-Radiolysis of Methane Adsorbed on γ-Alumina, Part 2 - Kinetics of Reactions Occurring During Irradiation", Journal of the Chemical Society, Faraday Transactions I, *74*, 1676 - 1686, (1978).

19. D. J. Norfolk and T. Swan, "γ-Radiolysis of Methane Adsorbed on γ-Alumina, Part 3 - Influence of Additives on Product Desorption", Journal of the Chemical Society, Faraday Transactions I, *75*, 192 - 204, (1979).

20. R. L. Faircloth, K. S. Norwood and H. A. Prior, "Coolant Chemistry of the Advanced Carbon Dioxide Cooled Reactor", United Kingdom Atomic Energy Authority report AERE-R-10063, (1981).

21. G. R. Marsh, D. J. Norfolk and R. F. Skinner, "The Modelling of Gas-Phase Chemistry in Irradiated $CO_2/CO/CH_4$ Mixtures", Society of Chemical Industry, Carbon '82 extended abstracts, 302 - 304 (1982).

22. D. J. Norfolk, R. F. Skinner and W. J. Williams, "Hydrocarbon Chemistry in Irradiated $CO_2/CO/CH_4/H_2O/H_2$ Mixtures I - A Survey of the Initial Reactions", Radiation Physics and Chemistry, *21*, 307 - 319, (1983).

23. M. D. U. Gonzales and D. J. Norfolk, "The Effect of Surfaces on AGR Coolant Chemistry: Critical Assessment of Gas-Phase Rate Constants Relevant to Ethane Pyrolysis", Central Electricity Generating Board report TPRD/B/1060/R88, (1988).

24. M. D. U. Gonzales and D. J. Norfolk, "Modelling of Ethane Pyrolysis: Reactions in a Silica Flow Reactor", Central Electricity Generating Board report RD/B/6053/R88, (1988).

Figure 1.1.1. Hinkley Point B AGR cross section.

1   CORE
2   DIAGRID
3   DIAGRID SUPPORTS
4   UPPER NEUTRON SHIELD
5   CORE RESTRAINT SYSTEM
6   BOILER SHIELD WALL
7   BOTTOM SHIELD RINGS
8   GAS BAFFLE
9   CIRCULATOR OUTLET GAS DUCT
10 BOILERS
11 BOILER REHEAT HANGERS
12 BOILER SUPPORTS
13 PRESSURE VESSEL LINER ROOF
14 PRESSURE VESSEL LINER WALL
15 PRESSURE VESSEL LINER FLOOR
16 INSULATION
17 THERMAL SHIELD
18 CONCRETE PRESSURE VESSEL
19 CHARGE STANDPIPES
20 CONTROL STANDPIPES
21 REHEAT STEAM PENETRATIONS
22 MAIN STEAM PENETRATIONS
23 BOILER FEED PENETRATIONS
24 CIRCULATOR HOUSINGS
25 STRESSING GALLERY
26 CHARGE HALL SHIELD FLOOR
27 CHARGE MACHINE GANTRY ACCESS WALKWAY
28 CHARGE MACHINE GANTRY
29 CHARGE MACHINE
30 CHARGE HALL AND CHARGE MACHINE MAINTENANCE CRANE 25 TON
31 CHARGE HALL VISITORS VIEWING ANNEXE
32 CIRCULATORS
33 CIRCULATOR OIL TANKS
34 CIRCULATOR TRAVELLING CRANE TROLLEY 17 TON
35 PRESSURE VESSEL COOLING   SEA WATER PIPING
36 PRESSURE VESSEL COOLING   TREATED WATER PIPING
37 PRESSURE VESSEL COOLING   TREATED WATER COOLERS
38 PRESSURE VESSEL COOLING   TREATED WATER PUMPS
39 PRESSURE VESSEL COOLING   TREATED WATER RING MAINS
40 STEAM AND FEED PIPING
41 BOILER START-UP VESSEL
42 CLEAN DRAINS VESSEL
43 FLASH VESSEL
44 CABLE FLATS
45 ACCESS TO SWITCHGEAR
46 VENTILATION PLANT ROOM
47 OFFICES
48 SHIELD WALL
49 PRESSURE VESSEL COOLING TREATED WATER TREATMENT PLANT ROOM
50 CO_2 STORAGE PLANT
51 CONTAMINATED VENTILATION PLANT ROOM
52 MARSHALLING AND MONITORING ROOM

EAVES OF ROOF   77.0 m. (252.5 ft)
TOP OF CRANE RAIL   71.8 m. (235.5 ft.)
TOP OF CHARGE MACHINE RAIL   48.7 m. (156.5 ft)
ROOF LEVEL   47.2 m. (155 ft)
CHARGE HALL SHIELD FLOOR   37.0 m. (121.5 ft)
PILE CAP   35.4 m. (116 ft)
ROOF LEVEL   34.0 m. (111.5 ft)
UNDERSIDE OF LINER ROOF   29.9 m. (98 ft.)
BOILER ANNEXE GALLERY   20.0 m. (65.6 ft)
₵ OF CIRCULATOR   12.6 m. (41.6 ft)
GROUND FLOOR   10.4 m. (34 ft.)
PIPEWELL   2.7 m. (9 ft.)
0.6 m. (2 ft.)

Figure 1.1.2. a) clean; and b) deposit covered AGR fuel pins.

Figure 1.1.3. An AGR coolant map.

Figure 1.1.4. Carbon deposition on a 25% Cr / 20% Ni / Nb stabilised stainless steel
exposed in the gamma cell.

2 LITERATURE REVIEW

2.1 Introduction

Due to its importance in a wide range of industrial applications, the deposition of carbon on transition metal and oxide surfaces has been much studied. The formation of carbon as an undesirable by-product of hydrocarbon synthesis via the Fischer-Tropsch or methanation reactions, deactivating the transition metal catalyst concerned, has been a major impetus to such work. Palmer and Cullis[1] reviewed the work up to 1965 on carbon formation from gases. They differentiated between gas phase and surface formed carbon. The surface deposits arising through catalysis are of relevance to the current work. Mention of carbon deposition in gas cooled reactors is made. Radiolysis of CO and the radiolysis and/or thermal decomposition of products of CO radiolysis are implicated. C_3O_2, carbon suboxide, and the solid products thereof, are said to be observed. The polymerisation of C_3O_2 under thermal conditions and the radiolytic production of graphitic particles are both said to occur. Baker and Harris[2] reviewed the literature up to 1978.

This chapter summarises work of relevance to carbon deposition within AGRs.

2.2

Transition Metals

Kehrer and Leidheiser[3] showed that carbon deposition from CO on iron single crystals at 550°C occurred least rapidly on the [100] face and most rapidly on minor faces such as [321], [432] and [431]. The carbon was deposited in the form of fine needles. Graphite and cementite, Fe_3C, were detected. The cementite formed before any visible carbon deposit. Coiled filaments were observed. Similar results were obtained off nickel and cobalt crystals, where the metal was found in the deposit after reaction.

Tamai, Nishiyama and Takahashi[4] studied the deposition of carbon from methane, ethane and ethene on iron and nickel sheets at temperatures of 870 - 1030°C. Deposition on iron was seen to proceed five times faster than on nickel. A mechanism involving a metal carbide intermediate was suggested. The deposition from methane and ethane was said to proceed through ethene, which, in the iron case, will readily interact with the metal surface. Nickel appeared to have a higher affinity for the saturated hydrocarbons, giving higher deposition rates than the iron with methane and ethane. The small temperature and pressure dependence of the deposition from ethene implied that gas phase reactions were not a major factor.

Ruston, Warzee, Hennaut and Waty[5] studied the deposition of carbon from CO over iron at 550°C. They concluded that the laminar carbons observed close to the metal surface arose from the decomposition of cementite, Fe_3C, while the filamentous carbon seen originated in catalysis by Fe_7C_3 crystals. Fe_3C was said not to catalyse the CO decomposition while Fe could. Some workers[6] have claimed cementite to be a catalyst for carbon deposition, however.

γ-Fe_2O_3 has been suggested as the catalytic species in the decomposition of CO over single crystal iron[7]. The defect structure of this oxide was said to allow Fe^{3+} diffusion to the surface, where it facilitated CO decomposition. Above 550°C, conversion of the γ-Fe_2O_3 to α-Fe_2O_3 reduced the Fe^{3+} diffusion rate and the carbon formation rate with it. The same authors[8] implicated intermediate carbides in the cases of nickel and cobalt single crystals. Both laminar and filamentous carbon were formed.

Transmission electron microscopy has shown the formation of hollow filaments from the thermal decomposition of methane and acetone over iron, stainless steel and nickel at temperatures as low as 500°C [9]. Controlled atmosphere electron microscopy is a technique that has also been applied to this problem, looking at the decomposition of ethyne over iron, cobalt and nickel[10]. Metallic particles were seen at the end of growing hollow graphitic filaments. The diffusion of carbon through the metal particle due to a temperature gradient present, and its subsequent deposition at the back of the particle, were suggested as the filament formation mechanism. The catalyst particle becomes deactivated when a layer of carbon grows to encapsulate it.

Harris, Baker and Birch[11] suggested that ketene, CH_2CO, was the depositing intermediate in the decomposition of propanone over oxidised nickel.

A mechanism for the deposition of carbon on metal foil surfaces has been proposed[12]. This involves the diffusion of metal atoms, in association with hydrocarbon species, from the foil or catalytic particle into the layer structure of the filament. In experiments, decomposition occurred at the edges of the layers and metal was seen entrapped in the filaments.

In the deposition of carbon on stainless steels, chromium acts to retard deposit growth, nickel enhances it and manganese has no effect[13]. Any sulphur present in the gas also acts to inhibit deposit growth. The growth started at breaks in the magnetite oxide layer formed on the steel surfaces.

Different carbon deposits, one laminar, the other nodular, have been formed on iron foils that have had differing hydrogen pretreatments[14], nodular growth occurring on low pretreatment temperature samples. The nodular growth

appeared to occur at sites of local lattice disorder and at gaps in the surface oxide layer. The lower treatment temperature was also more likely to produce small reduced metal particles on the foil surface, which could promote deposition.

Rostrup-Nielsen and Trimm[15] reviewed earlier mechanism propositions for carbon deposition. In place of a temperature profile driven diffusion of carbon through a metallic catalyst particle, they proposed a concentration profile driven mechanism to explain the formation of carbon filaments behind a catalyst tip.

Emsley and Hill[16] observed deposition originating at the oxide-metal interface of fuel can alloy samples exposed to CO at 515°C. Nodules, with filamentous outer layers, were formed.

Water vapour has been shown to enhance the deposition rate from CH_4 over nickel[17].

It has been shown that with typical AGR coolant compositions, deposition on AGR fuel can alloy only occurs when irradiation (in the form of ^{60}Co γ-rays) is also present[18]. Surface catalysis was involved. The deposition was said to be likely to occur through radiolytic decomposition of ethene, via C_2H_3 and C_2H_2.

Exposure of AGR fuel can material to irradiated $CO_2/CO/CH_4/H_2O$ gas mixtures showed that the deposit arose from CH_4[19]. Radiation was required. The deposition occurred on top of the outer manganese-iron-chromium-nickel spinel oxide layer on the steel. Ethene was suggested as the immediate precursor to deposition.

Galuszka and Back[20] showed how the fragmentation of a bulk iron surface was necessary for the formation of filamentous carbon, in preference to any other form. The balance between carbon deposition and oxidation in any particular system will determine the optimum particle size for filamentous growth. Other work[21] highlighted the fact that particles that were too small (~10 nm) did not catalyse carbon filament formation.

Baker and Sherwood[22] showed how iron particles could not only catalytically gasify graphite but also, under the right conditions, deposit carbon in the channels they had earlier produced in the crystalline carbon. These results were obtained in C_2H_6/H_2O atmospheres. Particles smaller than 30 nm across were seen to deposit material at temperatures above 1100°C.

In a series of papers[23, 24, 25, 26], Holm and Evans studied the effects of surface grain size, internal oxidation, carburisation, cold work, preoxidation and alloy silicon content on the deposition resistance of 20 % Cr / 25% Ni stainless steels. Niobium, titanium and titanium nitride stabilised steel were used to look at the effect

13

of grain size, the nitride stabilised steel having the smallest grains, and the niobium stabilised the largest. It was found that the smaller the grain size, the greater the resistance to carbon deposition. The smaller grains provide an increased number of ready diffusion pathways for chromium to segregate at the surface to form a protective chromium rich oxide. The niobium stabilised steel had iron rich regions remaining at the grain centres, where chromium had not diffused, which acted to catalyse the carbon deposition reactions. Cold working the samples increased the diffusion pathways for chromium, allowing the niobium stabilised steel to more rapidly form a protective chromia layer. A similar result was achieved by selectively preoxidising the niobium steel to form the chromia layer in advance of introduction into the depositing environment. However, spalled oxide sometimes left iron and nickel rich regions of high deposition propensity. Increasing silicon content was matched by decreasing carbon deposition rate. A protective silica layer was believed to be formed at higher silicon contents.

The classical model for carbon filament formation[27] involves the detachment of a catalysing particle, production of adsorbed carbon from decomposition of gaseous molecules, diffusion of carbon through the particle and formation of the filament behind. Figure 2.2.1 (taken from Reference 27) summarises this mechanism. Temperature and concentration gradients have been suggested as driving forces for the diffusion. More recent work[28] has put forward the proposition that, with supported transition metal catalysts, unstable carbides are formed during the observed induction period, prior to filament formation. These decompose to deposit carbon, leaving behind the metal (or cementite in the case of iron). However, a surface carbide remains, through which carbon diffuses as the filament grows. The carbon concentration gradient through this carbide drives the reaction on.

$CH_4/H_2/H_2O/CO/CO_2$ gas mixtures (dissimilar to AGR coolant compositions) have been used for studying deposition on iron, cobalt and nickel foils[29]. Iron was shown to have the higher deposition rate, and nickel the lowest. The formation of carbides and subsequent increase in surface area was suggested as the cause of the enhanced rates of deposition, with the deposition rates in proportion to the carbide deposition temperatures. Nickel only gave filamentous deposition, localised also and not uniformly distributed over the surface, as was the case with the iron and cobalt. Iron and cobalt yielded a mixture of filaments, flake-like and amorphous carbon.

2.3   FeO

FeO has been shown[30, 31] to be an active catalyst for the formation of filamentous carbon from hydrocarbons such as ethylene and ethane (at 700°C), an

order of magnitude more active than iron metal. This increased activity derives from the porous nature of the iron formed on reduction of FeO, with the metal being the actual catalytic agent.

2.4 Manganese Oxides

Burch, Chalker, Squire and Tsang[32] investigated methane coupling over both potassium-promoted and unpromoted manganese oxide catalysts. MnO_2, MnO, Mn_3O_4 and Mn_2O_3 were looked at. Mn_3O_4 was seen to be stable to heating at 750°C with only a low oxygen content present in the atmosphere. Mn_2O_3 decomposed to Mn_3O_4 on heating in helium to this temperature. MnO was unaffected. Heating under nitrogen reduced the MnO_2 and Mn_2O_3 to Mn_3O_4. Heating unpromoted Mn_3O_4 or Mn_2O_3 in methane produced CO_2 and small amounts of C_2 products. The oxygen removal from the oxide lattice commenced at 575°C and stopped above 800°C. The oxide ultimately reduces to MnO. Passing mixed CH_4 and O_2 over the oxides produced a reaction in all cases. MnO converted 2% of the CH_4 into other products. Mn_3O_4 converted 5.6% of the methane. The unpromoted Mn_3O_4 phase was shown to be less selective to the formation of ethane than the MnO, in contrast to the K-promoted forms. All of these changes in oxidation are summarised in Figure 2.4.1, taken from Reference 32.

The authors point out the importance of rate of cooling of the catalysts, from the reaction temperatures to analysis ones. MnO cooling from 400°C to room temperature in 5 - 10 min has time to react with residual oxygen to form Mn_3O_4.

A mechanism has been proposed[33] where the cracking of methane takes place at an Mn^{3+}-O^{2-} site, with the carbon bonding to the Mn^{3+} and the hydrogen to the O^{2-}. The $\cdot CH_3$ radical formed reduces the Mn^{3+} to Mn^{2+}. This reaction scheme and the oxidative coupling network for methane are illustrated in Figure 2.4.2.

2.5 Magnetite

Lambiev and Dimitrov[34] looked at the reduction kinetics of Fe_2O_3 and Fe_3O_4 in CO at temperatures of 300 - 1000°C. Carbon deposition on Fe_2O_3 was seen to occur, maximising at a temperature of 500°C. Fe_3O_4, likewise, showed deposition. It is likely that this deposition occurred on the metallic iron formed in the samples. In comparison to those produced off FeO, the filaments generated by Fe_3O_4 are fewer in number but wider[30].

Lund, Kubsh and Dumesic[35] reviewed studies of the water gas shift reaction (CO + H_2O ⇌ CO_2 + H_2) catalysed by magnetite, Fe_3O_4. The reaction

15

was seen to occur via repeated oxidation and reduction of the 10% of the catalyst surface that was active. The octahedral Fe(II) and Fe(III) cations, with their rapid electron exchange, would appear to be the favoured location for this regenerative reaction to occur. Coordinatively unsaturated cations provided the adsorption sites for the CO, which acts to reduce anion sites. Steam oxidises the resulting oxygen vacancies to regenerate the catalyst. CO_2 adsorption was associated with surface oxygen species.

2.6   Spinels

Balasubramanian and Krishnasamy[36] have studied the decomposition of propan-2-ol over nickel, manganese and magnesium chromite spinels. The nickel and manganese spinels acted via dehydrogenation reactions, to produce propanone, whereas the manganese compound also acted to dehydrate, producing propylene.

Previous work at BNL on carbon deposition on characterised spinels[37] has confirmed that chromium acts to reduce the overall deposition rate, and prevent the formation of filamentous carbon. Iron was shown to catalyse deposition. In particular, Fe^{2+}/Fe^{3+} couples appeared to catalyse the formation of dense carbon layers while any reduction of Fe^{3+} to form FeO sites brought about filamentous growth. Manganese / iron spinels were shown to be good catalysts for deposition, while manganese / chromium ones were not. MnO was a catalyst. Nickel was found to promote deposition only when present in the metallic state, formed on decomposition of nickel rich spinels. No filamentous deposition was observed for any of the nickel containing spinels studied. At 550°C, magnetite and nickel(II) spinels only formed dense carbon layers, with the deposition rate dependent on the concentration of iron, and Fe^{2+}/Fe^{3+} sites. Magnetite was seen to produce filaments at 650°C, probably from FeO sites, but nickel ferrites only generated a small amount of dense deposition.

2.7   Carbonyls

The transportation of volatile nickel species, in particular $Ni(CO)_4$, formed within the recombination beds in the coolant reconditioning sections of the gas circuit, to the core, where they decompose to leave nickel as an active catalyst for carbon deposition, has been suggested as a means of explaining the quadrant effect observed in the deposition within AGRs, where deposition is greatest in the quadrant fed with gas fresh from the beds.

Baird[38] has looked at the α-particle induced deposition of carbon from CO in the presence and absence of transition metal carbonyl species. Deposits were not seen when the iron or nickel carbonyls were absent. The metal from the carbonyl was observed in the deposits.

Castle, Emsley and Surman[39] showed that iron could be transported in volatile forms in CO_2/CO atmospheres.

2.8   The Forms of Deposited Carbon

Audier, Oberlin, Oberlin, Coulon and Bonnetain[40] have looked at the effect of temperature and catalyst composition (Fe/Co, Fe/Ni or Ni) on the disproportionation of CO, and on methane decomposition over a Ni catalyst. The carbon products contained $<0.25\%$ of the metal. At low temperatures, filamentous products are formed, while more granular carbon was deposited at higher temperatures. Tubes (hollow), 30 - 90 nm or <10 nm in diameter, filaments (solid), >60 nm in diameter and carbon shells, ~60 nm across, were all obtained. Bitubes, defined as tubes where the catalyst particle is located centrally, and not at one end of the tube, were also sometimes seen. For the Fe/Co catalysts, the carbon shells started appearing at temperatures above 750°C. For the Fe/Ni catalyst, the transition temperature was between 550°C and 600°C. The Ni catalyst tended to produce only shells with a few filaments.

2.9   References

1. H. B. Palmer and C. F. Cullis, "The Formation of Carbon from Gases", in "Chemistry and Physics of Carbon, volume 1", edited by P. L. Walker, Jr., Edward Arnold / Marcel Dekker, 265 - 382, (1965).

2. R. T. K. Baker and P. S. Harris, "The Formation of Filamentous Carbon", in "Chemistry and Physics of Carbon, volume 14", edited by P. L. Walker, Jr. and P. A. Thrower, Marcel Dekker, 83 - 165, (1978).

3. V. J. Kehrer, Jr. and H. Leidheiser, Jr., "The Catalytic Decomposition of Carbon Monoxide on Large Metallic Single Crystals", Journal of Physical Chemistry, *58*, 550 - 555, (1954).

4. Y. Tamai, Y. Nishiyama and M. Takahashi, "Carbon Deposition on Iron and Nickel Sheets from Light Hydrocarbons, "Carbon, *6*, 593 - 602, (1968).

5. W. R. Ruston, M. Warzee, J. Hennaut and J. Waty, "The Solid Reaction Products of the Catalytic Decomposition of Carbon Monoxide on Iron at 550°C", Carbon, *7*, 47 - 57, (1969).

6. A. Sacco, Jr. and J. C. Caulmare, "Growth and Initiation Mechanism of Filamentous Coke", in "Coke Formation on Metal Surfaces" edited by L. F. Albright and R. T. K. Baker, American Chemical Society, 177 - 192, (1982).

7. G. D. Renshaw, C. Roscoe and P. L. Walker, Jr., "Disproportionation of CO I - Over Iron and Silicon-Iron Single Crystals", Journal of Catalysis, *18*, 164 - 183, (1970).

8. G. D. Renshaw, C. Roscoe and P. L. Walker, Jr., "Disproportionation of CO II - Over Cobalt and Nickel Single Crystals", Journal of Catalysis, *22*, 394 - 410, (1971).

9. E. L. Evans, P. A. Thrower, J. M. Thomas and P. L. Walker, "Growth of Filamentary Carbon on Metallic surfaces during the Pyrolysis of Methane and Acetone", Carbon '72 preprints, Deutsch Keramische Gesellschaft, 284 - 287, (1972).

10. R. T. K. Baker, P. S. Harris and R. B. Thomas, "Mechanism of Filamentous Carbon Growth from Catalysed Decomposition of Acetylene", Carbon '72 preprints, Deutsch Keramische Gesellschaft, 291 - 292, (1972).

11. P. S. Harris, R. T. K. Baker and R. A. Birch, "The Formation of Carbon Deposits from Decomposition of Acetone over Nickel", Carbon, *11*, 531 - 539, (1973).

12. T. Baird, J. R. Fryer and B. Grant, "Carbon Formation on Iron and Nickel Foils by Hydrocarbon Pyrolysis - Reactions at 700°C.", Carbon, *12*, 591 - 602, (1974).

13. J. E. Castle and M. J. Durbin, "The Surface Composition of Steels Oxidised in Carbon Depositing Atmospheres", Carbon, *13*, 23 - 31, (1975).

14. A. M. Emsley and M. P. Hill, "The Effect of Surface Pre-Treatment on Carbon Solution and Deposition in the Iron-Methane Reaction", Carbon, *15*, 205 - 210, (1977).

15. J. Rostrup-Nielsen and D. L. Trimm, "Mechanisms of Carbon Formation on Nickel-Containing Catalysts", Journal of Catalysis, *48*, 155 - 165, (1977).

16. A. M. Emsley and M. P. Hill, "The Rôle of Surface Oxide Layers in Carbon Deposition on a 20/25 Niobium Stabilised Stainless Steel", Society of the Chemical Industry, proceedings of the 5th. Carbon and Graphite Conference, 757 - 765, (1978).

17. J. Macák, P. Knízek and J. Malecha, "Formation of Carbonaceous Deposits on Metallic Ni From Methane-Water Vapour Mixtures", Carbon, *16*,

111 - 114, (1978).

18. D. J. Norfolk, R. F. Skinner and W. J. Williams, "Mechanisms Involved in Radiolytic Carbon Deposition from $CO_2/CO/CH_4$", in "Gas Chemistry in Nuclear Reactors and Large Industrial Plant" edited by A. Dyer, Heyden, 67 - 74, (1980).

19. M. J. Bennet, R. L. Faircloth, R. J. Firth, M. R. Houlton, K. S. Norwood and H. A. Prior, "Survey of the Principal Parameters Underlying Carbon Deposition on a 20% Cr / 25% Ni / Niobium Stabilised Austenitic Stainless Steel from $CO_2/CO/CH_4/H_2O$ Gas Mixtures in DIDO 6V3 Gas Loops", in "Gas Chemistry in Nuclear Reactors and Large Industrial Plant" edited by A. Dyer, Heyden, 81 - 89, (1980).

20. J. Galuszka and M. H. Back, "Iron Surface Morphology Factor in the Growth of Filamentary Carbon", Carbon, *22*, 141 - 145, (1984).

21. J. R. Bradley, Y.-L. Chen and H. W. Sturner, "The Structure of Carbon Filaments and Associated Catalytic Particles Formed During Pyrolysis of Natural Gas in Steel Tubes", Carbon, *23*, 715 - 722, (1985).

22. R. T. K. Baker and R. D. Sherwood, "Reversible Gasification/Deposition Behaviour of Iron Particles on Graphite in Ethane/Steam", American Carbon Society, 17th. Biennial Conference on Carbon extended abstracts, 178 - 179, (1985).

23. R. A. Holm and H. E. Evans, "The Resistance of 20Cr/25Ni Steels to Carbon Deposition I - The Rôle of Surface Grain Size", Werkstoffe und Korrosion, *38*, 115 - 124, (1987).

24. R. A. Holm and H. E. Evans, "The Resistance of 20Cr/25Ni Steels to Carbon Deposition II - Internal Oxidation and Carburisation", Werkstoffe und Korrosion, *38*, 166 - 175, (1987).

25. R. A. Holm and H. E. Evans, "The Resistance of 20Cr/25Ni Steels to Carbon Deposition III - Cold Work and Selective Pre-Oxidation", Werkstoffe und Korrosion, *38*, 219 - 224, (1987).

26. R. A. Holm and H. E. Evans, "The Resistance of 20Cr/25Ni Steels to Carbon Deposition IV - The Influence of Alloy Silicon Content", Werkstoffe und Korrosion, *38*, 224 - 229, (1987).

27. R. T. K. Baker, "Catalytic Growth of Carbon Filaments", Carbon,

27, 315 - 323, (1989).

28. I. Alstrup, "A New Model Explaining Carbon Filament Growth on Nickel, Iron, and Ni-Cu Alloy Catalysts", Journal of Catalysis, *109*, 241 - 251, (1988).

29. A. Sacco, Jr., F. W. A. H. Geurts, G. A. Jablonski, S. Lee and R. A. Gately, "Carbon Deposition and Filament Growth on Fe, Co, and Ni Foils using CH_4-H_2-H_2O-CO-CO_2 Gas Mixtures", Journal of Catalysis, *119*, 322 - 341, (1989).

30. R. T. K. Baker, J. R. Alonzo, J. A. Dumesic and D. J. C. Yates, "Effect of the Surface State of Iron on Filamentous Carbon Formation", Journal of Catalysis, *77*, 74 - 84, (1982).

31. D. J. C. Yates and J. A. McHenry, "Studies on the Low-Temperature Synthesis and Surface Chemistry of Iron Monoxide", Inorganic Chemistry, *26*, 3193 - 3201, (1987).

32. R. Burch, S. Chalker, G. D. Squire and S. C. Tsang, "Oxidative Coupling of Methane over Manganese Oxide Catalysts", Journal of the Chemical Society, Faraday Transactions, *86*, 1607 - 1614, (1990).

33. J. S. Lee and S. T. Oyama, "Oxidative Coupling of Methane to Higher Hydrocarbons", Catalysis Reviews in Science and Engineering, *30*, 249 - 280, (1988).

34. D. K. Lambiev and D. G. Dimitrov, "Kinetics of Reduction of Iron Oxides with CO and Secondary Reaction of Carbon Deposition", Comptes rendus de l'Académie bulgare des Sciences, *20*, 919 - 922, (1967).

35. C. R. F. Lund, J. E. Kubsh and J. A. Dumesic, "Water Gas Shift over Magnetite-Based Catalysts", in "Solid State Chemistry in Catalysis", edited by R. K. Grasselli and J. F. Brazdil, American Chemical Society, 313 - 338, (1985).

36. K. Balasubramanian and V. Krishnasamy, "Catalytic Decomposition of Isopropanol over Chromite Spinels MCr_2O_4 (M = Ni, Mn and Mg)", Journal of the Chemical Society, Faraday Transactions I, *82*, 2665 - 2672, (1986).

37. J. A. Jutson, "The Deposition of Carbon on Transition Metal Oxide Surfaces", Ph.D. thesis, Council for National Academic Awards, (1989).

38. T. Baird, "The Effect of Metal Carbonyls on the α-Radiolysis of Carbon Monoxide", Carbon, *11*, 252 - 254, (1973).

39. J. E. Castle, A. M. Emsley and P. L. Surman, "Chemical Transport of Iron in CO/CO_2 Atmospheres", Nature Physical Science, *231*, 86 - 87, (1971).

40. M. Audier, A. Oberlin, M. Oberlin, M. Coulon and L. Bonnetain, "Morphology and Crystalline Order in Catalytic Carbons", Carbon, *19*, 217 - 224, (1981).
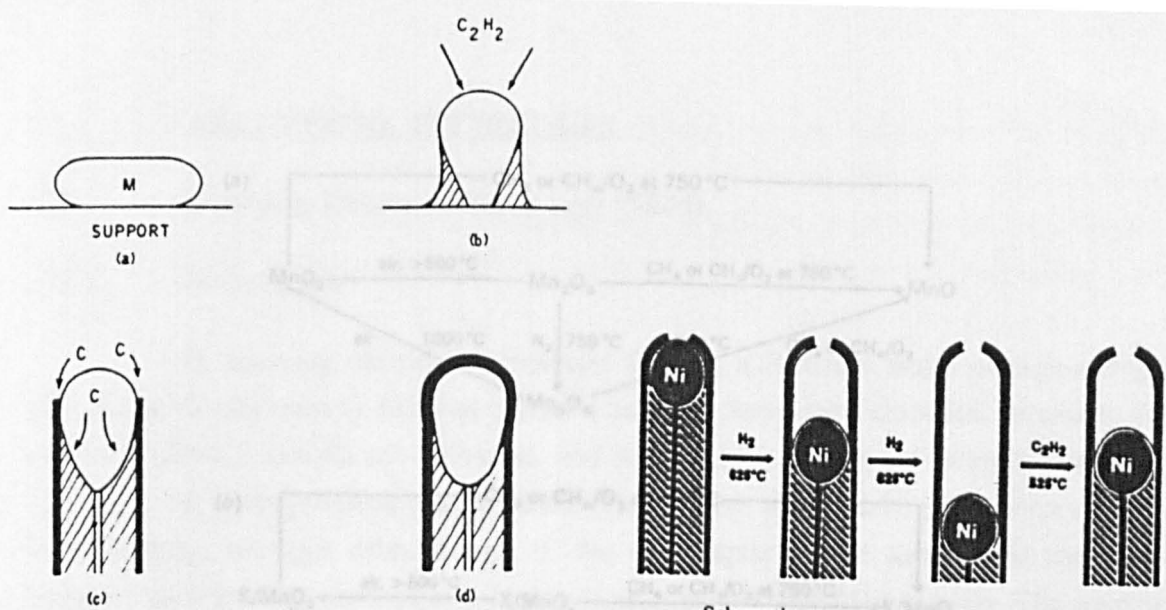
Mechanism of carbon filament formation.

Schematic representation of the reversible nature of the growth and gasification of carbon filaments produced from nickel particles.
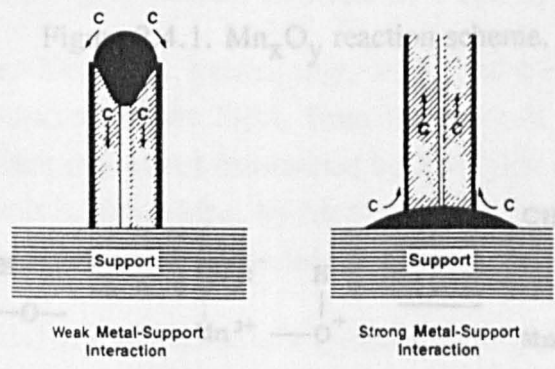
Influence of the metal–support interaction on the mode of growth of filamentous carbon.
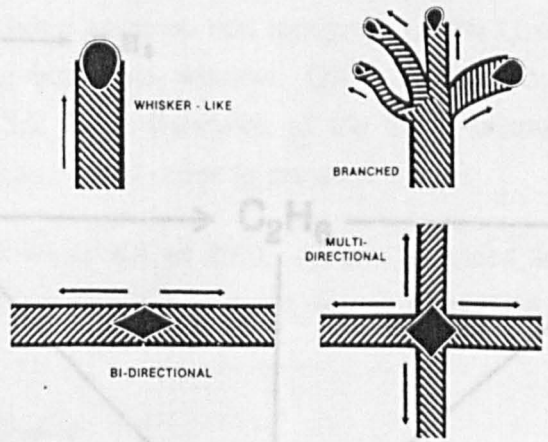
Schematic representation of different types of growth observed in carbon filaments.

Figure 2.2.1. The classic carbon filament formation mechanism.

(a)

┌─────────── CH₄ or CH₄/O₂ at 750 °C ───────────┐
│   ▼
MnO₂ ──── air, >500 °C ──── Mn₂O₃ ──── CH₄ or CH₄/O₂ at 750 °C ────► MnO
     │   │   ▲
     │ air   1000 °C   N₂ │ 750 °C   750 °C   CH₄ or CH₄/O₂ │
     └──────────────────────► Mn₃O₄ ◄──────────────────────────────────┘

(b)

┌─────────── CH₄ or CH₄/O₂ at 750 °C ───────────┐
│   ▼
K/MnO₂ ──── air, >500 °C ──── K/MnOₓ ──── CH₄ or CH₄/O₂ at 750 °C ────► K/MnO
      │   │   ▲
      │ air   1000 °C   N₂ │ 750 °C   750 °C   CH₄ or CH₄/O₂   │
      └───────────────────────► K/Mn₃O₄ ◄──────────────────────────────────┘
                                                           CH₂Cl₂ │ pulse
                                                           KCl/Mn₃O₄-like
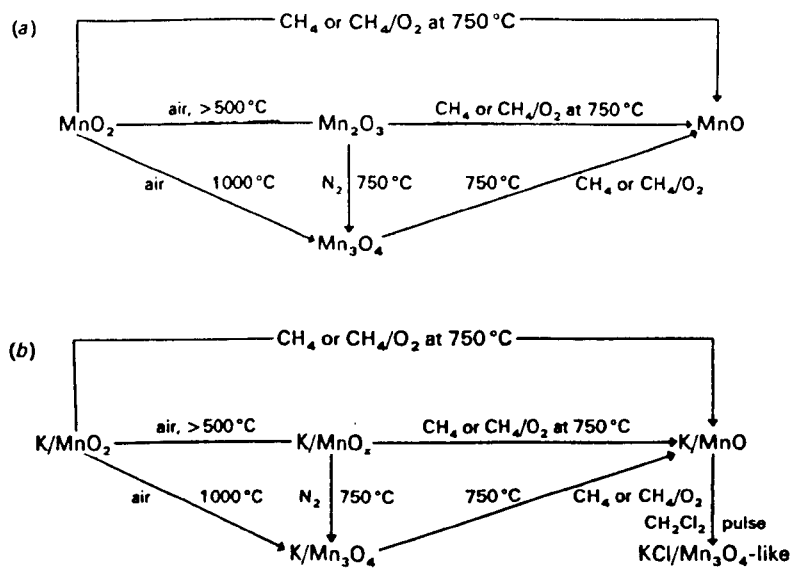
Figure 2.4.1. Mn_xO_y reaction scheme.

$$CH_3-H \qquad CH_3\!:^- \quad H \qquad\qquad CH_3\cdot$$
$$Mn^{3+}-O- \;\longrightarrow\; Mn^{3+}-O^+- \;\longrightarrow\; Mn^{2+}-O^+-$$

$$2(Mn^{2+}-O^+-) + \tfrac{1}{2}O_2 \;\longrightarrow\; 2(Mn^{3+}-O-) + H_2O$$

$$2\,CH_3\cdot \;\longrightarrow\; C_2H_6$$

$$CH_4 \longrightarrow C_2H_6 \longrightarrow C_2H_4$$
$$\searrow \quad \downarrow \quad \swarrow$$
$$CO_x$$
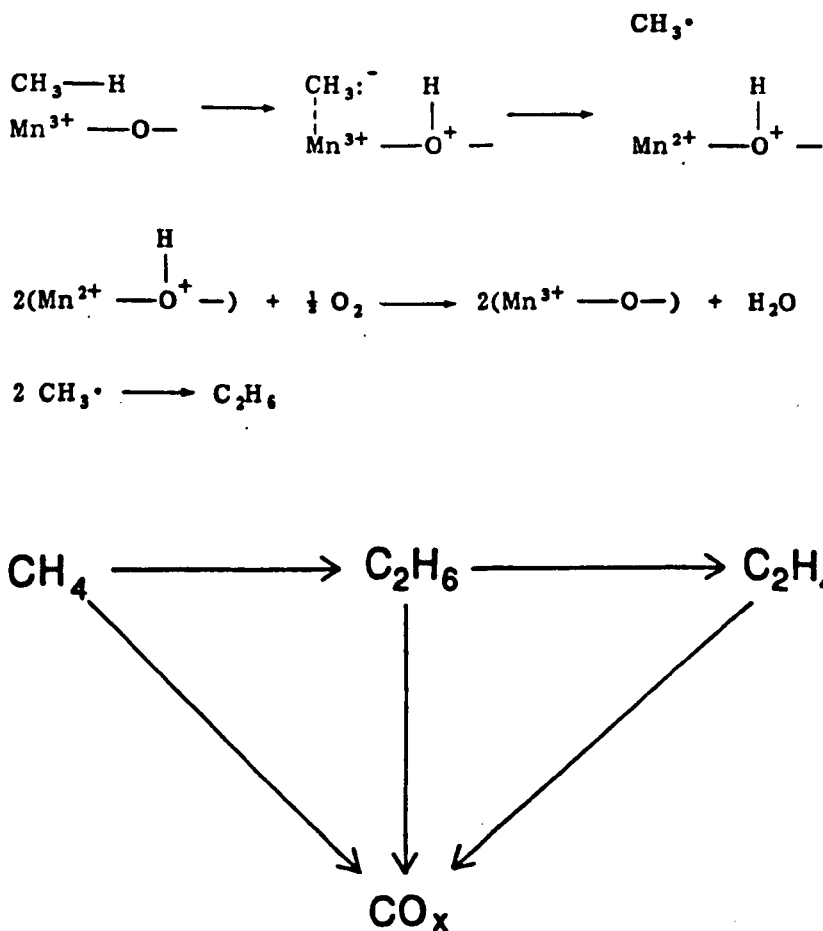
Figure 2.4.2. Oxidative methane coupling reaction scheme.

3 ANALYTICAL TECHNIQUES

3.1 Scanning Electron Microscopy (SEM)

3.1.1 Introduction

In scanning electron microscopy (SEM), a focussed beam of high energy (5 - 60 keV) electrons is rastered across a sample. Secondary electrons caused to be emitted from the sample are collected, and the intensity of this emission is displayed as a function of two-dimensional position. The number of secondary electrons emitted is a function, amongst other things, of the topography of the sample, so we get a realistic view on the monitors of a highly magnified region of the sample. The images have a large depth of field. Backscattered electrons and x-rays are also produced, both of which can give us information on the elemental composition of the sample, in relative terms (one region, say, having a higher average atomic number than another), and absolute terms (this region contains elements X, Y and Z) respectively.

Goldstein, Newbury, Echlin, Joy, Firoi and Lifshin[1] provide a brief history on the development of the SEM, from the work of van Ardenne in 1938, through the first modern instrument constructed by Zworykin and co-workers in 1942 and the first SEM built in Cambridge, by McMullan and Oatley around 1950, to the first commercial instrument, built by Cambridge Scientific Instruments in 1965.

Figure 3.1.1 is a schematic of a typical scanning electron microscope. The various components will be described in the following sections.

Two scanning electron microscopes were used in this study. Both were used to investigate sample surface topography, and the effect of exposure to etching solutions or the depositing gases on that topography. The Cambridge S180 was fitted with a Link Systems beryllium window, QX200 energy dispersive x-ray analysis system (see Section 3.2 for a discussion of the EDX technique). This was used to check on the transmission metal ratios in prepared oxides.

The windowless Kevex EDX system, attached to the Cambridge S150 SEM, was used to determine the relative degree of carbon deposition on exposed samples.

3.1.2 Electron Sources

The electrons used in an SEM commonly originate from a resistively heated tungsten filament. Both of the microscopes used in this work housed such sources. Brighter, by a factor of ten, electron sources, based around lanthanum hexaboride, or field emission sources (one hundred times brighter than a tungsten

filament) both give higher probe currents, allowing higher spatial resolutions to be achieved. The increase in electron brightness is paid for in increased cost and more stringent vacuum requirements, necessitating additional pumping to that usually supplied as standard on most SEMs. Greater care has to be taken in operating these sources.

Figure 3.1.2, taken from Reference 1, illustrates a typical tungsten filament electron source.

3.1.3   The Electron Column

The electron column consists of a series of electromagnetic lenses that are used to columnate and focus the electron beam, and then, ultimately, to deflect it in a defined raster pattern across the sample.

In the two microscopes used in this work, there are three sets of condensing lenses. Beneath the final lens are the deflection coils to raster the focussed electron beam across the face of the sample. Reducing the strength of the deflection field generated by the scan coils, we get a reduced deflection of the beam. Thus, a smaller area of the sample is rastered, increasing the effective magnification of the microscope. The scan coils have no effect on the focussing of the beam, allowing zooming through the available magnification range without the need for any refocussing.

In addition to the condensing and scanning coils in the microscope column, there are also coils present to allow for correction of any astigmatism in the image. Astigmatism is visible in the form of stretching of the image in perpendicular directions as the focussing is adjusted from an underfocussed state to an overfocussed one. It arises through imperfections in the condensing coils or due to the effects of asymmetric magnetic fields (internal or external to the column). The astigmator-controlling field strength and orientation can be adjusted by the operator to optimise the final image. It is only possible to correct for imperfections in the final condensing lens. Incorrect alignment of the source filament or dirt on an aperture cannot be corrected for by use of astigmator coils[1].

The strength of the probe current and the diameter of the beam go together, such that probe current strength can only be increased at the expense of increased probe diameter, and, so, degraded spatial resolution.

3.1.4   Secondary Electron Images (SEI)

Interaction of the incident electron beam with the sample brings about the emission of, so-called, secondary electrons. They originate from the outer orbitals of

25

the sample atoms[2] and are of low energies, typically less than 50 eV [2]. Though scattering electrons within the sample generate some secondaries, the majority of the signal results from the primary incident beam, giving a spatial resolution little larger than the diameter of the beam. For low atomic number elements, electrons suffer fewer elastic scattering events, and are able to penetrate deeper into the sample, than is the case with high Z elements. The higher the beam energy, the greater the penetration depth, though the shape of the interaction volume is little affected. This can have quite dramatic effects on the image obtained - the lower the beam energy, the greater is the contribution of surface features to the image.

Secondary electrons are of sufficient energy to escape from a depth of around 2 - 50 nm, depending on the material being examined.

Figure 3.1.3 shows how the sample topography has an effect on the image contrast. A higher electron yield can be expected from areas with a clear view towards the detector (though electrons are attracted towards the detector no matter what their angle of emission from the sample) compared to those with obstructions, simply from the absorption of electrons by a bulk of sample too thick for them, with their low energies, to penetrate. Areas of the sample tilted with respect to the detector generate more secondary electrons. The image seen appears as if the operator is looking down the column of the microscope, with the detector acting as a light source.

3.1.5   The Scintillator and Photomultiplier

The type of secondary electron detector now used in scanning electron microscopes was first described by Everhart and Thornley[3]. Secondary electrons are attracted, including those not originally travelling in the direction of the detector, by a positively charged grid, which also shields the primary electron beam from the scintillator bias voltage[3], towards a scintillating material, such as a phosphor or an yttrium-aluminium-garnet (YAG) crystal. The impinging electrons cause light to be emitted. The light is transmitted via a Perspex light guide towards a photomultiplier, where an electrical current is generated, proportional to the original secondary electron flux.

The output from the photomultiplier is used to modulate the brightness of a cathode ray tube (CRT), which is being rastered in synchronisation with the rastering of the electron beam across the face of the sample. Thus, the bright and dark regions on the screen correspond to the morphology of the sample.

Compared to an optical microscope operating at similar magnifications, an SEM has a much, up to forty times, greater depth of field. For a rough sample, much

more is in focus. This arises from the small convergence angle of the focussed beam on the sample. The depth of field of an image from a sample tilted with respect to the electron beam can be further increased by the application of dynamic focussing. Here, the focussing of the beam is adjusted as the beam rasters across the sample to account for the different working distances at the top and bottom of the sample. The beam is then in focus all across the sample, instead of just along the central strip of the sample.

3.1.6   *Backscattered Electron Images (BEI)*

A proportion of the incident electrons lose energy and change direction within the sample but emerge from the sample surface with some remaining energy. These are backscattered electrons. Due to their scattering within the sample, and their range of energies, backscattered electrons originate from larger volumes than do secondary electrons. For materials of medium atomic mass, the effective diameter is around 0.1 μm, no matter how narrow the incident electron beam may be. Figure 3.1.4 compares the secondary and backscattered electron production volumes.

The backscattered electron yield is a function of the average atomic number of the area analysed. Therefore, the images obtained from monitoring the backscattered electron current contain atomic number contrast. The higher the atomic number of the area analysed, the greater the number of backscattered electrons produced and, so, the brighter the backscattered electron image (BEI). Provided that the yield difference is sufficiently high (between adjacent elements, the contrast is typically only 1 - 5% [2]), then compositional imaging is possible. Usually, the electron beam current has to be increased to obtain sufficient contrast in the compositional image, degrading the spatial resolution beyond the, already poor, ~0.1 μm of backscattered electron images.

3.1.7   *Backscattered Electron Detectors*

By applying a small negative potential to the grid at the front of an Everhart-Thornley detector, the low energy secondary electrons can be excluded and only higher-energy backscattered electrons can impinge on the scintillator and yield a signal. (Backscattered electrons arrive at the detector along with secondaries and so do contribute, slightly, to secondary electron images.) However, this is not an efficient detector as only those electrons emitted from the sample in the direction of the detector are collected. Scintillator-lightpipe-photomultiplier detectors designed to maximise the collection angle are available, but their bulk can sometimes be a disadvantage if there is limited space available inside the analysis chamber.

The microscopes used in this work both housed KE Developments Limited

four quadrant solid state backscattered electron detectors. Such detectors are configured to detect electrons of energies greater than 50 eV. Backscattered electrons have greater kinetic energies than do secondaries, so the secondary electrons also emitted from the sample will not affect the backscattered image. Arriving electrons interact with the semiconductor material of the detector to produce electron/hole pairs. A bias voltage separates these pairs to produce a detectable current.

Multielement, solid state backscattered electron detectors can be used to extract topographical information as well as atomic number contrast, though they were not operated in this mode in the present study. Of course, the spatial resolution of the images obtained is poorer than with secondary electron detectors.

3.1.8   Other Signals

A wide range of other signals can be obtained from an SEM with the correct detectors in place. Of these, only the x-rays produced in the sample were collected and analysed in the present work (see Section 3.2 on energy dispersive x-ray analysis). Only a brief mention will be made of some of the other available techniques.

Electron channelling and diffraction can be used to obtain information on the crystallinity of the sample, and the orientation of the crystals with respect to the incident electron beam. This technique is particularly useful for the analysis of microstructure and texture in alloys.

Electron/hole pairs produced in a semiconducting sample can be separated by application of a bias voltage to the specimen. The electron beam induced current (EBIC) signal gives information on the variation of electronic properties across the sample.

Some samples cathodoluminesce, with the degree and colour of the luminescence varying as a function of the composition.

The domain structure of a magnetic sample will manifest itself due to the effect of the magnetism on both the backscattered and secondary electrons.

The specimen current gives a signal that is the inverse of the total sample electron emission. Nowadays, it is mostly used just as a monitor of the beam current.

Rapid switching on and off of the beam can generate acoustic waves within the sample This scanning electron acoustic microscopy (SEAM) can reveal subsurface structure in a sample, akin to sonar.

3.1.9 Image Processing and Storage

The image that appears on the microscope screens can be modified in several ways. Obviously, brightness and contrast can be adjusted for optimum viewing. Gamma controls change the response of the CRT to the supplied signal, enhancing either the high or low end of the signal. This can be useful to highlight image detail within generally dark or bright regions of the image. The signal can be differentiated before being sent to the CRT, emphasising regions of the sample where there are rapid changes in signal intensity while reducing the contrast of gradually changing background areas. Signals from different detectors can be added or subtracted. Corrections for the tilt of the sample can be applied. However, if a correction for tilt is applied to an image of a regular, square grid, so that the apertures now appear square and not rectangular, any spherical object sitting on the grid will then appear elongated. It is not always possible to have all portions of the image looking as desired.

High scan rates are required for ease of positioning the sample to the region of interest. To be able to use high scan rates, the beam will tend to have to be defocussed to produce a higher probe current than normal. However, to produce a good image for permanent recording, smaller probe sizes and longer scan periods are necessary. Obviously, the longer the image acquisition time, the greater the number of electron emission events recorded, and so the better the signal-to-noise ratio. Changing of the microscope operating conditions to optimise the obtained signal for the task in hand is a necessity.

By modulating the brightness of a CRT positioned in front of a Polaroid camera as the electron beam slowly scans the sample, a permanent recording can be made of the sample image. It is also possible to record backscattered electron images and x-ray dot maps, where a bright spot on the image corresponds to a point on the sample where x-rays of a chosen characteristic energy were generated as the electron beam passed over it.

Though neither of the instruments used in this study were so equipped, it is possible to output the signal from an SEM to a framestore, or digital analyser. Then, the image may be manipulated in any number of ways, such as changing the grey scale, introducing false colours, calculating areas or sizes of parts of the sample, enhancing edges, etc.

3.1.10 Sample Preparation

Unlike the case with transmission electron microscopy, very little sample preparation is required for scanning electron microscopy. The limitations on sample

size are set by the design of the specimen chamber and stage.

Electrically conducting samples are more readily examined. Insulating samples may be coated in a conducting medium, such as carbon or gold evaporated or sputtered onto the surface. As long as the film isn't too thick ($<$ 10 nm), the effect on the images obtained is negligible while the sample no longer charges up under the primary beam. Only at low voltages, in the range 1 - 5 kV, are the rates of electron arrival and departure sometimes equal[2]. At normal SEM operating voltages, an accumulation of electrons is seen on sample surfaces. Conducting samples may remove this charge readily to ground, via the microscope stage structure. Insulating samples, if not coated, accumulate charge, giving rise to distortion of both the primary and secondary electrons and the images obtained.

3.1.11   Instrumentation and Experimental

Both of the Cambridge Instruments Stereoscan microscopes used in this work have most of the usual SEM facilities[4, 5]. Each has two displays, e.g. for simultaneous secondary and backscattered electron image display; a degree of image processing, such as differentiation; specimen stages with x, y, z, Θ and tilt control; continuously variable kV, magnification and working distance; Polaroid cameras; a choice of final aperture sizes; secondary and backscattered electron detectors; and EDX detectors (windowless on the S150) and analysers.

The S150 can go up to 40 kV electron energy while the S180 can reach 60 kV.

A check was made of the magnification calibration of the S180. It was discovered that distances measured using the μ-markers, while accurate at medium to high magnifications, became increasingly in error as the magnification was reduced. 100 μm holes in a TEM grid appeared to be only ~74 μm across at the lowest magnification possible.
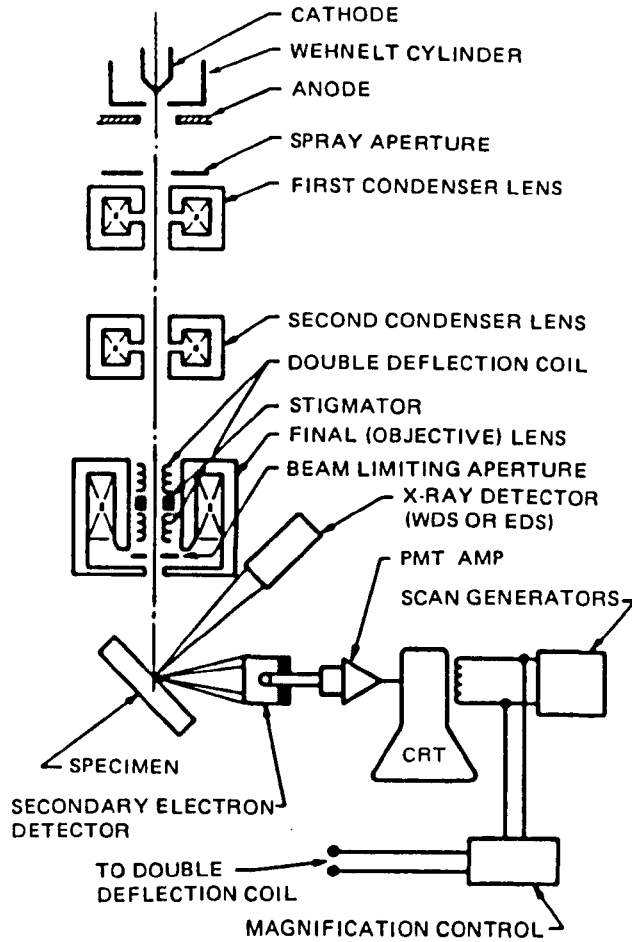
Figure 3.1.1. Schematic drawing of the electron and x-ray optics of a combined SEM-EPMA.
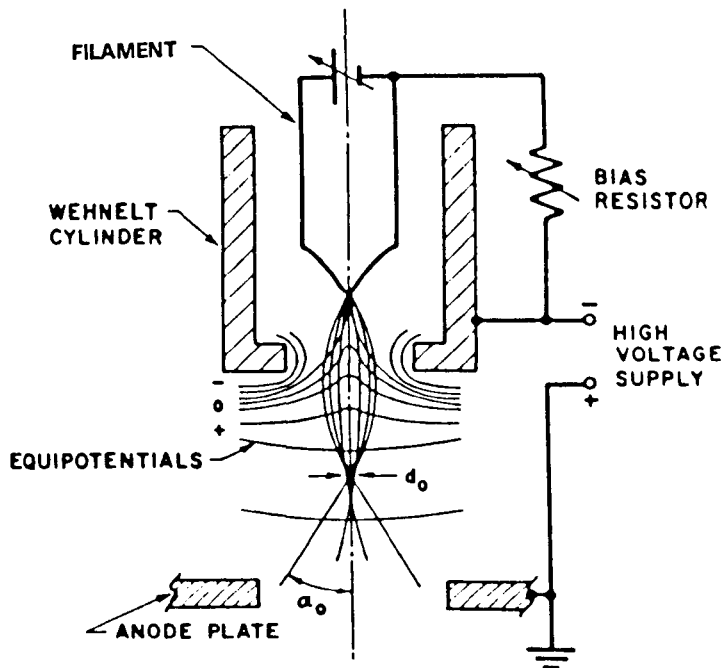
Figure 3.1.2. Configuration of a self-biased electron gun.

31
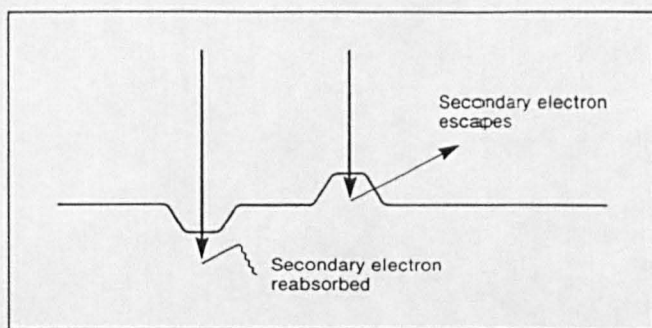
Figure 3.1.3. An illustration of the topographic sensitivity of low-energy secondary electrons.
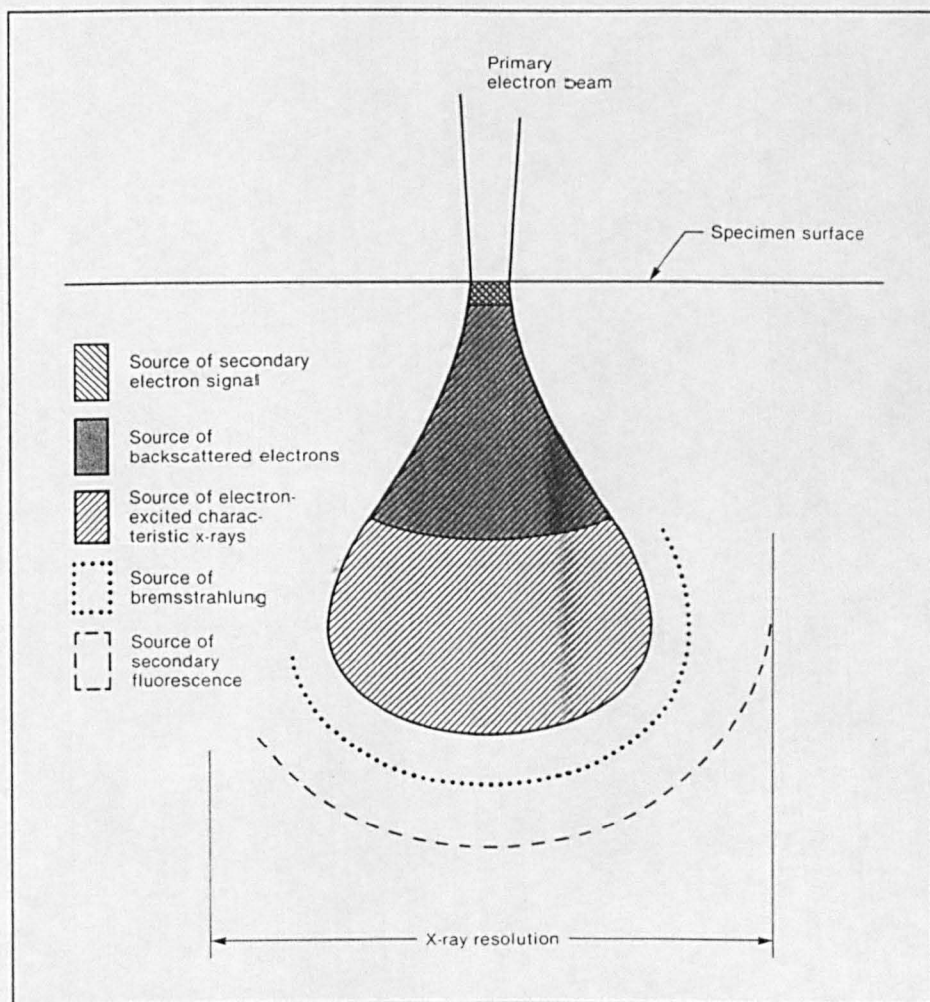
Figure 3.1.4. Generalised illustration of interaction volumes for various electron-specimen interactions.

3.2   Energy Dispersive X-Ray (EDX) Analysis

3.2.1   Introduction

When the electron beam of a scanning electron microscope enters the bulk of a sample, x-rays are one of the species emitted (alongside others, such as the secondary electrons generally used to obtain images in the microscope (see Figure 3.2.1)). The energies of the x-rays emitted are characteristic of the element(s) present in the sample and can, therefore, be used as a means of identification. An energy spectrum of the emitted x-rays is required, and may be obtained by use of either a wavelength or energy dispersive system.

The x-ray peak positions, along the energy scale (which is usually expressed in eV units, the energy acquired by an electron in travelling through a potential of 1 V), identify the elements present in the sample, while the integrated peak areas, after the application of appropriate correction factors, can give us the percentage concentrations of each of these elements.

With appropriate detectors, all elements above lithium may be detected. With an x-ray acquisition time of around 100 s, all constituents with concentrations ≥ 0.5 wt% may be analysed for.

Energy dispersive x-ray (EDX) analysis has been used in this work to confirm the elemental compositions of reagent oxides, carbonates, etc., to determine the compositions of product spinel oxides and other samples prior to exposure to radiation and gas flows in the gamma cell, to monitor any changes occurring in the surface composition or morphology of samples exposed in the gamma cell and to estimate the extent of carbon deposition on samples exposed in the gamma cell.

3.2.2   X-Ray Production

The energies of the x-rays produced in a sample bombarded by an electron beam range from zero up to an energy equal to the maximum energy of the impinging electrons. These x-rays fall into two classes, background radiation and characteristic radiation.

The background (also known as the continuum, bremsstrahlung or white radiation) arises from the slowing down of electrons by the electric and magnetic fields of the sample atoms (see Figure 3.2.2). The kinetic energy lost by the electrons reappears as a flux of x-rays of variable energy. Statistically, a small amount of energy is more likely to be lost than a large one (the maximum that can be lost is equal to the kinetic energy of the electron prior to interaction with the sample), so the background ought to rise towards the lower end of the energy scale. This it does, up

to a point. But at low energies, the x-rays generated cannot so easily escape from the sample, and are, instead, likely to be absorbed. This gives us the typical humped background appearance on EDX spectra. The only information contained within this flux is the mean atomic number of the sample. The maximum x-ray energy obtainable is equal to the maximum kinetic energy of the incoming electrons. This last fact can be useful in showing whether or not a particular sample has charged under the electron beam. If it has, then the negative potential accumulated on the sample will act to reduce the kinetic energy of the primary electrons by the time they reach the sample. The high energy cutoff of the background radiation spectrum will then appear at a lower energy than that given to the primary electrons as they were accelerated down the microscope column. The difference between the expected and the observed upper energy will be equal to the charging of the sample.

If an incoming electron interacts with an electron in one of the sample atoms, then that sample electron may be emitted from the atom, to leave a vacancy. The atom is unstable in this state, and an electron from a higher-lying orbital will tend to "fall" into the vacancy to lower the potential energy. The energy difference between the outer electron shell and the inner one (with the now-filled vacancy) has to be lost, and is so in the form of an x-ray (see Figure 3.2.2). As all elements have unique configurations of electron energy levels, the energy spectrum from any particular element will be unique, and provides a means of identification of the elemental composition of an unknown sample.

The x-ray peak arising from the initial ejection of an electron from a K shell in an atom is termed a K line. Likewise, L and M lines originate in the removal from an atom of an L or M electron. Within each line, there will, actually, be a number of different x-ray energies, dependant on the particular atomic orbital from which an electron falls to fill the vacancy.

Electric dipole selection rules dictate from precisely which higher energy orbitals electrons may drop to fill the inner orbital vacancy. The requirements may be summarised as:

$\Delta n \geq 1$, where n is the principal quantum number;
$\Delta l = \pm 1$, where l is the angular momentum quantum number; and
$\Delta j = 0$ or ± 1, where j = l+s and s is the spin quantum number.

Figure 3.2.3 illustrates these selection rules for the case of $K\alpha$ emission.

The higher the atomic number of an element, the greater the number of characteristic x-rays that may be generated. Carbon, containing two K shell electrons and four L electrons, only produces $K\alpha$ x-rays. Though the L electrons can (and will)

be removed from the atom by primary electrons of sufficient energy (in all elements, an incoming electron can only remove sample atom electrons which are bound to their nucleus with energies less than or equal to that of the primary electron, the so-called critical ionisation energy), there are no higher-lying (*M* shell) electrons to fill the vacancy produced, and generate x-rays in so doing. Sodium, with its one *M* electron, is able to generate both *Kα* and *Kβ* x-rays, while heavy elements, such as uranium, give rise to several series of lines. (See Figure 3.2.4.)

The probability of producing emission of a particular x-ray from an element is dependent on the energy of the primary electron, accelerated in the microscope column. It is the ultimate kinetic energy of the electron that we are talking about here, i.e. the given energy less any lost in overcoming sample charging. As a rule of thumb, the primary electron beam ought to be accelerated to an energy some two-and-a-half times greater than the critical ionisation energy for the x-ray in question to efficiently generate the x-ray.

The efficiency of x-ray production, even at a fixed primary electron energy, varies with atomic number, giving us the first correction factor required for quantitative x-ray analysis (see Section 3.2.15, later).

The ionisation cross section for a particular element, a function of the critical ionisation energy for the electron shell concerned and the energy of the primary electron beam, gives us the probability that an atom will be ionised to give us the initial vacancy in a low-lying orbital.

However, not all ionisations will yield an x-ray emission. The energy difference between the energy levels, that has to appear as an x-ray for this type of analysis to be possible, may, instead, be given to another outlying electron, giving it sufficient energy to escape from the potential energy well of the atom. This is the Auger process, named after its discoverer, Pierre Auger. The fraction of ionisation events that lead to the emission of an x-ray is termed the fluorescence yield. It is a function of atomic number. When looking at *K* shell x-ray emissions, the element beryllium represents the lowest atomic number that can readily be seen to emit characteristic x-rays. Calcium is at the lower limit for *L* shell x-rays while lanthanum is the lightest element readily identified from its *M* lines.

3.2.3   X-Ray Production Volume

The electron probe, that gives rise to the x-ray production, has been focussed by the microscope column (though, to obtain sufficient x-ray yield for analysis to take a reasonably short period of time, the beam tends to have to be defocussed to a certain extent) to a fine point. However, the x-rays that are emitted

originate from a larger volume. The dimensions of this volume depend on the primary electron beam energy and the mean atomic number of the sample being probed. The higher the energy of the primary electrons, the greater will be their penetration into the sample. For the case of a sample material of density 3 g.cm^{-3}, a 30 kV electron beam will enter the sample to depth of around 3 μm. A 10 kV beam will penetrate around 1 μm.

The lower the atomic number of a material, the fewer are the electrons in it that can scatter the primary beam. The primary electrons are then able to penetrate further into the material before the accumulated collisions with sample atoms have robbed them of all their original kinetic energy. For our original example of a 30 kV beam and material of density 3 g.cm^{-3}, where the penetration depth equalled some 3 μm, if we increase the density to 10 g.cm^{-3} we get a penetration of only 0.8 μm.

There are both empirical and fundamentally based formulae for the estimation of the depth of analysis in EDX. The one used in the current work is[6]:

$$R = \frac{4120}{\rho} \cdot E(1.265 - 0.0954 \ln E)$$

where: R = electron penetration depth /μm;
          ρ = absorber density /g.cm^{-3}; and
          E = primary electron energy /MeV.

This equation is applicable over the primary electron energy range of 0.01 - 3 MeV, or 10 - 3000 keV.

Figure 3.2.5 illustrates the effects of beam energy and sample density on the x-ray production volume. X-rays will be generated at all points within the electron scattering volume, where the electrons still have sufficient energy to excite the appropriate core electron out of the atom. This diagram also shows the volumes from which electrons are emitted to generate backscattered and secondary electron images in the microscope. As the x-ray emission volume is much greater than the secondary electron one, and has a larger diameter, the spatial resolution of our x-ray analysis is less than are any secondary electron images produced under the same microscope operating conditions. At, or around, 20 kV primary beam energy, we tend to get an x-ray spatial resolution of the order of 1 - 2 μm, compared to the image resolution of nearer 50 - 100 nm.

3.2.4   Wavelength Dispersive X-Ray (WDX) Analysis

Wavelength dispersive analysers employ crystals chosen to selectively reflect and diffract the x-rays falling on them. The Bragg relationship describing the requirements for constructive diffraction of x-rays (see Section 3.3) applies, so a

measurement of the source-crystal-detector angles can give us the wavelength (and, so, energy) of the impinging x-rays.

The crystals used are usually made of an organic material, e.g. potassium acid phthalate (KAP), and are made with concave surfaces, with radii of curvature related to the radius of the Rowland, or focussing, circle that they, along with the sample and detector, are placed around.

During the analysis, the diffracting crystal and detector are moved around the circle, so that x-rays of differing energies are, in turn, constructively diffracted. A plot of signal strength against x-ray energy can then be plotted. This technique is the same as that used in x-ray diffraction (see Section 3.3).

Proportional gas-filled detectors are most commonly used. The diffracted x-rays enter a gas-filled chamber (a typical detector gases are a mixture of 90% argon and 10% methane in a flowing system, or krypton or xenon in sealed detectors[1]), causing ionisation of the gas and the production of photoelectrons. These electrons are attracted to a positively charged wire running down the centre of the detector tube. Secondary ionisations occur in the gas amplifying the signal. These primary and secondary electrons give rise to a current proportional to the energy of the original x-ray and the intensity of the x-ray flux. The current is integrated over a set time period to create the signal intensity at the particular wavelength that the spectrometer is set up for during that time. The positions of the crystal and detector are then adjusted to collect data on the next wavelength.

Most WDX systems employ two or more crystals, as each is limited in the wavelength/energy range it can diffract.

The resolution of WDX systems is such that it is possible to detect chemical shifts in the peak positions, akin to those seen in x-ray photoelectron spectroscopy (see Section 3.4), from some samples. These shifts arise through the changes in the atomic energy levels due to the differing oxidation states and chemical environments of the sample atoms. Detectable shifts have to be of the order of 10 eV or greater, so the technique is not as useful as XPS, in this respect.

3.2.5   The EDX Detector

An energy dispersive x-ray analysis system basically consists of a detector that responds to an arriving x-ray by generating a pulse of electric charge, a preamplifier that converts this charge into a voltage, a processor that amplifies the voltage before actually measuring it, and an analogue-to-digital converter (ADC) that produces an output that can be placed into a multichannel analyser at a position

appropriate to the original x-ray energy. EDX detectors were first employed on electron microprobes by Fitzgerald, Keil and Heinrich[7].

An EDX detector applies the photoelectric effect. Figure 3.2.6 is a diagrammatic representation of a typical lithium-drifted silicon EDX detector. The silicon crystal is doped with indium to transform it into a p-type semiconductor, with an excess of "holes"[8]. Further lithium doping is then applied to compensate for the impurities already present in the silicon and to give the final required characteristics[9].

It is necessary to maintain the crystal at liquid nitrogen temperatures to reduce the mobility of the dopant atoms through the silicon and thus to retain the performance of the detector. The low temperatures are maintained by use of a liquid nitrogen dewar, thermally in contact with the crystal (and field effect transistor (FET, see below, Section 3.2.6)) via a copper rod. If the liquid nitrogen level in the dewar is not maintained, then the crystal will warm up, increasing the ability of the lithium atoms to migrate through the body of the crystal, with consequent loss of performance of the detector.

Housing the crystal in a region of relatively high vacuum ($\sim 1 \times 10^{-6}$ τ) minimises contamination of the crystal face, that might otherwise reduce the transmission of x-rays, especially those of low energy, to the crystal. An 8 μm window of beryllium is used in standard detectors to isolate the crystal from the specimen chamber of the microscope, which is let up to air, or dry nitrogen, during each sample change (at least with the Cambridge microscopes used in this study). The presence of this window prevents x-rays of energies lower than 0.8 keV reaching the detector crystal[8], limiting analysis to the elements of sodium and higher atomic number. If the liquid nitrogen is allowed to run out in the dewar, molecules trapped in a region of molecular sieve material, housed within the walls of the dewar, will be released and are likely to deposit on the face of the crystal, increasing system noise and reducing transmission efficiency of low energy x-rays to the crystal.

An impinging x-ray raises a number of electron/hole pairs from the valence band up to the conduction band of the crystal. The energy required to raise one such pair is 3.8 - 3.9 eV [9]. The number of pairs raised is directly proportional to the energy of the incoming x-ray. A bias voltage, usually around 500 V, applied to the crystal then pulls the electrons and holes apart to produce a charge. This charge, for a 5 keV x-ray, is of the order of 2×10^{-16} C [8], arising from the elevation of some 1300 electron/hole pairs[1].

Comparing the technique to wavelength dispersive analysis, we have here a parallel technique, where all x-ray energies are monitored simultaneously, whereas in WDX the energy range is swept through, with acquisition for a set time at each

energy. EDX allows us to monitor the spectrum and cease acquisition once the desired signal-to-noise ratio has been achieved or once a particular intensity has been reached for an element of interest. With WDX, once an acquisition has been started, it is difficult to increase or decrease the duration without restarting the whole run.

Since mechanical movement of the crystal and detector are required in WDX, spectral acquisition time is increased.

The higher geometrical collection and quantum (percentage of impinging x-rays actually analysed and assigned to an energy channel) efficiencies of the EDX detector mean that lower beam currents are needed, which is useful for delicate samples that might be damaged by the electron beam.

Since the focussing requirements are less critical, EDX may be used to analyse or x-ray map relatively large sample areas and rough samples. WDX systems are sensitive to variations of only a few microns in the surface finish of the sample.

Another advantage of EDX is its price - the systems, being mechanically simpler, are much cheaper to buy.

There are some disadvantages of EDX over WDX analysis. The detector resolution is some 15 times poorer, giving increased problems of peak overlaps and the need for more sophisticated spectral deconvolution routines. Chemical shifts are also too small to be identifiable with EDX analysis. The spreading out of counts into more channels reduces the peak heights, and, so, increases the minimum detection limits. At 0.1 - 0.5 wt%, the detection limits for EDX are an order of magnitude worse than those for WDX[8]. Also, the maximum count rates are lower compared to those obtainable with the WDX technique.

3.2.6   The Field Effect Transistor (FET)

As mentioned earlier (Section 3.2.5), the field effect transistor (FET) converts the charge built up in the detector crystal into a voltage.

Instead of being reset after each charge conversion, i.e. after each x-ray incident, as might be expected, the FET is only reset, using light from a light emitting diode (LED), once the accumulated voltage across the FET is such that to further increase it would cause the transistor to enter a non-linear region. Figure 3.2.7 shows how the FET voltage increases in a step function, with each step height proportional to an x-ray energy, until it is reset. The time while the LED is switched on, to reset the FET, contributes to the dead time of the EDX system, the fraction of the total acquisition time during which actual x-ray detection and recording is not possible.

The FET, like the detector crystal, has to be cooled to liquid nitrogen temperature, this time to reduce to a minimum electronic noise in the system. If the bias voltage is on while the detector warms up due to lack of liquid nitrogen, the noise generated can saturate and destroy the FET.

3.2.7   Spectral resolution

Though the natural full width half maximum (FWHM) of an x-ray peak is of the order of 2 eV, the EDX system degrades this to nearer to 150 - 200 eV. This increase is contributed to by the 3.8 - 3.9 eV energy involved in the electron promotion in the crystal, statistical variation in the number of electron/hole pairs produced by an x-ray of specific energy and the uncertainty introduced by the amplification process. The equation[1]:

$$FWHM \propto \sqrt{(C^2E+N^2)}$$

where: C = uncertainty in number of electron/hole pairs produced;
E = energy of incoming x-ray; and
N = the contribution to the noise from the amplification process,

describes this peak broadening. C is dependent on the material used for the crystal.

The higher the x-ray pulse rate, the greater is the increase in FWHM. External vibration and electronic interference contribute to the ultimate resolution, the higher the levels the broader are the peaks. Also, the detector capacitance is a factor, the smaller the better, implying the use of small crystals, at the expense of reduced x-ray collection rate due to the reduction in surface area. If any light or infrared radiation falls on the detector, by, for instance, the leaving off of the dewar lid or the analysis of a cathodoluminescent specimen in a windowless system (beryllium or thin windows prevent access for light from the specimen chamber), noise in the spectrum will be increased. Any ice crystals that form or accumulate inside the nitrogen dewar may "tap dance" due to the boiling nitrogen, degrading the resolution[1] by up to 30 eV.

There is tailing apparent at the low energy side of peaks, causing deviation from the ideal gaussian shape, and so increased peak widths at low heights. There is incomplete charge collection, due to increased inefficiencies in the detection process in the detector at the sides and edges (recombination of electron/hole pairs occurs more often). The x-ray is measured as having a lower energy than it actually originally had. Energy may also be lost to the continuum by the emission of x-rays from inelastically scattering photoelectrons generated in the silicon crystal by the

40

impinging x-ray. Again, we see an increase in the background, and a broadening of the peak, on the low energy side.

3.2.8   The Signal Processor

The pulse processor in the EDX system performs several functions. It activates the FET resetting routine at the appropriate moments, it ensures that only one pulse at a time is amplified (pulse pile-up rejection) and amplifies, shapes and integrates the pulse before passing it onto the analogue-to-digital convertor.

Pulse pile-up, the arrival at the detector of two temporally close x-rays, leading to interpretation as a higher energy single x-ray, is prevented by a discriminator, set to only allow the measurement of pulses that arrive more than 1×10^{-6} s apart. A "slow" discriminator is tuned to distinguish between noise and a genuine signal.

While one pulse is being analysed, the processor will reject all further incoming signals. The time taken to measure the energy of the x-ray that gave rise to the pulse is a contributor to the system dead time.

The longer the processor integrates a pulse for, the greater will be the spectral resolution, at the expense of increased acquisition time for a spectrum of set total number of counts. This integration time adds to the dead time of the system. A processing time of 20 μs is most commonly employed. Higher count rates normally require the use of shorter integration times, and vice versa.

3.2.9   The Analogue-to-Digital Convertor

This section of the EDX system allows the pulse, that has been integrated and handed to it by the pulse processor, to decay at a fixed rate. The time taken for the pulse to decay to zero is, then, a function of the energy of the pulse and, thus, of the energy of the original x-ray. Once the decay time has been determined, then an additional entry is made in the appropriate channel of the multichannel analyser, which is usually displayed on a computer display unit as a bar graph, with the height of a bar being proportional to the number of x-rays of the energy represented by that channel that have been detected during the course of the acquisition.

3.2.10   System Calibration

A noise peak, nominally at 0 eV, is generated by the spectrometer. A potentiometer on the pulse processor is adjusted so as to bring the centre of this peak into line with the origin of the energy scale.

A standard material, in our case cobalt, is placed under the electron beam. The energy of the x-rays generated by this sample is known from the literature (for cobalt, the $K\alpha$ x-ray is of 6.930 eV energy[6]) and it is then a simple matter to adjust the "gain" potentiometer to ensure that the signal falls at the correct value on the energy scale.

3.2.11 Qualitative Analysis

Qualitative analysis of an EDX spectrum requires the accurate measurement of an x-ray peak position, and, so, energy, followed by the comparison of that energy with known energies for the elements so as to determine the elemental composition of the sample.

The relative peak intensities for a family of lines from one element, for instance the $K\alpha$:$K\beta$ ratio, may be used to separate out the influence of overlapping peaks. The first row of transition elements tends to create problems with the $K\beta$ peak of one element being overlapped by the $K\alpha$ peak from the element one higher in atomic number. The ratios that may be expected are:

$$K\alpha{:}K\beta = 100{:}20$$
$$Ll{:}L\alpha{:}L\beta_1{:}L\beta_2{:}L_l = 1{:}100{:}70{:}20{:}10$$
$$Mz{:}M\alpha = 1{:}100.$$

The asymmetric broadening of a peak, away from the usual gaussian shape, is also indicative of the presence of an overlapping peak, centred at a slightly different energy.

3.2.12 Spectral Artifacts

Of all the x-rays that impinge on the detector crystal, a small fraction may bring about fluorescence of a silicon x-ray from the crystal material. This x-ray may then be either reabsorbed to produce additional electron/hole pairs or may escape from the detector. If the latter occurs, then we have, in effect, a loss of 1.74 keV, the energy of the silicon x-ray, from the incident x-ray. The x-ray will then be measured and allocated to a channel 1.74 keV lower than it ought to have been. A peak will appear in the spectrum 1.74 keV below the parent x-ray line. Such a signal is called an escape peak. Phosphorus generates an escape peak ~1.8 % of the time while zinc only generates an escape peak ~0.01% as intense as the parent $K\alpha$ signal[1]. Obviously, x-rays of insufficient energy, less than the 1.838 keV silicon K shell binding energy[1], cannot generate escape peaks.

It is possible to have a computer calculate the contributions to the spectrum from all the escape peaks expected due to the elements known to be present

in the sample. These can then be subtracted from the raw data.

If a silicon x-ray is generated in the inactive, dead layer at the front of the detector crystal, which is ≤ 0.5 μm thick[10], and then finds its way into the active layer, it will contribute to the formation of an internal fluorescence silicon peak in the final spectrum[1]. This peak ought not to indicate a silicon concentration greater than 0.2 wt%. The thin (~20 nm) gold electrode layer on the front face of the crystal can also contribute to the spectrum, giving a slight absorption edge[1].

X-rays of energies slightly above that of the Si $K\alpha$ line are preferentially absorbed by the dead layer in the crystal. A drop is, therefore, seen in the background spectrum around this energy. The extent of the drop is a function of the thickness of the dead layer.

If two x-rays arrive simultaneously at the detector and are not discriminated by the electronic circuitry, then a contribution to the spectrum will be made at an energy equal to the sum of the two x-rays. This pulse pile-up is most often seen with elements present at high concentrations at energies equal to twice that of the $K\alpha$ radiation. The probability of sum peaks appearing in a spectrum increases with increasing count rate.

Not all of the x-rays detected may originate from the sample being examined. Electrons from the probe beam may strike the final aperture of the column and generate x-rays which may then either be detected or may themselves fluoresce x-rays from areas of the sample other than that intended or from regions inside the microscope specimen chamber (see Figure 3.2.8). The large solid angle for x-ray collection of EDX detectors, in comparison to WDX crystal systems, compounds this problem. Use of apertures thick enough to prevent the x-rays generated in the aperture from passing through into the chamber area or of materials such that the x-rays generated are of sufficiently low energy not to penetrate the aperture can readily solve this problem.

If any electrons were to enter the crystal, they would behave the same as x-rays, generating electron/hole pairs, degrading the resolution, increasing the dead time and changing the background shape[1, 8]. The beryllium windows usually fitted to detectors prevent all electrons ≤ 25 keV from entering the crystal area. Windowless detectors (see Section 3.2.14) have magnetic shielding to divert electrons away from the detector.

3.2.13   Semi-Quantitative Analysis

Peak areas may be used to identify trends in relative concentrations of the

43

elements contributing to a spectrum. The background beneath a peak has first to be removed. A simple straight line is usually sufficient for this type of work. Because the peak area is not only a function of the concentration of the element present but also of the relative x-ray generation efficiency, the efficiency of the detector to monitor x-rays of differing energies, the operating voltage of the microscope and of the other elements present in the sample, the results obtained from this semi-quantitative approach may be quite a way out from the actual composition.

The above factors dictate that semi-quantitative analysis is most applicable to determining the relative concentrations of elements of similar atomic number. The various influences on the peak area are then most alike. It is possible to determine sensitivity factors for elements if a range of samples is available. Taking one of known composition, correction factors may be applied to the peak areas until a result is obtained similar to the expected answer. The same correction factors may then be applied to samples of similar, if not identical, composition to obtain results that may be expected to be not too far out.

If we have peak overlapping, then semi-quantitative analysis becomes impractical and a more quantitative approach is required (see Section 3.2.15).

3.2.14   Light Element Analysis

As was stated earlier (Section 3.2.5), x-rays of insufficient energy, including the $K\alpha$ x-rays from elements of atomic number <11, are unable to penetrate the beryllium window at the front of the detector. This is unfortunate as the light elements are often of great interest. For instance, this work involves study of carbon deposition on oxide surfaces - neither carbon nor oxygen are detectable with a standard energy dispersive detector. If the window is removed from the detector, then the low-energy x-rays, from the elements down to, and including, boron, are able to reach the detector crystal, and be counted. Windowless x-ray detectors usually have a turret arrangement at the front which allows either a standard beryllium window, an ultrathin window (made out a suitable polymeric material) or no window to be placed in front of the crystal. However, for selection of the windowless mode to be safe, and to prevent the detector crystal, which is maintained at low temperatures, from icing up (having condensable species deposited at too rapid a rate onto its face out of the residual gases present in the microscope), it is necessary to have the microscope vacuum at pressures of $<1 \times 10^{-5}$ τ.

When operating with the thin window in place, it is not possible to analyse for nitrogen, as the carbon in the window heavily absorbs the nitrogen x-rays. However, the crystal is then protected from contamination and any stray light present in the chamber, which might otherwise act like stray electrons, producing a large

number of electron/hole pairs and degrading the resolution of the detector.

Quantitative light element analysis is difficult. The absorption correction factors that are found to have to be applied are large, giving the possibility of small measurement errors being multiplied into large concentration errors. Also, these low energy x-rays are greatly affected by the condition of the surface of the sample. Contamination overlayers can have a large attenuation effect on the x-ray signal, especially when low kV (<10 kV) electron beams are used during spot analyses[11]. Carbon is readily deposited onto a sample surface by the cracking of residual hydrocarbon contaminants in the sample chamber by the electron beam. It can then act not only to attenuate the x-ray flux leaving the sample but also to deflect the incoming electrons away from the intended analysis area. Any roughness of the sample surface will also act to reduce the effective x-ray production, with peaks on the surface absorbing the low energy x-rays.

3.2.15   Quantitative Analysis

As stated earlier, electron backscattering and x-ray production levels depend on the elemental nature of the sample being examined. The three factors (Z - atomic number correction to account for backscattering; A - absorption correction to account for generated x-rays that do not manage to leave the sample; and F - fluorescence correction to account for extra x-rays generated by the absorption by an atom of a higher energy, first generation x-ray) that have to be taken into consideration when beginning to quantify an EDX spectrum are incorporated into the ZAF method of quantitative analysis.

There are requirements for the successful application of this technique. In particular, for the Link QX200 system used for some of the work described here, spectra need to be acquired from standards which are:

of known elemental composition;
flat;
of homogeneous composition within the x-ray production volume;
electrically conducting;
stable when irradiated by the electron beam; and
stable under the vacuum present in the analysis chamber.

The ZAF method is based on fundamental principles, and, so, is not empirically-based. The iterative calculations required make it particularly suitable for use on computers.

Castaing's original treatment for quantitative analysis of data from his

45

electron microprobe used intensity values for the characteristic x-rays[12]. Since these can be difficult to determine, intensity ratios are the preferred choice, as suggested by Castaing. As a first approximation,

$$\text{Concentration} = I(\text{specimen})/I(\text{standard})$$

if the standard has a concentration of 100%. The correction factors mentioned previously (Section 3.2.2) now have to be applied and added into this equation.

$$\text{Concentration} = (\text{ZAF factor}) \cdot I(\text{specimen})/I(\text{standard})$$

There are restrictions both on the operating conditions of the microscope used for the analysis and on the sample if accurate quantitative analysis is to be performed. The aim is to minimise the magnitude of the corrections that have to be applied to the data while, at the same time, minimising also the degradation in microscope performance. The absorption correction is usually the largest and this can be reduced by using an electron beam of as low energy as necessary and by analysing the x-rays emitted in directions as close to the path of the electron beam as possible.

The kV of the electron beam governs the penetration depth - the higher the kV the higher the penetration. Of course, sufficient energy must be available to excite the lines necessary to identify the elements present in the sample. 15 - 20 kV is best for most samples, though going up to 40 kV is sometimes necessary to see if higher energy lines are present in order to unambiguously identify elements where there are doubts due to overlapping of lower energy x-rays.

The x-rays leaving the samples at angles close to the incident electron beam are the best to analyse since these will have passed through the minimum depth of sample. At low take-off angles, a greater depth of sample is passed through, maximising the chances for x-ray absorption and maximising the necessary correction factor. The geometry of the stage and microscope analysis chamber may limit the freedom of choice with regard to the x-rays analysed, so routines are included in quantitative EDX software to correct for different take-off angles, but angles greater than 45° are not recommended. At high angles, the assumption that all of the incident electron beam is contained within the sample may no longer hold, as scattered electrons may more readily escape from the sample surface, and so not generate the number and type of x-rays expected by the software.

Before the ZAF corrections can be applied to a spectrum, it is necessary to distinguish overlapping peaks from each other and to subtract away the effect of the background. There are two approaches to this problem. The first attempts to fit a calculated background to the specimen spectrum before using a least squares method

to calculate the peak intensities. The second method subtracts the background and then fits standard peaks, from which the backgrounds have also been removed, to the remainder.

The software provided with the Link Systems QX200 EDX system used for some of the work described here (work not involving a windowless detector) used the second approach. Suppression of the background is achieved by passing the specimen spectrum through a filter which, in effect, only allows through rapidly changing information. The slowly changing background signal is removed. Distortion of the peak shapes occurs, but since the standard spectra that are fitted next have also been passed through the same filter, this effect is cancelled out. The application of the "top hat" filter used to a gaussian function and to a straight line are shown in Figure 3.2.9. Any straight line (e.g. a linear background) yields a zero response out of the digital filter. The gaussian peak is given negative regions either side. By comparing the count rate and peak shape and position recorded off a standard, usually, and in this case, a piece of cobalt (the polished surface does not oxidise to any great extent), both at the time all of the standard spectra are recorded when setting up the Link EDX system originally and when a specimen spectrum is acquired, it is possible to correct for the effects of differing beam current, detector resolution and spectral shift. This is providing that the geometries on both occasions are the same and that none of the above variables are too far from their original values. After the original and current cobalt spectra have been compared by the computer, the specimen spectra are shifted so that their zero channels fall at the same place as when the system was first set up, their gain is adjusted so that the cobalt $K\alpha$ peak position falls in the same detector channel and their peak FWHM values are adjusted to be the same as when the standard peaks were recorded. The peak areas for both cobalt spectra are used as a monitor of the differences in beam current on the two occasions. In effect, these corrections simulate a system where all the operating conditions are stable. Small fluctuations in these parameters are corrected for in the calculations. Only when the system performance degrades dramatically or if it is to be operated under different operating conditions (kV, take-off angle, etc.) do new standard peaks have to be recorded.

A variation of the ZAF routines for the analysis of rough or particulate samples is available on the Link computer. This utilises peak-to-background ratios. These ratios are, to a first approximation, independent of sample geometry.

$$C_i' = \frac{(P/B)_i^{specimen}}{(P/B)_i^{standard}} C_i^{standard}$$

where: C_i' = apparent concentration of element i;
           P = peak intensity;
           B = background intensity; and
           i = element number.

The concentration C_i', determined solely from the peak-to-background ratios, is related to the actual atomic concentration, C_i, by the equation below, that brings in the ZAF corrections.

$$C_i' = \frac{(f_{ZAF})_i^{standard}}{(f_{ZAF})_i^{specimen}} C_i$$

where: C_i = atomic concentration of element i;
           C_i' = apparent concentration of element i; and
           i = element number.

Alterations to the Z and A corrections are required to account for the different characteristic and continuum radiation backscatter coefficients and absorption factors respectively.

Standard peaks with associated backgrounds are used to obtain peak areas from the specimen spectrum. Profiles with scaled peak-to-background ratios are then subtracted from the original spectrum to determine the background associated with each specimen peak. Comparison of these ratios with those on the original standard spectra yields the first approximation to the composition. This approximation is used to calculate a theoretical background which can be subtracted from the original spectrum, and then obtain a better fit to the background, from which better peak-to-background ratios can be got. The ZAF corrections are applied to the new ratios.

This ZAF-PB programme cannot be expected to yield results as accurate as those from the classic ZAF routine for polished samples. The statistical error in the peak-to-background ratio is higher than just measuring peak areas as the background will tend to contain fewer counts overall.

The Kevex Delta EDX analysis system, attached to the windowless capable Kevex Extra Model 3500 detector, uses a standardless means of analysis. Gaussian peak shapes are fitted to the experimental data in order to calculate the quantitative results.

3.2.16   Instrumentation and Experimental

For this work, two sets of energy dispersive x-ray analysis systems were

48

employed. The first, with only a beryllium window detector, and so only able to analyse down to sodium (though the oxygen content of sample may be estimated via the appropriate software routines), was a Link Analytical QX200. This was attached to a Cambridge Stereoscan S180 scanning electron microscope. Standard peak spectra for the quantitative analysis work were recorded off a Micro Analysis Consultants Limited forty-two element standards block and processed as per the instructions provided with the Link system[12, 13]. The spectra were recorded with a beam accelerating potential of 20 kV and a take-off angle of 45°. Cobalt standard spectra were taken either immediately before or after each specimen spectrum. Acquisition times, unless stated otherwise, of 100 s were used. The K x-ray lines were used for all quantitative work.

The other system, complete with a Kevex Extra Model 3500 windowless detector, and so able to analyse for all elements above boron, was a Kevex Delta. This was operating on a Cambridge Stereoscan S150 scanning electron microscope. Though light elements (in particular, carbon) could be detected, quantitative analysis of such elements is not readily possible. However, relative deposition rates may be obtained by determination of the area of the carbon signal (in counts) - the greater the number of counts in the peak, obviously the greater the carbon present on/in the sample.

Both detectors were mounted horizontally on their respective microscopes and the systems were operated in accordance with their manufacturers' instructions.
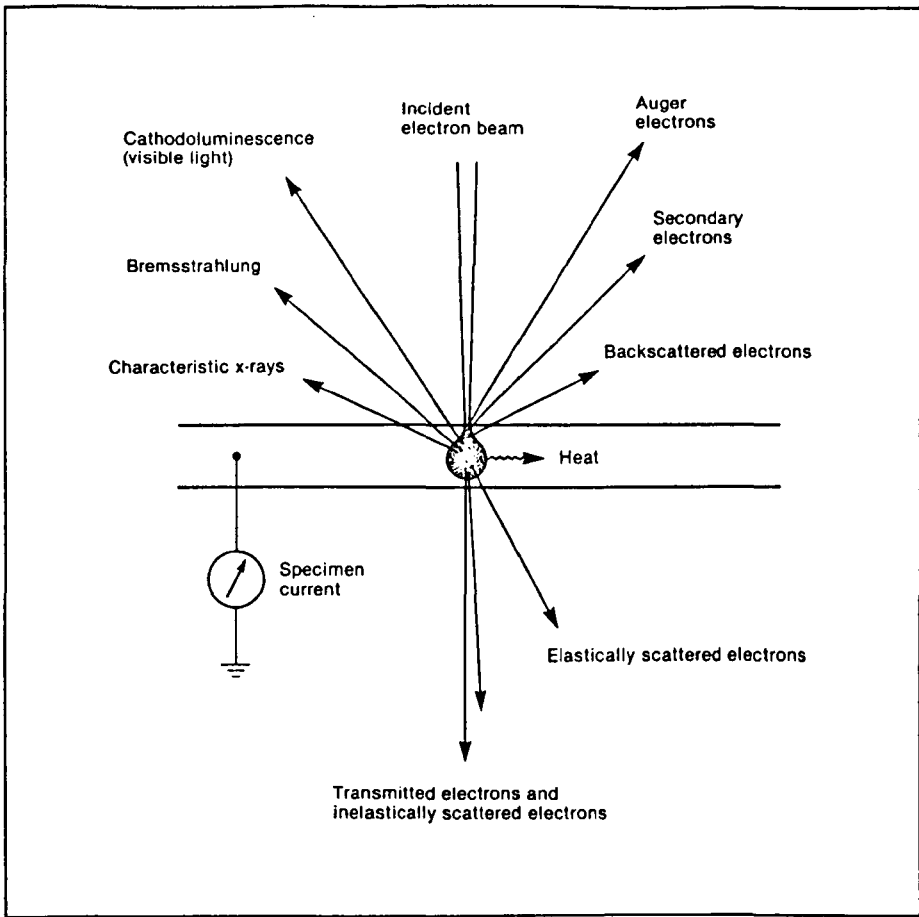
Figure 3.2.1. Schematic illustration of the principal results of the interaction of an electron beam with a specimen.
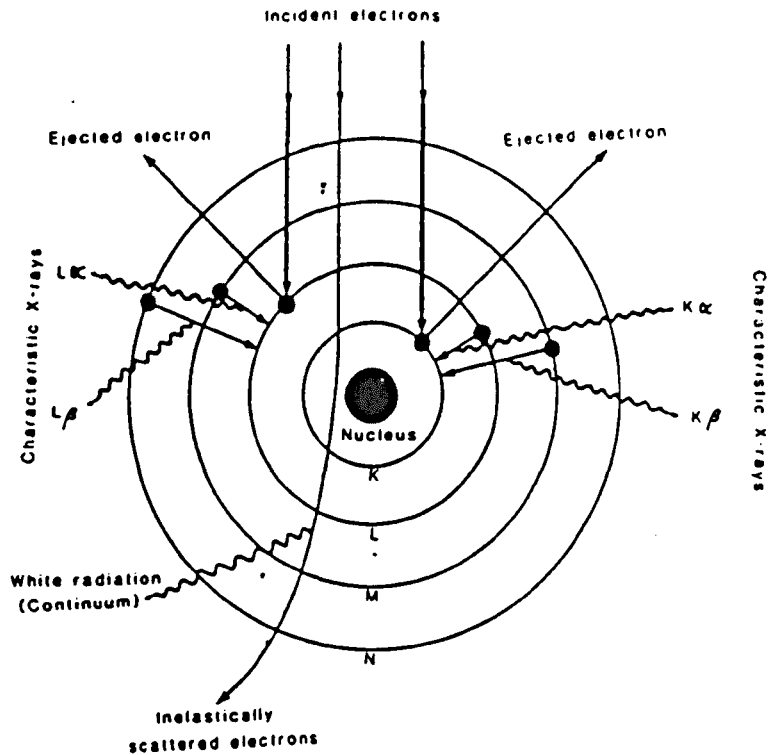
Figure 3.2.2. Production of characteristic x-rays.
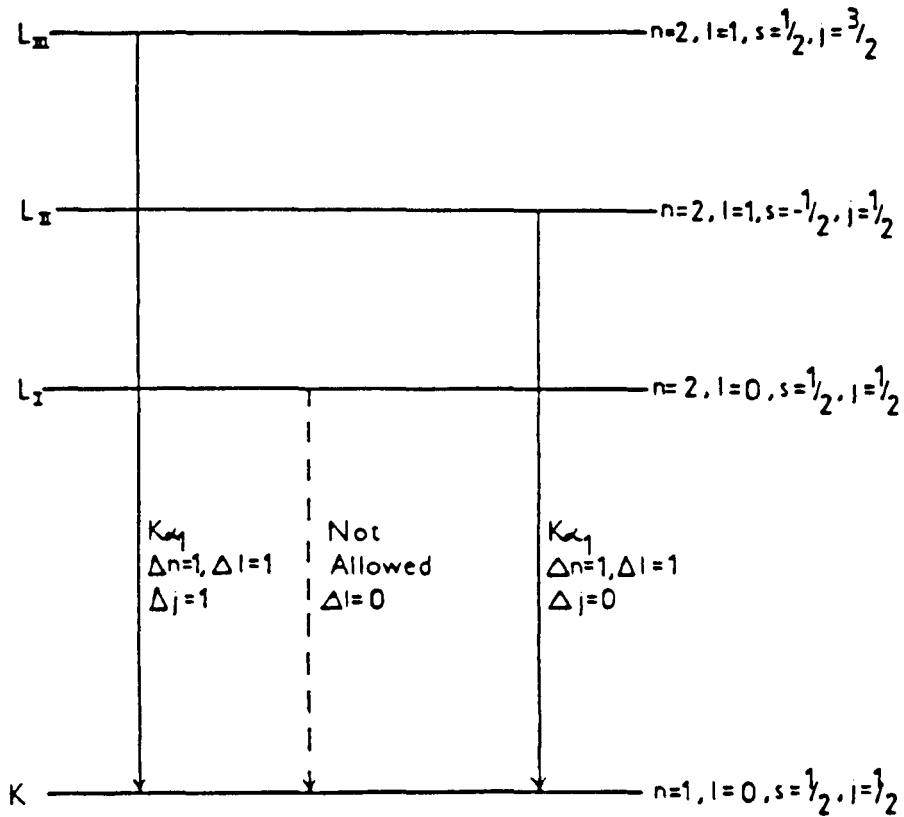
Figure 3.2.3. X-ray emission selection rules, as applied within the K and L shells.
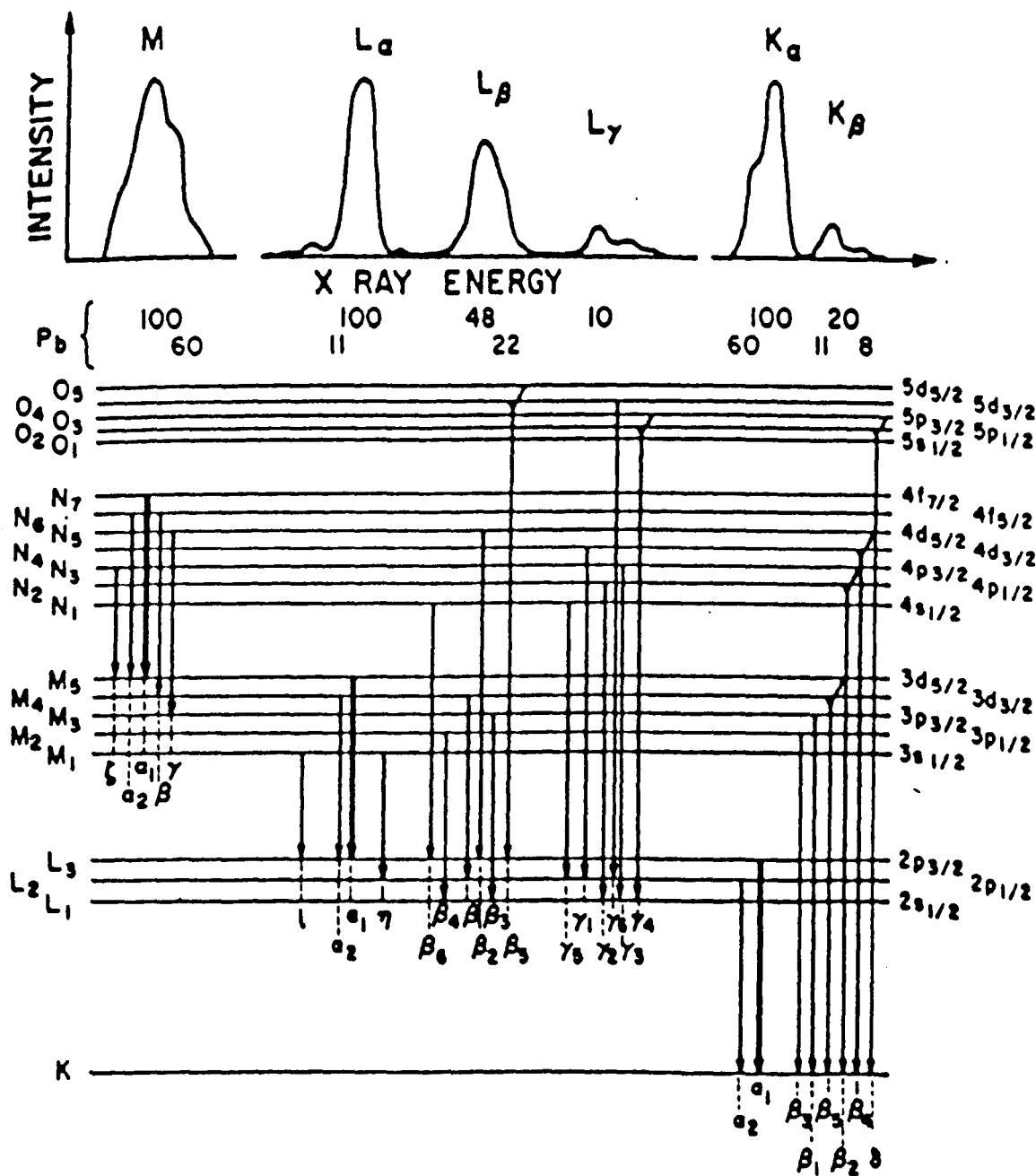
Figure 3.2.4. X-ray emissions possible for high atomic number elements.

52
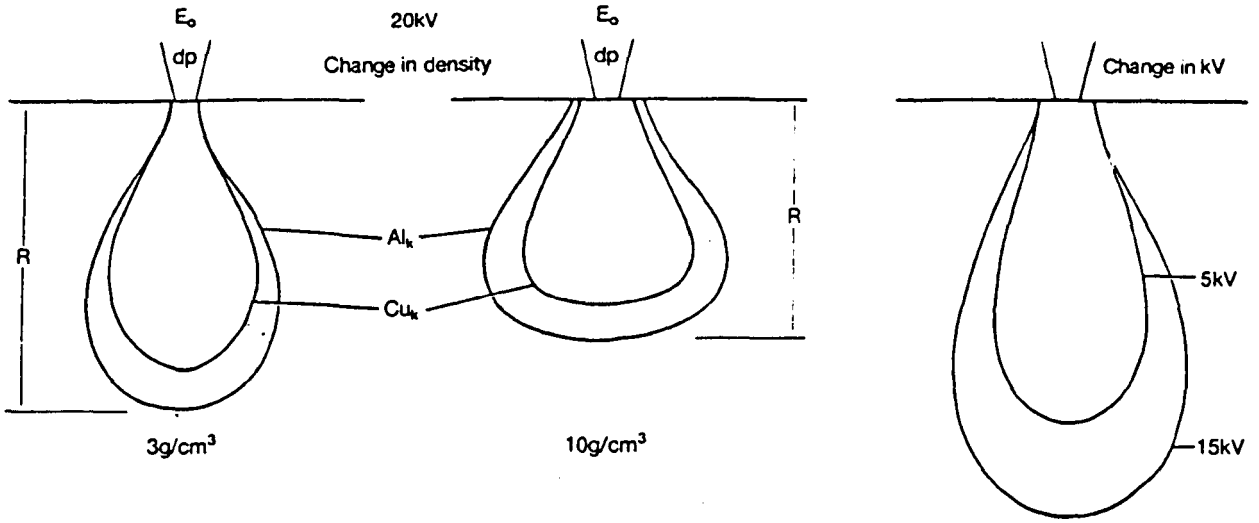
Figure 3.2.5. Variation of the x-ray interaction volume with density and operating voltage.
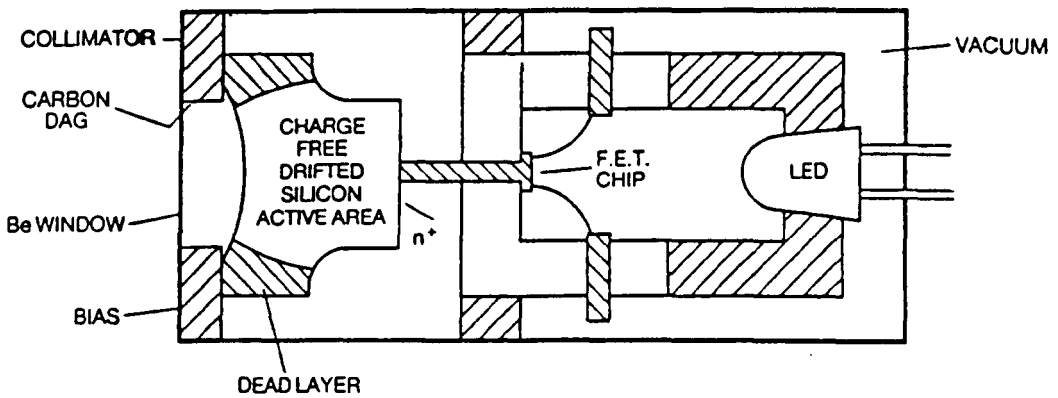
Figure 3.2.6. Schematic of the crystal and FET.
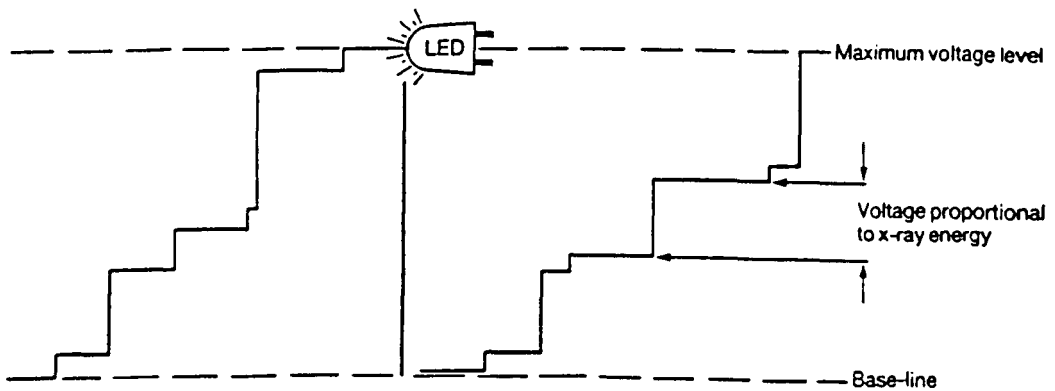
Figure 3.2.7. Schematic of pulsed optical feedback.

53
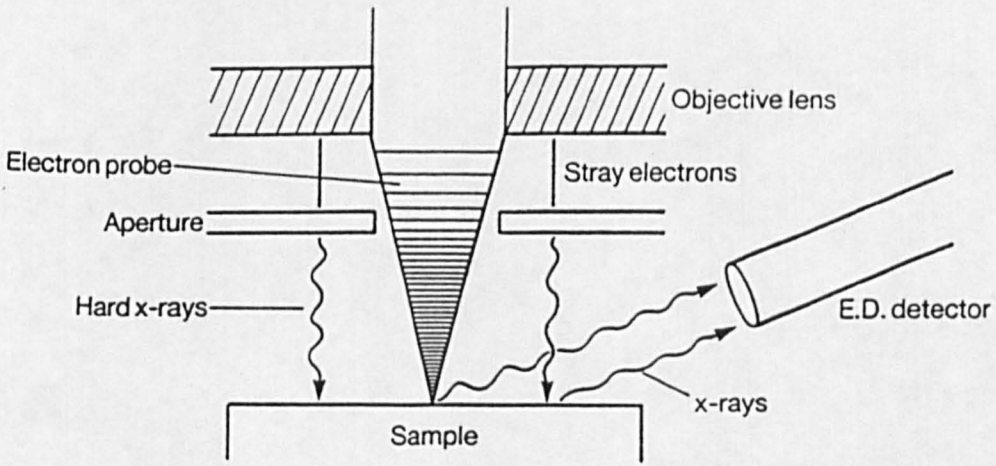
Figure 3.2.8. Sources of stray radiation in an SEM.

Representation of digital
filter applied to a gaussian
function superimposed on a
linear function.

"TOP HAT"

GAUSSIAN PLUS
LINEAR

FILTERED SPECTRUM

Digital filter applied to
linear function.
Result is always 0.

Result of filter-

$2-(1+3)/2 = 0$
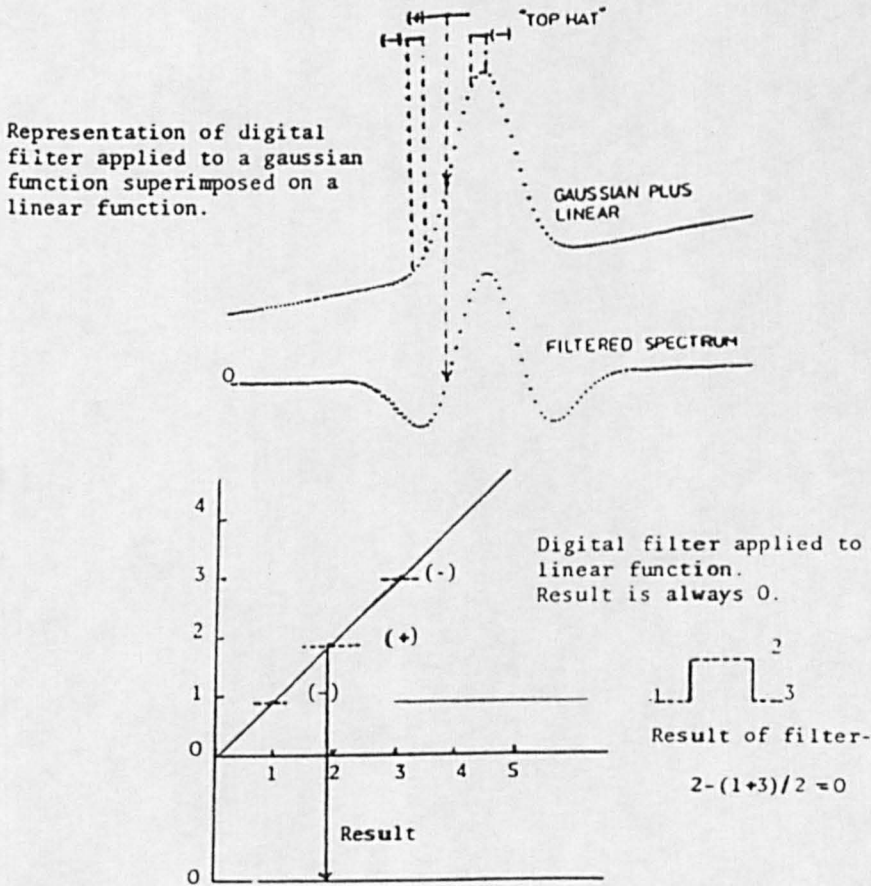
Result

Figure 3.2.9. Result of digital filter on a gaussian and on a straight line.

54

3.3   X-Ray Diffraction (XRD)

3.3.1   Introduction

X-ray diffraction is used to determine the crystalline phases present in a sample. It is also useful for monitoring the purity of a sample, as any additional phases present readily manifest themselves by creating additional features in the spectra. It is not necessary for the sample to be housed in a vacuum, of any degree. All the samples analysed for the current work were exposed to the atmosphere during the analysis. XRD was used to monitor the purity of the reactants used for spinel oxide preparation and of the resultant products. Changes (or otherwise) in the oxides following exposure in the gamma cell were also identified.

3.3.2   X-Ray Production

The rapid deceleration of electrically charged particles of high initial kinetic energy, usually high energy electrons in a vacuum tube, leads to the production of x-rays. A cathode maintained at a high negative potential, such as a tungsten filament located within a sealed and evacuated vessel, acts as the electron source. Alternatively, ionisation of a gas can produce the electrons we require. An anode, positively charged with respect to the cathode, attracts the electrons.

The interaction of the electrons with the anode material gives rise to x-rays with energies characteristic of the element(s) from which the anode is made. The incident electron, on "colliding" with an anode atom, and suffering an inelastic collision, may cause the ejection from that atom of an electron. The vacancy thus left in the anode atom is then filled by a higher energy electron, from the same atom. The energy difference between the two energy levels involved in this vacancy-filling process may then manifest itself by either causing the ejection from the atom of a further higher electron shell electron (the Auger process) or by the emission from the atom of an x-ray. Figure 3.3.1 illustrates how several discrete x-rays may be emitted as electrons from different energy shells fill lower-lying vacancies. The $K\alpha_1$, $K\alpha_2$ and $K\beta_1$ lines, being the most intense from usual sources, are the only ones observed in normal diffraction work. The energies of the $K\alpha_1$ and $K\alpha_2$ x-rays, depending on the anode material, may be too alike to be clearly resolved with the type of equipment generally used. In such a situation, they would be collectively referred to as $K\alpha$ radiation.

On a plot of number of x-rays against energy, the peaks associated with these characteristic energies are superimposed on a continuous background created by the release of kinetic energy, in the form of x-rays, from electrons that have suffered inelastic collisions with atoms in the anode, and consequent losses in kinetic energy

(see Figure 3.3.2).

It is highly desirable to only use one energy of x-rays for diffraction work. A filter, made of a material chosen to preferentially absorb unwanted energies from the spectrum emitted by the source, will leave us with, ideally, only the intense $K\alpha$ radiation to impinge on our sample (see Figure 3.3.3).

3.3.3   Principles of X-Ray Diffraction

A crystal lattice is constructed out of a regular, three-dimensional, arrangement of atoms, or groups of atoms. It may be considered to be built up out of an infinite number of repeated basic units, known as unit cells. The periodic arrangement of atoms gives rise to a continuous variation in electron density throughout the lattice. When an x-ray beam is directed at the surface of a crystal, a proportion of the beam is reflected off the thin surface layer. Another fraction is diffracted by parallel planes of high electron density within the lattice, if the correct conditions are satisfied (see below). The remainder of the beam will pass straight through the crystal. The diffracted beams can provide us with information on the precise structure of the crystal being examined - the spacings between atomic planes within the crystal and the orientation of those planes with respect to each other (i.e. the shape of the crystal unit cell).

The conditions for constructive interference of a diffracted x-ray beam were derived by Bragg and are summarised in the equation below and in Figure 3.3.4.

$$n.\lambda = 2d.\sin\Theta$$

where: n is an integer;

k = x-ray wavelength;

d = spacing between planes of high electron density; and

Θ = angle between the plane of electrons and the path of the incident radiation.

For the case of a crystal with given d-spacings, subjected to irradiation by monochromatic x-rays, only particular angles of incidence will give rise to constructive interference of the diffracted x-rays, and a large signal to be detected. In contrast, the, more efficient, reflection of x-rays off the crystal surface may take place at any incident angle.

Any unit cell may be defined in terms of three dimensions, a, b and c, and three angles, α, ß and γ. For the simplest, cubic, crystal structure, a = b = c and $\alpha = ß = \gamma = 90°$. Six other crystal classes arise through different combinations of

unit cell edge lengths and angles. Table 3.3.1 describes the edge and angle properties of the seven crystal classes while Figure 3.3.5 illustrates the fourteen Bravais lattices that are derived from these.

Planes passing through atoms in the lattice may be described in terms of the Miller indices h, k and l. For a lattice with unit cell dimensions a, b and c, and a plane hkl, the plane intercepts the edges of the unit cell at a/h, b/k, and c/l. If a plane is parallel to a given axis, then its intercept on that axis is at infinity, and the corresponding Miller index is zero. Intercepts on negative axes are indicated by placing a bar over the Miller index. As an example, the plane along one face of a cubic unit cell will have Miller indices h = 1, k = 0 and l = 0, and will, therefore, be known as the [100] plane. The plane cutting the unit cell in half parallel to the [100] plane is described as being the [200] plane. Figure 3.3.6 illustrates the planes present in a cubic lattice. Note that the parallel planes with the smallest spacings are represented by larger Miller indices.

The interplanar spacing, d_{hkl}, is measured perpendicular to the plane. The calculation of d_{hkl} includes the plane indices and the unit cell dimensions and angles. For the cubic system (the easiest to calculate):

$$d_{hkl}(\text{cubic}) = a/\sqrt{(h^2+k^2+l^2)}.$$

With each different crystalline compound having unique arrangements of atoms of differing types, each compound ought to contain unique combinations of d-spacings. So, measuring the diffraction angles for a beam of monochromated x-rays ought to produce a unique spectrum for each crystalline material analysed, and, thus, a means of identification when presented with a material of unknown composition.

3.3.4   The Powder Diffraction Method

So far, x-ray diffraction has been considered in terms of single crystal samples. If a single crystal sample is examined, with, say, the [100] plane diffracting, obviously the only apparent peaks will be those designated [100], [200], etc. Altering the orientation of the crystal with respect to the x-ray source and the detector will remove the [n00] signals from the spectra and introduce, say, [110] peaks. Samples containing many small crystallites may also be examined. If the crystallites are randomly oriented with respect to each other and present in sufficient numbers, a cone of diffracted x-rays will be produced with a semi-vertical angle of 2θ. The intensity of the diffracted beam will be consistent throughout the full 360° of the cone. The resultant spectrum will then be a combination of all the contributions from the full range of diffracting planes.

Powder samples have to be mounted on a substrate that will not give rise to additional peaks in the spectra. A silicon slice, cut so as to minimise reflections within the range of angles of interest, is generally used.

3.3.5 Depth of Analysis

The depth analysed in XRD depends on the incident (and emergent) angle the x-ray beam makes with the surface of the sample. The smaller the incident angle, the shallower the analysis depth. With $2\Theta = 30°$, and, so, an incident angle of $15°$, the analysed depth is only 25% of that as 2Θ approaches $180°$.

Table 3.3.2 (based on information contained within Reference 14) compares the analysis area and depth for XRD with the other techniques utilised in this study.

3.3.6 Instrumentation and Experimental

In a commercial x-ray diffractometer, the diffracted x-ray intensity is monitored as the incident beam angle is varied, typically in steps of 0.01 - 0.02°. The sample surface - detector angle is adjusted to keep it the same as the source - sample surface one. Figure 3.3.7 is a schematic of the sort of diffractometer utilised in the work described in this thesis. The slits before and after diffraction by the sample reduce beam divergence and scatter. The monochromator filters out reflections from unwanted radiation before it reaches the detector. Detectors can either be in the form of Geiger-Müller tubes or scintillation counters. The scintillators consist of a gallium doped sodium iodide crystal. This fluoresces visible light when x-rays impinge upon it. A photomultiplier tube then converts the light into an electrical signal which can then be amplified and displayed.

For the work described here, a Siemens D500 x-ray diffractometer was used. This was controlled by a Digital Equipment Corporation PDP 11/73 microcomputer system and Siemens Diffrac500 software. Unfiltered Cu $K\alpha$ radiation was used, generated in a tube operating at 40 kV and 40 mA. A curved graphite crystal monochromator removed unwanted radiation before it reached the scintillation detector.

In the case of a powder sample, a silicon slice was first wetted with methanol. The powder was then sprinkled onto the slice and evenly distributed over it. After the methanol had evaporated, the powder would be sufficiently well adhered to the slice to allow handling to load the slice into the diffractometer and to record the spectrum. Pellet samples were held in place on the silicon slice by small pieces of BluTack, placed so as to be outside the area irradiated by the x-ray beam. Analysis of

the silicon slice showed the presence of two peaks, at $2\Theta = 116.64°$ and $117.10°$, with relative intensities of 100% and 42.4% respectively (see Figure 3.3.8). BluTack gave a spectrum consisting almost entirely of calcium carbonate, the filler material. A minimum amount of BluTack was used to hold pellet samples in place, and care was taken to try and keep the BluTack out of the analysis region so as to minimise its contribution to the spectra. The area irradiated by the x-ray beam could be seen either by use of a fluorescent material or by using a piece of suitable paper (Siemens plotter paper worked well, though a result was also obtained off of 70 g.m^{-2} dot matrix printer paper), where a permanent discolouration of the paper was brought about by the x-rays.

Large angle range survey scans were generally recorded over the range $15° \leq 2\Theta \leq 155°$, with steps of $0.02°$. Regional scans, to more accurately determine the positions of particular peaks, utilised steps of $0.008°$.

The Diffrac500 software was used to determine the positions of diffraction peaks and, from these, calculate lattice d-spacings. The software included the Joint Committee on Powder Diffraction Standards (JCPDS) spectral database for comparison with experimental spectra.

System	Axial lengths and angles	Bravais lattice
Cubic	Three equal lengths at right angles $a = b = c; \alpha = \beta = \gamma = 90°$	Simple Body-centred Face-centred
Tetragonal	Three axes at right angles, two equal $a = b \neq c; \alpha = \beta = \gamma = 90°$	Simple Body-centred
Orthorhombic	Three unequal axes at right angles $a \neq b \neq c; \alpha = \beta = \gamma = 90°$	Simple Body-centred Base-centred Face-centred
Rhombohedral (tetragonal)	Three equal axes, equally inclined $a = b = c; \alpha = \beta = \gamma \neq 90°$	Simple
Hexagonal	Three equal coplanar axes at 120° Third axis at right angles $a = b \neq c; \alpha = \beta = 90°; \gamma = 120°$	Simple
Monoclinic	Three unequal axes, one pair not at right angles $a \neq b \neq c; \alpha = \gamma = 90° \neq \beta$	Simple Base-centred
Triclinic	Three unequal axes, unequally inclined and none at right angles $a \neq b \neq c; \alpha \neq \beta \neq \gamma \neq 90°$	Simple

The symbol $\neq$ implies non-equality by reason of symmetry. Accidental equality may occur.

Table 3.3.1. Crystal systems and Bravais lattices.

Technique	Volume of sample analysed /cm^3	Spatial resolution /mm	Depth resolution /μm	Elements sensitive to /Z	Knowledge obtained
SEM	5×10^{-14}	$< 1 \times 10^{-5}$	5×10^{-3}	-----	Topo-graphic
BSE	1×10^{-12}	5×10^{-7}	0 - 15	1 $\rightarrow$	Elemental
EDX	1×10^{-18}	1×10^{-3}	1	11 $\rightarrow$	Elemental
Window-less EDX	1×10^{-18}	1×10^{-3}	1	6 $\rightarrow$	Elemental
XRD	1×10^{-8}	5	2	1 $\rightarrow$	Crystallo-graphic
XPS	1×10^{-9}	1	5×10^{-3}	3 $\rightarrow$	Elemental/chemical

Table 3.3.2. Comparison of technique resolutions.
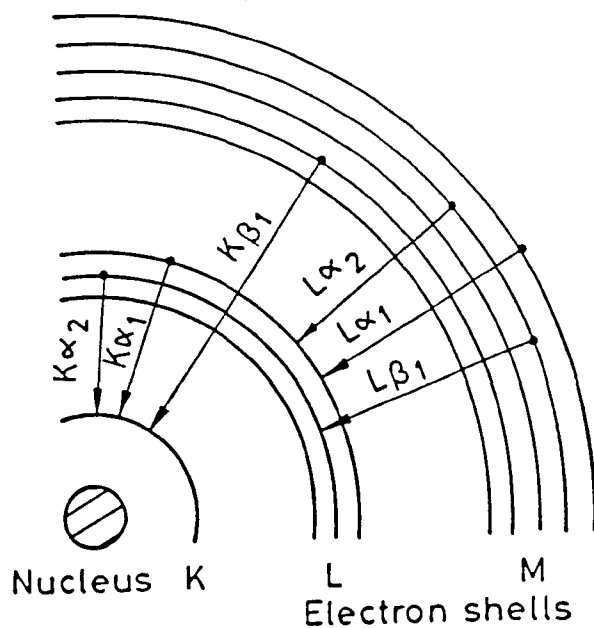
Figure 3.3.1. Origin of characteristic x-ray lines.
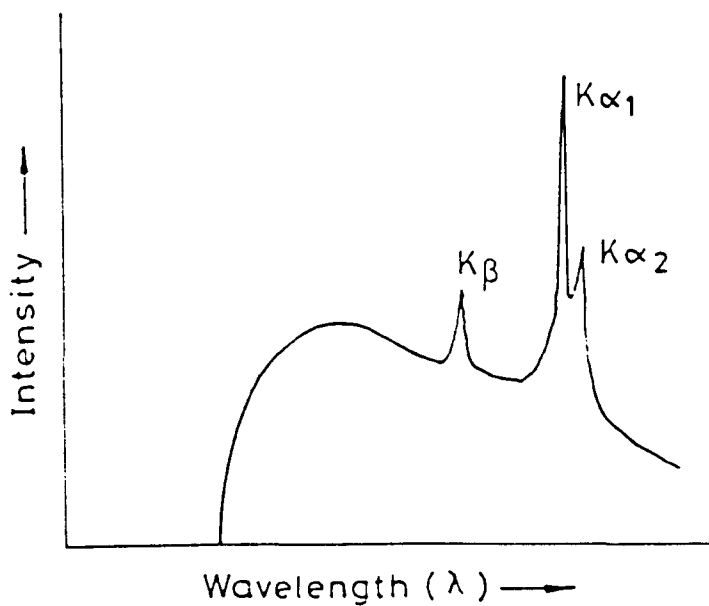
Figure 3.3.2. X-ray spectrum emitted by a typical tube showing characteristic bands superimposed upon a continuous background.
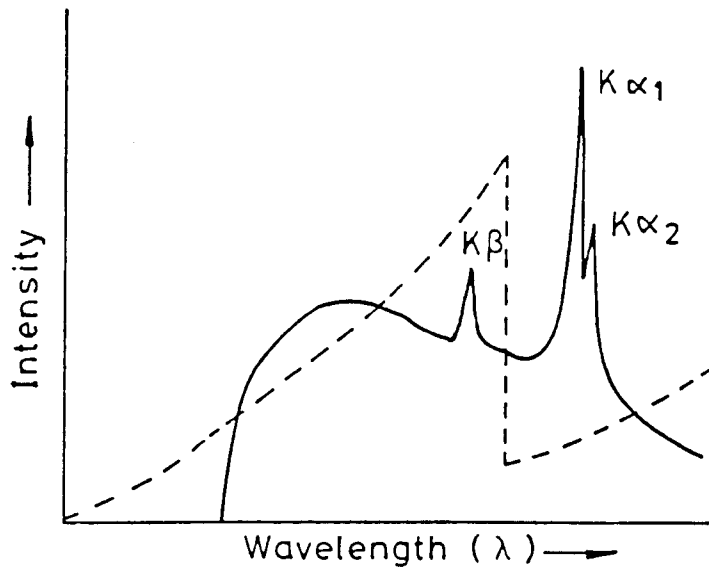
Figure 3.3.3. X-ray spectrum emitted by a typical tube with the dotted line showing the absorption characteristics of a suitable material for a *Kβ* filter.
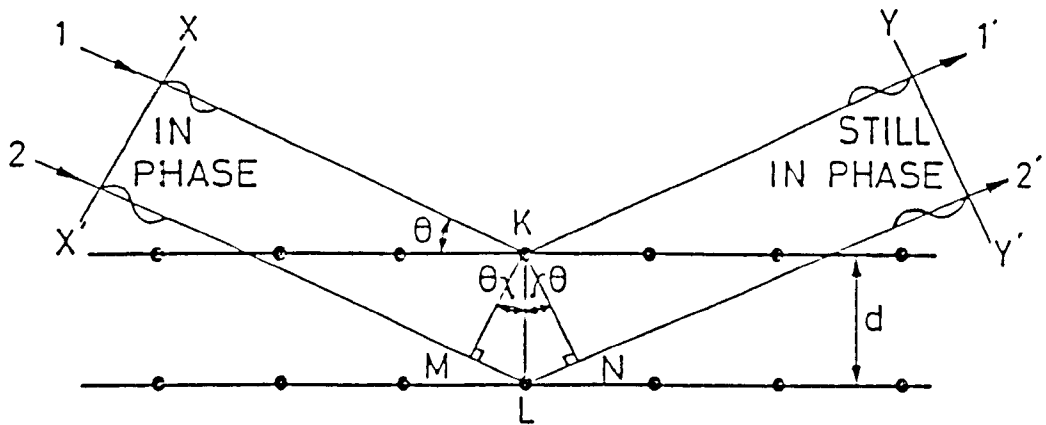
PATH DIFFERENCE FOR RAYS 1K1′ & 2L2′ IS

ML + LN = d sin θ + d sin θ

SCATTERED RAYS 1′ AND 2′ WILL BE COMPLETELY

IN PHASE IF THIS PATH DIFFERENCE IS EQUAL TO

A WHOLE NUMBER n OF WAVELENGTHS,

$$n\lambda = 2\,d\,\sin\theta \qquad \text{BRAGG'S LAW}$$

Figure 3.3.4. Diffraction of x-rays by a crystal.

Simple Cubic(P)

Body-centred Cubic (I)

Face-centred Cubic(F)

Simple Tetragonal (P)

Body-centred Tetragonal (I)

Simple Orthorhombic (P)

Body-centred Orthorhombic (I)

Base-centred Orthorhombic (C)

Face-centred Orthorhombic (F)

Rhombohedral (R)

Hexagonal (P)

Simple Monoclinic(P)

Base-centred Monoclinic(C)

Triclinic (P)
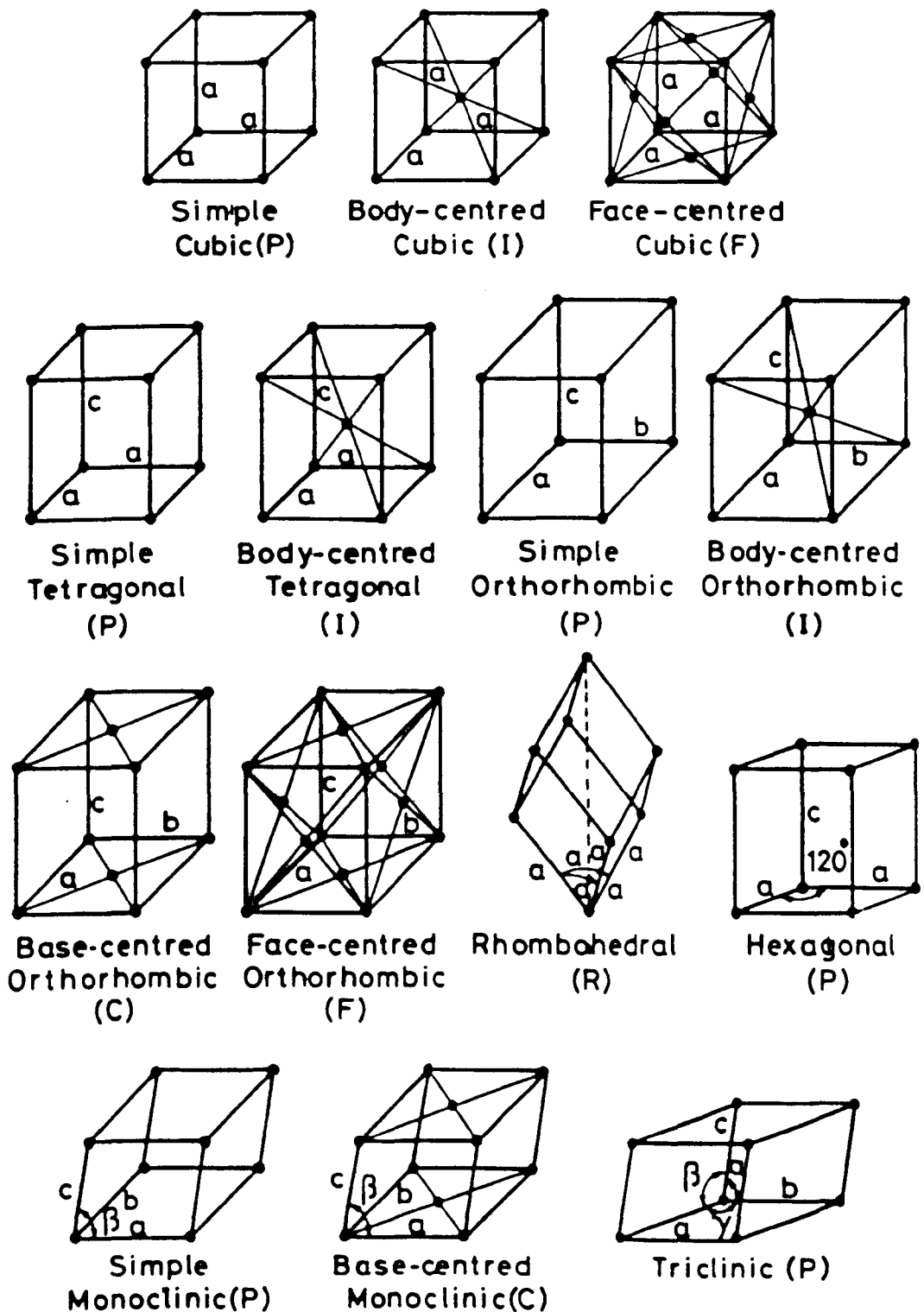
Figure 3.3.5. The fourteen Bravais lattices.
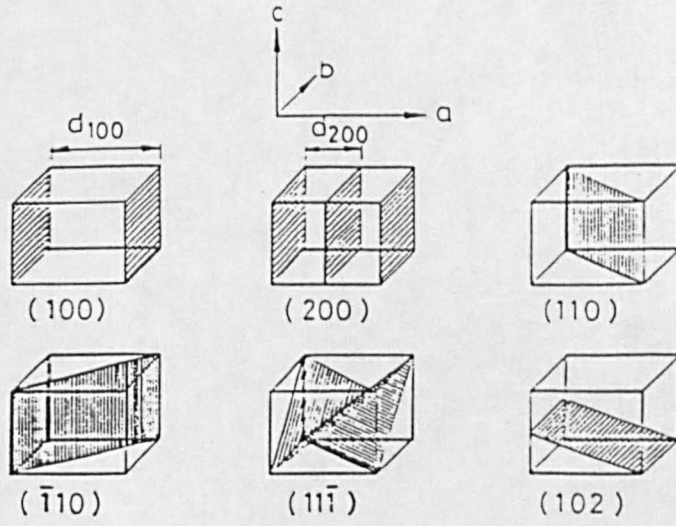
Figure 3.3.6. Miller indices of lattice planes.
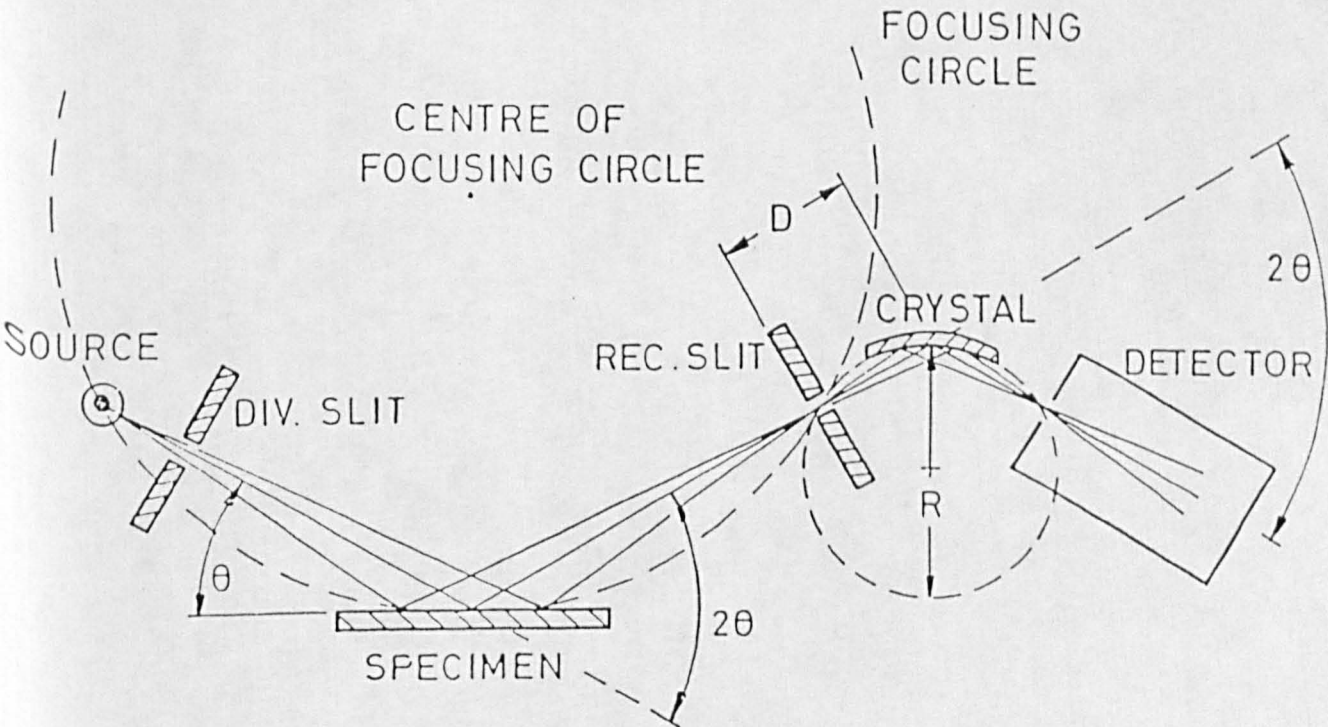
Figure 3.3.7. X-ray diffractometry with a curved-crystal monochromator in the diffracted beam.
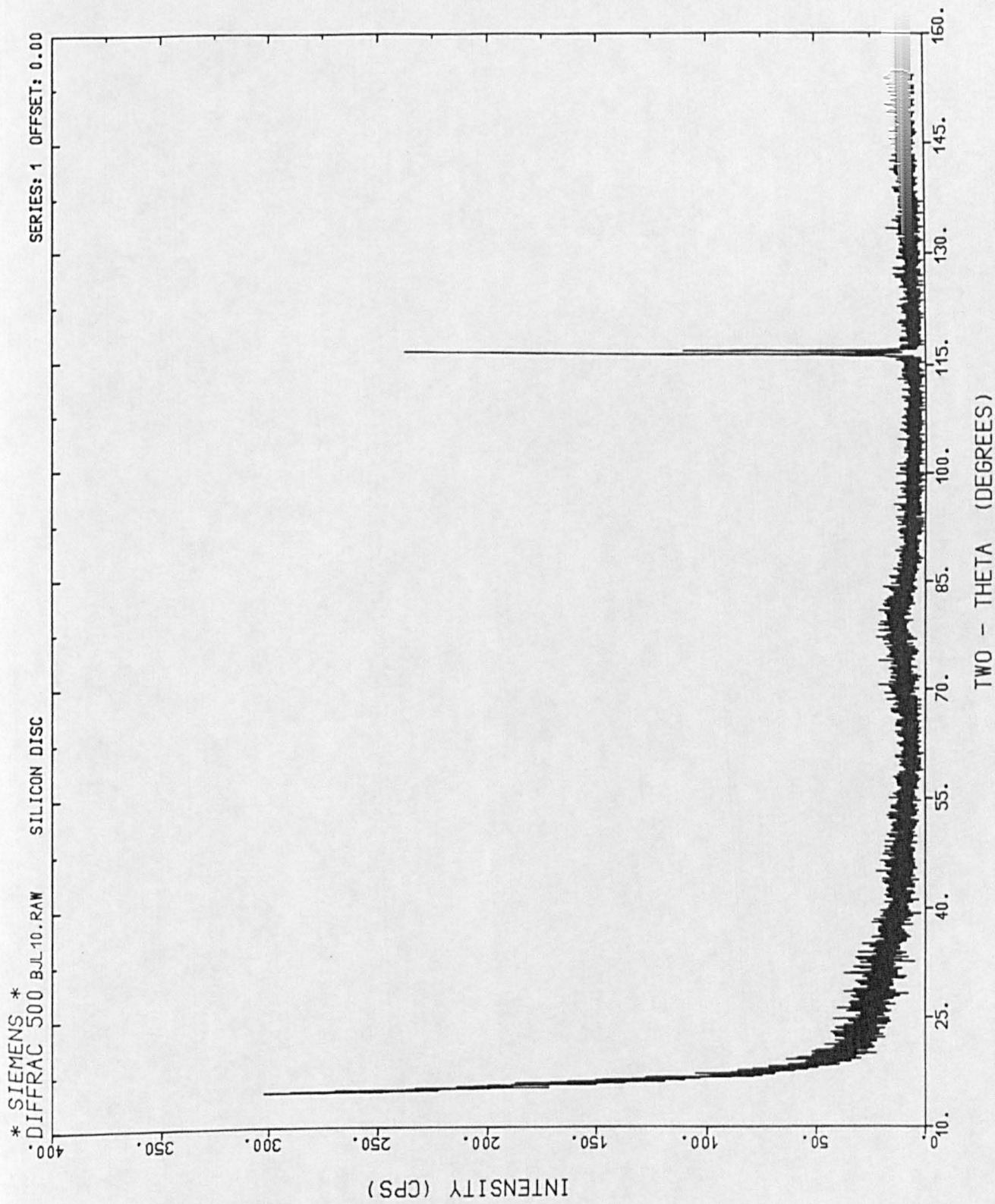
Figure 3.3.8. XRD spectrum of silicon disc sample holder.

3.4   X-Ray Photoelectron Spectroscopy (XPS)

3.4.1   Introduction

X-ray photoelectron spectroscopy is a surface sensitive technique, unlike XRD and EDX, in that it is only the outer 1 - 10 nm of the sample that is analysed. Figure 3.4.1 (from Reference 15) schematically illustrates the realms of surface, thin film and bulk analysis. XPS has comparable surface sensitivity to the likes of Auger electron spectroscopy (AES), and is only fractionally less surface specific than the sputtering secondary ion mass spectrometry (SIMS) and scanning ion microscopy (SIM) techniques. The inability to focus x-rays does mean, however, that a large sample area is examined. In the case of the XSAM 800 instrument used for this work, an area of some 10 mm diameter is illuminated by the x-ray source.

The accurate determination of the energies of electrons caused to be emitted from the sample by the incident x-ray beam allows the determination not only of the elements present in the sample but also of the chemical states of those elements. It is this latter ability that gives XPS its alternative name of ESCA, electron spectroscopy for chemical analysis. By application of appropriate correction factors to the peak areas, quantification of spectra is possible.

XPS has been used in the work described here to analyse all samples before and after exposure in the gamma cell.

3.4.2   Basic Principles of X-Ray Photoelectron Spectroscopy

Jenkin, Leckey and Liesegang[16] have written a review of the development of XPS from the beginning of this century to the point, around 1960, where it enters the world of commercial availability. Hertz discovered the photoelectric effect in 1887. He found that a spark would more easily cross a gap between two electrodes if ultraviolet light irradiated the space. Thompson and Lenard showed that this effect was due to electrons being emitted from the electrodes. The strength of this current was found to be proportional to the intensity of the light if the light was of a frequency above some threshold.

The explanation of this is due to Einstein, who put forward the theory that light came in quanta, of energy:

$$E = h\nu$$

where: h = Planck's constant /eV.s; and

ν = frequency of incident x-ray /s^{-1}.

The threshold frequency represents the minimum energy, ϕ, required to excite an electron from an electrode atom Fermi level to the continuum. If the energy in the light quantum is greater than this minimum, the excess energy appears as kinetic energy of the emitted electron.

$$E_K^{max} = h\nu-\phi$$

For electrons emitted from lower lying orbitals, the binding energy of the electron has to be overcome, reducing the kinetic energy of the emitted electron further:

$$E_K = h\nu-\phi-E_B, \text{ or}$$

$$E_B = h\nu-\phi-E_K$$

where: E_B = electron binding energy /eV;
         h = Planck's constant /eV.s;
         ν = frequency of incident x-ray /s^{-1};
         E_K = kinetic energy of emergent electron /eV; and
         ϕ = surface work function /eV.

An atom can be considered as a central, positively charged, nucleus, each element having a different positive charge, surrounded by a unique, for each element, set of electron orbitals. The electrons are divided, in the first instance, into outer lying, valence electrons, responsible for interatomic bonds, and inner core electrons. Valence electrons require energies in the ultraviolet region in order to escape from the atom. The energies required to liberate from the atom an inner, core electron is greater and can be supplied in the form of x-rays. Ultraviolet photoelectron spectroscopy (UPS) is the study of the binding energies of the outer, valence electrons and has applications in the study of bonds between atoms. X-ray photoelectron spectroscopy looks at the core energy levels. The XPS process is illustrated in Figure 3.4.2.

The energy spectrum of emitted electrons under x-ray bombardment of the sample is characteristic for all elements, resulting from the unique nuclear charge and core orbital energies. Narrow photoelectron peaks, 1 - 2 eV wide, are superimposed on a background of inelastically scattered electrons. Bond formation by an atom causes slight shifts in the core energy levels, affecting the position of the peaks in the photoelectron spectrum. The shifts, which are generally of energies large enough for the resolution of the technique, say >0.1 eV, to detect, don't prevent identification of the elements in the sample, but, instead, provide us with additional information on the chemical environment and oxidation state of the element. This change in peak position

is known as the chemical shift and is the most important aspect of XPS.

Innes carried out XPS experiments in 1907. Photoelectrons were energy selected using a magnetic field and trained towards photographic plates. Einstein's explanation of the photoelectric effect was not generally accepted at this time, however.

The likes of Robinson, Moseley and Rawlinson, working in Rutherford's Manchester laboratory, carried out much work on radioactivity and the nuclear atom model, including deriving the first form of the basic equation for XPS. Their work continued through to the First World War.

After the War, work resumed in both Britain and the United States. Several scientists, such as de Broglie, flirted with XPS only to return to other, more established, techniques. It was left to Robinson, variously at Cambridge, Edinburgh, Cardiff and London, to push XPS on, through until 1940. He was the first to present chemical shift (see Section 3.4.4) data, on chromium metal and hydroxide. However, the accuracy of the technique could still not compete with x-ray absorption and emission.

Steinhardt and Serfass came to the conclusion, after the Second World War, that XPS could be usefully applied to studies such as corrosion, plating and catalysis. However, their apparatus made no significant advances compared to pre-War models. Instead, it was Siegbahn and co-workers[17, 18], in Uppsala, who firmly established XPS as a powerful, and commercially practical, surface chemical analysis technique. Figure 3.4.3[18] compares gold spectra recorded by Robinson[19] and Siegbahn et al. It was this improvement in resolution that allowed chemical information to be readily extracted from the spectra.

3.4.3   XPS Peak Nomenclature

XPS peaks are named after the core level from which the electron has been excited. An electron from the iron *2p* orbital gives an Fe *2p* peak. Ionisation of an *s* orbital leaves a single energy ionic state. However, *p*, *d* and *f* orbitals create two states of different energies, appearing in spectra as two peaks, of unequal intensities. This arises from the interaction between the orbital and spin angular momenta, splitting the level. The j quantum number distinguishes these states, so that we get, for instance, for the ionisation of our iron *2p* electron, the two peaks Fe $2p_{1/2}$ and Fe $2p_{3/2}$. The subscripts are the possible j values for the ion.

The relative intensities of the two peaks in the resulting spectrum are proportional to 2j + 1. Thus, after removal of a *2p* electron, j values of $1/2$ and $3/2$

result, giving an intensity ratio of 2:4. Table 3.4.1 summarises the j values and the intensity ratios for *s*, *p*, *d* and *f* orbitals.

3.4.4 *The Chemical Shift*

As the energies of the valence orbitals change with differing chemical environment and oxidation state, the core levels are also affected, giving changes in the binding energies, and, so, peak positions on the binding energy scale. XPS can detect these chemical shifts and give us not only the elemental composition of a sample, but also the chemical states of its constituents. Figure 3.4.4 (taken from Reference 18) illustrates this principal with the spectrum from ethyl trifluoroethanoate. The four carbon atoms in this molecule each exist in a different chemical environment, giving different chemical shifts and, so, peaks at different binding energies. The more electronegative the environment around the carbon, the higher the C *1s* binding energy. It so happens, with this example, that the C *1s* signals appear in the same order as the corresponding carbon atoms, if the figure is drawn as given.

Calculations of binding energies from fundamental principles have been made (see, for instance, Reference 20).

3.4.5 *The Electron Inelastic Mean Free Path*, λ

It is the inelastic mean free path that give XPS its surface sensitivity. The depth of penetration of the incident x-ray into the sample is not the determining factor here (in EDX analysis, it is the electron penetration depth that helps set the analysis volume). Instead, it is the limited energy of the emitted electrons that determines the analysis depth. The kinetic energies of up to 1486.6 or 1253.6 eV (using aluminium or magnesium x-ray sources) of the electrons and the inelastic collisions that they may encounter leaving the body of the sample ensure that the average depth from which an electron may escape is of the order of 1 - 10 nm. Photoelectrons will be generated deeper into the sample, but will not be able to escape and be detected. Figure 3.4.5 shows how the electron escape depth is a function of energy. Electrons of low kinetic energy are unable to cause many of the energy loss processes (see Section 3.4.13) to occur, and, so, are unlikely to interact with the sample and can, therefore, escape from relatively deep inside the sample. High kinetic energy electrons will suffer inelastic collisions with the sample, but will be likely to still have sufficient energy to escape from the surface. The greatest surface sensitivity, at the minimum point in the mean free path curve, lies at electron kinetic energies of 30 - 200 eV, where the mean free path is of the order of 1 - 8.5 nm. For electron kinetic energies above 200 eV, the inelastic mean free path is approximately proportional to the square root of the energy. 98.5% of the analysed photoelectrons will tend to come from a depth up to

three times the mean free path.

3.4.6 Surface Sensitivity Enhancement

The surface sensitivity of XPS may be further increased by detecting electrons emitted at low angles relative to the plane of the surface of the sample. This, effectively, increases the distance between any one electron generation point and the sample surface. If the mean free path is unchanged, then the depth of sample analysed is decreased. Figure 3.4.6 illustrates this point. The effect of any surface contamination layer is greatly increased at shallow take-off angles. Also, the sample has to be flat, on a sub-micron level, if shadowing of emerging electrons is not to be an additional consideration that has to be made.

On single crystal materials, photoelectron diffraction may occur. Here, emitted photoelectrons, acting in a wave-like manner, are diffracted by the crystal planes, and will constructively or destructively interfere, in accordance with Bragg's law (see Section 3.3). Then, the measured photoelectron signal will suffer enhancement or diminution depending on the take-off angle used.

Varying the take-off angle is one way to attempt to determine the depth distribution of an elemental state. Another is to monitor the relative intensities of low and high binding energy lines from the same state. If high binding energy (= low kinetic energy) lines are reduced in intensity relative to the spectrum from a bulk standard of the same element, then it is likely that the element is located below the immediate surface of the sample, with the lower kinetic energy electrons suffering more from attenuation.

3.4.7 Photoionisation Cross Section

A knowledge of the cross sections for photoionisation of the elements is required prior to any attempt at quantification. Emitted photoelectrons will be attenuated by the sample, in accordance with the inelastic mean free path for electrons of the particular energy in question. Surface contamination will further reduce the signal intensity. Loss of strength in the parent line due to the creation of satellites of various kinds and multiplet splitting (see Section 3.4.13) must also be taken into consideration.

Valence band orbitals have low cross sections for ionisation by x-rays. If these regions need to be analysed, either long acquisition times are required to obtain the desired statistics or ultraviolet sources have to be turned to.

71

3.4.8 Photoelectron Peak Intensities

As a first approximation, the peak intensity, or area, for a particular element in a particular chemical environment will be proportional to its concentration.

$$dI_A = kFD\sigma dx$$

where: I_A = photoelectron peak intensity for electrons of a particular energy from atoms of type A /counts;

   k = proportionality constant to include instrumental electron detection efficiency and analyser transmission /counts.m^2;

   F = x-ray flux /m^{-2};

   D = density of atoms of type A in the sample /m^{-3};

   σ = photoelectron cross section /m^{-2}; and

   dx = thickness of a layer at a distance x from the surface /m.

The above equation has to be modified to take into account electron attenuation due to inelastic scattering as an electron attempts to leave the body of the sample. This reduction in electron yield is exponentially dependent on the depth within the solid that the electron is generated, giving us:

$$dI_A = kFD\sigma e^{(-x/\lambda)}dx$$

where: λ = electron inelastic mean free path /m.

Integration of this equation to give us the result for an infinitely thick sample yields:

$$I_{A\infty} = kFD\sigma\lambda.$$

For a film of thickness d and electrons detected normal to the sample surface, the integration gives:

$$I_{Ad} = kFD\sigma\lambda(1-e^{(-d/\lambda)})$$
$$= I_{A\infty}(1-e^{(-d/k)}).$$

3.4.9 Quantitative Analysis

We very often will require quantitative results from our XPS analysis. The application of sensitivity factors to the peak areas is the usual approach to this[21, 22]. For a spectrometer operating in the fixed analyser transmission (FAT) mode (where the analyser is operated at a constant pass energy while the input lens sweeps across the energy scale to allow only those electrons of the desired energy into the analyser), such as the XSAM 800 used in this work, we can say that:

$$I = nf\sigma\Theta y\lambda AT, \text{ or}$$

$$n = {}^I/_{f\sigma\Theta y\lambda AT}$$

where: n = atomic concentration for the element of interest /atoms.cm^{-3};

f = x-ray flux /photons.cm^{-2}.s^{-1};

σ = photoelectric cross section for the orbital of interest /cm^2;

Θ = angular efficiency factor for the instrumental arrangement, based on the photon path-emitted electron angle;

y = photoelectric effect efficiency factor;

λ = inelastic mean free path for the photoelectrons of interest /cm;

A = sampling area /cm^2; and

T = detection efficiency.

If we collect together, as S, the terms in the denominator, then we get, for two elements:

$$\frac{n_1}{n_2} = \frac{I_1/S_1}{I_2/S_2}$$

Assuming that the S_1/S_2 ratio is fairly matrix independent, this relationship can be applied to any sample. It then only remains to establish a set of relative S values to allow us to quantify spectra. For an element x:

$$C_x = \frac{n_x}{\Sigma_i n_i} = \frac{I_x/S_x}{\Sigma_i I_i/S_i}.$$

The sensitivity factors used in this study[22] are related to that of F $1s$, set equal to unity. As the spectrometer used is different from that used by Wagner, Davis, Zeller, Taylor, Raymond and Gale[22], there may be some slight errors in the quantitative analyses presented here. However, as the present work was based on changes in relative compositions between related samples, any errors ought not to affect the conclusions drawn.

The peaks that are used in such quantification have first to be separated from the inelastically scattered electron background. The simplest method of removing the background is to draw (or have the computer draw) a straight line between two points, either side of the peak of interest, chosen to be representative of the background signal. On the DS800 software used on the XSAM 800, running on a Digital Equipment Corporation PDP 11-73, it is possible to average the data for a few points either side of the chosen one to improve on the representation. The area

beneath this line is then subtracted from the peak before the area is calculated. The Shirley background[23, 24] subtraction algorithm assumes that the intensity of the background is proportional to the integrated photoelectron intensity for all binding energies less than the point in question and that the background consists solely of inelastically scattered electrons. A Shirley background has a curved profile, with the greatest rate of change of background intensity directly underneath the maximum point of the peak (see Figure 3.4.7). Shirley backgrounds were used for the work described here. Tougaard and co-workers[25] have developed background calculation algorithms that take into account both inelastic and elastic scattering of electrons.

After subtracting the background, it is then often necessary to determine the contributions of overlapping peaks to any particular spectral region. This was done within the Kratos DS800 software. Combinations of gaussian, lorentzian or previously acquired standard peaks can be fitted to the experimentally determined peak envelope. The software is then able to determine the best fit, within the user defined boundary conditions, to that data of the chosen number of peaks. A least squares method is used. Obviously, the computer relies on the user supplying it with a chemically justified number of peaks and sensible limiting peak height, width and position values. Better fits (as determined by the Fit Index parameter displayed on the computer screen) can always be obtained by including more peaks in the calculations, but these may not be justified with the knowledge of the sample that we have prior to the XPS analysis.

3.4.10   Vacuum Requirements

It is necessary to carry out the XPS experiment within an ultrahigh vacuum environment. The low background pressure then ensures a minimum in the number of collisions between ejected photoelectrons and residual gas molecules, which might otherwise reduce the signal intensity. It also reduces contamination of any samples that have been cleaned, using an ion beam, or fractured *in situ*. At 1×10^{-6} τ, one monolayer of gas will adsorb onto the surface of a sample in approximately one second, assuming a sticking probability of one. All modern XP spectrometers are constructed out of stainless steel or Mu-metal, with copper or gold gaskets between adjacent components. The systems regularly have to be baked out, especially if the vacuum has had to be broken for any reason, e.g. removal of a component from the analysis chamber, to drive adsorbed species off the chamber walls.

A variety of pumps and vacuum gauges may be used to obtain and monitor the required conditions inside the spectrometer. References 26, 27, 28 and 29 describe the types of pumps and gauges commonly found on UHV equipment, each having

their own advantages and disadvantages. These may be present on any particular instrument in any number of combinations.

3.4.11   X-Ray Sources

As in x-ray diffraction, an x-ray source for XPS contains a target that is bombarded by high energy electrons attracted to its high positive potential. The anode potential and electron current are controlled to better than 1%. Core and valence electrons in the target atoms are removed. Relaxation of a core vacancy brings about the emission of an x-ray, whose energy depends on the energy difference between energy levels in the atom and will be in the x-ray region of the electromagnetic spectrum. Any one target material will give rise to a set of x-rays, of discrete energies and differing intensities. Commonly, and for the work described here, aluminium and magnesium targets are used. The $K\alpha$ lines for these two elements lie at 1486.6 and 1253.6 eV, respectively. Figure 3.4.8[15] illustrates a typical dual anode x-ray source.

A thin aluminium foil between the x-ray anode and the sample prevents any high energy electrons from entering the analysis chamber and allows the vacuum within the source to be isolated to some extent from that in the main chamber. The foil also reduces the effect of radiant heat from the source filament on the sample.

3.4.12   X-Ray and Photoelectron Line Widths

There are several contributors to the ultimate measured full width, half maximum, FWHM, of an XP peak. If we assume that all the contributors have gaussian forms, the total line width can be represented by:

$$FWHM = (\Delta E_x^2 + \Delta E_n^2 + \Delta E_s^2)$$

where: ΔE_x = linewidth of the x-ray source /eV;

ΔE_n = natural width of the core level /eV; and

ΔE_s = absolute resolution of the analyser /eV.

For the aluminium and magnesium sources used in this work, the line widths are 0.85 and 0.7 eV respectively[30]. Use of a monochromator can reduce these down to around 0.2 eV, but at the expense of a reduction in x-ray flux to the sample. No monochromators were used in the present work.

Core level energy widths are a consequence of the uncertainty in the lifetime of the ionised state after photoemission. The Heisenberg uncertainty principle, applied to this question, gives lifetimes $\leq 1 \times 10^{-14}$ s. The shorter the lifetime, the broader the resulting peak.

The contribution to the peak widths of the analyser resolution is discussed in Section 3.4.15, but is small compared to that from the x-ray line width.

It is found that photoelectron lines of insulators are ~0.5 eV broader than those of conducting solids.

The XSAM 800's Ag $3d_{5/2}$ FWHM measured using aluminium x-rays was found to be 1.3 eV. Using the magnesium source, a value of 1.2 eV was obtained.

3.4.13 Spectral Artifacts

Apart from the intended photoelectron peaks, several other features may appear in an XP spectrum.

The removal of core electrons from a sample atom leaves it in an excited state. The vacancy may be filled in one of two processes. The first step in each relaxation process is the same, namely the dropping of a higher energy electron into the vacancy. The energy corresponding to the energy difference between the two orbitals concerned may then either appear as electromagnetic radiation, i.e. an x-ray (as in energy dispersive x-ray analysis, see Section 3.2) or be given to another higher level electron. This energy, if sufficient, can cause this third electron to escape from the atom, after overcoming its binding energy. This is the Auger process, named after its discoverer, Pierre Auger, and forms the basis of Auger electron spectroscopy, another surface sensitive analytical technique, though one not employed in the work described here. The Auger process for relaxation of the ionised atom occurs more than 99% of the time under XPS conditions[21].

Auger peaks in an XP spectrum may be distinguished by changing the energy of the x-ray source. On the instrument used for this work, both an aluminium and a magnesium source were available. If the spectra are being displayed with binding energies along the x-axis, then changing the x-ray energy by switching to a different target material will have no effect on the positions of photoelectron signals (though their widths may change - see Section 3.4.12). However, on, say, switching from an aluminium to a magnesium source, Auger peaks will move to positions 233 eV (the energy difference between the two x-rays) lower. The decreased energy available in the x-ray will reduce the kinetic energies of all the photoelectrons produced from the sample. The Auger electrons, with energies dependent only on the atomic energy levels and independent of the energy of the source x-ray, will have higher-than-expected kinetic energies, compared to when aluminium is the excitation source, and, so, appear to have come from levels with lower binding energies.

76

Samples containing cobalt are particular prone to Auger interference, with the Co $L_3M_{23}M_{45}$ Auger peak overlapping with the $2p_{3/2}$ signal[31]. Comparison of the spectra obtained from both aluminium and magnesium can be used to eliminate this problem.

The presence of unpaired electrons in the valence orbitals of a core-ionised atom brings about multiplet (or exchange) splitting. This feature is particularly prominent in the spectra of the first row transition metals. The unpaired valence electron will interact with the unpaired core electron to give a photoelectron peak split into two components. These peaks may be readily apparent or show just as broadening of the primary peak, if the interaction is not very strong. The strongest interactions occur when the two electron shells involved both have the same primary quantum number, e.g. a *3s* or a *3p* electron interacting with an unpaired *3d* electron.

Shake-up energy loss satellites arise form the transfer of some energy from the ionised atom to an electron, raising it to a higher, unoccupied orbital. This quantum of energy is, then, no longer available to the photoelectron, leaving it with a set reduced amount of energy, and, thus, creating on the spectrum a peak at a defined higher binding energy, the difference between the satellite and the parent line being equal to the energy given to the promoted electron. A shake-up satellite typically has an intensity 5 - 10% of that of the parent peak. The presence of unpaired valence electrons in *d* or *f* orbitals, e.g. in some transition metals, rare earths and lanthanides, can increase this ratio. In general, shake-up lines appear when paramagnetic forms are present and are absent with elemental or diamagnetic species.

The shake-off process is similar to the shake-up one, though, this time, the energy given to the promoted electron is sufficient to excite it into the continuum. Shake-off satellites are rarely seen in spectra off solid samples as the large energy losses involved tend to place the peak somewhere in the region of the broad inelastic tail of the parent peak. Also, since the energy involved is not a discrete amount (the electron may enter the continuum with any amount of kinetic energy), broad shoulders result, as opposed to sharper peaks.

The transfer of some energy from the photoelectron to conduction band electrons is another mechanism by which energy loss peaks can arise. The amount of energy transferred is, again, variable, between zero and the width of the conduction band. This process tends to broaden the parent peak, giving a tail to the high binding energy side.

Plasmon loss signals appear when energy is lost to vibrations of the sample lattice. With insulating samples, these features are not particularly sharp, but some metals can produce a series of equally spaced peaks, decreasing in intensity at

the progressively higher binding energies.

The x-ray source, if no monochromator is used, will emit several discrete x-rays of differing energies. The principal line, for an aluminium target, is the unresolved Al $K\alpha_{1,2}$, where $2p_{3/2}$ and $2p_{1/2}$ electrons descend to fill the vacancy. Other x-rays emitted will arise from filling of the core vacancy in the target atom by electrons from other levels. Table 3.4.2 lists these satellite x-rays, their relative intensities and their separations from the $K\alpha_{1,2}$ line. All of these x-rays will give peaks shifted from their expected locations, towards lower binding energies, but of reduced intensities.

X-ray ghost lines are produced from x-rays other than from the target material. The aluminium or magnesium target is a coating on a copper substrate. If the coating is incomplete or wears thin with use, then copper may be exposed to the electron flux, and copper x-rays will arise. These can excite photoelectrons, but as the spectrometer will be set up to measure binding energies assuming a set x-ray energy (say, the aluminium $K\alpha$ frequency), the peaks created by these spurious x-rays will fall incorrectly on the binding energy scale. Copper $L\alpha$ radiation has an energy 556.9 eV less than Al $K\alpha$. Therefore, the photoelectrons will finish up with 556.9 eV less kinetic energy. To the spectrometer, this will appear to mean that they originate from levels with 556.9 eV greater binding energies. The peaks will be shifted 556.9 eV higher in binding energy relative to the parent, Al $K\alpha$ induced, peak. With a dual anode source, there is the possibility of generating x-rays from both target materials simultaneously. If working with the aluminium source, any peaks generated from magnesium $K\alpha$ x-rays will be 233.0 eV higher in binding energy than their aluminium parent line. Contamination of the source may allow oxygen $K\alpha$ x-rays to be produced, giving signals 961.7 eV higher than expected. Table 3.4.3 summarises these possible ghost signals for both aluminium and magnesium sources.

3.4.14   Sample Degradation

X-ray photoelectron spectroscopy is generally regarded as a non destructive technique, which it is in comparison to such as those involving the use of high energy electrons (SEM, TEM, EPMA, AES, etc.) or ions (SIM, SIMS, etc.). However, some sample degradation can occur under the x-ray flux, giving, for instance, polymerisation, isomerisation, decomposition, reduction and redox reactions. The presence of UHV conditions often further facilitates these changes. It is also possible that low energy electrons emitted from the aluminium window across the face of the x-ray source will play a part in these reactions, especially reduction.

Ion bombardment, often used to clean samples prior to analysis, can bring about many changes. Different elements are likely to be sputtered away at different

rates (preferential sputtering), affecting the perceived composition, metal oxides can be reduced to lower oxides or the metal itself, the sample will be heated, allowing many processes to occur, and the surface topography is likely to be altered, with the production of features such as pyramids on the surface. The probability that a particular metal oxide will be reduced depends on the heats of formation of the oxides and the presence or otherwise of stable intermediate oxides. PbO_2, MoO_3 and Fe_2O_3 will reduce under a 400 eV argon ion beam while Ta_2O_5 and Al_2O_3 will not.

3.4.15   The Electron Analyser

There are several types of electron energy analysers. Cylindrical mirror analysers are most often found on Auger systems, where their increased counting efficiency is an advantage, making their reduced energy resolution a price worth paying.

The spectrometer used in this study utilised a 15 cm radius, 180° hemispherical electrostatic analyser. This discriminates between electrons of differing kinetic energy by passing them through an electric field, established between two concentric hemispheres. At any particular field strength, only electrons of one energy will be able to navigate the analyser and reach the detector. As the field strength is swept, so is the electron energy spectrum. A plot of detected signal against electron energy then gives us the XP spectrum. A Mu-metal shield surrounds the hemispheres to reduce the effect of any stray magnetic fields, including the Earth's, that may be present in the laboratory on the desired field. For a non dispersive instrument, such as the one used here, it is necessary[30] to reduce the field strength to 1×10^{-2} - 1×10^{-3} gauss. Figure 3.4.9 is a schematic of the analyser used in this study.

The energy resolution of the analyser depends on the diameter of the hemispheres and the width of the entrance and exit slits in to and out of the detector. The larger the radius of the hemispheres, the better the resolution, though the volume required to be pumped also increases. If the slits are reduced in width, the resolution improves, but at the expense of signal strength. This is illustrated in Table 3.4.4, where full width half maxima and total counts are recorded for the Ag $3d_{5/2}$ peak using the four exit slit widths available on our Kratos XSAM 800 and both x-ray sources. These results also show the inherently narrower lines obtained using magnesium x-rays.

Only electrons with energies within the range of the pass energy are able to enter the analyser.

$$\frac{1}{P} = \frac{\Delta E}{E} = \frac{W}{2R}$$

where: P = analyser resolving power;

E = mean photoelectron pass energy /eV;

W = sum of entrance and exit slit widths /m; and

R = mean hemispherical analyser radius /m.

The contribution of this resolution to the ultimate width of the detected spectral lines is small in comparison to that from the width of the incident x-ray source.

There are two modes in which to run an analyser such as this. The first decelerates all of the arriving electrons by a fixed proportion of their initial kinetic energy before they enter the hemispheres. The voltage across the hemispheres is then swept. This fixed retard ratio, or FRR, mode produces a differing resolving power at different points in the energy spectrum. This mode is mainly used for Auger analysis using a hemispherical analyser.

The fixed analyser transmission, FAT, mode involves the deceleration of the electrons to a fixed pass energy before analysis. The decelerating voltage is swept to scan the electron energy range. In this mode, the transmission efficiency of the analyser is constant across the energy range, at the expense of degrading signal-to-noise ratios towards the low kinetic energy (or high binding energy) end of the spectrum. Since the resolution is constant, quantification is simplified, and this mode is used for all the XPS work described here. In the Kratos XSAM 800 instrument used in this work, there is a lens system before the entrance slits to the analyser that not only decelerates the electrons but also focusses in photoelectrons towards the centre of the slits to improve detection efficiency. This allows the sample-to-analyser distance to be increased, which, in turn, allows the x-ray source to be positioned closer to the sample, to increase the x-ray flux experienced by the sample.

3.4.16   The Electron Detector

Most XP spectrometers use one, or more, channeltron-type electron detectors/multipliers. The XSAM 800 is no exception. An electron that has negotiated the analyser impinges on the inner surface of the channeltron, which consists of a lined glass tube. The electron causes emission from the channeltron lining of additional electrons. This cascade continues down the length of the detector, assisted by the high potential (2 - 3 kV) applied across the channeltron, until the end, where the current is measured. At this point, an amplification factor of some 1×10^6 - 1×10^8 has been achieved.

XPS reveals chemical information from the surface of the sample. It does this by the small chemical shifts that occur for a particular elemental peak in differing chemical environments. In order to accurately identify the binding energy value of a peak, and so the chemical nature of the sample, it is necessary for the spectrometer to be accurately calibrated, and for that calibration to be able to be related to the calibration of other spectrometers, so that comparisons with literature values may be made[32, 33]. The binding energy scale is generally referred to the Fermi level of the sample, which, by definition, is at the zero point of the scale[21].

The relationship given earlier between the binding and kinetic energies of a photoelectron included the work function of the sample. This may also be given in terms of the kinetic energy in the region of the analyser, and of the analyser work function:

$$E_B = h\nu - E_{Ka} - \phi_a$$

where: E_B = binding energy /eV;
           h = Planck's constant /eV.s;
           ν = frequency of incident x-ray /s^{-1};
           E_{Ka} = kinetic energy in the region of the analyser /eV; and
           ϕ_a = work function of the analyser /eV.

The photoelectron kinetic energy can be related to the voltage across the analyser hemispheres via the equation:

$$V = {(E_{Ka})/}_2 \cdot [(R_2/R_1) - (R_1/R_2)]$$

where: V = applied voltage /eV;
           R_1 = radius of the inner hemisphere /m; and
           R_2 = radius of the outer hemisphere /m.

The binding energy scale zero point can be established by measuring the applied voltage at the Fermi edge of a sample in good electrical contact with the spectrometer. Then, the analyser work function can be calculated. As this is constant, it is then possible to relate measured kinetic energies from unknown samples back to the sample binding energies. Nickel and palladium are the two most frequently used metals for the determination of the zero point.

The linearity of the spectrometer then needs to be determined. This is achieved by looking at the positions of sharp, intense photoelectron peaks from metals, where the peak binding energies are well known. Copper and silver are good

for this. For the particular dual anode instrument used in this study, it was necessary to adjust potentiometers in the back to ensure that the silver $3d_{5/2}$ peak used for calibration fell at the correct binding energy for both sources, 368.3 eV [34]. This method enables the determination, to ~$\pm$0.1 eV, of binding energies from conducting samples in good electrical contact with the spectrometer. Many samples, including the oxides described here, charge up under the x-ray beam, as electrons are emitted from the sample, despite the large neutralising effect of the flood of low energy electrons produced in the aluminium foil at the front face of the x-ray source[15]. Low energy (< 1 eV) electron flood guns may be used to enhance the neutralisation effect. Careful control has to be maintained to ensure that under- or over-compensation does not occur. The positive charging of the sample shifts peaks towards higher binding energy values (the positive charge requires electrons to expend more energy to escape from the surface) by up to 10 eV. It is then necessary to adjust the spectrum by the amount of this charging if accurate binding energy determinations are to be made. The presence of adventitious carbon, predominantly from the deposition of diffusion pump oil carbon out of the residual gas in the analysis chamber, on the sample surface provides a means of monitoring the extent of charging. If the contamination carbon signal is assumed to lie at 284.6 - 285.2 eV [15, 21], then its actual position, and the shift away from this expected value, shows us how far to shift the other peaks in the spectrum. This method assumes that the contamination is in good electrical contact with the sample, and that both are charged to the same extent.

A determination of the adventitious carbon $1s$ binding energy for the XSAM 800 used in this work was made by placing a clean piece of silver foil into the spectrometer. Measurements were taken before and after the foil was allowed to remain in the spectrometer for 48 hours. The contamination carbon peak was observed to grow, and to be located at 284.9 $\pm$0.1 eV. All spectra in this thesis have been calibrated to C $1s$ = 285.0 eV. It was found that samples tended to charge to a greater extent under aluminium x-ray irradiation than under magnesium x-rays. The aluminium source gave higher electron count rates, and, so, the sample might be expected to charge to a greater extent, as was observed.

3.4.18   Sample Preparation and Mounting

The surface sensitive nature of the technique and the UHV conditions under which it is performed dictate some requirements with regards to sample preparation.

In order to prevent unnecessary degradation of the vacuum, it is wise to outgas samples containing volatile material, perhaps solvent used to clean them or the solvents in the mounting dag or cement, prior to introduction into the analysis

chamber. This can be achieved (on the type of instrument used in this study) by allowing the sample to sit for a while in the introduction chamber. If it is a volatile material on the sample that is of interest, then it may prove necessary to carry out the analysis at low temperature, using a cooled probe.

The effects of ion bombardment for cleaning (or depth profiling) a sample have already been mentioned (Section 3.4.14).

Silicon carbide papers may be used to abrade samples. The high temperatures generated can cause the formation of oxides or nitrides on the surface from interaction with atmospheric gases.

Fracturing or scraping a sample in the UHV chamber prevents atmospheric contamination. However, a sample may preferentially cleave along grain boundaries or a soft material may be spread over a harder component in a multiphase system.

Bulk materials may be ground to powders in a mortar and pestle. Again, high temperatures may be created with ensuing reaction problems.

Powder samples can be mounted in several ways. Pressing the powder into indium foil or onto conducting copper adhesive tape are the most commonly used techniques. Pressed pellets may be prepared (such as those used in this study for exposing the oxides in the gamma cell).

3.4.19   Instrumentation and Experimental

The x-ray photoelectron spectrometer used in this study was an XSAM 800, manufactured by Kratos Analytical of Manchester, England. Kratos DS800 software was used for the acquisition and off-line analysis of spectra. The main analysis chamber was attached to an Edward's E04 diffusion pump and liquid nitrogen cold trap, backed by an Edward's E2M5 direct drive rotary pump, while the entry lock area used an Edward's EXT 6/200 turbomolecular pump, again rotary backed. The entry lock could be evacuated to ~1×10^{-7} τ. A gate valve between the analysis and sample introduction chambers allowed the analyser to remain below 1×10^{-9} τ at all times, bar maintenance periods. The dual, aluminium / magnesium, x-ray source was additionally evacuated by an ion pump system. The target material coatings had been applied onto a copper substrate. A 2 μm aluminium foil window was present at the front of the source. The source was operated at a power rating of 300 W (20 mA emission current x 15 kV anode potential). The instrument was based around a 30 cm diameter hemispherical analyser. This was operated in the FAT mode. An analyser exit slit width of 4 mm was used, as a compromise between

spectral resolution and count rate. At this slit width setting, a FWHM of 1.3 eV was achieved for the silver $3d_{5/2}$ using the aluminium source, and 1.2 eV with magnesium x-rays. The position of the Ag $3d_{5/2}$ peak off clean silver foil was used to calibrate the energy scale of the spectrometer, and the alignment between spectra recorded using the two different energy x-rays. A pass energy of 20 eV was used.

Samples were mounted onto aluminium stubs. Powder samples were pressed into the sticky side of 3M conducting copper tape, previously doubled over and attached to a stub. A spectrum was recorded off the sticky side of the copper tape so as to allow recognition of any contribution from it to future sample spectra. Bulk samples were usually attached using Acheson silver or carbon dag, or Leit C conducting carbon cement. Pressed pellet samples were mounted using a hat arrangement to hold them in place on a standard aluminium stub without actually binding them in place. Figure 3.4.10 illustrates this arrangement. The sample area then available for analysis was circular and 5 mm in diameter, half that illuminated by the x-ray source. These sample holders were designed to shield from analysis the outer 0.5 mm of the pellets. This region, when the pellets were mounted for exposure in the gamma cell, was covered by the silica spacers, and, thus, not exposed to the reactant gases. Aluminium and Al_2O_3 signals were seen from the surrounding stub, but as aluminium did not feature in any of the samples investigated, this was not too great a problem. The aluminium stubs were actually made out of a Dural aluminium alloy, containing small amounts of nickel and copper. Ni $2p$ and Cu $2p$ peaks could be identified in XP spectra recorded off the stubs, though the atomic percentages for both elements were less than 0.5%. Copper wasn't present in any of the samples, and, so, its appearance in the spectra would not be a problem. Nickel was present in some of the samples, but always at much greater percentages than in the stub material. Its potential for interference was considered to be negligible. The samples were mounted at an angle of 20° to the entrance plane of the analyser.

In general, wide scans (1000 - 0 eV binding energy (BE); 20 eV pass energy; 1.00 eV step size) and region scans (variable BE range; 20 eV pass energy; 0.05 eV step size) usually took 15 - 30 minutes each to acquire, with wider regional scans taking longer to give the same total acquisition time at each energy channel. The wide scans were used to highlight the presence of any unexpected peaks. The C $1s$ region was used to determine the charging correction required to be applied to all the spectra off that sample. Shirley backgrounds were subtracted from beneath peaks prior to quantitative analysis.

l	Symbol	Possible j values	Relative orbital populations
0	s	$(-1/2)$ $1/2$	-----
1	p	$1/2$ $3/2$	1:2
2	d	$3/2$ $5/2$	2:3
3	f	$5/2$ $7/2$	3:4

Table 3.4.1. Relative orbital populations for s, p, d and f orbitals.

X-ray line	Briggs and Seah[15]		Wagner et al[21]	
	Separation from $K\alpha_{1,2}$ /eV	Relative intensity	Separation from $K\alpha_{1,2}$ /eV	Relative intensity
$K\alpha_{1,2}$	0	100	0	100
$K\alpha_2$	-5.6	1.0	-----	-----
$K\alpha_3$	-9.6	7.8	-9.8	6.4
$K\alpha_4$	-11.5	3.3	-11.8	3.2
$K\alpha_5$	-19.8	0.4	-20.1	0.4
$K\alpha_6$	-23.4	0.3	-23.4	0.3
$K\beta$	-70.0	2.0	-69.7	0.55

Table 3.4.2. Positions of the aluminium x-ray satellites near to the $K\alpha_{1,2}$ peak, on a binding energy scale.

Contaminating radiation	Separation from Mg-induced peaks /eV	Separation from Al-induced peaks /eV
Oxygen $K\alpha$	+728.7	+961.7
Copper $L\alpha$	+323.9	+556.9
Magnesium $K\alpha$	-----	+233.0
Aluminium $K\alpha$	-233.0	-----

Table 3.4.3. Ghost x-ray lines resulting from a contaminated or damaged anode - binding energy shifts relative to the parent signal.

X-ray source	Slit width /mm	Peak position /ev	FWHM /ev	Peak area /counts
Al	0.1	368.1	1.2	32276
Al	1.5	368.1	1.3	107484
Al	4.0	368.1	1.3	793299
Al	8.0	368.1	1.4	685891
Mg	0.1	368.1	1.1	49428
Mg	1.5	368.1	1.1	233106
Mg	4.0	368.1	1.2	493018
Mg	8.0	368.1	1.2	775193

Table 3.4.4. The effect of slit width on the Ag $3d_{5/2}$ peak.
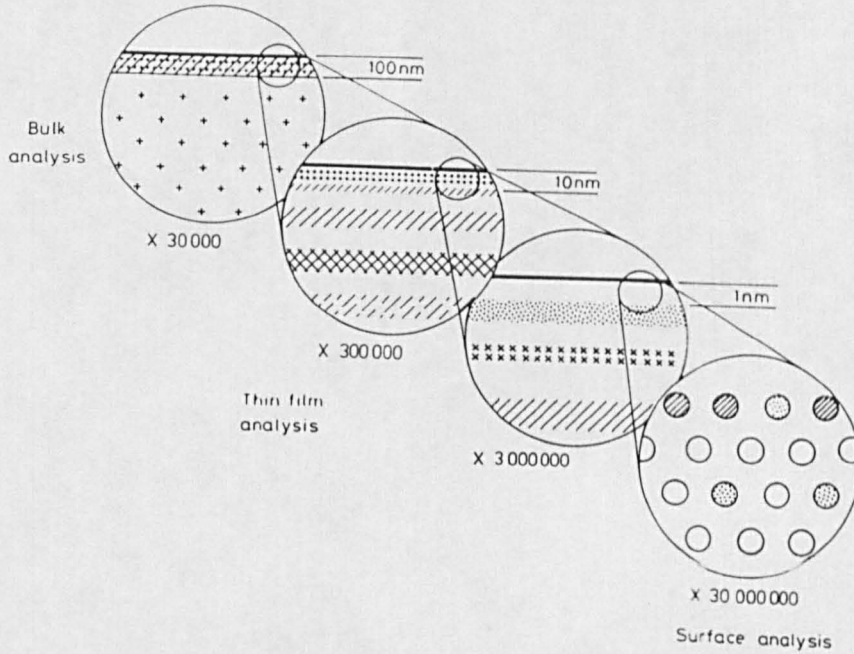
Figure 3.4.1. The regimes of surface analysis, thin film analysis and bulk analysis.
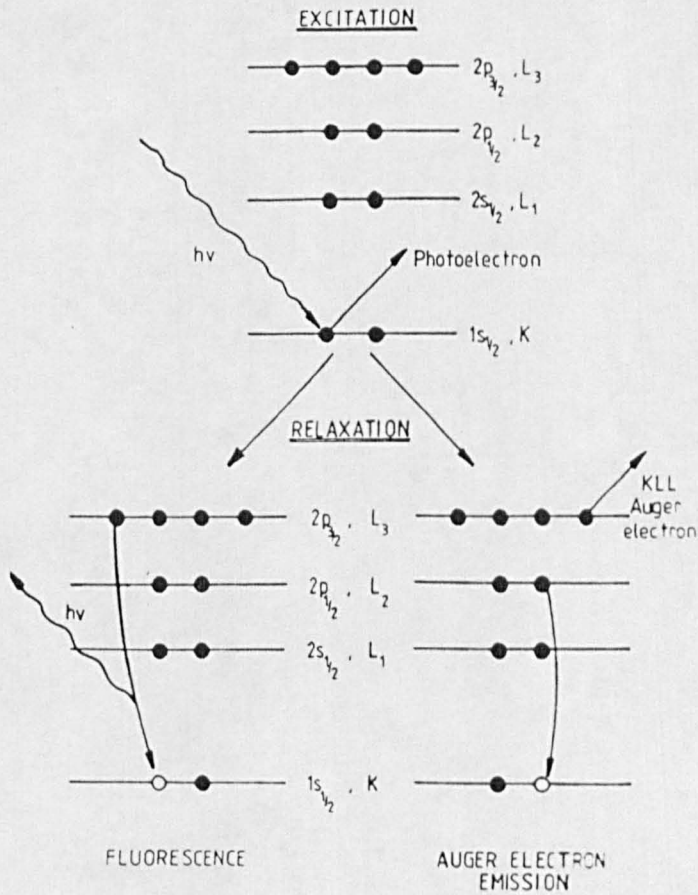
Figure 3.4.2. The XPS, AES and EDX processes.

87
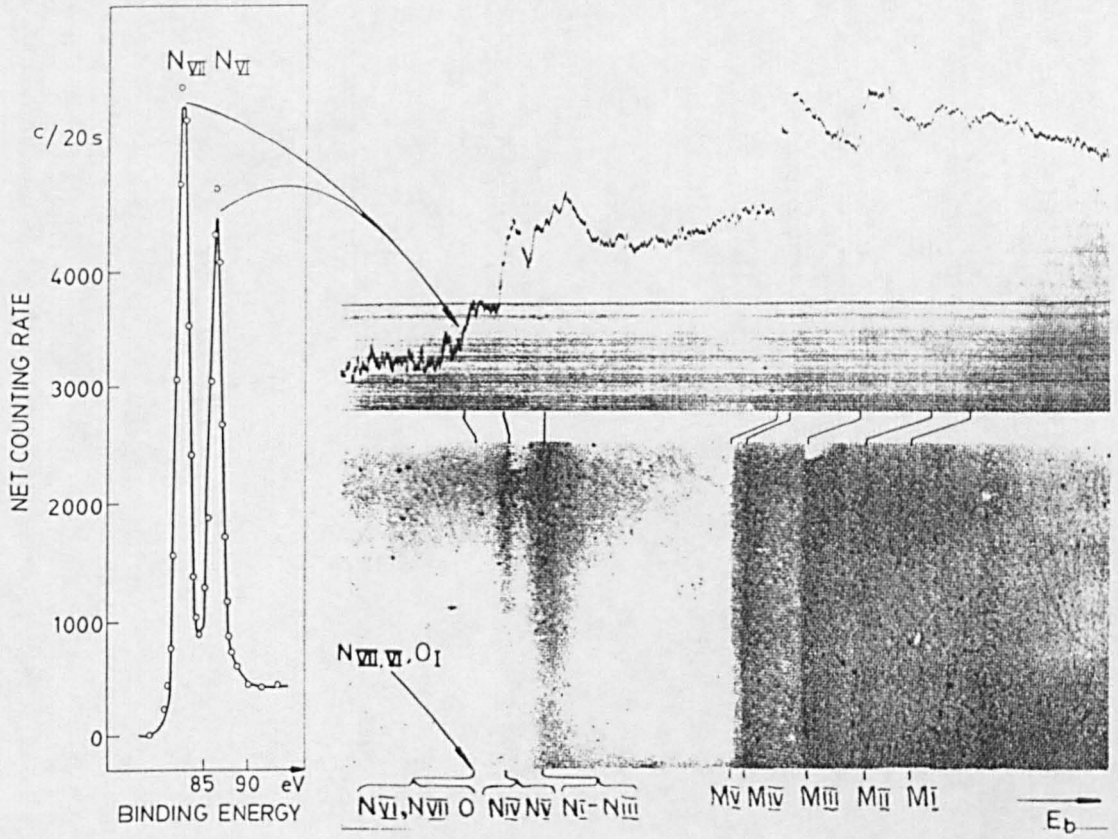
Figure 3.4.3. Comparison of the Au *4f* region as recorded by Robinson and Siegbahn.
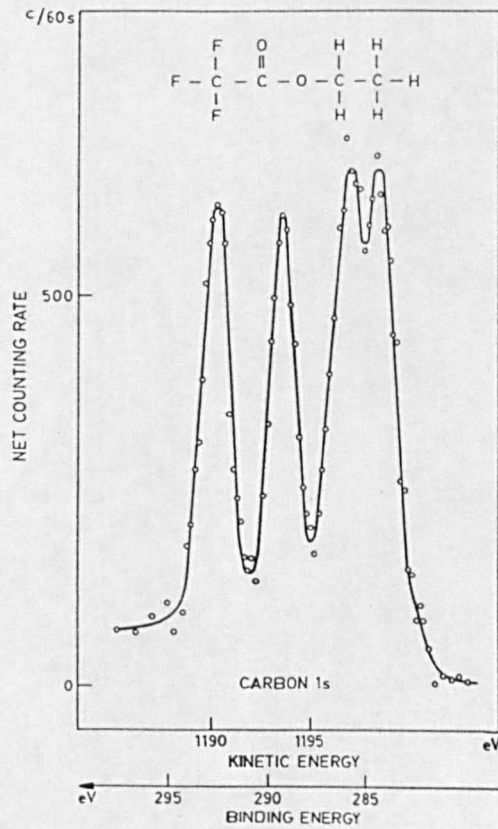
Figure 3.4.4. C *1s* region of ethyl trifluoroethanoate.

88
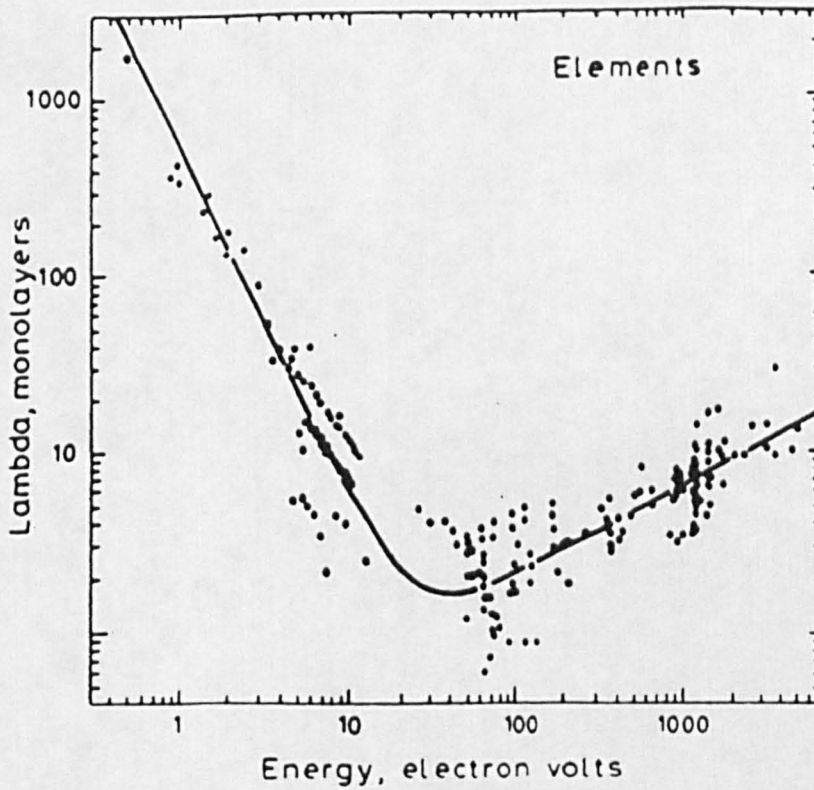
Figure 3.4.5. Energy dependence of the inelastic mean free path, λ.
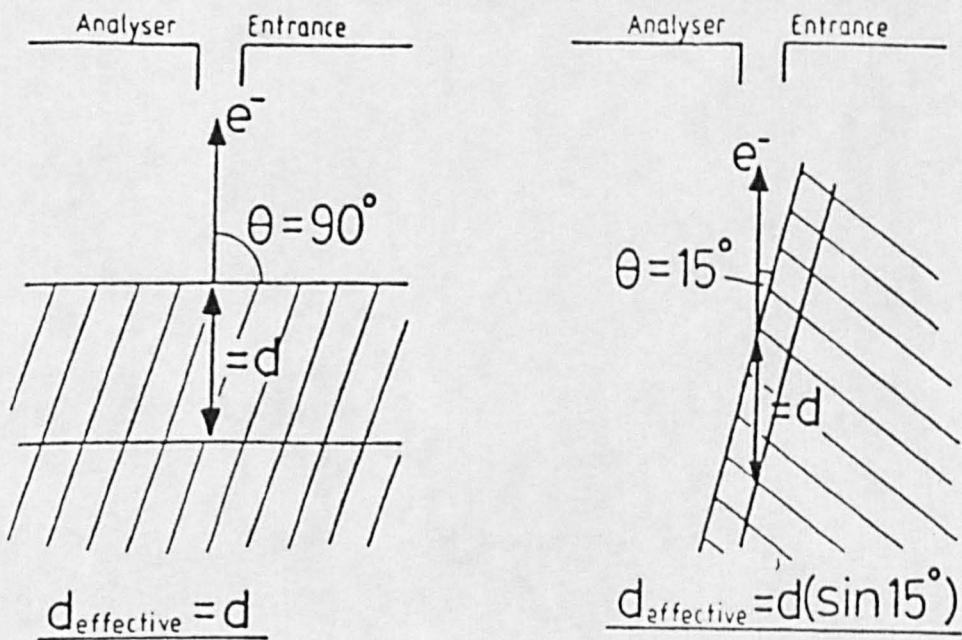
a) bulk sensitive angle.   b) surface sensitive angle.

Figure 3.4.6. The effect of take-off angle on surface sensitivity.
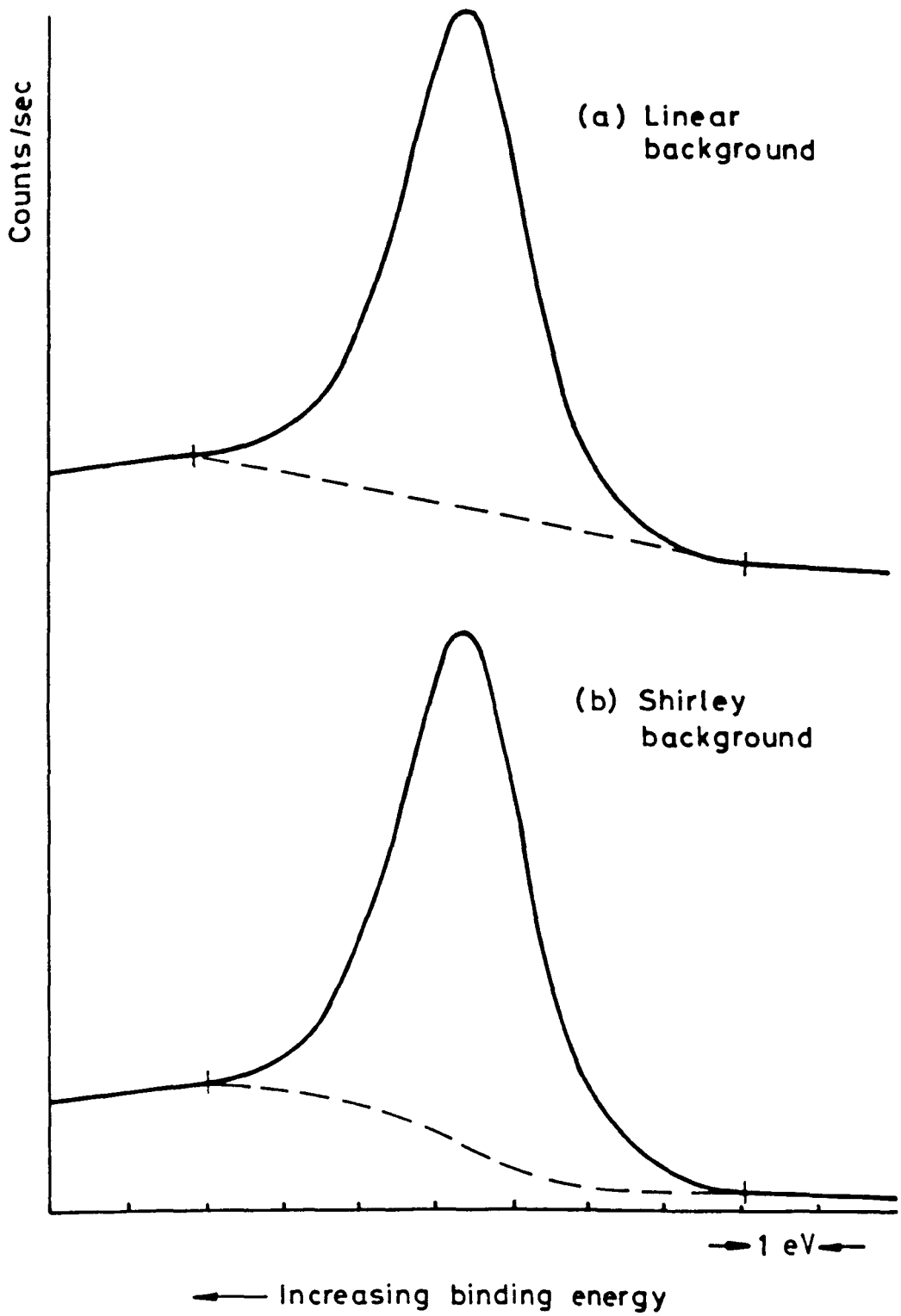
Figure 3.4.7. Subtraction of the inelastically scattered electron background under a photoelectron peak using: a) a linear; and b) a Shirley background.
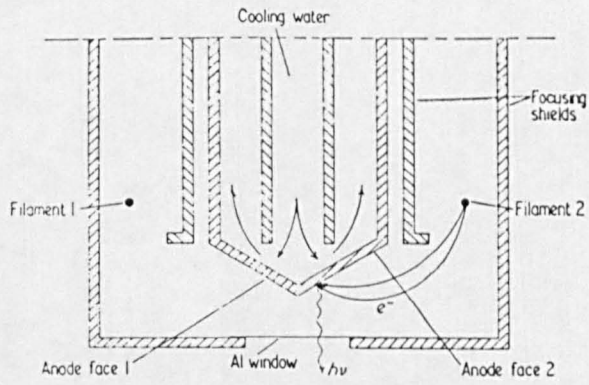
Figure 3.4.8. Schematic of a dual anode x-ray source.
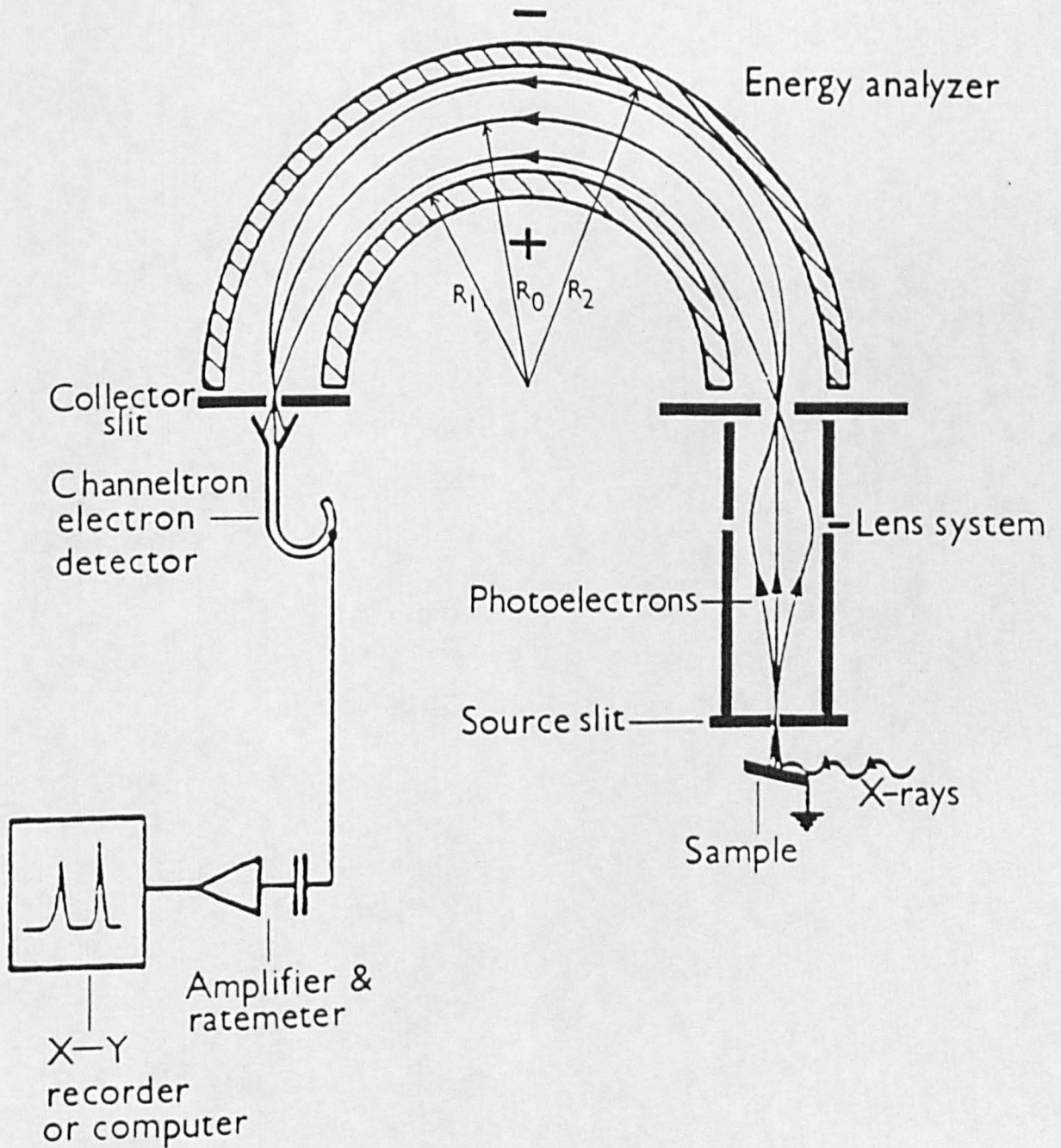
Figure 3.4.9. Hemispherical analyser and channeltron electron detector.

91
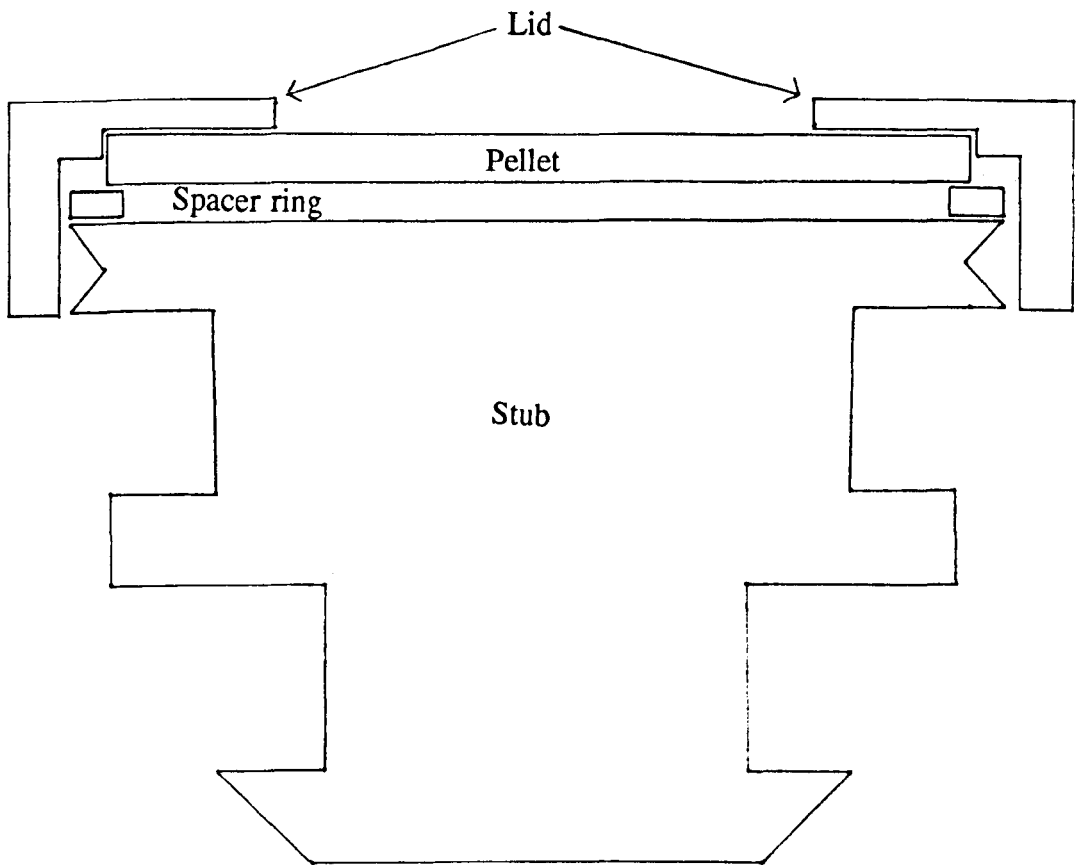
Figure 3.4.10. Pellet sample holder.

3.5   The Berkeley Nuclear Laboratories Gamma Irradiation Facility

3.5.1   Introduction

The gamma irradiation facility (or gamma cell) at Berkeley Nuclear Laboratories[35, 36] is a concrete- and lead-shielded room (see Figure 3.5.1) within which it is possible to safely expose samples of many kinds to gamma radiation, whilst, at the same time, if desired, also exposing them to an ambient or heated gas stream, supplied from any gas cylinder outside of the irradiated zone. The radiation provides a means of examining the effects of ionisation on a sample, or, as in the present work, of the effects of an irradiated gas (or gas mixture), where (in particular, radical) species, not normally produced by simply heating the gas, may be present. No creation of radioactive species takes place in the samples, so they are perfectly safe to handle, once removed from the cell.

3.5.2   Radiation Source

The gamma radiation is provided by stainless steel-encapsulated ^{60}Co sources, which are driven into position out of their store once the samples have been loaded and the operator has retreated from the cell. There are, actually, two independent sets of sources, providing a range of irradiation geometries. For the work described here, an outer, lower dose rate, irradiation position was chosen (see Figure 3.5.2), giving dose rates of the order of 7 - 9 $mW.g^{-1}$ [37].

3.5.3   Sample Capsules

Figure 3.5.3 illustrates the style of sample capsule used in these experiments. Depending on the temperatures to which they were to be exposed, the capsules were made of either a stainless steel (550°C) or an inconel (for the higher temperatures, 650°C). Figure 3.5.4 shows how the disc samples were held in the capsules. 5 mm silica ring spacers, with vents to allow ready flow of gas between the samples, held the discs upright inside a silica tube liner.

3.5.4   Gas Analysis

Gas chromatography is used to monitor the composition of the reaction gas, both before and after passing through the irradiated zone. These readings, along with the capsule temperature and gas flow rate, are logged on a computer every few hours for subsequent printout and analysis. In general, the CO concentration increases from the inlet towards the outlet of the gamma cell capsules. At the same time, CH_4 concentration falls. The overall flow rate is slightly higher at the outlet end of the capsules compared to the inlets. Problems with the chromatograph prevented gas analyses to be performed for the majority of the gamma cell experiments. With some

20% Cr / 25% Ni / Nb-stabilised fuel can stainless steel in one of the capsules during a run at 550°C, a rise of 830 vpm in CO concentration, fall of 290 vpm CH_4 and rise in flow of 0.01 - 0.02 ml.min^{-1} were obtained. These changes in gas composition arise from the reaction:

$$CH_4 + 3CO_2 \rightarrow 4CO + 2H_2O$$
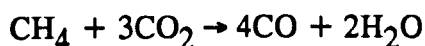
This gives an overall increase in the number of gas molecules present, manifesting itself in the increase in flow rate, an increase in CO and decrease in CO_2 and CH_4.

3.5.5 *Experimental*

Use of the gamma cell was often hindered, by problems both directly related to the cell and not so closely related to it. At various times, routine services, taking longer than expected, malfunctioning gas pumps, computer faults, building works, gas leaks, etc. all played their part to hinder progress.

The gas mixture the samples were exposed to was prepared by mixing of the appropriate single, pure gases. This, and the day to day operation of the gamma cell, was carried out by Richard Parfitt and Ray Westbury of the CEGB (now Nuclear Electric plc.). The gas mixture used for all sample exposures was CO_2 based, with 1% CO, 800 vpm CH_4 and 15 vpm C_2H_6. A pressure of 40 bar (= 4×10^6 Pa) and flow rates of 1 - 3 cm^3.min^{-1} were used. Exposure times of 18 - 24 days were employed. In commercial AGRs, pressures of 40 bar and coolant gas compositions approximating to 1 - 1.5% CO and 200 vpm CH_4 are found[38]. The higher CH_4 level and addition of C_2H_6 bring about increased deposition rates in comparison to AGRs.

Double Doors

Workshop Area

Rack Housing

Concrete Shielding

Gamma Cell

Source B Flask

Plug Door

Source A Teleflex Guides

Control Console
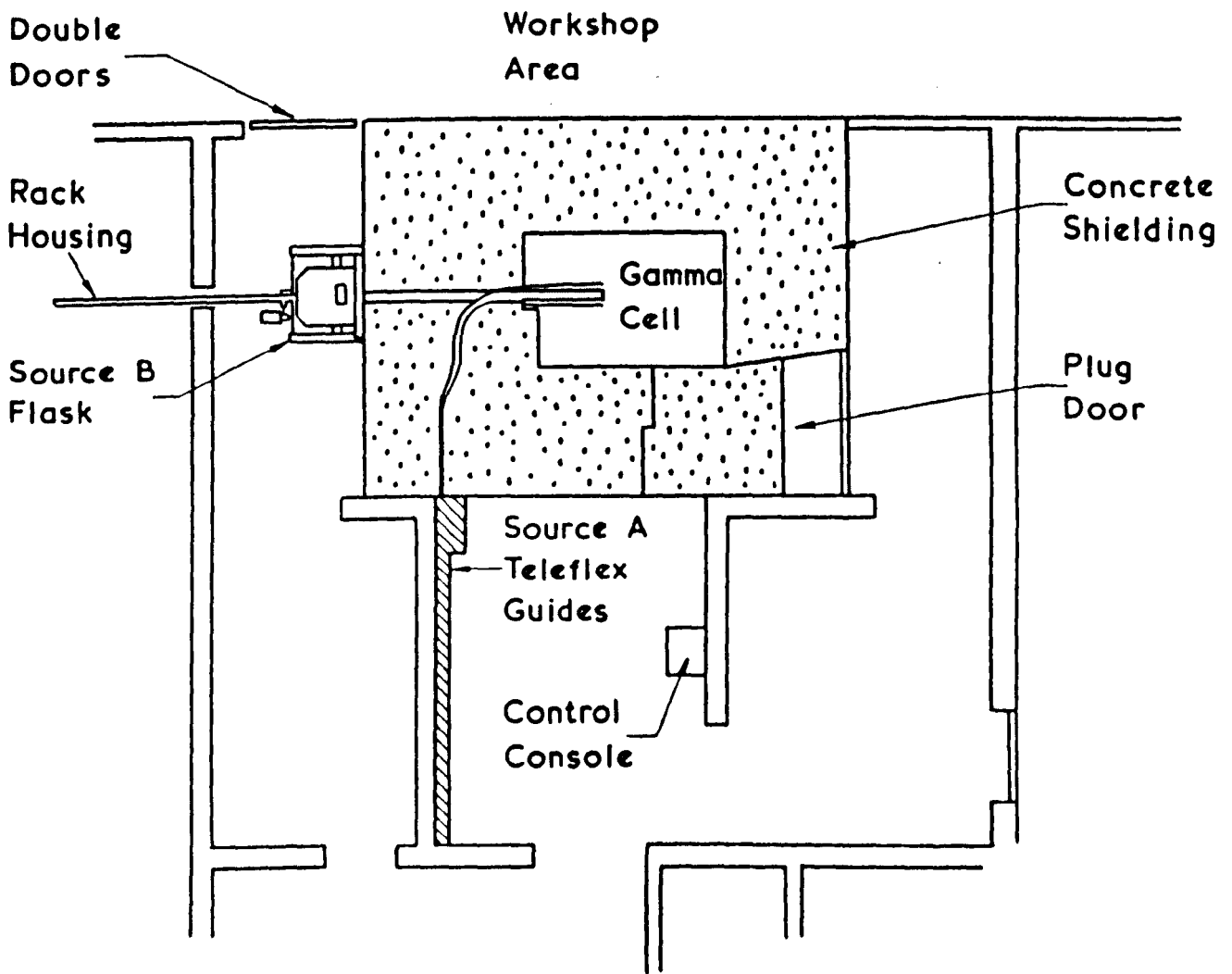
Figure 3.5.1. Plan of gamma cell.

SOURCE A

Sealed Bulb
Irradiation
Positions

Source
Guide
Tubes

Irradiation
Positions

SOURCE B

Irradiation
Positions

Source
Carrier
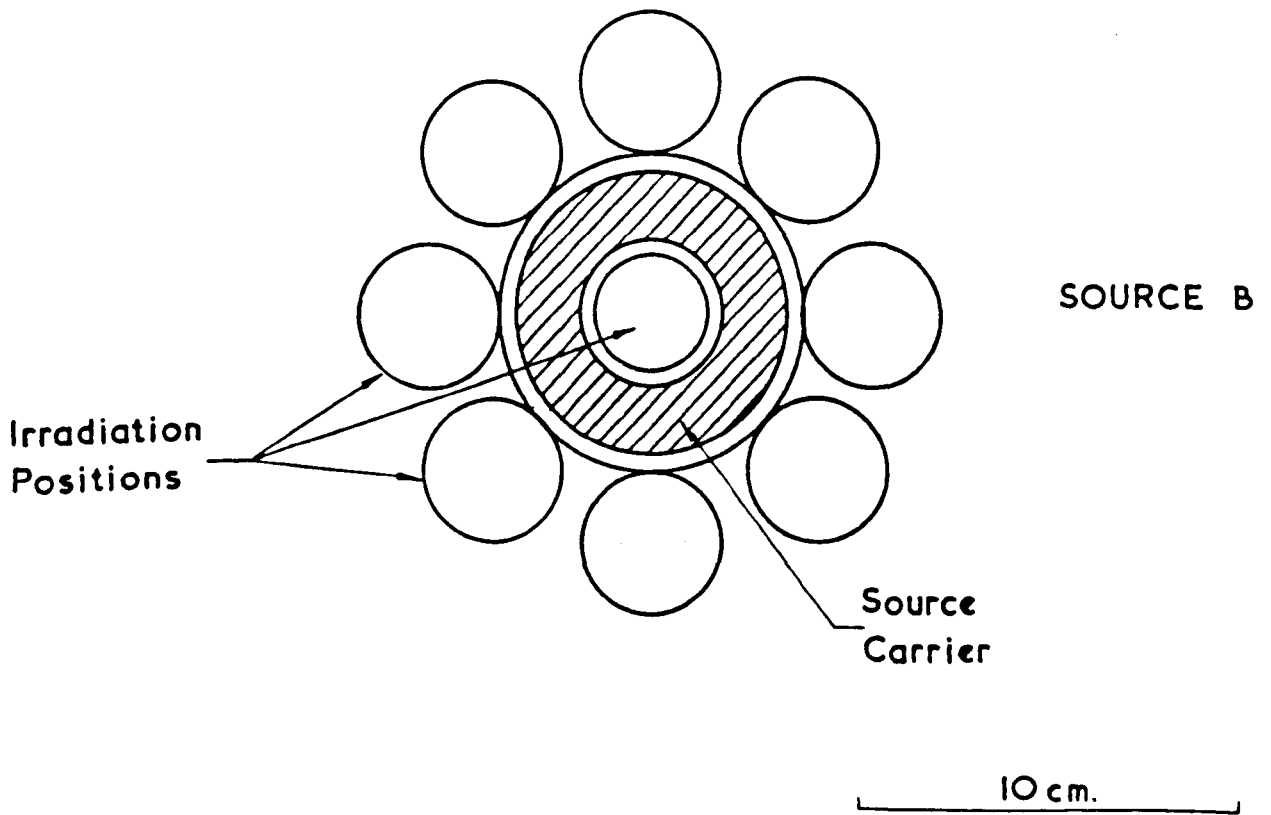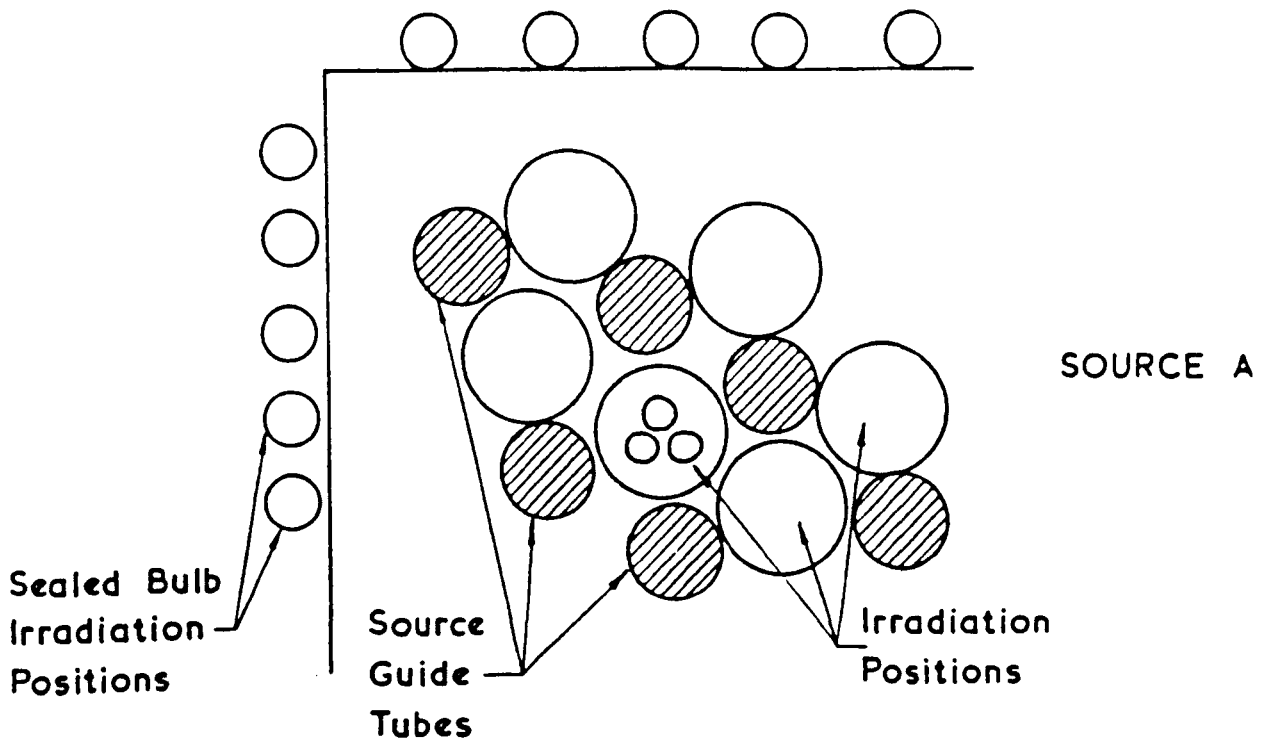
10 cm.

Figure 3.5.2. Arrangement of irradiation positions.

TYPE A.

Sample 10 x 70 m m.
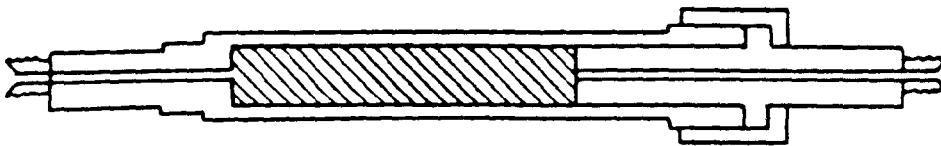
TYPE B.

Sample 15 x 90 m m.

Sample 10 x 80 m m.

TYPE C.

10 cm.

Figure 3.5.3. Types of irradiation capsule.

97
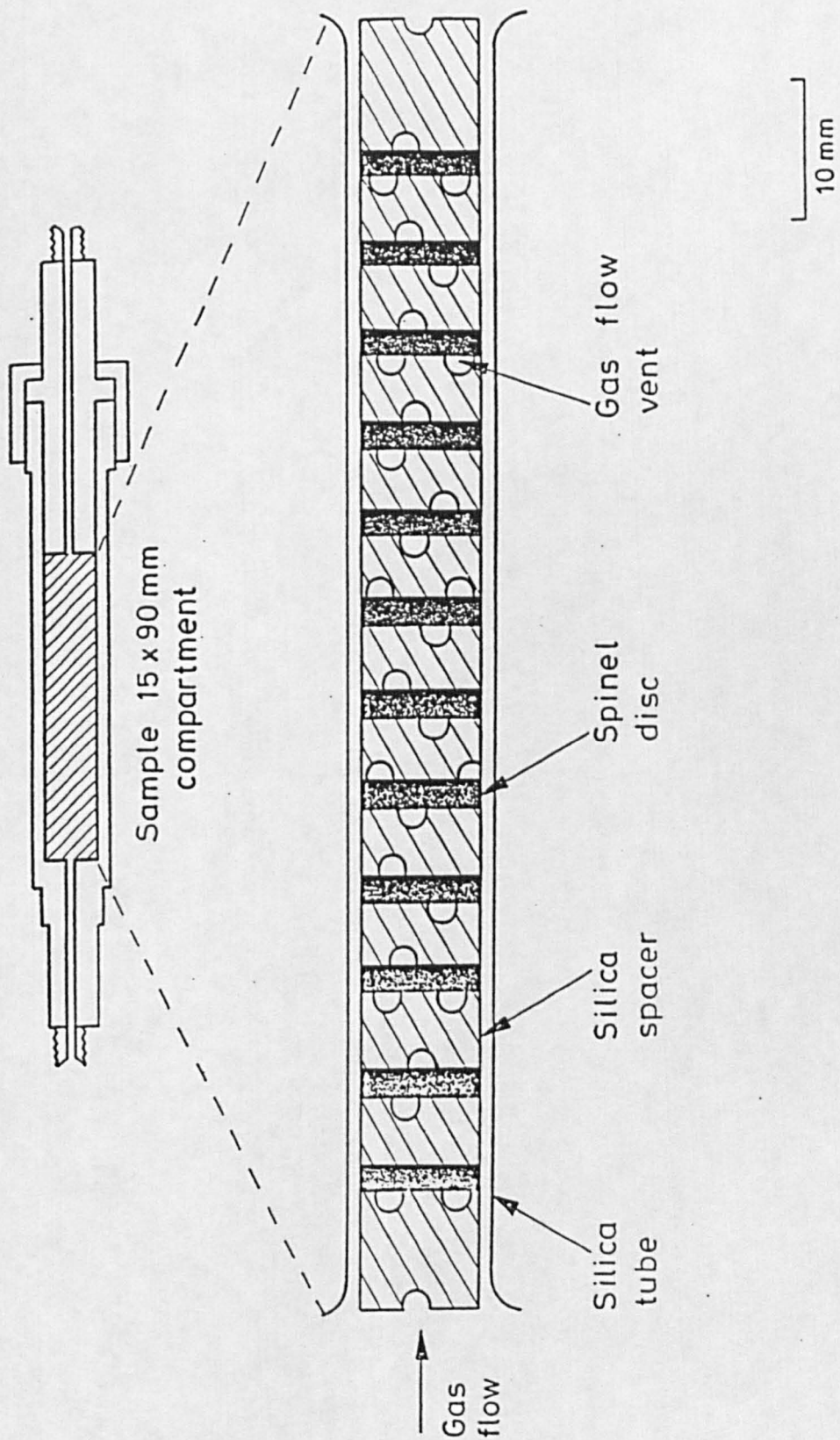
Figure 3.5.4. Arrangement of samples in gamma cell capsule.

3.6 References

1. J. I. Goldstein, D. E. Newbury, P. Echlin, D. C. Joy, C. Fiori and E. Lifshin, "Scanning Electron Microscopy and X-Ray Microanalysis", Plenum Press, (1981).

2. F. J. Humphreys, "Scanning Electron Microscopy" in "Characterisation of High Temperature Materials - Microstructural Characterisation", edited by E. Metcalfe, Institute of Metals, 94 - 159, (1988).

3. T. E. Everhart and R. F. M. Thornley, "Wide-Band Detector for Micro-Microampere Low-Energy Electron Currents", Journal of Scientific Instruments, *37*, 246 - 248, (1960).

4. Cambridge Scientific Instruments, "Cambridge Stereoscan 180" brochure.

5. Cambridge Scientific Instruments, "Cambridge Stereoscan 150 Mark 2 Scanning Electron Microscope" brochure.

6. Link Systems, EDX energy value slide, (1982).

7. R. Fitzgerald, K. Keil and K. F. J. Heinrich, "Solid-State Energy Dispersion Spectrometer for Electron-Microprobe X-Ray Analysis", Science, *159*, 528 - 530, (1968).

8. Link Systems, "A Guide to Energy Dispersive X-Ray Analysis".

9. Kevex Corporation, "Energy Dispersive X-Ray Microanalysis - An Introduction", (1983/1988).

10. J. T. Buswell and G. K. Rickards, "Quantitative Analysis Using an Energy Dispersive X-Ray Spectrometer Fitted to a Scanning Electron Microscope", Central Electricity Generating Board report RD/B/N3365, (1975).

11. J. T. Buswell, "The Effects of the Coating and Contamination of Specimens on Quantitative Energy Dispersive X-Ray Analysis", Central Electricity Generating Board report RD/B/N3703, (1976).

12. Link Systems, "Quantitative Electron Probe Microanalysis".

13. Link Systems, "ZAF-4/FLS Operating Instructions SR-500-Z4F-1083".

14. University of Bristol, "Interface Analysis at Bristol", pamphlet,

(1990).

15. D. Briggs and M. P. Seah (Editors), "Practical Surface Analysis, Second Edition, Volume 1 - Auger and X-Ray Photoelectron Spectroscopy", John Wiley and Sons / Salle and Sauerländer, (1990).

16. J. G. Jenkin, R. C. G. Leckey and J. Liesegang, "The Development of X-Ray Photoelectron Spectroscopy: 1900 - 1960", Journal of Electron Spectroscopy and Related Phenomena, *12*, 1 - 345, (1977).

17. C. Nordling, S. Hagström and K. Siegbahn, "Application of Electron Spectroscopy to Chemical Analysis", Zeitschrift für Physik, *178*, 433 - 438, (1964).

18. K. Siegbahn, C. Nordling, A. Fahlman, R. Nordberg, K. Hamrin, J. Hedman, G. Johansson, T. Bergmark, S.-E. Karlsson, I. Lindgren and B. Lindberg, "ESCA - Atomic, Molecular and Solid State Structure Studied by Means of Electron Spectroscopy", Almqvist and Wiksells, (1967).

19. H. R. Robinson, "X-Ray Terms and Intensities", Philosophical Magazine, Series 6, *50*(295), 241-250, (1925).

20. D. A. Shirley, "ESCA", Advances in Chemical Physics, *23*, 85 - 159, (1973).

21. C. D. Wagner, W. M. Riggs, L. E. Davis, J. F. Moulder and G. E. Muilenberg (Editor), "Handbook of X-Ray Photoelectron Spectroscopy: A Reference Book of Standard Data for use in X-Ray Photoelectron Spectroscopy", Perkin Elmer Corporation, (1979).

22. C. D. Wagner, L. E. Davis, M. V. Zeller, J. A. Taylor, R. H. Raymond and L. H. Gale, "Empirical Atomic Sensitivity Factors for Quantitative Analysis by Electron Spectroscopy for Chemical Analysis", Surface and Interface Analysis, *3*(5), 211 - 225, (1981).

23. D. A. Shirley, "High-Resolution X-Ray Photoemission Spectrum of the Valence Bands of Gold", Physical Review B, *5*, 4709 - 4714, (1972).

24. J. Végh, "The Analytical Form of the Shirley-Type Background", Journal of Electron Spectroscopy and Related Phenomena, *46*, 411 - 417, (1988).

25. S. Tougaard, "Quantitative Analysis of the Inelastic Background in Surface Electron Spectroscopy", Surface and Interface Analysis, *11*, 453 - 472, (1988).

26. "UHV Pumps - A Comparison of Performance", Vacuum Generators Limited technical information pamphlet.

27. "Pressure Measurement in UHV", Vacuum Generators Limited technical information pamphlet.

28. G. F. Weston, Measurement of Ultra-High Vacuum. Part 1. Total Pressure Measurements", Vacuum, *29*(8/9), 277 - 291, (1979).

29. G. F. Weston, Measurement of Ultra-High Vacuum. Part 2. Partial Pressure Measurements", Vacuum, *30*(2), 49 - 67, (1980).

30. W. M. Riggs and M. J. Parker, "Surface Analysis by X-Ray Photoelectron Spectroscopy", in A. W. Czanderna (editor), "Methods and Phenomena - Their Applications in Science and Technology, Volume 1: Methods of Surface Analysis", Elsevier, 103 - 158, (1975).

31. N. G. Farr and H. J. Griesser, "XPS Excitation Dependence of Measured Cobalt $2p_{3/2}$ Peak Intensity Due to Auger Peak Interference", Journal of Electron Spectroscopy and Related Phenomena, *49*, 293-302, (1989).

32. M. T. Anthony and M. P. Seah, "XPS: Energy Calibration of Electron Spectrometers", Surface and Interface Analysis, *6*(3), 95 - 106, (1984).

33. T. X. Carroll, M. R. F. Siggell and T. D. Thomas, "Electron Spectrometer Calibration. Consistency Between Magnesium- and Aluminium-Excited Spectra", Journal of Electron Spectroscopy and Related Phenomena, *46*, 249 - 253, (1988).

34. M. P. Seah, "Post-1989 Calibration Energies for X-Ray Photoelectron Spectrometers and the 1990 Josephson Constant", Surface and Interface Analysis, *14*, 488, (1989).

35. H. E. Evans and B. Knight, "The 16,000 Ci Cobalt-60 Gamma Irradiation Facility at Berkeley Nuclear Laboratories", Central Electricity Generating Board, internal report RD/B/N1066, 1968.

36. J. V. Best, "The Addition of a Second Cobalt-60 Source to the BNL Gamma Irradiation Facility", Central Electricity Generating Board, internal report RD/B/N2431, 1972.

37. J. A. Jutson, "The Deposition of Carbon on Transition Metal Oxide Surfaces", Ph.D. thesis, Council for National Academic Awards, (1989).

38. J. M. Butterfield, C. J. Knights, D. J. Norfolk and D. G. Abbott, "A Longer Moderator Life for Advanced Gas-Cooled Reactors", CEGB Research, *16*, 18 - 33, (1984).

4 EXPERIMENTAL

4.1 Characterisation of the Spinel Starting Materials

4.1.1 Introduction

X-ray diffraction was used to confirm the state of the oxides, oxalates and carbonates used in the spinel preparation. Manganous oxalate ($Mn(COO)_2.2H_2O$), calcined ferric oxide (Fe_2O_3), ferrous oxalate ($Fe(COO)_2.2H_2O$), cobaltous carbonate ($CoCO_3$) and nickel carbonate ($NiCO_3.2Ni(OH)_2.4H_2O$), were the starting materials analysed.

4.1.2 Experimental

The reagents were mounted on a silicon disc using anhydrous methanol as a means of dispersing them. (With the methanol in place, the sample can be evenly distributed across the disc. When it evaporates, the sample only is left in place.)

The spectra acquired were compared to reference spectra stored with the analysis software, and based on the JCPDS database.

4.1.3 Results

All of the reagents produced spectra in good agreement with the JCPDS reference database. Table 4.1.1 gives the reference spectra which matched those off the samples.

4.1.4 Conclusion

It was seen that the starting materials were all as described, and suitable for use in the preparation of the spinels desired.

Starting material	JCPDS reference spectrum number
Manganous oxalate $Mn(COO)_2.2H_2O$	25-544
Calcined ferric oxide Fe_2O_3	33-664
Ferrous oxalate $Fe(COO)_2.2H_2O$	23-293
Cobaltous carbonate $CoCO_3$	11-692
Nickel carbonate $NiCO_3.2Ni(OH)_2.4H_2O$	16-164

Table 4.1.1. Spinel starting material XRD analysis.

4.2   Spinel Preparation

4.2.1   Introduction

The spinel oxides prepared, characterised and exposed in the gamma cell for this work were made via solid solution reactions. Atmospheres of CO_2 or CO_2 / 2% CO and temperatures of 950°C were utilised.

4.2.2   Spinel Structure

Spinels of the form AB_2O_4, where A and B are transition metal cations (alike, to form a mixed valence compound, or dissimilar) can have one of two regular structures. Both are based on a close packed arrangement of oxygen atoms, with cations located in the octahedral and tetrahedral sites (see Figure 4.2.1). Normal spinels have a half of the octahedral sites occupied by B^{3+} ions and an eighth of the tetrahedral sites filled by A^{2+} cations. Inverse spinels have all of the A^{2+} and half of the B^{3+} ions occupying the octahedral sites, and the remainder of the B^{3+} ions in tetrahedral sites. For inverse spinels, with 2+ and 3+ ions both in octahedral sites, there exists the possibility for rapid electron exchange between these ions. Whether a particular spinel takes up one or the other of these two forms depends on a variety of factors, including the relative sizes of A and B, the Madelung constants for the two possible structures and the influence of ligand field stabilisation energies.

For the spinels studied in this work, all the members of the $Mn_xCo_{1-x}Fe_2O_4$ series are inverse, due to the greater crystal field preference energy of Mn^{2+} and Co^{2+} compared to Fe^{3+}, with the exception of $MnFe_2O_4$, which is best considered as an intermediate spinel[4] and having the formula (octahedral ions in brackets):

$$Mn_{0.8}^{2+}Fe_{0.2}^{3+}(Mn_{0.2}^{2+}Fe_{1.8}^{3+})O_4$$
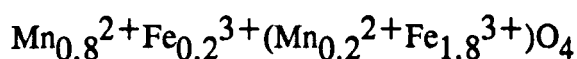
Manganese and cobalt locate themselves in the octahedral sites while the iron divides itself equally between octahedral and tetrahedral sites. All the members of the $Fe_xCo_{1-x}Fe_2O_4$ and $Ni_xCo_{1-x}Fe_2O_4$ series would be expected to adopt the inverse spinel structure.

4.2.3   Solid Solutions

A crystalline phase where a variable composition is possible is called a solid solution. In the case of AB_2O_4 spinels, the introduction of a cation is possible where it directly replaces another cation of like charge and similar size. The idea is to not form any vacancies or interstitial ions. It is also necessary that the two end members of the compound series have the same structure, e.g. both being normal

spinels or both being inverse spinels. As an example, Mn^{2+} can substitute for Fe^{2+} in $FeCr_2O_4$ to give $Mn_xFe_{1-x}Cr_2O_4$. The probability of any particular tetrahedral site being occupied by Mn^{2+} or Fe^{2+} depends solely on the value of x as the ions will be randomly distributed amongst those sites. Other parameters will also have an average value, such as lattice size, which will change gradually from that of the starting material steadily towards the other end member of the series (Vegard's Law). Any deviations from this ideal behaviour can be spotted by plotting the lattice parameters of successive members of such as series, to create a calibration curve.

4.2.4   Solid State Reaction

In order to get two polycrystalline powders to react together on a suitable time scale, it is necessary to use high temperatures and to have the reactants in intimate contact, necessitating the use of finely ground powders. Reaction of the appropriate single oxides, AO and B_2O_3, at temperatures approaching $1000°C$, can yield the AB_2O_4 spinel. The ease of formation varies with the spinel concerned.

The reaction is initiated by the formation of some of the spinel phase at the surfaces of two adjacent AO and B_2O_3 crystals. The similarity in structure between the spinel product and AO reactant then helps the diffusion of ions required to complete the reaction. The ions are believed[1] to diffuse via alternating octahedral and tetrahedral sites. Ions with no great preference for either octahedral or tetrahedral sites (e.g. Mn^{2+} and Fe^{3+}) can rapidly diffuse through the matrix. Those ions with a strong preference for being located in octahedral sites (e.g. Cr^{3+}, Ni^{2+} and Fe^{2+}) will diffuse more slowly, as they struggle to pass through the tetrahedral sites.

It is the surface area dependence of the rate of reaction that dictates the use of fine powders, if the product is to be obtained within a reasonable period of time.

4.2.5   General Method for Spinel Preparation

This method of spinel preparation has been successfully used by other workers[2, 3, 4].

Table 4.2.1 details the reactants and conditions used for each of the spinels prepared for this work.

Since FeO is unstable in air, it was necessary to produce it *in situ* by decomposition of the iron(II) oxalate. Likewise, nickel carbonate, manganese oxalate and cobaltous carbonate were used in place of the respective oxides.

The appropriate oxides, carbonates and/or oxalates (general purpose

reagent grade, BDH Chemicals Limited) were carefully weighed, to obtain the desired cation ratio, thoroughly mixed, ground in an agate mortar and pestle to a fine powder, and then compacted into a silica boat. The oxides $M_xCo_{1-x}Fe_2O_4$, where M = Mn, Fe or Ni and $0 \leq x \leq 1$, were prepared with x = 0, 0.25, 0.5, 0.75 and 1. Obviously, with x = 1, no $CoCO_3$ was needed for the preparation, and with x = 0, no M-containing compound was required. The silica boat would then be placed into the hot zone of an electrically heated furnace (Figure 4.2.2). The appropriate gas mixture would then be set flowing through the furnace at a rate of approximately 15 ml per minute for 1 hr with the furnace at room temperature. Once the reactor tube had been purged, the furnace would be set to heat up to the desired temperature, with the gas flow kept constant. The 200°C step in the process was to drive off H_2O from the oxalates or hydrated carbonates. The mixtures were then left to react at temperature and with the gas flowing for the required reaction time. After the required reaction time, the furnace would be cooled back to room temperature, with the gas still flowing, before the products of reaction were removed for characterisation. The reaction products were ground again prior to analysis.

The hot zones of the furnaces used were determined by placing a thermocouple inside the furnace tube, and measuring temperatures along the length of the tube. It was found that there was sufficient hot zone within both furnaces to safely house up to three silica boats at a time in each. Figure 4.2.3 illustrates the temperature profile along one of the furnaces.

4.2.6   Pellet Pressing

For insertion into the gamma cell, the oxide powder samples were formed into pressed pellets. A Specac die holder and hand operated hydraulic press were used. The sample powder was sandwiched between the two 8 mm dies and the assembly then evacuated to $<5x10^{-2}$ τ for a period of two minutes. A pressure of 5 tons was then applied for a further two minutes. After removal from the press, the pellets (ideally ~1 mm thick) were strong enough to survive future handling.

Spinel, $0 \leq x \leq 1$	Reagents	Atmosphere, temperature and time
$Mn_xCo_{1-x}Fe_2O_4$	$Mn(COO)_2.2H_2O$ + $CoCO_3$ + Fe_2O_3	CO_2 gas 200°C x 16 hr + 950°C x 150 hr
$Fe_xCo_{1-x}Fe_2O_4$	$Fe(COO)_2.2H_2O$ + $CoCO_3$ + Fe_2O_3	CO_2 / 2% CO gas 200°C x 16 hr + 950°C x 150 hr
$Ni_xCo_{1-x}Fe_2O_4$	$NiCO_3.2Ni(OH)_2.4H_2O$ + $CoCO_3$ + Fe_2O_3	CO_2 gas 200°C x 16 hr + 950°C x 150 hr

Table 4.2.1. Preparation conditions for the $M_xCo_{1-x}Fe_2O_4$ spinels.
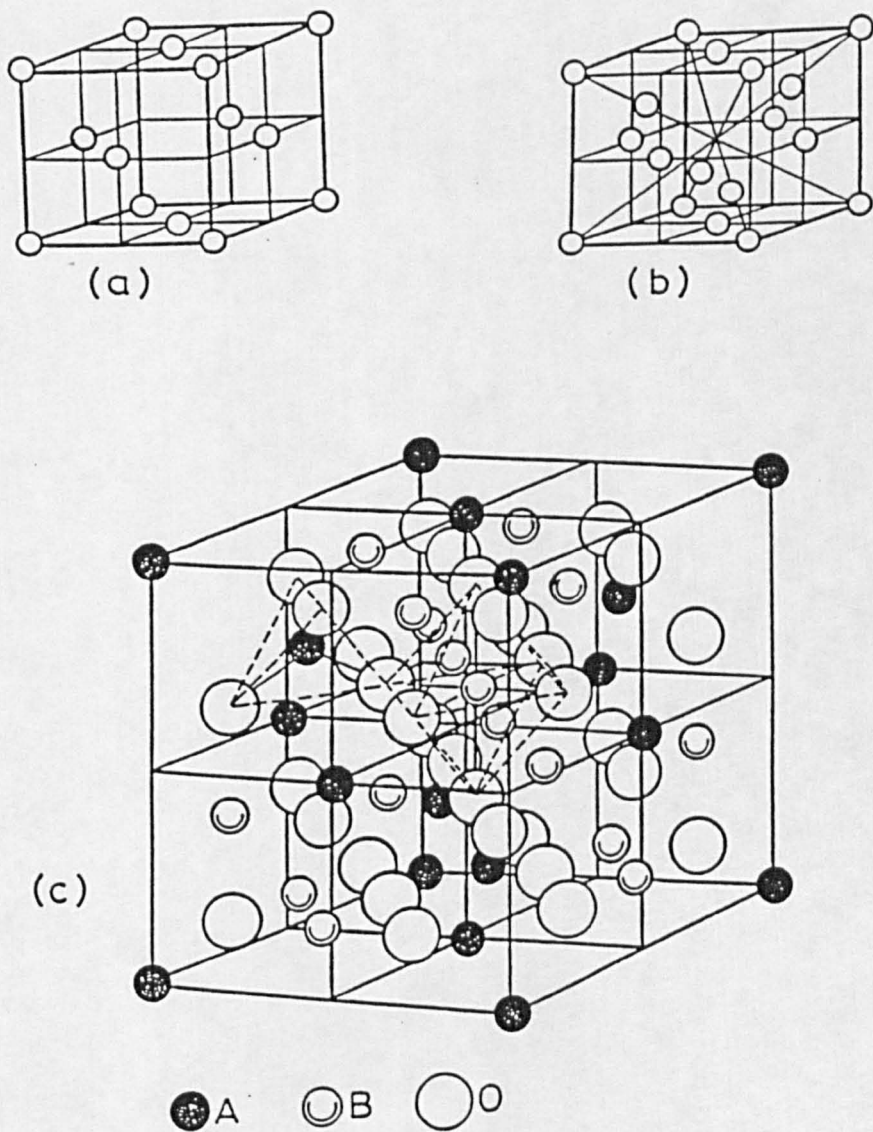
Figure 4.2.1. The relationship between a simple fcc lattice and the spinel lattice structure: a) face centred cubic structure; b) diamond structure; and c) spinel structure, AB_2O_4.
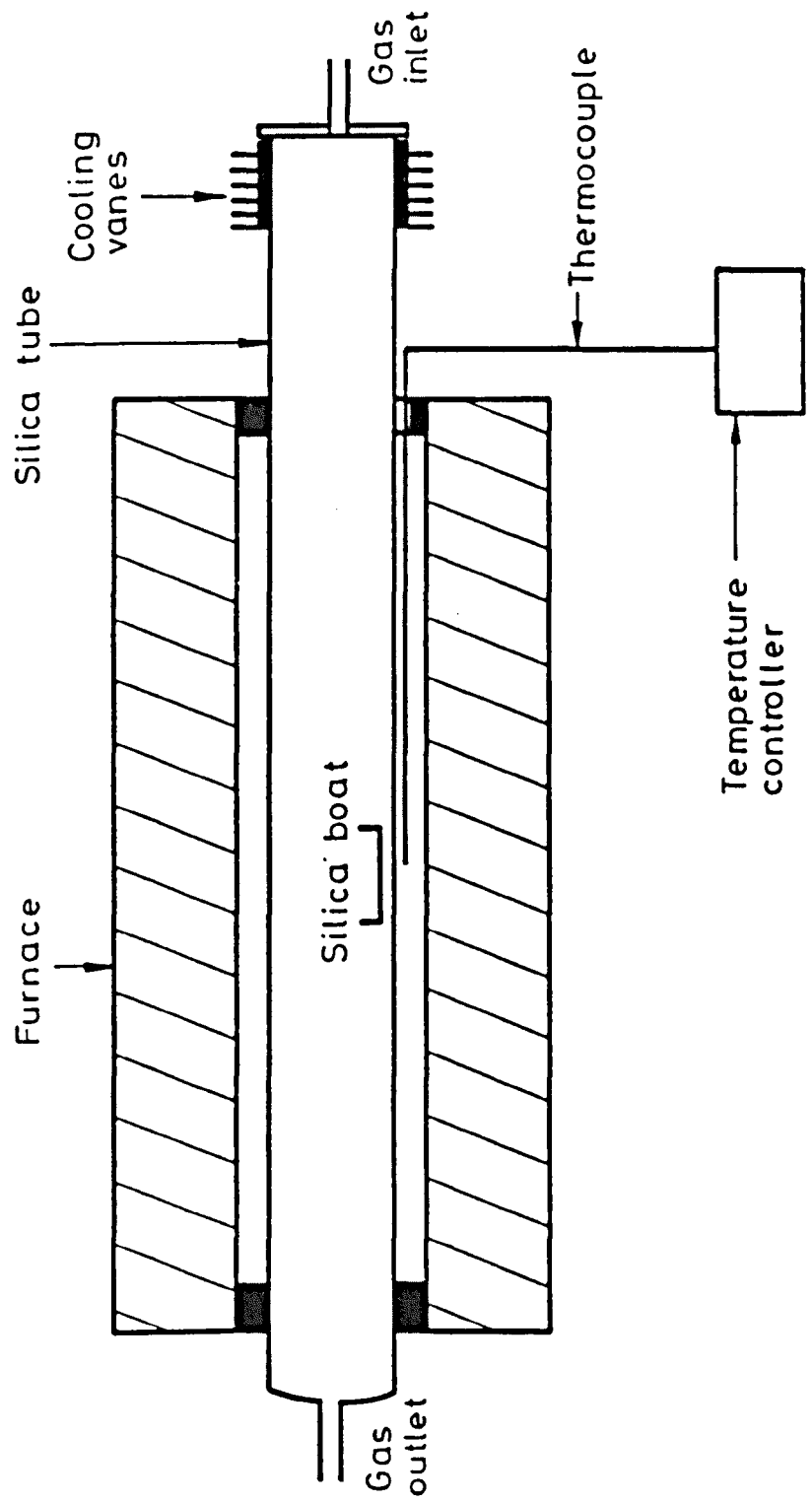
Figure 4.2.2. Furnace for spinel preparation.

110
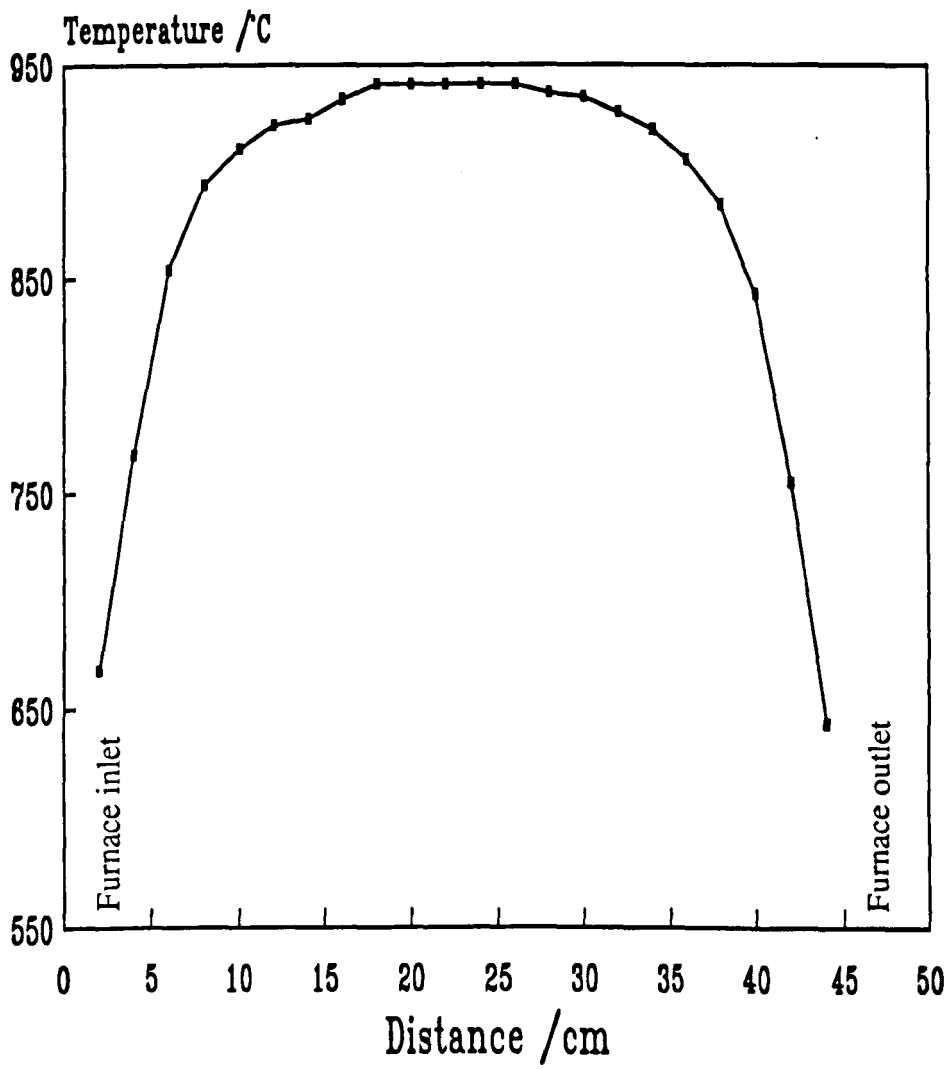
Figure 4.2.3. Temperature profile along furnace.

111

4.3 Characterisation of the Spinels $M_xCo_{1-x}Fe_2O_4$ (M = Mn, Fe or Ni; $0 \leq x \leq 1$)

4.3.1 Introduction

A range of analytical techniques was used to characterise the $M_xCo_{1-x}Fe_2O_4$ spinels prior to their exposure in the gamma cell.

4.3.2 Optical Observations

The spinels were all black in colour after leaving the furnace. The mixtures before treatment in the furnace tended to be brown, the colour being dominated by the brick red Fe_2O_3 component.

The pellets formed from these spinels required careful handling to avoid breakage. All were attracted to a permanent magnet, unlike any of the starting materials.

4.3.3 Energy Dispersive X-Ray Analysis

The beryllium window EDX system and its associated ZAF correction routines were used to determine the cation ratios in the three spinel series. Tables 4.3.1, 4.3.2 and 4.3.3 list the calculated values, all being given to two decimal places. The results obtained for the three series were all in reasonable agreement with the expected values.

4.3.4 X-Ray Diffraction

This technique quickly showed that the three batches of $CoFe_2O_4$ prepared were equivalent, giving identical spectra (see Figure 4.3.1).

X-ray diffraction showed that in all cases, the preparation had brought about 100% conversion from the starting materials to the desired product. Figures 4.3.2, 4.3.3, 4.3.4 and 4.3.5 show the shifts in the [10$\bar{2}$0], [951] and [10$\bar{2}$2] reflections and the a_0 lattice parameter for the three sets of spinels as x varies from 0 to 1. In all cases, it can be seen that there is a steady shift in peak positions as x varies. The magnitude and direction of the lattice parameter changes reflect the different sizes of the ions involved. Replacing Co^{2+} (75 pm [5]) with the larger Mn^{2+} (83 pm [5]) forces an increase in the dimensions of the unit cell, and, so, a_0 lattice parameter. Conversely, the increasing presence of the smaller Ni^{2+} ion (69 pm [5]) contracts the structure and decreases the observed a_0 value. Fe^{2+} (78 pm [5]), being closest of the replacement ions to Co^{2+} in size, gives the least effect, producing only a slight increase in lattice parameter. As all the spinels prepared adopt the inverse

112

structure, with the exception of $MnFe_2O_4$, which is best considered as an intermediate spinel[4] and having the formula:

$$Mn_{0.8}^{2+}Fe_{0.2}^{3+}(Mn_{0.2}^{2+}Fe_{1.8}^{3+})O_4$$

where the octahedral sites are occupied by the ions in brackets, there would be expected to be a steady shift in lattice parameter with increasing substitution. If the increase in x had necessitated a change from inverse to normal (or *vice versa*) then a more complex relationship between x and a_0 might have been expected. Table 4.3.4 lists the a_0 lattice parameter values for the end points of the series.

4.3.5   X-Ray Photoelectron Spectroscopy

Table 4.3.5 summarises the Mn $2p_{3/2}$, Fe $2p_{3/2}$, Co $2p_{3/2}$, Ni $2p_{3/2}$ and O $1s$ peak positions obtained. The samples were all analysed in the form of powders pressed onto sticky copper tape. It can be seen in both the Al $K\alpha$ and Mg $K\alpha$ results for $Fe_xCo_{1-x}Fe_2O_4$ that the Fe $2p_{3/2}$ binding energies tend towards lower values as x increases. When x = 0, all the iron present in the sample will be as Fe(III). The iron added to replace cobalt does so as Fe(II). Therefore, as x increases, whereas the Fe(III) contribution to the Fe $2p_{3/2}$ XPS peak envelope remains constant, the Fe(II) part increases. This will tend to shift the peak position towards lower binding energies, as seen. The value obtained for $FeFe_2O_4$, 710.5 eV, is a little low compared to previously reported values of the position of the combined Fe $2p$ peak[6, 7, 8]. The manganese and nickel spinel series show no such shift in Fe $2p_{3/2}$ binding energy. Previously reported values for Fe(III) in Fe_2O_3 range from 711.0 eV [8] to 711.4 eV [10] and 711.6 eV [7]. The values obtained in this work for Fe(III), in the manganese and nickel spinels, generally fall within this range. This contrasts with a study of the Fe(III) binding energy values in $MnFe_xCr_{2-x}O_4$ and $NiFe_xCr_{2-x}O_4$ spinels[11], where Fe $2p_{3/2}$ binding energies were lower than in Fe_2O_3. $CoFe_xCr_{2-x}O_4$ gave binding energies around those for Fe_2O_3 at high iron contents, but tending to lower values with decreasing iron concentration. Tables 4.3.6 and 4.3.7 detail the results obtained from the Fe $2p$ XP spectra.

The Mn $2p_{3/2}$ binding energy from $MnFe_2O_4$ of 640.9 eV is in good agreement with the literature value of 640.8 eV [11]. The Mn $2p_{3/2}$ peak position doesn't change with increasing x and is consistent with the presence of divalent manganese in an oxide lattice[11].

In disagreement with one set of similar data[12], but agreement with another[13], there is no increase in Co $2p_{3/2}$ binding energy with decreasing cobalt content within the nickel series. However, there does appear to be an increase in Co $2p_{3/2}$ binding energy with increasing x within the manganese series. All of the cobalt

spectra included the presence of a shake-up satellite, some 3.6 - 6.5 eV higher in binding energy than the $2p_{3/2}$ signal (see Section 3.4.13), indicative of Co(II) species. Low spin Co(III) gives much weaker satellite features[11, 12, 14] than does high spin Co (II), owing to the presence of unpaired valence electrons in the Co(II) $3d$ orbital. The cobalt present in the prepared spinels is expected to be in the Co(II) oxidation state. Figure 4.3.6, mentioned more fully below, shows these satellite structures in the spectra recorded off the $Mn_xCo_{1-x}Fe_2O_4$ spinel series, while Tables 4.3.8 and 4.3.9 record the details of the Co $2p$ region. It can be seen that the Co $2p_{3/2}$ FWHM from the aluminium x-ray spectra are greater than from the magnesium spectra, as expected. The FWHM, in both cases, tend to increase as the quality of the spectra decreases, with decreasing cobalt content.

Some care has to be taken in interpreting the XP spectra from these spinels. There are combinations of cations and exciting radiation that bring about overlaps of Auger peaks with the XPS signals of interest. In particular, when using Al $K\alpha$ radiation to look at the iron- and cobalt-containing spinels, the Fe L_3VV Auger peak at 784.4 eV [15] falls just to the high binding energy side of the Co $2p_{3/2}$ signal. The effect of this on the Co $2p$ envelope is illustrated in Figure 4.3.6, where, as x increases, the contribution of the Fe Auger signal increases in relation to that of the Co. With x = 1, only the Auger peak remains. Switching to the Mg $K\alpha$ source, the peak shape stays more constant and the lack of the Auger signal is revealed in the $CoFe_2O_4$ spectrum. Another indication of this effect is seen in Tables 4.3.8 and 4.3.9. Whereas the ratio of satellite intensity to $2p_{3/2}$ photoelectron peak intensity remains steady for the magnesium spectra (with the exception of the $Ni_{0.5}Co_{0.5}Fe_2O_4$ result), it increases in the aluminium spectra as the cobalt content of the oxides decreases. This is an indication of the increasing prominence of the Fe L_3VV Auger signal. An additional complication is the overlap of the Co $L_3M_{23}V$ Auger line at 776.4 eV [15], when using Al $K\alpha$ radiation. This has been shown[16] to affect quantitative results on Co_4Ni alloy by up to 15%. The more oxidised the cobalt, the less the interference as the Co $2p_{3/2}$ peak shifts to higher binding energies. Using Mg $K\alpha$ x-rays to avoid this interference only succeeds in shifting the Auger peak to overlap with O $1s$. One conclusion reached was the recommendation of using Al $K\alpha$ when analysing Co-O systems.

There was no change in Ni $2p_{3/2}$ peak position with increasing substitution of cobalt by nickel. The value of around 855.5 eV is in agreement with those found for nickel / iron / chromium spinels[11], being higher than the value for NiO. As with the cobalt spectra, intense satellite features were observed in the Ni $2p$ region. Tables 4.3.10 and 4.3.11 detail the results obtained. There is a decrease in $2p_{3/2}$ photoelectron peak FWHM with increasing nickel content. This is likely to be due to the improved counting statistics in the higher nickel samples.

Tables 4.3.12 and 4.3.13 give quantitative estimates of the surface composition of the spinel oxides as determined from the XP spectra. The values given assume a stoichiometric spinel composition AB_2O_4 and do not take into account the oxygen concentrations. Only cation ratios were determined. The manganese spinels all appear to be depleted in iron within the surface region analysed by XPS. Cobalt concentrations are all higher than would be expected from the bulk compositions. The depletion of iron agrees with previous work on similar spinel oxides[12]. The $Fe_xCo_{1-x}Fe_2O_4$ spinels were also enhanced in surface cobalt concentration. The measured cobalt content fell, as expected, as x increased. With the exception of $NiFe_2O_4$, the iron concentrations determined for the nickel spinels using aluminium x-rays were also low. Cobalt gave high values. For the magnesium x-ray induced spectra, iron concentrations tended, if anything, to be a little on the high side. Only $Ni_{0.25}Co_{0.75}Fe_2O_4$ gave a stoichiometry of less than two for iron. Except for $CoFe_2O_4$, cobalt, again, gave higher than anticipated concentrations. $NiFe_2O_4$, in both cases, appeared surface depleted in nickel and enhanced in iron. This result agrees with one obtained elsewhere[11].

An attempt may be made to attribute such surface segregation as this to the relative mobilities of the ions concerned through the bulk via tetrahedral and octahedral lattice sites, with the relative preferences for the two sites affecting rates of diffusion. The relative ion mobilities may be deduced to be[11]:

$$Fe^{3+} > Mn^{2+} > Fe^{2+} > Co^{2+} > Ni^{2+}$$
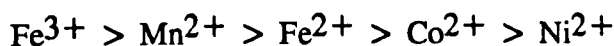
This would tend to suggest that the samples ought to be surface enriched in iron, at the expense of cobalt, which was not the case. The kinetic factors involved in this approach will not act alone, however. Thermodynamic considerations have to be made in cases of high temperature and low oxygen partial pressure, as present in the furnaces when the spinels were formed. In such cases, the more thermodynamically favoured oxide will tend to form on the surface of the material. With FeO and Fe_2O_3 having heats of formation[17], $\Delta H°_{298}$, of -267 and -823 kJ.mol^{-1}, respectively, compared to the -239 and -854 kJ.mol^{-1} of CoO and Co_3O_4, there would appear to be little to choose between the two elements with regards to thermodynamic stability of their oxides. The fact that $CoFe_2O_4$ appeared surface depleted in iron, whereas similar material in a previous study[11] gave a surface composition like that of the bulk, suggests that the low surface iron concentrations found here may be a function of the peak regions chosen for quantification.

Sample	Cation ratio		
	Mn	Co	Fe
$CoFe_2O_4$	-----	1.07	1.93
$Mn_{0.25}Co_{0.75}Fe_2O_4$	0.22	0.80	1.98
$Mn_{0.5}Co_{0.5}Fe_2O_4$	0.50	0.35	2.15
$Mn_{0.75}Co_{0.25}Fe_2O_4$	0.74	0.22	2.04
$MnFe_2O_4$	0.95	-----	2.05

Table 4.3.1. Cation ratios for the series $Mn_xCo_{1-x}Fe_2O_4$ as determined by EDX.

Sample	Cation ratio	
	Co	Fe
$CoFe_2O_4$	1.00	2.00
$Fe_{0.25}Co_{0.75}Fe_2O_4$	0.73	2.27
$Fe_{0.5}Co_{0.5}Fe_2O_4$	0.49	2.51
$Fe_{0.75}Co_{0.25}Fe_2O_4$	0.28	2.72
$FeFe_2O_4$	-----	3.00

Table 4.3.2. Cation ratios for the series $Fe_xCo_{1-x}Fe_2O_4$, as determined by EDX.

	Cation ratio		
Sample	Ni	Co	Fe
$CoFe_2O_4$	-----	0.99	2.01
$Ni_{0.25}Co_{0.75}Fe_2O_4$	0.24	0.71	2.05
$Ni_{0.5}Co_{0.5}Fe_2O_4$	0.48	0.46	2.05
$Ni_{0.75}Co_{0.25}Fe_2O_4$	0.70	0.30	2.00
$NiFe_2O_4$	0.90	-----	2.10

Table 4.3.3. Cation ratios for the series $Ni_xCo_{1-x}Fe_2O_4$, as determined by EDX.

	Lattice parameter a_0 /Å	
Sample	Experimental	Literature
$CoFe_2O_4$ (Mn)	8.391	JCPDS 22-1086 8.392
$MnFe_2O_4$	8.507	JCPDS 10-391 8.499
$CoFe_2O_4$ (Fe)	8.392	JCPDS 22-1086 8.392
$FeFe_2O_4$	8.400	JCPDS 19-629 8.396
$CoFe_2O_4$ (Ni)	8.393	JCPDS 22-1086 8.392
$NiFe_2O_4$	8.345	JCPDS 10-325 8.339

Table 4.3.4. Experimental and literature a_0 lattice parameter values for some spinels.

	Binding energy /eV									
	$Mn\ 2p_{3/2}$		$Fe\ 2p_{3/2}$		$Co\ 2p_{3/2}$		$Ni\ 2p_{3/2}$		$O\ 1s$	
Sample	Al	Mg	Al	Mg	Al	Mg	Al	Mg	Al	Mg
$CoFe_2O_4$ (Mn)	-----	-----	711.6	711.3	780.8	781.0	-----	-----	530.1	530.4
$Mn_{0.25}Co_{0.75}Fe_2O_4$	641.6	641.6	711.5	711.4	780.8	780.9	-----	-----	530.2	530.3
$Mn_{0.5}Co_{0.5}Fe_2O_4$	640.7	641.2	711.6	711.6	781.2	780.9	-----	-----	530.2	530.5
$Mn_{0.75}Co_{0.25}Fe_2O_4$	641.5	641.5	711.8	711.7	781.5	781.0	-----	-----	530.8	530.8
$MnFe_2O_4$	640.9	641.3	711.5	711.9	-----	-----	-----	-----	530.2	530.5
$CoFe_2O_4$ (Fe)	-----	-----	711.2	711.5	780.8	780.9	-----	-----	530.3	530.6
$Fe_{0.25}Co_{0.75}Fe_2O_4$	-----	-----	711.1	711.3	780.7	780.7	-----	-----	530.2	530.5
$Fe_{0.5}Co_{0.5}Fe_2O_4$	-----	-----	711.3	711.4	780.8	780.5	-----	-----	530.3	530.5
$Fe_{0.75}Co_{0.25}Fe_2O_4$	-----	-----	711.0	710.5	781.1	780.4	-----	-----	530.2	530.1
$FeFe_2O_4$	-----	-----	710.6	710.4	-----	-----	-----	-----	530.4	530.3
$CoFe_2O_4$ (Ni)	-----	-----	711.3	711.6	780.6	780.9	-----	-----	530.2	530.7
$Ni_{0.25}Co_{0.75}Fe_2O_4$	-----	-----	711.3	711.3	780.5	780.7	855.4	855.7	530.1	530.4
$Ni_{0.5}Co_{0.5}Fe_2O_4$	-----	-----	711.2	711.4	780.6	780.7	855.2	855.4	530.0	530.3
$Ni_{0.75}Co_{0.25}Fe_2O_4$	-----	-----	711.3	711.2	781.0	780.7	855.4	855.7	530.2	530.3
$NiFe_2O_4$	-----	-----	711.0	711.3	-----	-----	855.3	855.5	530.2	530.4

Table 4.3.5. Binding energies in the prepared spinels.

Sample	BE $2p_{3/2}$ /eV	FWHM /eV	Δ Sat /eV [a]	I(Sat)/I(Main) [b]	BE $2p_{1/2}$ /eV	Δ $2p$ /eV [c]
$CoFe_2O_4$ (Mn)	711.6	5.3	5.6	0.43	723.4	11.9 [d]
$Mn_{0.25}Co_{0.75}Fe_2O_4$	711.5	4.8	5.6	0.47	724.2	12.7
$Mn_{0.5}Co_{0.5}Fe_2O_4$	711.6	4.8	6.0	0.37	724.8	13.2
$Mn_{0.75}Co_{0.25}Fe_2O_4$	711.8	4.4	5.0	0.40	725.1	13.2 [d]
$MnFe_2O_4$	711.5	4.1	5.3	0.38	725.1	13.6
$CoFe_2O_4$ (Fe)	711.2	4.7	5.3	0.61	724.4	13.2
$Fe_{0.25}Co_{0.75}Fe_2O_4$	711.1	4.4	4.8	0.60	724.0	12.9
$Fe_{0.5}Co_{0.5}Fe_2O_4$	711.3	4.6	4.8	0.52	724.2	12.9
$Fe_{0.75}Co_{0.25}Fe_2O_4$	711.0	5.8	7.6	0.32	724.1	13.1
$FeFe_2O_4$	710.6	5.4	5.7	0.32	723.7	13.1
$CoFe_2O_4$ (Ni)	711.3	4.4	5.2	0.50	724.6	13.3
$Ni_{0.25}Co_{0.75}Fe_2O_4$	711.3	4.4	5.2	0.50	724.5	13.3 [d]
$Ni_{0.5}Co_{0.5}Fe_2O_4$	711.2	4.3	4.6	0.50	724.3	13.1
$Ni_{0.75}Co_{0.25}Fe_2O_4$	711.3	4.2	4.6	0.49	724.5	13.3 [d]
$NiFe_2O_4$	711.0	4.1	4.3	0.43	724.2	13.2

a) Separation in eV between the main $2p_{3/2}$ peak and its associated shake-up satellite.
b) Intensity ratio between the shake-up satellite and the $2p_{3/2}$ photoelectron peak.
c) The separation in eV between the $2p_{3/2}$ and $2p_{1/2}$ photoelectron peaks.
d) Rounding errors affect this value.

Table 4.3.6. Fe $2p$ details from the aluminium XP spectra of the prepared spinels.

Sample	BE $2p_{3/2}$ /eV	FWHM /eV	Δ Sat /eV [a]	$I_{(Sat)}/I_{(Main)}$ [b]	BE $2p_{1/2}$ /eV	Δ $2p$ /eV [c]
$CoFe_2O_4$ (Mn)	711.3	4.2	5.0	0.33	724.3	13.0
$Mn_{0.25}Co_{0.75}Fe_2O_4$	711.4	4.5	5.6	0.39	724.4	13.1 [d]
$Mn_{0.5}Co_{0.5}Fe_2O_4$	711.6	4.2	4.7	0.40	724.7	13.0 [d]
$Mn_{0.75}Co_{0.25}Fe_2O_4$	711.7	4.5	5.5	0.41	725.1	13.4
$MnFe_2O_4$	711.9	4.4	5.8	0.36	725.2	13.4 [d]
$CoFe_2O_4$ (Fe)	711.5	4.4	5.4	0.34	724.7	13.2
$Fe_{0.25}Co_{0.75}Fe_2O_4$	711.3	4.4	5.4	0.35	724.8	13.5
$Fe_{0.5}Co_{0.5}Fe_2O_4$	711.4	4.8	5.7	0.26	724.4	13.0
$Fe_{0.75}Co_{0.25}Fe_2O_4$	710.5	5.3	6.2	0.28	723.6	13.1
$FeFe_2O_4$	710.4	5.1	4.8	0.38	723.5	13.1
$CoFe_2O_4$ (Ni)	711.6	3.6	3.3	0.49	724.3	12.7
$Ni_{0.25}Co_{0.75}Fe_2O_4$	711.3	3.7	3.9	0.44	724.5	13.2
$Ni_{0.5}Co_{0.5}Fe_2O_4$	711.4	3.5	4.1	0.47	724.8	13.4
$Ni_{0.75}Co_{0.25}Fe_2O_4$	711.2	3.9	4.2	0.41	724.4	13.1 [d]
$NiFe_2O_4$	711.3	4.0	4.8	0.36	724.7	13.4

a) Separation in eV between the main $2p_{3/2}$ peak and its associated shake-up satellite.

b) Intensity ratio between the shake-up satellite and the $2p_{3/2}$ photoelectron peak.

c) The separation in eV between the $2p_{3/2}$ and $2p_{1/2}$ photoelectron peaks.

d) Rounding errors affect this value.

Table 4.3.7. Fe $2p$ details from the magnesium XP spectra of the prepared spinels.

Sample	BE $2p_{3/2}$/eV	FWHM /eV	Δ Sat /eV [a]	I(Sat)/I(Main) [b]	BE $2p_{1/2}$/eV	$\Delta 2p$ /eV [c]
$CoFe_2O_4$ (Mn)	780.8	4.2	5.2	0.51	796.5	15.7
$Mn_{0.25}Co_{0.75}Fe_2O_4$	780.8	4.1	5.3	0.53	796.5	15.7
$Mn_{0.5}Co_{0.5}Fe_2O_4$	781.2	5.0	5.5	0.77	794.0	12.8
$Mn_{0.75}Co_{0.25}Fe_2O_4$	781.5	4.8	5.1	0.94	796.2	14.7
$MnFe_2O_4$	-----	-----	-----	-----	-----	-----
$CoFe_2O_4$ (Fe)	780.8	3.7	4.7	0.59	796.5	15.7
$Fe_{0.25}Co_{0.75}Fe_2O_4$	780.7	4.1	4.7	0.65	796.5	15.8
$Fe_{0.5}Co_{0.5}Fe_2O_4$	780.8	4.2	5.2	0.80	796.7	15.8 [d]
$Fe_{0.75}Co_{0.25}Fe_2O_4$	781.1	4.7	5.2	0.81	796.2	15.2 [d]
$FeFe_2O_4$	-----	-----	-----	-----	-----	-----
$CoFe_2O_4$ (Ni)	780.6	3.8	4.9	0.72	796.4	15.8
$Ni_{0.25}Co_{0.75}Fe_2O_4$	780.5	3.9	5.0	0.68	796.2	15.7
$Ni_{0.5}Co_{0.5}Fe_2O_4$	780.6	4.0	4.7	0.87	796.3	15.7
$Ni_{0.75}Co_{0.25}Fe_2O_4$	781.0	4.6	4.9	0.96	796.3	15.3
$NiFe_2O_4$	-----	-----	-----	-----	-----	-----

a) Separation in eV between the main $2p_{3/2}$ peak and its associated shake-up satellite.

b) Intensity ratio between the shake-up satellite and the $2p_{3/2}$ photoelectron peak.

c) The separation in eV between the $2p_{3/2}$ and $2p_{1/2}$ photoelectron peaks.

d) Rounding errors affect this value.

Table 4.3.8. Co $2p$ details from the aluminium XP spectra of the prepared spinels.

Sample	BE $2p_{3/2}$ /eV	FWHM /eV	Δ Sat /eV [a]	$I(Sat)/I(Main)$ [b]	BE $2p_{1/2}$ /eV	Δ $2p$ /eV [c]
$CoFe_2O_4$ (Mg)	781.0	3.8	5.2	0.44	796.7	15.7
$Mg_{0.25}Co_{0.75}Fe_2O_4$	780.9	3.7	5.1	0.40	796.5	15.7 [d]
$Mg_{0.5}Co_{0.5}Fe_2O_4$	780.9	4.0	5.5	0.54	796.1	15.3 [d]
$Mg_{0.75}Co_{0.25}Fe_2O_4$	781.0	4.6	6.5	0.48	796.8	15.7 [d]
$MgFe_2O_4$	-----	-----	-----	-----	-----	-----
$CoFe_2O_4$ (Fe)	780.9	3.6	4.8	0.49	796.8	15.9
$Fe_{0.25}Co_{0.75}Fe_2O_4$	780.7	3.4	4.8	0.53	796.7	16.0
$Fe_{0.5}Co_{0.5}Fe_2O_4$	780.5	3.7	4.9	0.47	796.9	16.4
$Fe_{0.75}Co_{0.25}Fe_2O_4$	780.4	3.2	4.9	0.45	797.6	17.2
$FeFe_2O_4$	-----	-----	-----	-----	-----	-----
$CoFe_2O_4$ (Ni)	780.9	2.4	3.6	0.51	797.0	16.2 [d]
$Ni_{0.25}Co_{0.75}Fe_2O_4$	780.7	3.2	4.2	0.48	796.7	16.0
$Ni_{0.5}Co_{0.5}Fe_2O_4$	780.7	3.1	4.7	0.29	796.7	16.0
$Ni_{0.75}Co_{0.25}Fe_2O_4$	780.7	4.2	5.6	0.45	796.6	15.9
$NiFe_2O_4$	-----	-----	-----	-----	-----	-----

a) Separation in eV between the main $2p_{3/2}$ peak and its associated shake-up satellite.

b) Intensity ratio between the shake-up satellite and the $2p_{3/2}$ photoelectron peak.

c) The separation in eV between the $2p_{3/2}$ and $2p_{1/2}$ photoelectron peaks.

d) Rounding errors affect this value.

Table 4.3.9. Co $2p$ details from the magnesium XP spectra of the prepared spinels.

Sample	BE $2p_{3/2}$ /eV	FWHM /eV	Δ sat /eV [a]	I(sat)/I(Main) [b]	BE $2p_{1/2}$ /eV	Δ 2p /eV [c]
$CoFe_2O_4$ (Ni)	-----	-----	-----	-----	-----	-----
$Ni_{0.25}Co_{0.75}Fe_2O_4$	855.4	3.2	6.3	0.49	872.6	17.2
$Ni_{0.5}Co_{0.5}Fe_2O_4$	855.2	2.9	6.4	0.39	873.0	17.8
$Ni_{0.75}Co_{0.25}Fe_2O_4$	855.4	3.0	6.3	0.44	873.0	17.6
$NiFe_2O_4$	855.3	2.8	6.0	0.36	872.8	17.5

a) Separation in eV between the main $2p_{3/2}$ peak and its associated shake-up satellite.
b) Intensity ratio between the shake-up satellite and the $2p_{3/2}$ photoelectron peak.
c) The separation in eV between the $2p_{3/2}$ and $2p_{1/2}$ photoelectron peaks.

Table 4.3.10. Ni $2p$ details from the aluminium XP spectra of the prepared spinels.

Sample	BE $2p_{3/2}$ /eV	FWHM /eV	Δ sat /eV [a]	I(sat)/I(Main) [b]	BE $2p_{1/2}$ /eV	Δ 2p /eV [c]
$CoFe_2O_4$ (Ni)	-----	-----	-----	-----	-----	-----
$Ni_{0.25}Co_{0.75}Fe_2O_4$	855.7	3.2	7.5	0.33	873.5	17.8
$Ni_{0.5}Co_{0.5}Fe_2O_4$	855.4	3.2	6.8	0.43	873.2	17.8
$Ni_{0.75}Co_{0.25}Fe_2O_4$	855.7	3.1	5.9	0.27	873.1	17.5 [d]
$NiFe_2O_4$	855.5	2.9	6.6	0.38	873.3	17.8

a) Separation in eV between the main $2p_{3/2}$ peak and its associated shake-up satellite.
b) Intensity ratio between the shake-up satellite and the $2p_{3/2}$ photoelectron peak.
c) The separation in eV between the $2p_{3/2}$ and $2p_{1/2}$ photoelectron peaks.
d) Rounding errors affect this value.

Table 4.3.11. Ni $2p$ details from the magnesium XP spectra of the prepared spinels.

Sample	Surface composition determined by XPS
$CoFe_2O_4$ (Mn)	$Co_{1.55}Fe_{1.45}O_4$
$Mn_{0.25}Co_{0.75}Fe_2O_4$	$Mn_{0.39}Co_{1.26}Fe_{1.35}O_4$
$Mn_{0.5}Co_{0.5}Fe_2O_4$	$Mn_{0.31}Co_{0.93}Fe_{1.76}O_4$
$Mn_{0.75}Co_{0.25}Fe_2O_4$	$Mn_{0.69}Co_{0.79}Fe_{1.52}O_4$
$MnFe_2O_4$	$Mn_{1.15}Fe_{1.85}O_4$
$CoFe_2O_4$ (Fe)	$Co_{1.55}Fe_{1.45}O_4$
$Fe_{0.25}Co_{0.75}Fe_2O_4$	$Co_{1.42}Fe_{1.58}O_4$
$Fe_{0.5}Co_{0.5}Fe_2O_4$	$Co_{1.22}Fe_{1.78}O_4$
$Fe_{0.75}Co_{0.25}Fe_2O_4$	$Co_{1.04}Fe_{1.96}O_4$
$FeFe_2O_4$	Fe_3O_4
$CoFe_2O_4$ (Ni)	$Co_{1.29}Fe_{1.71}O_4$
$Ni_{0.25}Co_{0.75}Fe_2O_4$	$Ni_{0.24}Co_{1.19}Fe_{1.57}O_4$
$Ni_{0.5}Co_{0.5}Fe_2O_4$	$Ni_{0.42}Co_{1.02}Fe_{1.57}O_4$ [a]
$Ni_{0.75}Co_{0.25}Fe_2O_4$	$Ni_{0.53}Co_{0.84}Fe_{1.63}O_4$
$NiFe_2O_4$	$Ni_{0.84}Fe_{2.16}O_4$

a) Rounding errors affect this value.

Table 4.3.12. Surface composition of the spinels as determined by aluminium XPS.

Sample	Surface composition determined by XPS
$CoFe_2O_4$ (Mn)	$Co_{1.71}Fe_{1.29}O_4$
$Mn_{0.25}Co_{0.75}Fe_2O_4$	$Mn_{0.64}Co_{1.12}Fe_{1.24}O_4$
$Mn_{0.5}Co_{0.5}Fe_2O_4$	$Mn_{0.70}Co_{0.33}Fe_{1.97}O_4$
$Mn_{0.75}Co_{0.25}Fe_2O_4$	$Mn_{0.87}Co_{0.28}Fe_{1.84}O_4$ [a]
$MnFe_2O_4$	$Mn_{1.16}Fe_{1.84}O_4$

Sample	Surface composition determined by XPS
$CoFe_2O_4$ (Fe)	$Co_{1.72}Fe_{1.28}O_4$
$Fe_{0.25}Co_{0.75}Fe_2O_4$	$Co_{1.51}Fe_{1.49}O_4$
$Fe_{0.5}Co_{0.5}Fe_2O_4$	$Co_{0.88}Fe_{2.12}O_4$
$Fe_{0.75}Co_{0.25}Fe_2O_4$	$Co_{0.46}Fe_{2.54}O_4$
$FeFe_2O_4$	Fe_3O_4

Sample	Surface composition determined by XPS
$CoFe_2O_4$ (Ni)	$Co_{0.91}Fe_{2.09}O_4$
$Ni_{0.25}Co_{0.75}Fe_2O_4$	$Ni_{0.17}Co_{1.18}Fe_{1.65}O_4$
$Ni_{0.5}Co_{0.5}Fe_2O_4$	$Ni_{0.22}Co_{0.73}Fe_{2.05}O_4$
$Ni_{0.75}Co_{0.25}Fe_2O_4$	$Ni_{0.53}Co_{0.31}Fe_{2.16}O_4$
$NiFe_2O_4$	$Ni_{0.59}Fe_{2.41}O_4$

[a] Rounding errors affect this value.

Table 4.3.13. Surface composition of the spinels as determined by magnesium XPS.
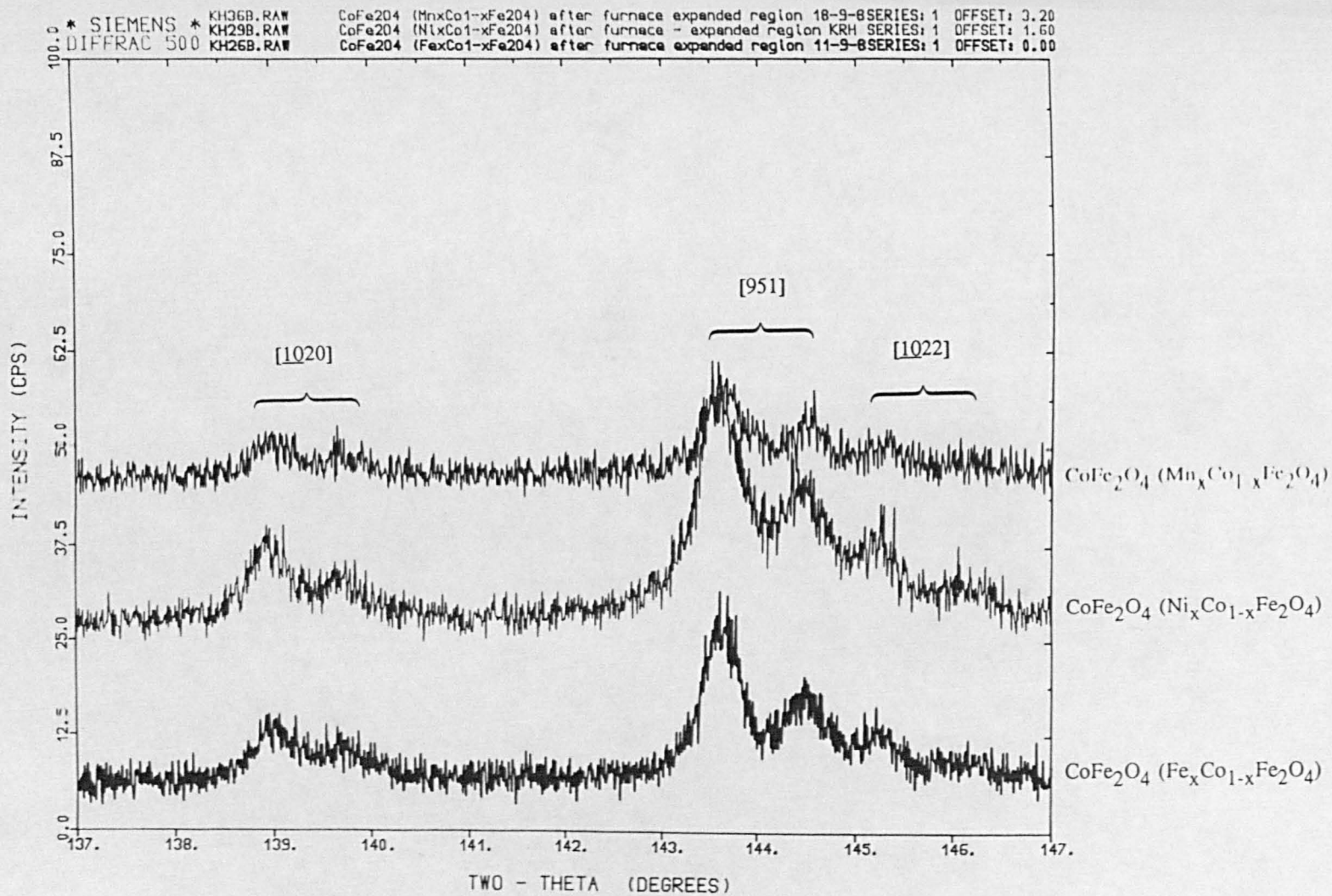
Figure 4.3.1. [1020], [951] and [1022] regional XRD spectra of the three CoFe₂O₄ batches.

126
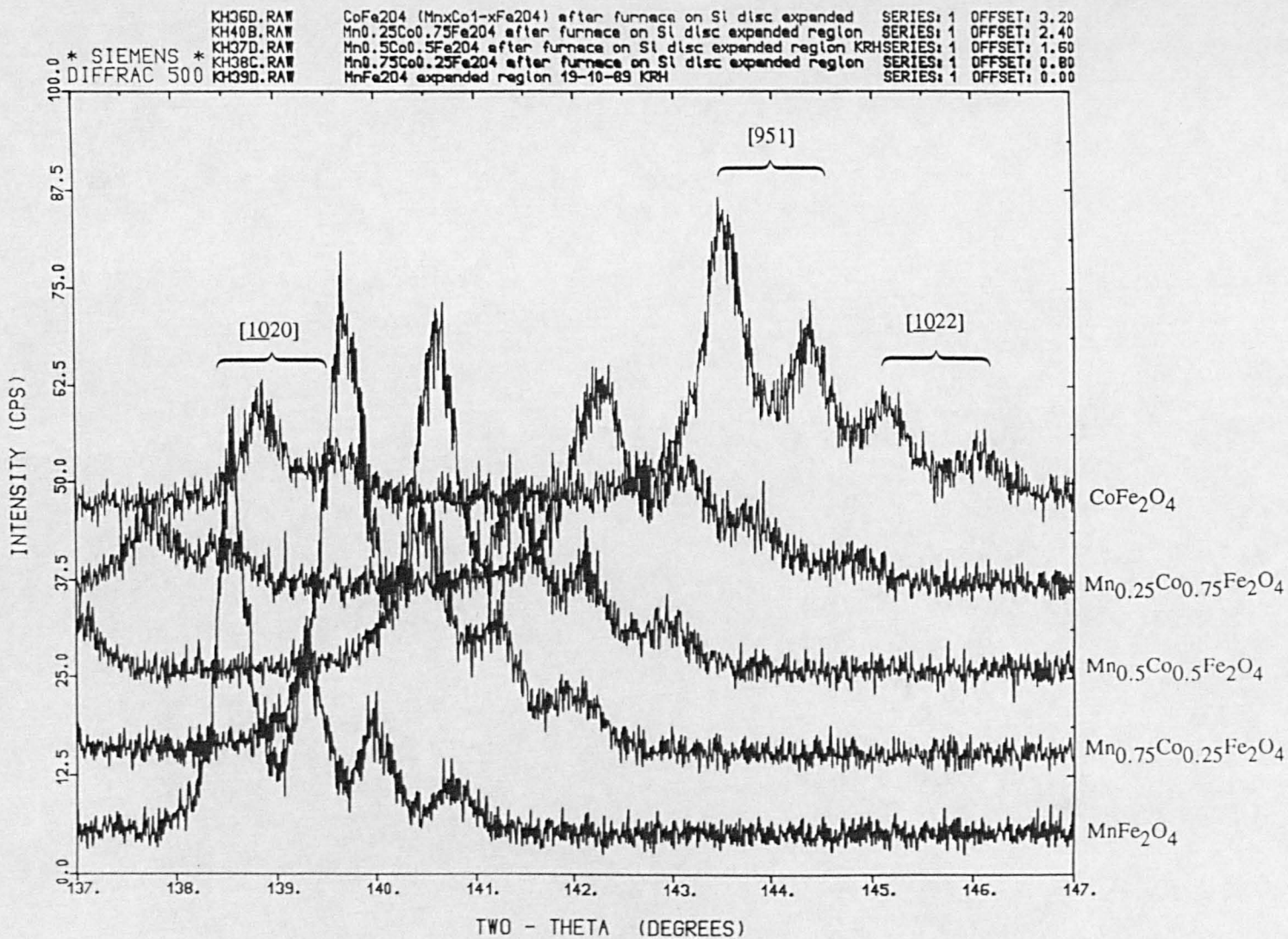
Figure 4.3.2. [1020], [951] and [1022] regional XRD spectra of the $Mn_xCo_{1-x}Fe_2O_4$ ($0 \leq x \leq 1$) series.

127
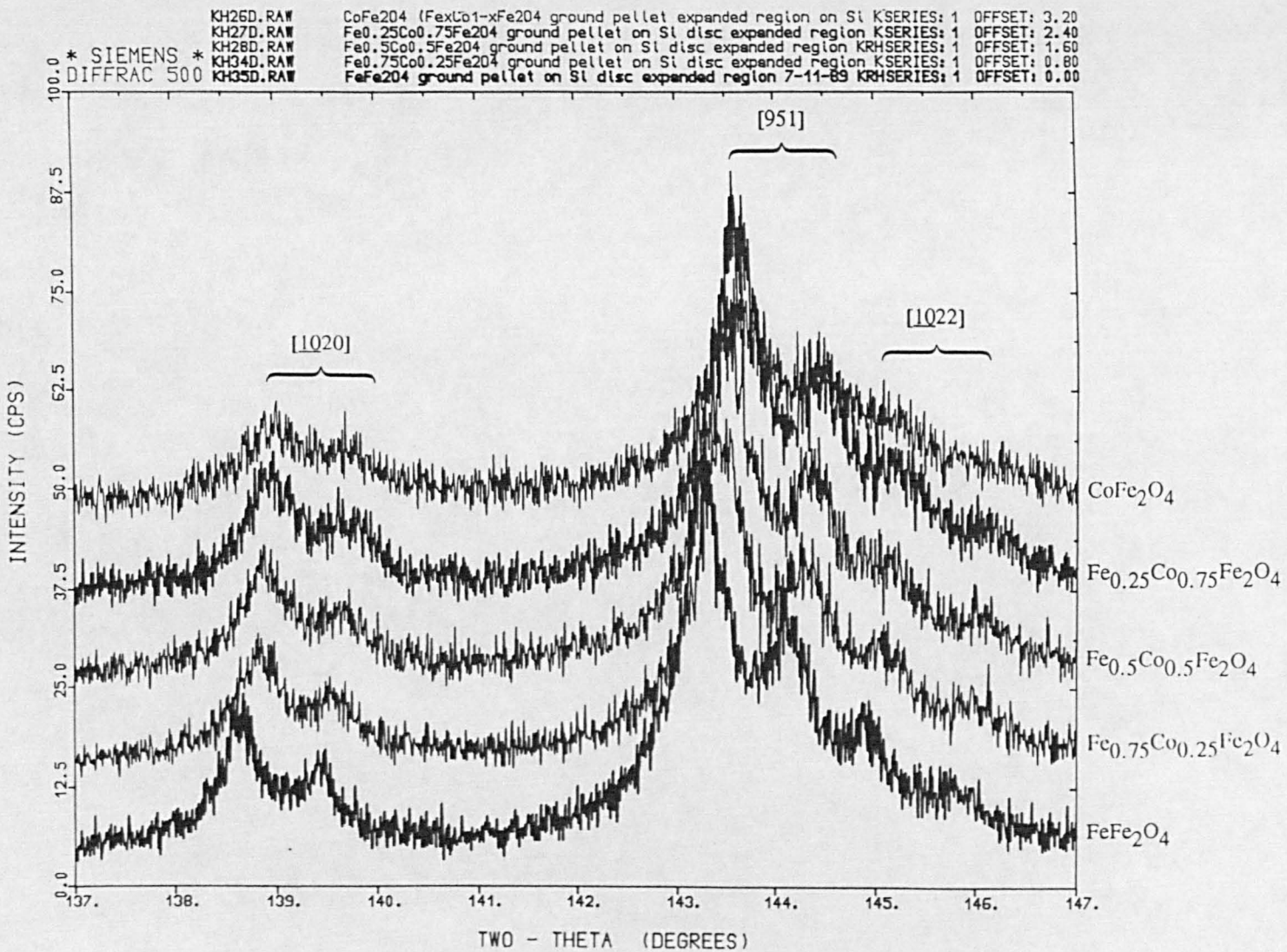
Figure 4.3.3. [10̄20], [951] and [10̄22] regional XRD spectra of the $Fe_xCo_{1-x}Fe_2O_4$ $(0 \le x \le 1)$ series.

128
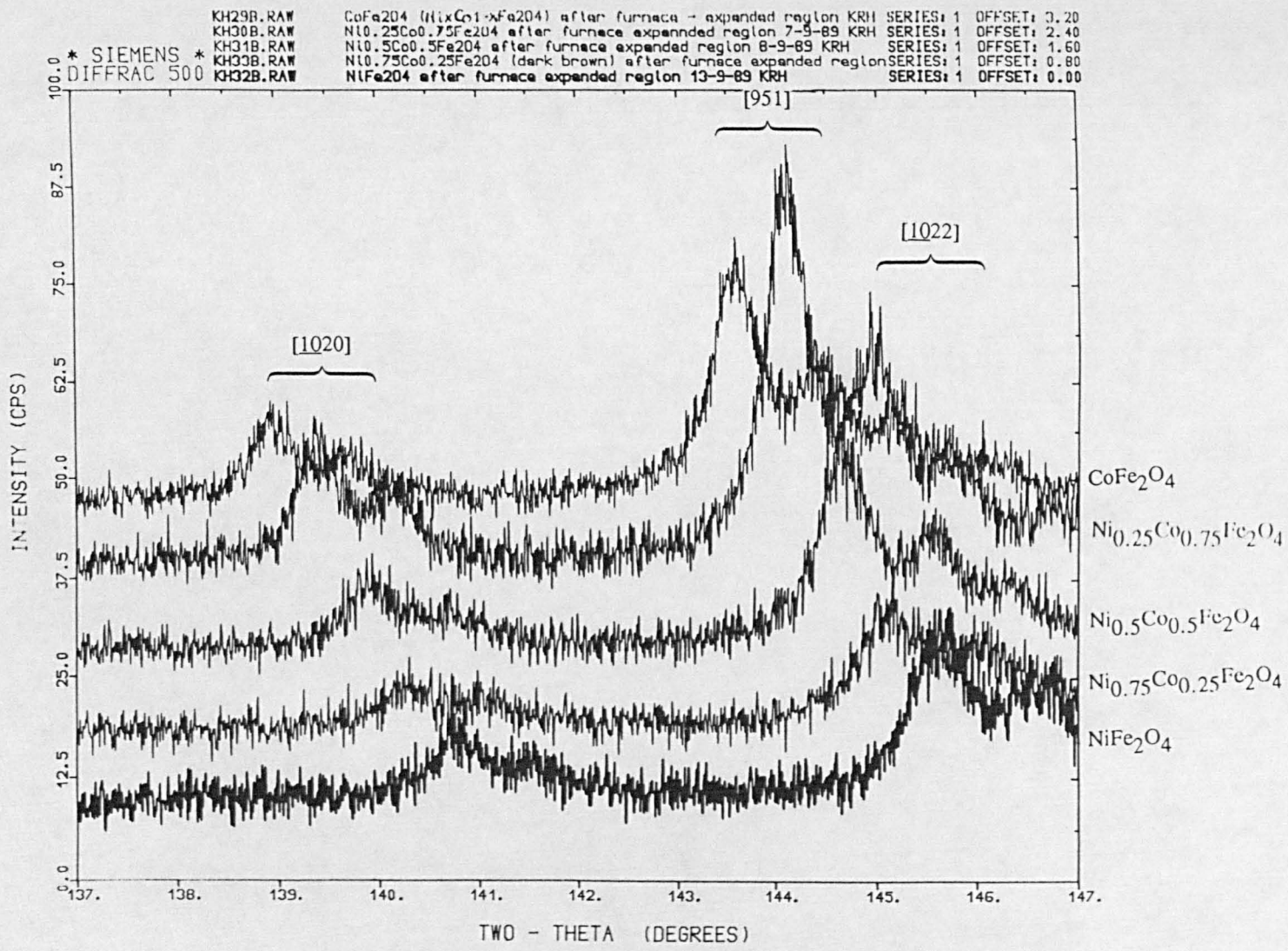
Figure 4.3.4. [1020], [951] and [1022] regional XRD spectra of the $Ni_xCo_{1-x}Fe_2O_4$ (0 ≤ x ≤ 1) series.

129
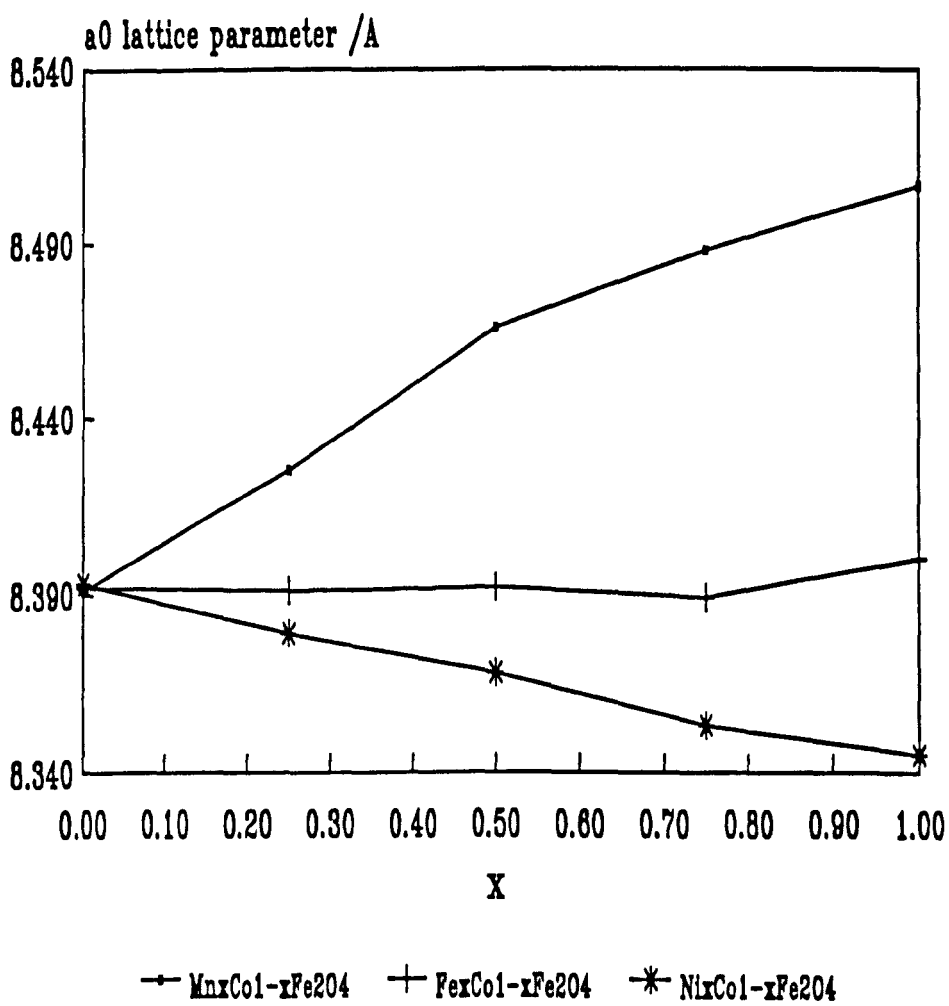
Figure 4.3.5. a_0 lattice parameters for the spinels $Mn_xCo_{1-x}Fe_2O_4$, $Fe_xCo_{1-x}Fe_2O_4$ and $Ni_xCo_{1-x}Fe_2O_4$.
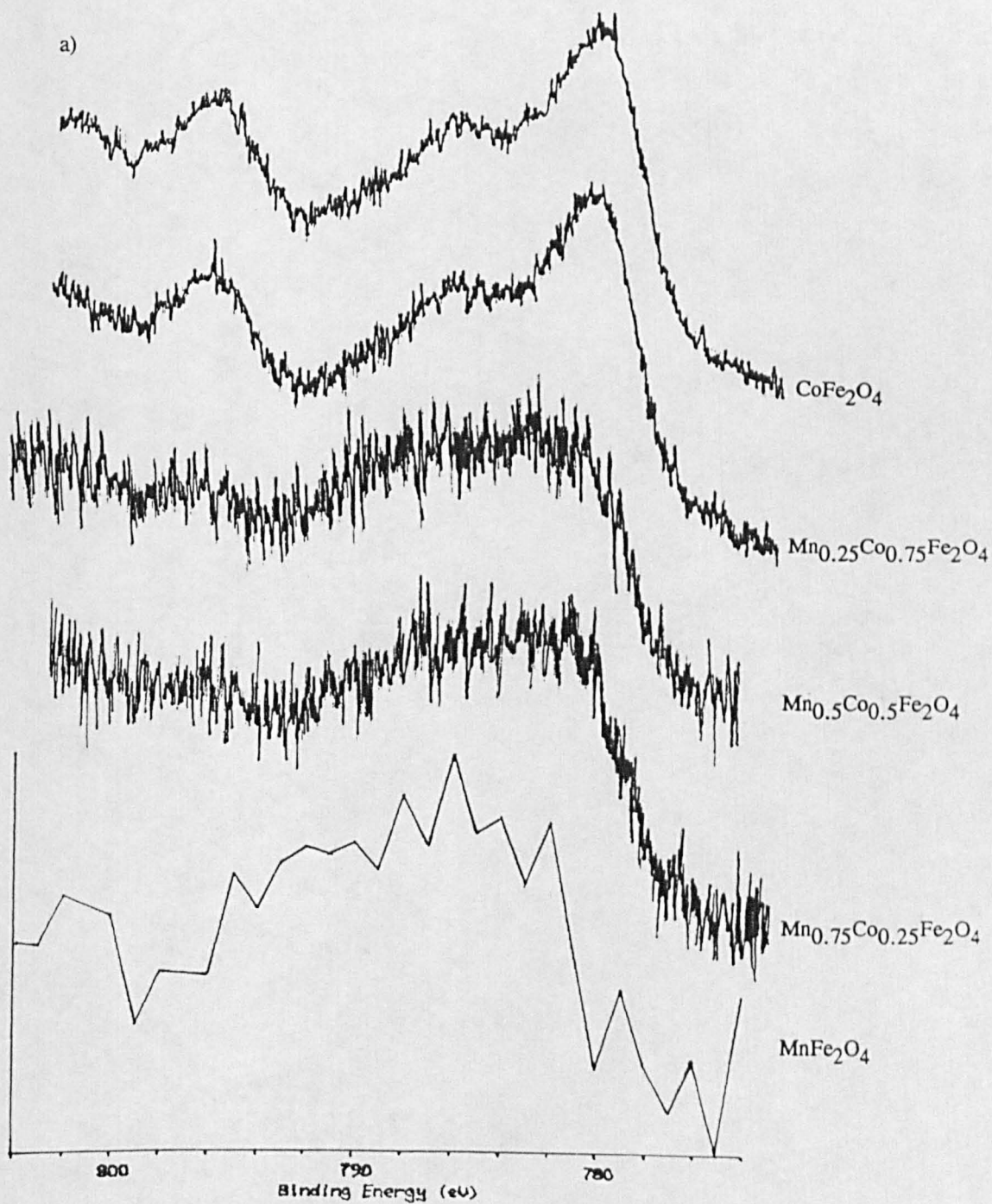
Figure 4.3.6. Co *2p* XP spectra for the $Mn_xCo_{1-x}Fe_2O_4$ series: a) Al *K* radiation; and b) Mg *K* radiation.
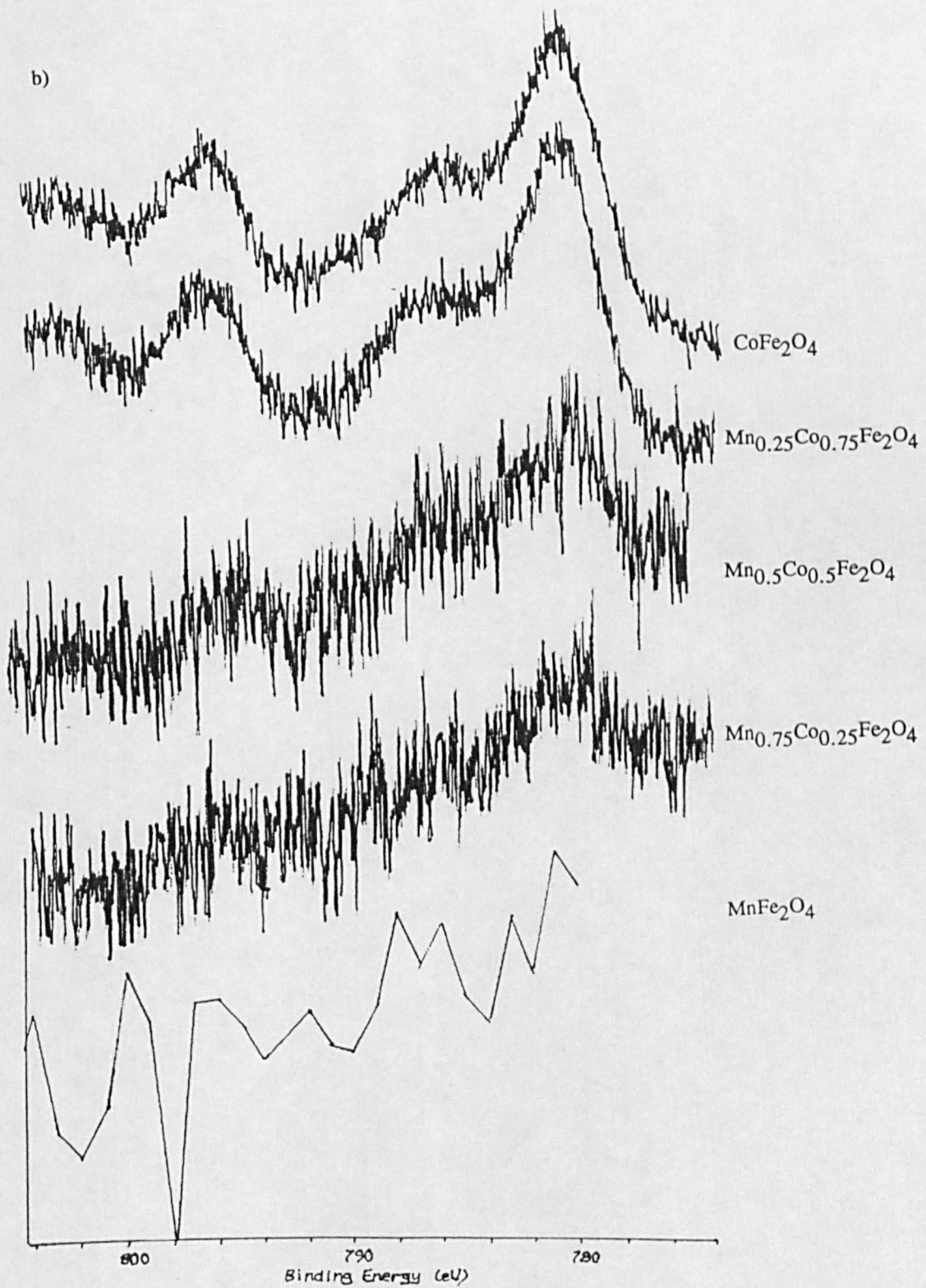
Figure 4.3.6 (continued). Co $2p$ XP spectra for the $Mn_xCo_{1-x}Fe_2O_4$ series: a) Al K radiation; and b) Mg K radiation.

4.4.1   Introduction

The three manganese oxides, MnO (99.5%), Mn_3O_4 (99.8%) and Mn_2O_3 (98%), used in this study, were obtained from Johnson Matthey GmbH., Karlsruhe, Germany.

At all temperatures above its Curie point, 122 K, MnO has the cubic structure of NaCl[18]. Mn_3O_4 is an example of a mixed valence compound. Unlike magnetite, and all of the spinel oxides prepared for this study, it adopts the normal spinel structure[19]. Mn_2O_3 has a structure related to that of CaF_2. The cubic arrangement is irregular, with each Mn^{3+} having four close oxygen neighbours and two distant[20].

The oxides were characterised, prior to exposure in the gamma cell, by the range of analytical techniques used throughout this work.

MnO_2 was also initially investigated, with XRD and XP spectra being recorded. However, it was found impossible to successfully prepare pellets out of this material and no further work was carried out on this oxide.

4.4.2   Optical Observations

MnO, out of the jar, was green in colour. The Mn_3O_4 was brown while the Mn_2O_3 was black. Unlike the MnO_2, these oxides formed good pellets that were, also, less susceptible to breakage than cobalt spinel ones.

4.4.3   Energy Dispersive X-Ray Analysis

It was found that the quantitative beryllium window EDX results, with the oxygen concentrations calculated by the software, were closer to the expected values when the oxides were analysed as pressed pellets as opposed to powders held down with bex film. Pellets present a flatter surface to the system, and the software used assumes that the sample is flat. Thus, better results would be expected from the pellets. For all three oxides, higher than expected oxygen concentrations are calculated for the powder samples. The results of these analyses are presented in Tables 4.4.1 and 4.4.2. The pressed pellet spectra gave manganese : oxygen ratios in good agreement with the expected values, based upon their stated stoichiometries.

There were no impurities apparent in the EDX spectra of the three oxides.

4.4.4   X-Ray Diffraction

XRD spectra were recorded of both the oxide powders and pressed pellets. There were no differences between the two sets of spectra. MnO gave a spectrum in agreement with the 7-230 JCPDS manganese oxide / manganosite data. The Mn_3O_4 spectrum agreed with the 24-734 hausmannite JCPDS data. The Mn_2O_3 XRD spectrum was in agreement with the JCPDS standard spectra 31-825 and 24-508, for manganese oxide / bixbyite. Thus, the three oxides all gave the expected spectra, showing their bulk compositions to be stoichiometrically correct.

4.4.5   X-Ray Photoelectron Spectroscopy

Table 4.4.3 compares the Mn $2p_{3/2}$ binding energies obtained from the oxides with literature values[21]. The values from Reference 21 have been corrected to the C $1s$ = 285.0 eV value used throughout this thesis. All three samples gave peaks of similar shape and structure. There were no prominent satellite structures observed between the $2p_{3/2}$ and $2p_{1/2}$ peaks. Table 4.4.4 details the XPS data from the Mn $2p$ regions. It can be seen that the FWHM of the Mn $2p_{3/2}$ peaks decreased as oxidation state increased, in agreement with a previous report[11]. The $2p_{3/2}$ binding energies did not follow the expected upward trend with increasing manganese oxidation state. However, as the FWHM values seemed to change as expected, it is likely to have been a C $1s$ calibration problem that gave erroneous Mn $2p_{3/2}$ energies. These spectra were recorded from the powders dispersed on graphite slices. There was, therefore, a large carbon signal arising from the graphite, preventing accurate location of the position of the adventitious carbon signal from the sample itself.

	Atomic ratios	
Sample	Mn	O
MnO	0.70	1.30
Mn_3O_4	0.79	6.21
Mn_2O_3	1.92	3.08

Table 4.4.1. Manganese and oxygen ratios, as calculated from beryllium window EDX spectra of the manganese oxide powders.

	Atomic ratios	
Sample	Mn	O
MnO	1.07	0.93
Mn_3O_4	2.93	4.07
Mn_2O_3	2.04	2.96

Table 4.4.2. Manganese and oxygen ratios, as calculated from beryllium window EDX spectra of the manganese oxide pellets.

	Binding energy /eV	
Sample	Present work	Literature value[21]
MnO	640.9	640.7
Mn_3O_4	640.9	-----
Mn_2O_3	640.6	642.6

Table 4.4.3. Mn $2p_{3/2}$ binding energies of the manganese oxides.

Sample	BE $2p_{3/2}$ /eV	FWHM /eV	BE $2p_{1/2}$ /eV	$\Delta\ 2p$ /eV [a]
MnO	640.9	3.8	652.3	11.4
Mn_3O_4	640.9	3.6	652.5	11.6
Mn_2O_3	640.6	3.1	652.1	11.5

[a] The separation in eV between the $2p_{3/2}$ and $2p_{1/2}$ photoelectron peaks.

Table 4.4.4. Mn $2p$ details from the XP spectra of the manganese oxides.

4.5   Characterisation of the Uranium Oxides UO_2, α-U_3O_8 and γ-UO_3

4.5.1   Introduction

The uranium oxides used in this study were UO_2, α-U_3O_8 and γ-UO_3. The UO_2 was 99.97% pure, depleted in ^{235}U and supplied by Koch-Light. The α-U_3O_8 (natural) and γ-UO_3 (depleted) both derived from earlier work at BNL. They were pressed into pellets in the same way as the spinels (though a separate press and dies were used to prevent the spread of radioactive contamination).

UO_2 has a fluorite structure[22]. Both the uranium and oxygen atoms occupy the ideal crystal sites. The mixed valence α-U_3O_8 is orthorhombic and adopts a layer type structure. Planes of hexagonally packed uranium are stacked one on top of another, with U-O-U chains linking the layers. Other oxygens are coplanar with the uranium atoms. γ-UO_3 has a pseudo-tetragonal structure[23].

The oxides were characterised prior to exposure in the gamma cell by the majority of the range of analytical techniques used throughout this study.

4.5.2   Optical Observations

Both UO_2 and α-U_3O_8 are black in colour, while the γ-UO_3 used in this study was a bright yellow. Pellets could readily be prepared which survived handling.

4.5.3   Energy Dispersive X-Ray Analysis

No EDX analyses were performed on the uranium oxides, in either powder or pellet forms, prior to their exposure in the gamma cell. EDX analysis was performed after the samples were exposed (see Section 4.10).

4.5.4   X-Ray Diffraction

XRD spectra were recorded off the α-U_3O_8 and γ-UO_3 samples. The spectrum obtained off the α-U_3O_8 powder before exposure was in agreement with the JCPDS reference spectrum 24-1172 for α-U_3O_8.

The spectrum recorded off γ-UO_3 was complicated by being from the powder mounted on conducting copper adhesive tape (a powder sample previously analysed by XPS was being looked at). The copper signals dominated the spectrum. However, the main non-copper peaks did tally with the 15-201 JCPDS γ-UO_3 reference spectrum.

137

Table 4.5.1 gives the U $4f_{7/2}$ binding energies for the uranium oxides studied here. It can be seen that the U $4f_{7/2}$ peak position shifts to higher binding energies as the mean oxidation state of the uranium in the compounds increases. The α-U_3O_8 spectrum ought to contain contributions from U(IV) and U(VI). Using the DS800 peak synthesis software, the U $4f_{7/2}$ peak was separated into its two components. The U(IV) : U(VI) ratio was fixed at 1 : 2 and the peaks were set to have the same FWHM value. Values of U $4f_{7/2}$ (U(IV)) = 380.6 eV and U $4f_{7/2}$ (U(VI)) = 381.7 eV were obtained. These are the values included in Table 4.5.1. All of the binding energies are a little high compared to the literature, but do form a self consistent set. It would appear that the UO_2 was slightly surface oxidised, giving its high U $4f_{7/2}$ binding energy. Actually, UO_2 left in the atmosphere at 25°C will oxidise, though very slowly[24].

Sample	Binding energy (FWHM)[a] /eV	
	Experimental	Literature[22]
UO_2	381.2 (2.9)	380.3 (-----)
α-U_3O_8	380.6 (2.5) 381.7 (2.5)	380.2 (2.5) 381.5 (2.5)
γ-UO_3	382.8 (2.8)	382.0 (1.9)

a) Figures given in brackets are FWHM values, in eV units.

Table 4.5.1. U $4f_{7/2}$ binding energies for the uranium oxides.

4.6   Magnetite, Fe_3O_4, Preparation

4.6.1   Slicing

After ultrasonic cleaning in propan-2-ol, the magnetite crystals were mounted in cold setting resin (Buehler SW). A diamond cutting wheel was used to slice the crystals parallel to the three principal planes, [100], [110] and [111]. The 1.5 mm thick slices were then polished down to ¼ μm with graded silicon carbide papers and diamond pastes. Oil based lubricants were used for these operations to minimise oxidation of the sample surfaces. After removal of the mounting medium, the prepared slices were given another ultrasonic clean before examination and subsequent exposure in the gamma cell. X-ray diffractometry was used to confirm the orientation of these slices to within 5°. Figure 4.6.1 shows the orientation of the different planes to the overall octahedral geometry of the crystals.

4.6.2   Etching

While some magnetite slices were exposed in the gamma cell in the polished state, a selection of etching solutions were investigated to see if it was possible to improve on the surfaces exposed by slicing, to leave behind purer versions of the desired crystallographic planes.

The dissolution of magnetite films on iron in citrate and ethylenediaminetetraacetate (EDTA) solutions has been studied by Shoesmith, Rummery, Lee and Owen[25]. This work was carried out as part of a study looking at decontamination of water-cooled nuclear reactor coolant circuits. In general, the Fe^{2+} ions are taken into solution by the cations, and the Fe^{3+} is released as the surrounding ions are removed from the crystal lattice. Citrate brought about dissolution of Fe^{2+} at a greater rate than did EDTA. Much of the discussion in this reference related to the relative dissolution rates of the oxide and the metal substrate. $H_2SO_{4(aq)}$ did not dissolve Fe_3O_4. When this work was continued[26], it was shown that the Fe(II)/Fe(III) electron transfer was facilitated by the presence of a bridging ligand, and that the oxalate anion was more effective in this, increasing the dissolution rate. Also, the lower the pH, the faster the rate of dissolution.

Magnetite is effectively dissolved using oxalic acid[27]. A mechanism for this process[27] involves the replacement of surface hydroxyl groups by oxalate. Dissolution of the Fe^{2+} and Fe^{3+} ions then takes place. Fe^{3+} is only slowly taken into solution. Therefore, the Fe^{2+} also only slowly accumulates. However, once enough Fe^{2+} is in solution, reductive dissolution can occur, with the Fe^{2+} in solution reducing the complexed bulk Fe^{3+}. The iron can then rapidly dissolve, the Fe^{2+} complex being more readily soluble. The induction period, prior to the increase

to a rapid dissolution rate, is shorter than with EDTA.

Allen, Sellers and Tucker[28] reported that potassium permanganate solutions oxidised the surface Fe^{2+} ions to Fe^{3+}, giving a passive Fe_2O_3 layer on the surface of the Fe_3O_4 single crystals under examination and stopping dissolution. There were no apparent surface morphological changes after this treatment. Tris-picolinatovanadium(II) solutions preferentially removed Fe^{3+} ions, via reduction to Fe(II), leaving the surface enhanced in Fe^{2+}. No Fe^{2+} arising from reduction was detected in the surface, suggesting that reduction and dissolution occurred concurrently. The surface became pitted and facetted, with the appearance of regular pits indicative of enhanced dissolution at the sites of screw dislocations. There appeared to be a preference for attack to occur perpendicular to the [111] plane. $HCl_{(aq)}$ dissolved both cations at an equal rate, with no preference for any specific direction. This paper also reported an enhancement in the Fe^{3+} contribution to XPS peaks following metallographic polishing. A continuation of this work[29] gave etching rates for different magnetite faces in the tris-picolinatovanadium(II) solution of [111] > [100] ≥ [110]. The fastest rate was three times greater than the slowest. Fe^{2+} enhancement of the surface on treatment was shown to occur for all three planes. Conversion electron Mössbauer spectroscopy showed that it was the octahedral sites that were preferentially, if not exclusively, attacked. The [111] face became generally roughened, with approximate [100] faces bounding etch pits (the [100] plane dissolving more slowly than the [111]) and the formation of some small (~1 μm) pyramidal structures. The [110] surface also undergoes general roughening and pyramid formation. However, the [100] face remained smooth with some scalloping and furrows, terminating with pyramids on the walls of cracks, the reverse of the [111] behaviour. The enhanced dissolution rate for the [111] plane was explained by the close packed array of oxygen atoms that it is possible to have in this direction. These were said to be readily protonated.

In the present study, [100] slices were exposed, in an ultrasonic bath, to 0.5 M oxalic acid for periods of up to 240 min. The surfaces became generally rougher but there were no signs of preferential etching occurring in any direction. 12 M $HCl_{(aq)}$ gave more selective dissolution.

30 min etching of [100] slices in 12 M $HCl_{(aq)}$ (no ultrasonic bath) created eight sided dimples on the surface (Figure 4.6.2). The [111] edges of the slices etched in a similar manner to the [111] oriented slices (see later in this Section). At the edges of the slices, the dimples could be seen to be oriented parallel to the smoothed and triangular pitted [111] faces (Figure 4.6.3). Shorter etch periods saw the formation of proportionally fewer dimples on the surface of the slices. The use of an ultrasonic bath allowed shorter etch times to be used for the same effect on the

magnetite. In all cases, the solution became yellow in colour as Fe^{3+} ions were released into solution.

Neither 18 M $H_2SO_{4(aq)}$ nor 0.1 M $Na_2H_2EDTA_{(aq)}$ had any significant effect on the [100] magnetite surface.

[110] slices exposed to 0.5 M oxalic acid in an ultrasonic bath initially showed increased surface roughness. Extending the exposure to the acid to 240 min left regions of the slice, between rough areas, covered in angular projections (Figure 4.6.4).

Etching in an ultrasonic bath of [110] slices in 12 M $HCl_{(aq)}$ for 2½ min smoothed the surface, but not to a flat finish. Some slices had spines left proud of the surface (Figure 4.6.5) which were shown, using EDX, to be titanium rich. These arose from non etching of impurities in the magnetite. If no ultrasonic bath was used, and the etch time was increased to compensate, deposits were left behind on the slice face, though preferentially etched regions could be seen through gaps in the covering layer (Figure 4.6.6).

Neither 18 M $H_2SO_{4(aq)}$ nor 0.1 M $Na_2H_2EDTA_{(aq)}$ had any significant effect on the magnetite surface.

[111] slices exposed to 0.5 M oxalic acid in an ultrasonic bath initially showed solely increased roughening of the surface. After longer etch times, some structure to the surface could be seen. Figure 4.6.7 shows the surface of a slice after a total of 240 min etching. The formation of some triangular pits can be observed, but a large proportion of the slice area is still rough.

Etching [111] slices in 12 M $HCl_{(aq)}$ and an ultrasonic bath for 5 min introduced facetting to the surface. Triangular pits and pyramids appeared. The magnetite was more rapidly dissolved at any cracks present in the slices. The triangular pits (see Figure 4.6.8) covered the majority of the slice face. Increasing the etch time to a total of 10 min increased the general roughness across the face of the slice (Figure 4.6.9). Longer etch times degraded the slice surface, creating deep fissures and a much rougher surface. Figure 4.6.10 shows the effect of not using an ultrasonic bath and compensating for this by increasing the etch time. Material removed from the bulk of the slice forms a skin over the surface. Lower acid concentrations increased the time required for the formation of any particular surface morphology. The [111] edges of [100] and [110] slices showed similar changes on etching as the larger [111] faces on the [111] slices.

Both 18 M $H_2SO_{4(aq)}$ and 0.1 M $Na_2H_2EDTA_{(aq)}$ had no significant

effect on the surface during etches up to 390 and 240 minutes respectively. There was no yellowing of the solution.

Though it was not found possible to produce well defined crystallographic faces on the magnetite slices using the etchants investigated, it was decided to expose magnetite slices in the gamma cell that had been etched in an ultrasonic bath for periods of 2½ and 5 min. Accordingly, slices of each of the three orientations were prepared.

(111)   (110)   (100)
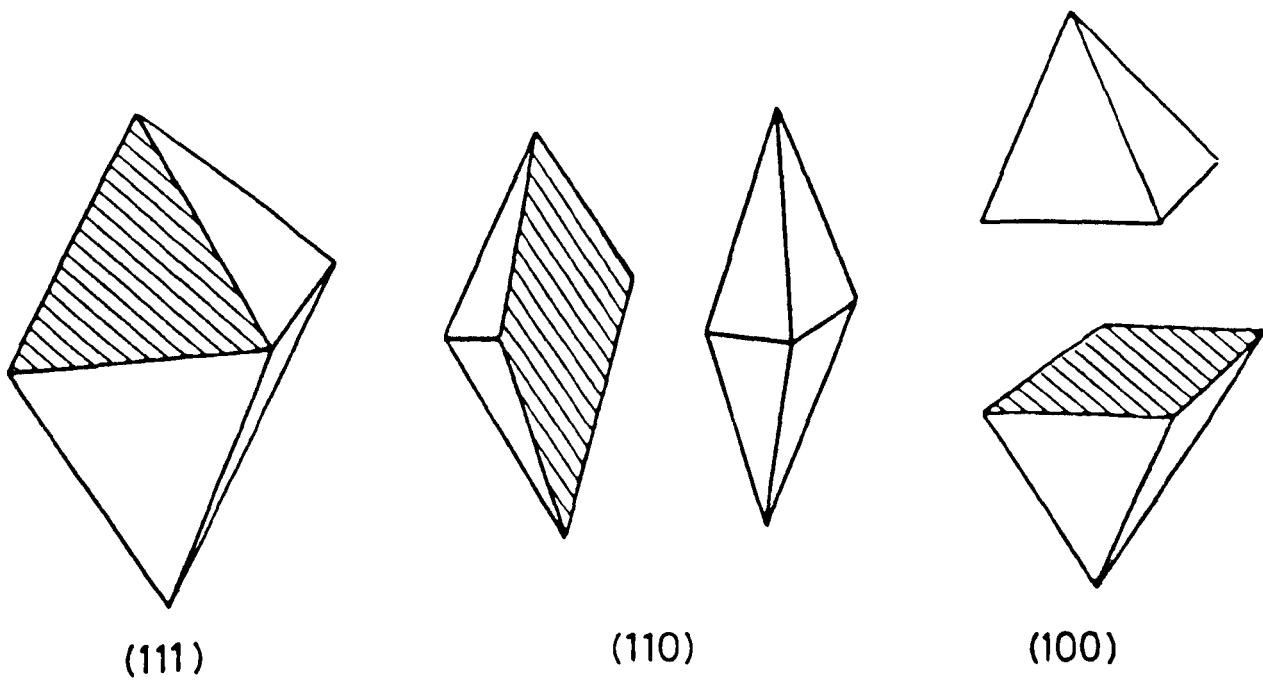
Figure 4.6.1. Relationship of the various crystallographic planes prepared for the present study.

a)

b)
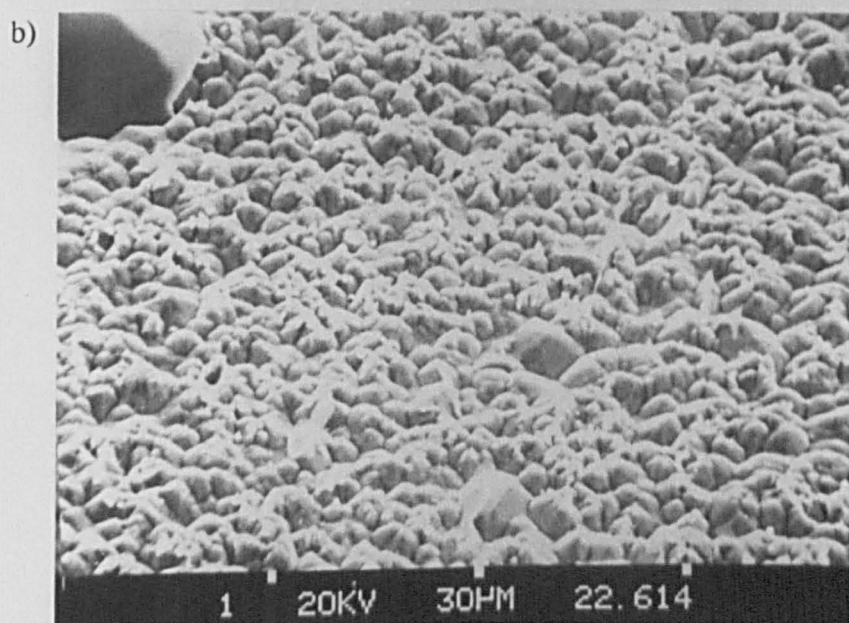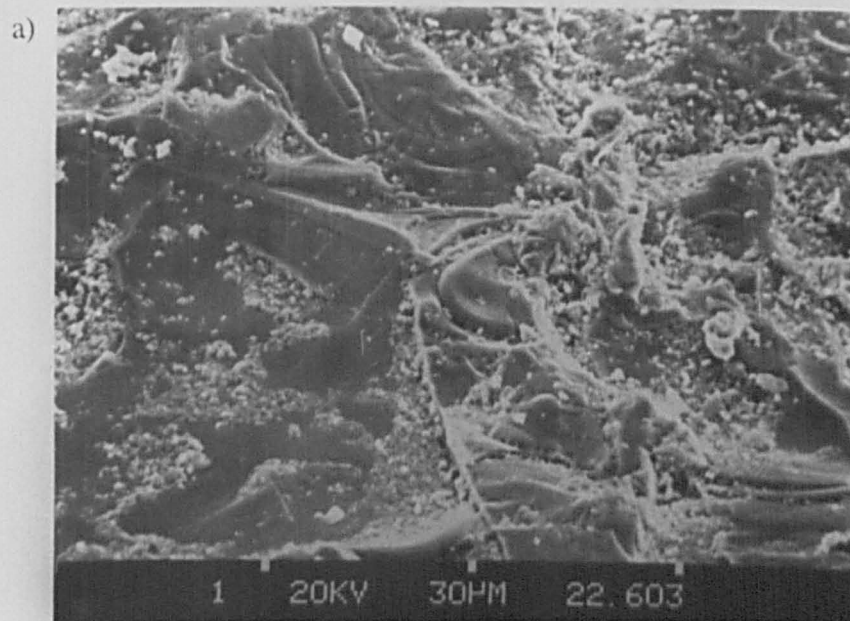
Figure 4.6.2. SEI of a [100] magnetite slice:a) before; and b) after 30 min non ultrasonic etch in 12 M HCl$_{(aq)}$.

145
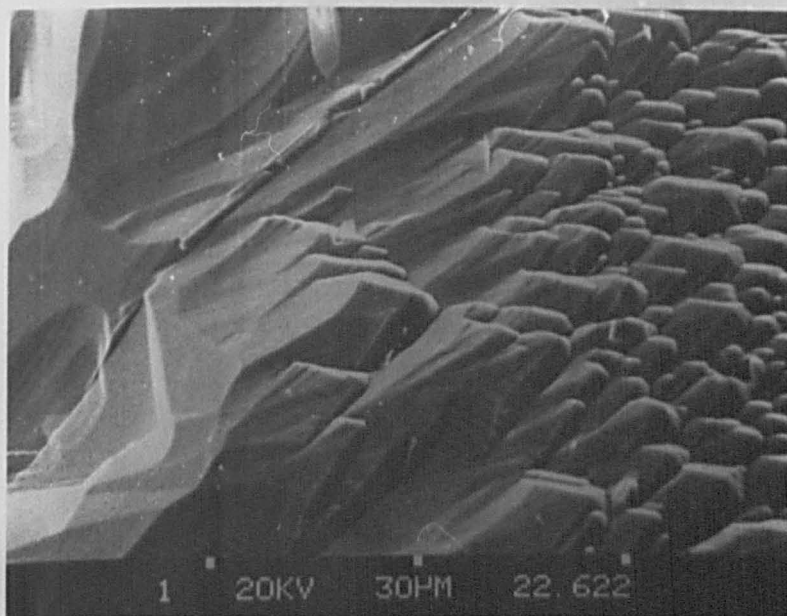
Figure 4.6.3. SEI of a [100] magnetite slice after 30 min non ultrasonic etch in 12 M $HCl_{(aq)}$, edge region.
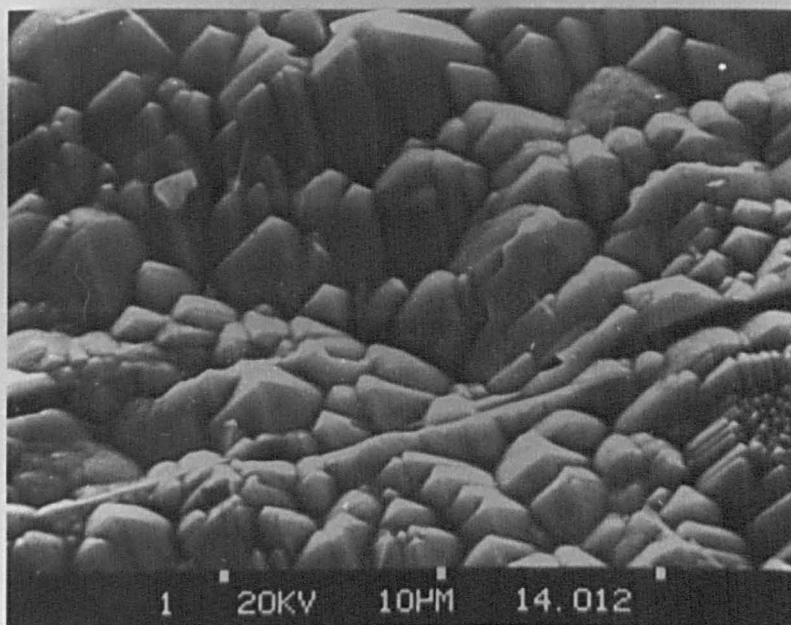
Figure 4.6.4. SEI of a [110] magnetite slice after 240 min ultrasonic etch in 0.5 M oxalic acid.
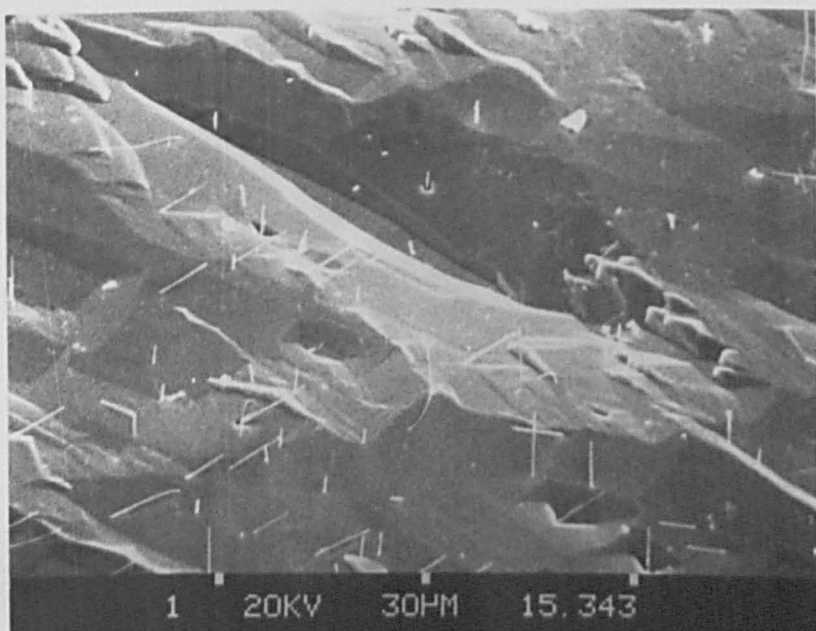
Figure 4.6.5. SEI of a [110] magnetite slice after 2½ min ultrasonic etch in 12 M HCl$_{(aq)}$.
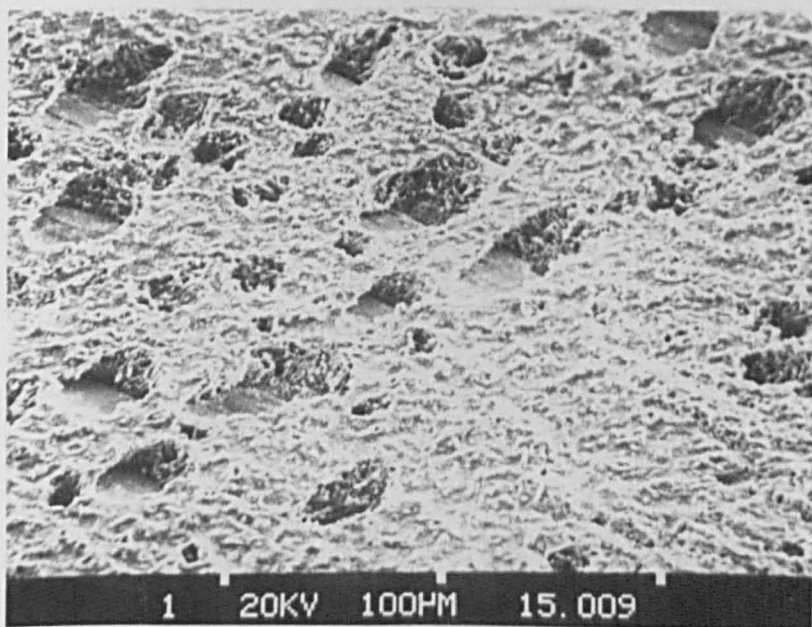
Figure 4.6.6. SEI of a [110] magnetite slice after 30 min non ultrasonic etch in 12 M HCl$_{(aq)}$.

147
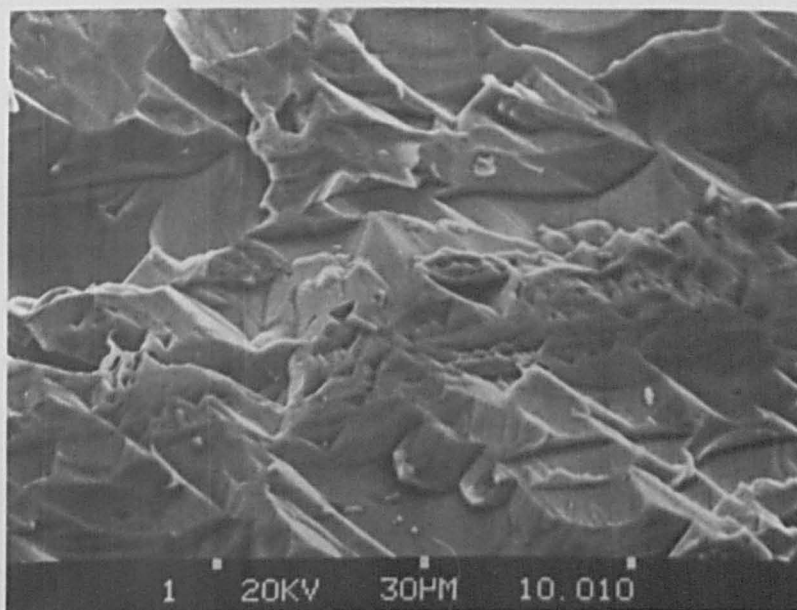
Figure 4.6.7. SEI of a [111] magnetite slice after 240 min ultrasonic etch in 0.5 M oxalic acid.
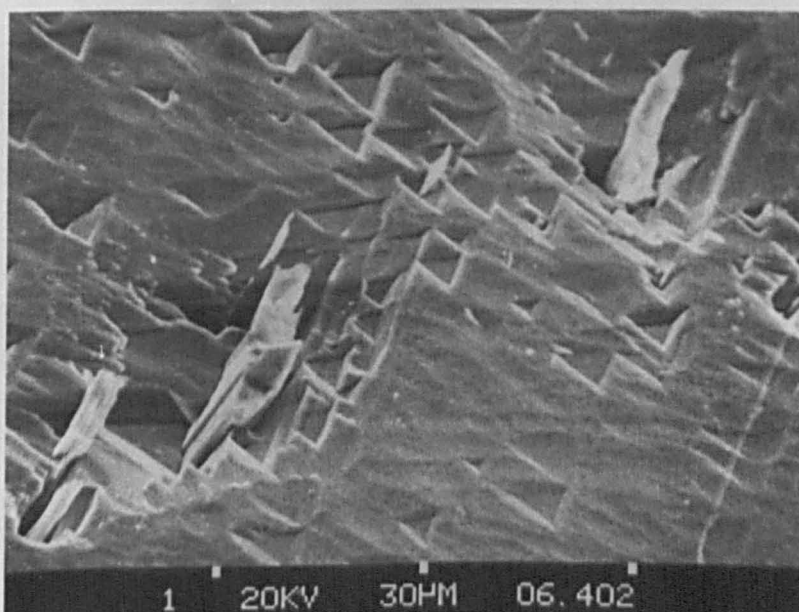
Figure 4.6.8. SEI of a [111] magnetite slice after 5 min ultrasonic etch in 12 M $HCl_{(aq)}$.
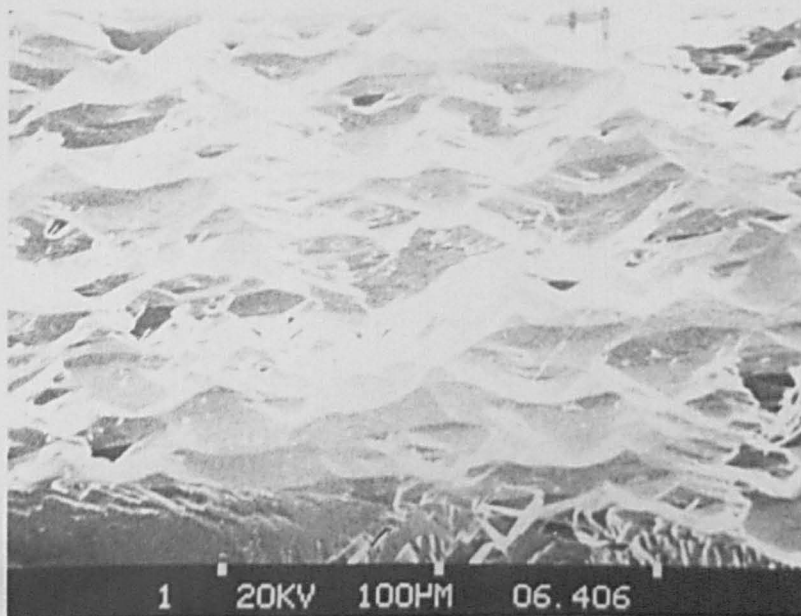
Figure 4.6.9. SEI of a [111] magnetite slice after 10 min ultrasonic etch in 12 M
$HCl_{(aq)}$.
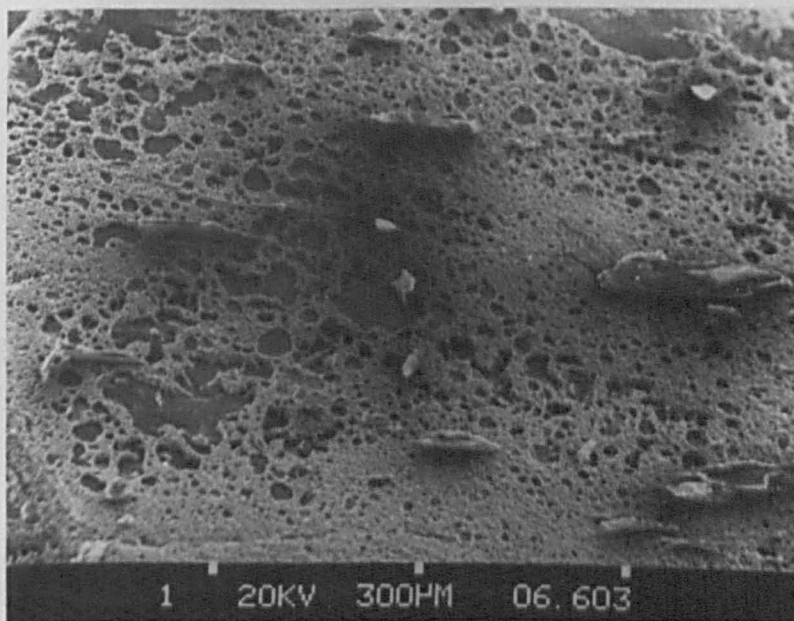
Figure 4.6.10. SEI of a [111] magnetite slice after 30 min non ultrasonic etch in
12 M $HCl_{(aq)}$.

149

4.7 Characterisation of Magnetite, Fe_3O_4

4.7.1 Introduction

The magnetite single crystals used in this study were natural, and obtained from Richard Taylor Minerals of Cobham, England. They exhibited an octahedral habit and ranged in size from 0.5 - 1.5 cm across. Some showed obvious Fe_2O_3 regions and others were too brittle to successfully slice. The importance of analysis of samples prior to exposure in the gamma cell was highlighted by the discovery that some of the octahedral crystals were, in fact, martite, and not magnetite, or a mixture of the two. Martite is a form of haematite, Fe_2O_3, which is a pseudomorph of magnetite. I.e., despite the chemical change (oxidation) the external appearance is retained[30]. Examples were found among the crystals of ones containing both magnetite and Fe_2O_3 regions. When such crystals were sliced, the lubricant turned red in colour, instead of the usual black/grey found with genuine magnetite crystals, indicative of the presence of Fe_2O_3. Slicing also tended to take longer with these crystals. The XRD spectrum off a polished [110] slice of one of these Fe_2O_3 containing crystals showed not only a set of [220], [440] and [660] peaks but also a series of Fe_2O_3 signals, in particular a [300] peak that was the strongest in the spectrum (Figure 4.7.1). [111] slices also gave XRD spectra with both Fe_3O_4 and Fe_2O_3 contributions. The expected [xxx] peaks were present along with many Fe_2O_3 signals, with the most intense being [006] (Figure 4.7.2, recorded from an unpolished slice). Slices from such crystals tended not to conduct electricity (unlike magnetite ones). A banded structure was sometimes apparent, with magnetite strips in a martite matrix. Silica, SiO_2, inclusions were sometimes seen. Using the EDX software to calculate the oxygen content of a (beryllium window) spectrum recorded off one of these inclusions, the silicon : oxygen ratio was correct to within 1 at%. Analysing a region away from any obvious inclusions, an iron : oxygen atomic percentage ratio of 1 : 1.27 was obtained. After eighteen days in the gamma cell at 550°C, an almost pure Fe_3O_4 XRD spectrum was obtained off one of these slices, showing the effect of the reducing conditions on the sample. An Fe : O atomic ratio of 1 : 1.2 was found using EDX, again showing the reduction of the oxide. Fe $2p_{3/2}$ XPS peaks shifted to lower binding energies on exposure in the gamma cell, indicating reduction of the surface of the magnetite / martite slices, supporting the bulk results of EDX. C $1s$ signals increased in the XP spectra. The slices also tended to be cracked upon removal from the gamma cell due to the reduction of Fe_2O_3 to Fe_3O_4. Magnetite surfaces showed no ill effects of their exposure.

Fe_3O_4 adopts the inverse spinel structure, with Fe^{2+} ions located in octahedral sites and Fe^{3+} equally placed in octahedral and tetrahedral positions. The octahedral Fe^{2+} and Fe^{3+} ions undertake a rapid exchange of electrons at room

temperature (and above), with simultaneous oxidation and reduction, of Fe^{2+} and Fe^{3+} respectively[31].

4.7.2   Energy Dispersive X-Ray Analysis

EDX spectra often showed the presence of titanium and vanadium as impurities in the crystals, with concentrations <0.1 at%. In various slices, Al/Si/Ca, Mg/Al/Si, Ba/S and Mg/Al/Si/K particles were identified embedded in the magnetite. In magnetite regions, calculation of the oxygen content using the ZAF routines in the software gave atomic percentages close to those expected for Fe_3O_4 when sliced samples were analysed. Polished samples often gave results high in iron and low in oxygen. Table 4.7.1 gives Fe : O ratios recorded off various magnetite samples. Samples 5, 6 and 25 were analysed in a polished state while 15, 22 and 57 were looked at just after slicing.

4.7.3   X-Ray Diffraction

[100] slices gave peaks at the [400] and [800] positions (see Figure 4.7.3, recorded from an unpolished slice). It should be remembered that as the lattice spacing decreases, the Miller indices increase. Therefore, the [800] reflection derives from planes of atoms in the lattice that are half as far apart as those that give rise to the [400] signal. The [100] and [200] signals are absent from the spectrum as they would require 2Θ to be less than the starting value for the spectrum given here. Other reflections, e.g. [300] and [600], are missing since there are no planes of atoms at multiples of, in these cases, $1/3$ and $1/6$ of the unit cell dimension.

[110] slices give [220], [440] and [660] reflections. Figure 4.7.4 is a typical [110] XRD spectrum from an unpolished slice. For similar reasons to those given above, other [xx0] reflections are absent from the spectrum.

For the [111] slices, [111], [222], [333], [444], [555] and [666] peaks were seen in the spectra. It was noted that the signals generally peaked at the [333] position. With increasing gamma cell exposure, the peak in intensity shifted to the lower signals, [222] and [111]. Figure 4.7.5 illustrates a typical [111] XRD spectrum, this one recorded off an unpolished and unetched slice. The $K\alpha_2$ x-ray contribution becomes more apparent at higher 2Θ values. Figure 4.7.6 shows how the spectra off the three orientations compare to one another.

4.7.4   X-Ray Photoelectron Spectroscopy

The Fe_3O_4 unit cell contains eight Fe(II) ions and eight Fe(III) ions in the sixteen octahedral sites, and a further eight Fe(III) ions in the tetrahedral sites. At room temperature, there is ready electron exchange between the octahedral cations,

151

and we might, therefore, only expect to see one XPS signal from these ions. The Fe(III) ions in the tetrahedral sites, however, are not able to electron exchange with the octahedral Fe(II), and, so, might give a second, higher binding energy, signal in any XP spectra. However, distinct Fe(II) peaks have been seen in XP spectra of Fe_3O_4[6]. This is explained in terms of the time scale of the XPS experiment in comparison to the time required for electron exchange. Reference 6 obtained an electron transfer time, t_{hop}, such that 10^{-16} s $< t_{hop} < 10^{-8}$ s.

Literature values for the Fe $2p_{3/2}$ peak in Fe_3O_4 (not deconvoluting the peak into its two, overlapping, components) include, when referenced to C $1s$ = 285.0 eV, 711.4 - 711.0 eV [6], 710.8 eV [7] and 710.8 eV [8]. When the two contributors have been separated, values for the Fe(II) component of 709.2 eV [6], 710.2 eV [32], 708.3 eV [9], 708.5 eV [33], 709.5 eV [34] and 709.5 eV [35] have been recorded, and 711.0 eV [6], 710.4 eV [9], 711.2 eV [34] and 711.2 eV [35] for the Fe(III) contribution. Literature values of FWHM(Fe(II)) = 2.4 eV [9], 2.2 - 2.9 eV [33] and 4.5 eV [34] and FWHM(Fe(III)) = 4.5 eV [34] are given.

In the present study, the values obtained off the magnetite slices (prior to any gamma cell exposure) are summarised in Table 4.7.2. In all cases, experimentally determined peak shape envelopes, derived from pure Fe(II) and pure Fe(III) compounds, were used to fit the Fe $2p$ signals. Samples 5 and 6 were examined after polishing while the remaining samples were analysed in the as-sliced state. Looking at the overall Fe $2p_{3/2}$ peak envelope, the values obtained here, centred on 710.4 eV, fall lower than those quoted above, which average 710.9 eV. Good agreement between the values recorded here and the above literature values was obtained for both the Fe(II) and Fe(III) peaks. The area ratio values recorded here show no systematic effect of polishing on the Fe(II) : Fe(III) ratio at the surface of the slices. The FWHM values for Fe(III) were all greater than those for Fe(II).

For an unpolished [111] slice, there were no shifts in binding energies after leaving in a vacuum desiccator for several months, though the C $1s$ intensity increased at the expense of the other sample signals. Neither were there any binding energy changes upon leaving a sample in the spectrometer for four days. Again, though, there was an increase in hydrocarbon contamination on the sample over this time, as would be expected.

XP spectra were recorded for a [110] slice before and after a 5 min etch in 12 M $HCl_{(aq)}$ (using an ultrasonic bath). Figure 4.7.7 illustrates how the etching process has slightly increased the intensity at the high binding energy side of the peak, akin to the results published in Reference 28. The Fe(II) : Fe(III) ratio has increased from 1:1.98 to 1:2.73. Both contributing peaks have broadened

(FWHM$_{Fe(II)}$ = 3.4 eV; FWHM$_{Fe(III)}$ = 4.3 eV). There is also an increase in the high binding energy component of the O $1s$ peak, attributed (as in Reference 29) to an increase in hydroxyl groups on the surface of the sample (Figure 4.7.8).

Sample	Atomic ratios	
	Fe	O
5 [100]	3.31	3.69
6 [111]	3.34	3.66
15 [110]	3.07	3.93
22 [100]	3.00	4.00
24 [111]	2.98	4.02
57 [111]	3.17	3.83

Table 4.7.1. Iron and oxygen ratios, as calculated from beryllium window EDX spectra of magnetite slices.

	Binding energy /eV			FWHM /eV			
Sample	Fe $2p_{3/2}$	Fe(II) $2p_{3/2}$	Fe(III) $2p_{3/2}$	Fe $2p_{3/2}$	Fe(II) $2p_{3/2}$	Fe(III) $2p_{3/2}$	Area ratio Fe(II) : Fe(III)
5 [100]	710.5	709.5	711.0	4.3	3.3	3.7	1:1.46
6 [111]	710.3	709.2	710.9	4.3	3.3	3.6	1:1.86
9 [100]	-----	709.0	711.0	-----	3.1	4.2	1:3.10
10 [111]	-----	709.5	711.3	-----	3.5	3.8	1:1.48
14 [110]	-----	709.4	711.2	-----	3.3	3.8	1:1.98
15 [110]	-----	709.0	711.1	-----	3.4	4.0	1:1.86
22 [100]	-----	709.3	711.3	-----	3.4	3.9	1:1.45
57 [111]	-----	709.3	711.2	-----	3.5	4.0	1:1.35

Table 4.7.2. Fe $2p_{3/2}$ XPS binding energy values obtained off Fe_3O_4 slices prior to gamma cell exposure.

Figure 4.7.1. XRD spectrum of a martite-containing [110] magnetite slice.
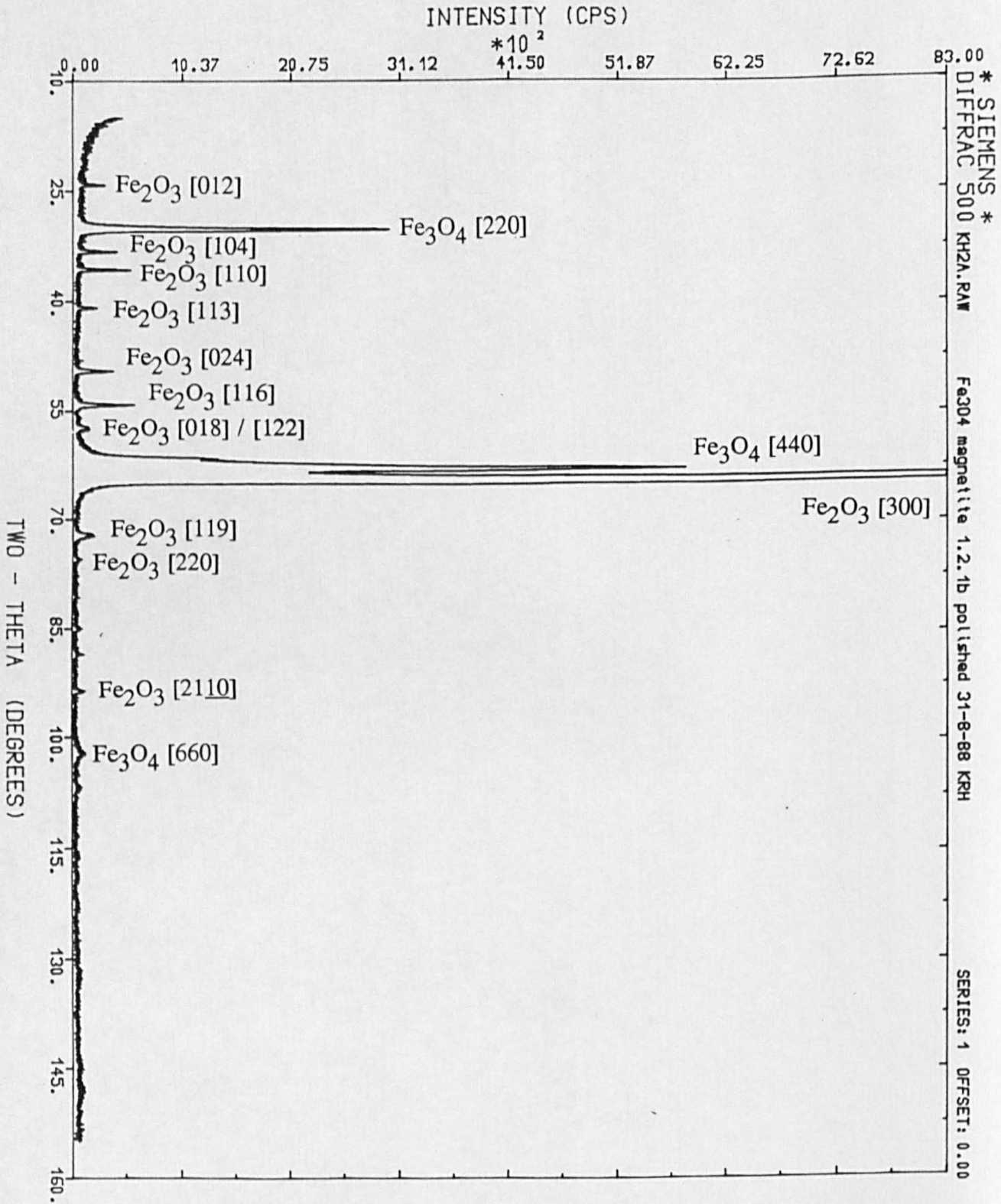
Figure 4.7.2. XRD spectrum of a martite-containing [111] magnetite slice.
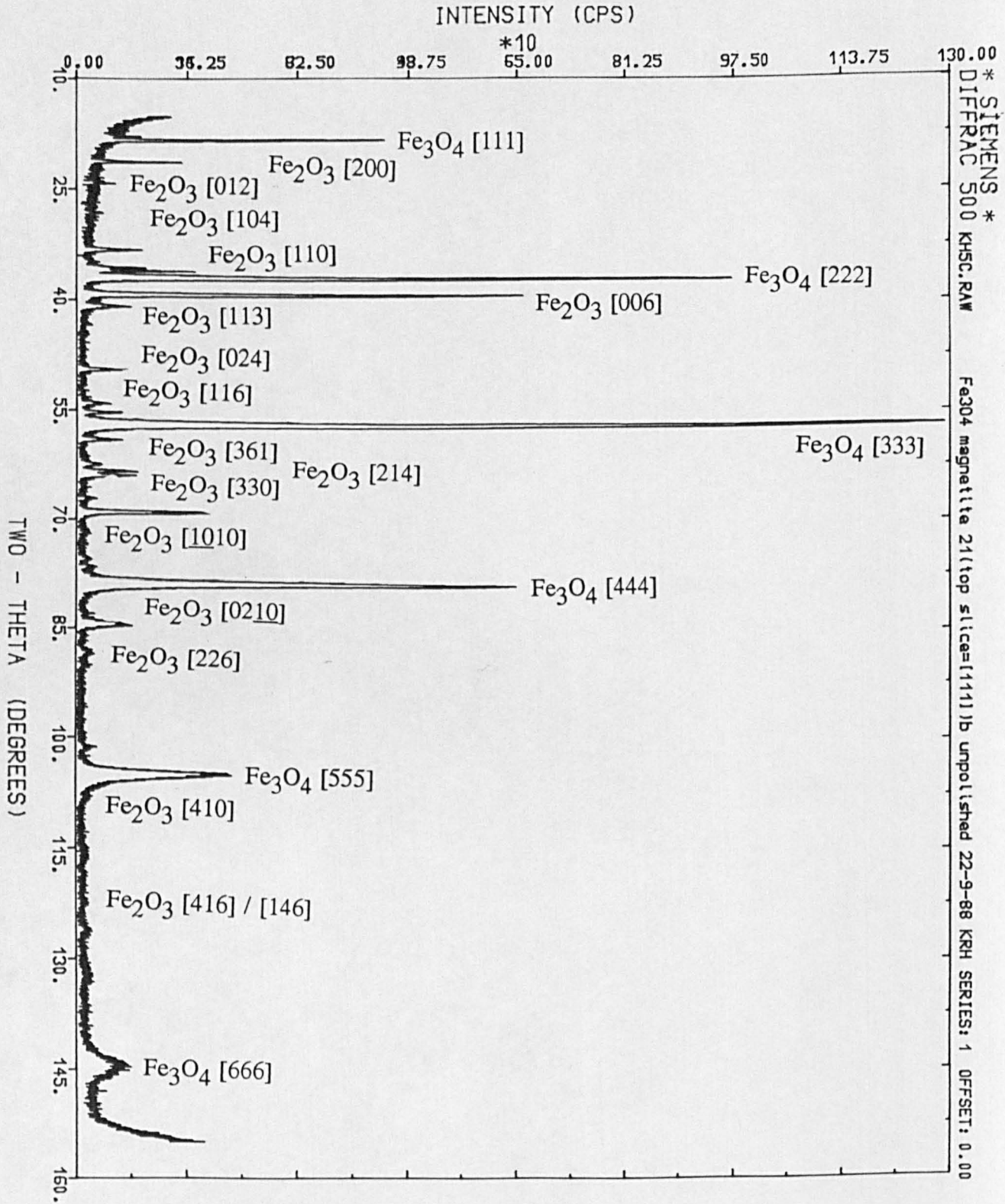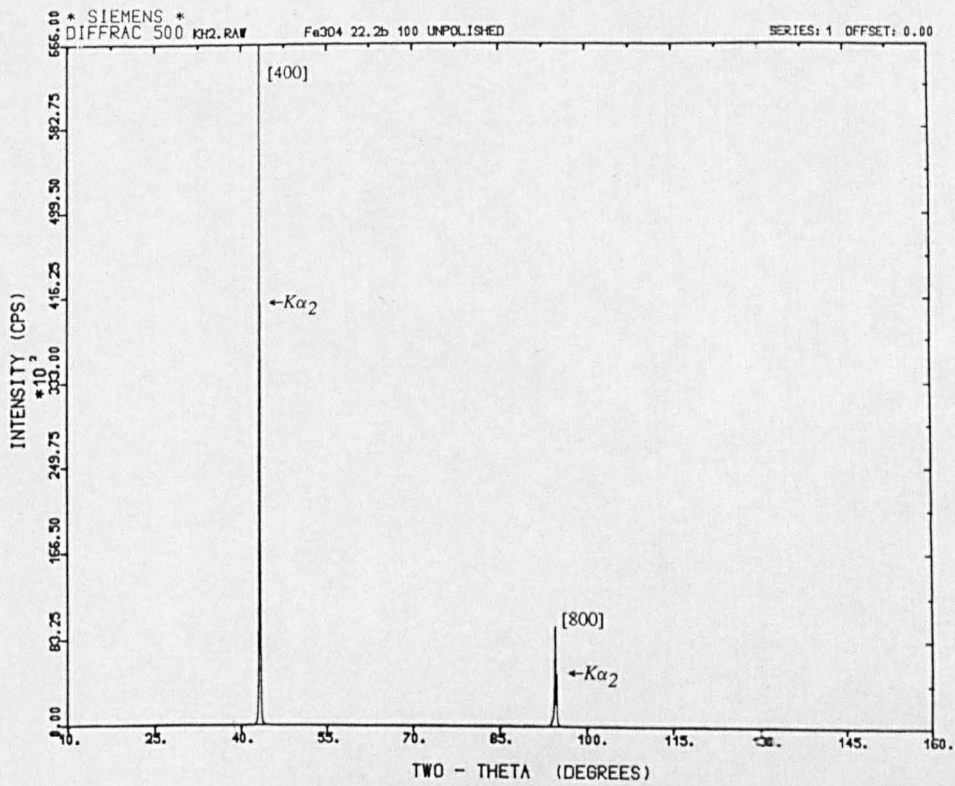
Figure 4.7.3. XRD spectrum of a [100] magnetite slice.
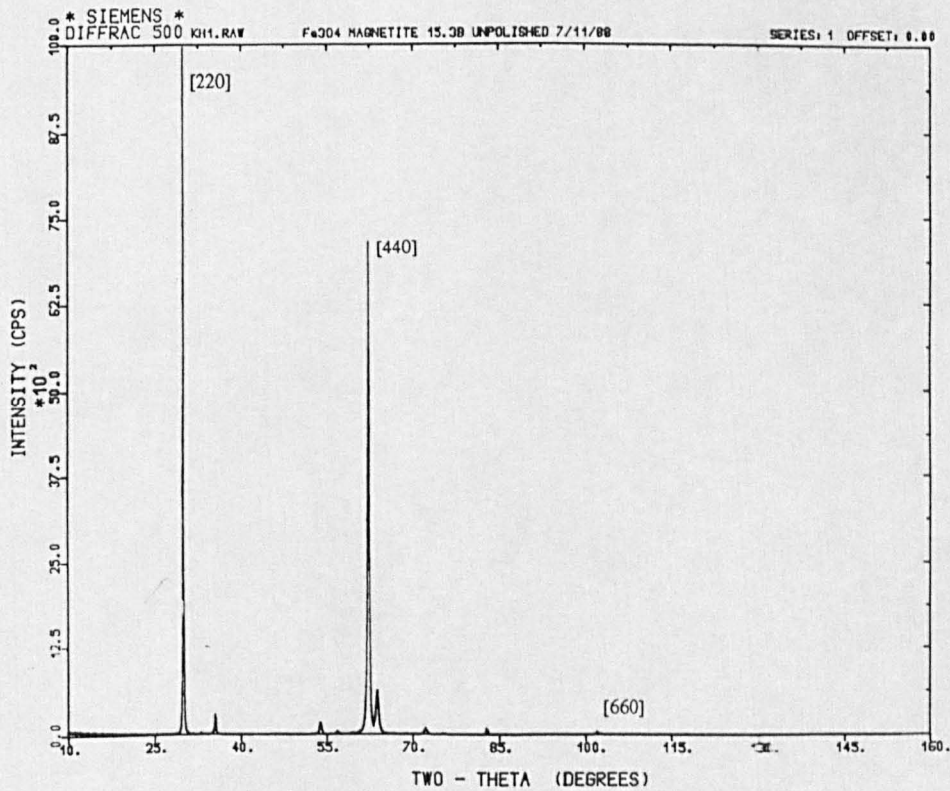
Figure 4.7.4. XRD spectrum of a [110] magnetite slice.

158
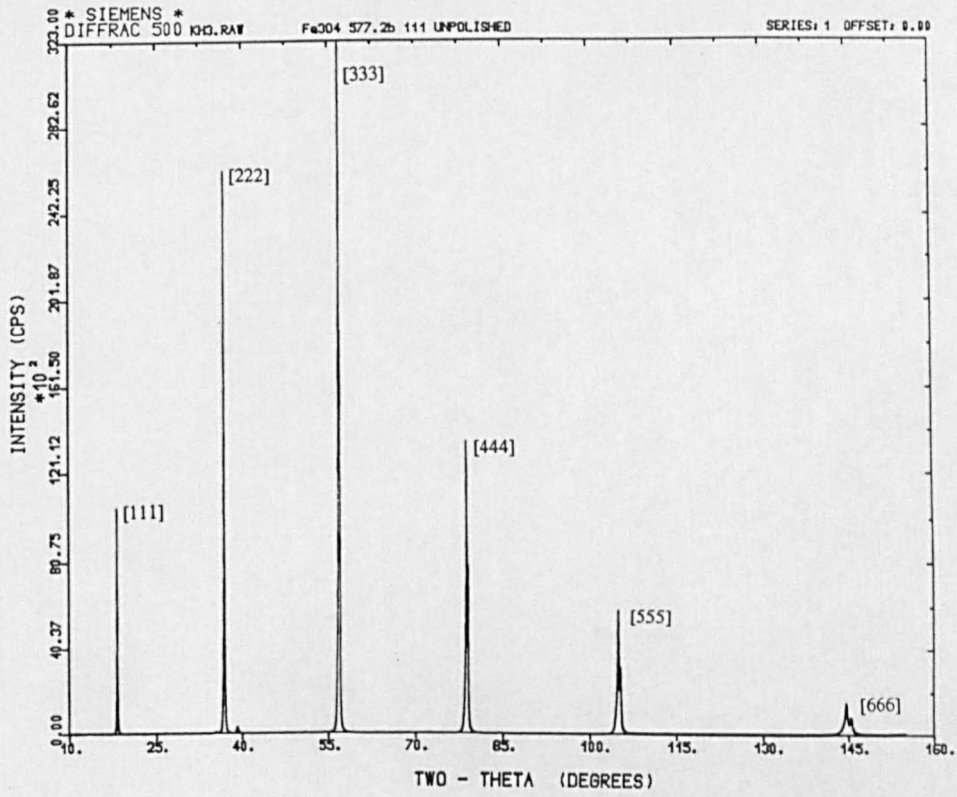
Figure 4.7.5. XRD spectrum of a [111] magnetite slice.
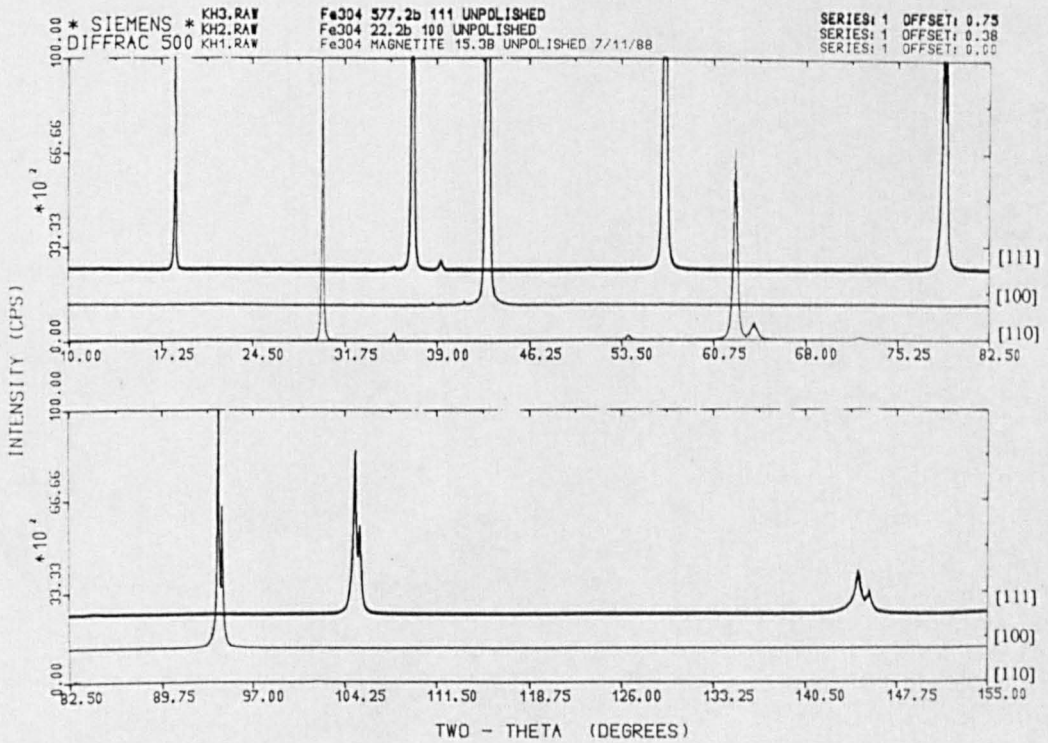
Figure 4.7.6. Comparison of [100], [110] and [111] XRD spectra.

159
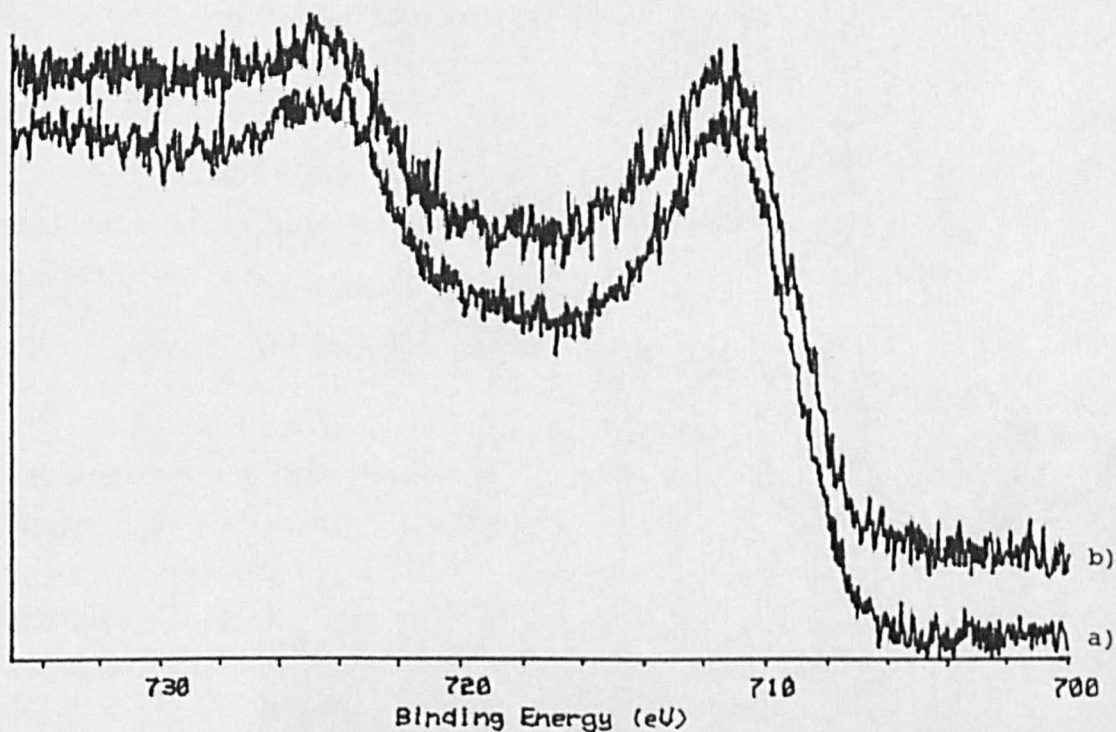
Figure 4.7.7. Fe *2p* XPS region of a [110] magnetite slice: a) before; and b) after
ultrasonic etching for 5 min in 12 M $HCl_{(aq)}$.
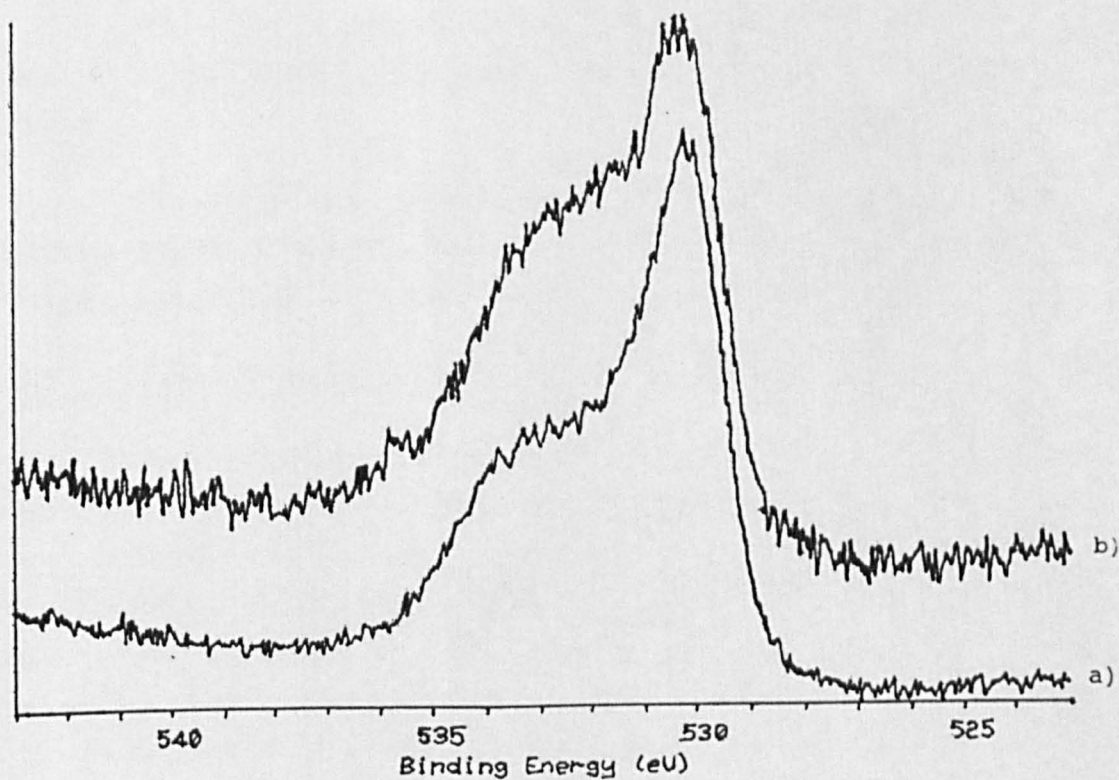
Figure 4.7.8. O *1s* XPS region of a [110] magnetite slice: a) before; and b) after
ultrasonic etching for 5 min in 12 M $HCl_{(aq)}$.

4.8 Characterisation of $M_xCo_{1-x}Fe_2O_4$ Spinels after Exposure

4.8.1 Introduction

Table 4.8.1 lists the exposure times for the spinel pellets at both temperatures. After exposure, the pellets were examined with the range of available techniques.

4.8.2 Optical Observations

At 550°C, there was little change to see in most of the spinel pellets. There were some less shiny regions (the smooth surfaces of the pressed pellets before exposure were quite shiny in appearance), but these were seen in both central and edge regions of different pellets. The $FeFe_2O_4$ pellet had a darker edge and a slight interference pattern of rainbow colours in the central region. The greatest change to occur was the disappearance of the $NiFe_2O_4$ pellet. In its place, there was a large amount of black material filling the capsule liner either side (upstream and downstream) of where the pellet had been originally located (Figure 4.8.1). There were no noticeable pieces of the pellet remaining. Samples were extracted from the liner of material either side of where the pellet had been (the silica spacers provided the location).

As at 550°C, the 650°C $FeFe_2O_4$ pellet had dark edges and a shimmering centre. The 650°C $NiFe_2O_4$ pellet was intact, but had cracked and warped during exposure.

The spinels were, as before exposure in the gamma cell, attracted to a permanent magnet. The deposit formed around the remains of the $NiFe_2O_4$ pellet during exposure at 550°C was also attracted to a magnet.

4.8.3 Energy Dispersive X-Ray Analysis

As was the case for all the samples exposed in the gamma cell and all the experimental techniques, the side facing the gas inlet of the gamma cell capsule was the one analysed. In the secondary electron images recorded off the SEM, it was seen that the outer edge of the pellets, shielded by the silica spacers when installed in the capsule, generally appeared more electron bright. Figure 4.8.2, of the $Mn_{0.75}Co_{0.25}Fe_2O_4$ pellet after 24 days exposure at 650°C, best illustrates this (the bright object towards the bottom right of the micrograph is the clamp holding the sample onto the stub). The surface of this sample also had on it some whiskers and nodules. Figure 4.8.3 shows some of these. EDX spectra recorded on these fibres and nodules (Figure 4.8.4) showed them to contain copper, along with sulphur and chlorine. The aluminium, silicon, manganese, iron and cobalt can be seen to be

present in the spinel, with copper only in the fibres. Similar features were not seen on any other spinel oxide samples, and no explanation for their appearance could be identified. Copper did not feature in any experiments, in either samples or apparatus, in any form that would be expected to produce such features.

EDX spectra were recorded on the windowless Kevex system. Spectra were acquired over 100 s time periods and the number of counts in the C K peak determined. Spectra were recorded from the central, exposed, region and outer edge (shielded by the spacers during gamma cell exposure) of each pellet. Two sets of spectra were recorded, at 10 kV and 20 kV accelerating voltage respectively. The 10 kV spectra are more surface specific then those recorded at 20 kV. An estimate of the electron penetration depth, and, so, the sampling depth of the technique, can be made for these two voltages using the equation given in Section 3.2.3. Assuming a density of 2.2 g.cm^{-3} for the pressed pellets, electron penetration depths of 0.7 and 3.1 μm are obtained for the 10 and 20 kV experiments respectively.

Table 4.8.2 gives the carbon counts obtained off the spinel pellets. Table 4.8.3 converts these to estimated carbon film thicknesses using the calibration charts in Reference 4. Figures 4.8.5, 4.8.6 and 4.8.7 show the variation in carbon counts in the central regions of the pellets as a function of x, the degree of substitution.

The carbon count rates determined from the 10 kV spectra are almost always greater than those recorded using 20 kV electrons, as would be expected with the greater surface selectivity of the lower energy primary beam. Except for the $Ni_{0.25}Co_{0.75}Fe_2O_4$ sample exposed at 650°C, all edge spectra gave higher carbon signals than their corresponding middle spectra, as expected if there is carbon deposition occurring in the exposed regions of the pellets. The material collected from either side of where the $NiFe_2O_4$ pellet had originally been prior to exposure at 550°C gave high carbon count rates. The 20 kV results were higher than any obtained from the other spinels. The downstream deposit 10 kV result was only bettered by the $Ni_{0.75}Co_{0.25}Fe_2O_4$ pellet, also exposed at 550°C. The downstream deposit gave carbon count rates around twice those obtained off the upstream (closer to the gas inlet of the capsule) deposit. Interestingly, both deposit samples gave increased carbon count rates with a 20 keV primary electron beam than with 10 keV electrons. This suggests that the material is not simply a carbon coating on an underlying substrate, where the increased surface sensitivity of the lower energy electron beam would bring about an increased proportion of carbon in the spectra, but, rather, a more bulk form of carbon. The original transition metal components of the pellet, nickel and iron, are still to be seen in the spectra, but the carbon signals are the most prominent seen during the present study.

162

The estimated carbon film thicknesses obtained from the 10 kV spectra are all less than those determined from the 20 kV carbon count rate results. This suggests that the calibration curves used[4], which were determined from spectra recorded on the same SEM / EDX combination as the current results, are not equivalent over the range of carbon count rates found here. However, either set of results is still useful for determining any trends that may be present in the deposition results over the range of spinels investigated.

For the $Mn_xCo_{1-x}Fe_2O_4$ spinels, there is a drop in carbon count rate with increasing manganese content in the 550°C 10 kV spectra. With the exception of the $Mn_{0.25}Co_{0.75}Fe_2O_4$ sample, this trend is also apparent in the 20 kV results. However, the 650°C results show an increase in deposition with increasing x.

The results off the $Fe_xCo_{1-x}Fe_2O_4$ samples are more confusing. The 550°C 20 kV spectra give an overall downward trend in carbon deposition with increasing substitution of cobalt by iron. This, though, is not mirrored in the 10 kV results, where the deposition appears to peak at intermediate substitution values. The 650°C spectra, both 10 kV and 20 kV, show an inverse result, with carbon signal intensity being a minimum when x = 0.5.

The $Ni_xCo_{1-x}Fe_2O_4$ spinels exposed at 550°C show increasing deposition with increasing nickel content, until the point is reached where catastrophic carbon formation has occurred, destroying the $NiFe_2O_4$ pellet. The 650°C samples also show the maximum carbon signal on the $NiFe_2O_4$ pellets, though these were fully intact upon removal from the gamma cell. The lower substituted nickel spinels, however, gave a more even range of values, whereas the 550°C samples with the same degrees of substitution showed an unequivocal rise in deposition with increasing x. The 650°C samples all gave lower carbon signals than the 550°C pellets.

4.8.4   X-Ray Diffraction

Table 4.8.4 lists the a_0 lattice parameter values obtained from the spinels before and after exposure, as calculated using the Diffrac500 software. No value is listed for $NiFe_2O_4$ after exposure at 550°C since, as mentioned previously, the disc was found to have disintegrated upon removal from the capsule. Large quantities of carbon deposit were found either side of the original location of the $NiFe_2O_4$ disc. The spectra all showed similar shifts in the high order (e.g. [1020], [951] and [1022]) peaks to those recorded before loading the samples into the gamma cell. Figures 4.8.8, 4.8.9 and 4.8.10 show these high order peaks for the exposed spinels. The JCPDS a_0 lattice parameter value for $CoFe_2O_4$ (spectrum 22-1086) is 8.3919 Å, in good agreement with all six values obtained here. For Fe_3O_4, JCPDS (19-629) = 8.396 Å. $MnFe_2O_4$ JCPDS (10-319) = 8.499 Å   and

163

$NiFe_2O_4$ JCPDS (10-325) = 8.339 Å. The largest deviations in a_0 lattice parameter from the expected values occur for the $Mn_xCo_{1-x}Fe_2O_4$ samples exposed at 650°C. Here, as x increases, the lattice parameter value increasingly becomes greater than that expected from the application of Vegard's rule to the two expected end point values.

The 550°C $Ni_xCo_{1-x}Fe_2O_4$ spinels have undergone some reduction, evidenced by the appearance of nickel metal peaks (JCPDS file 4-850), in the spectra after exposure. As x increases, and, so, the concentration of nickel in the sample, the intensity of the nickel metal peaks in relation to the spinel signals increases. The 650°C spectra have undergone a greater degree of reduction, as seen in the increased intensity of the nickel peaks relative to the equivalent 550°C sample. Figure 4.8.11 labels the nickel peaks in the spectrum recorded off the $Ni_{0.5}Co_{0.5}Fe_2O_4$ pellet after exposure at 650°C. All remaining peaks are due to the remaining spinel. The reduction is also apparent in the high lattice parameter values obtained off the exposed pellets (Table 4.8.4). Removal of nickel from the spinel will reduce the nickel content. As nickel is the smallest of the cations expected to be present in the lattice, increasing nickel content (i.e. increasing x) will tend to decrease the lattice parameter. With less than the expected content of nickel remaining in the lattice after exposure, the lattice parameter will be higher than anticipated. The unexposed nickel spinel spectra showed no evidence for the presence of any nickel metal. It is likely that reduction of the spinel in the gamma cell conditions present, producing catalytic nickel metal atoms / small particles, followed by deposition of carbon from the gas phase, brought about the destruction of the $NiFe_2O_4$ pellet when exposed at 550°C. This will be discussed further in Chapter 5.

4.8.5   X-Ray Photoelectron Spectroscopy

Tables 4.8.5 and 4.8.6 list the binding energies obtained off the exposed spinel pellets. In many cases where the original pellet contained a particular element, it was not possible to detect a signal for that element after exposure owing to the layer of carbon deposit covering the exposed sample face. This layer was often thick enough to prevent detection of the characteristic photoelectrons that would have been seen in the spectrum off an unexposed pellet. For example, the manganese oxides exposed at 550°C gave no metal $2p$ spectra. Where obliteration of the photoelectron peak had not occurred, reduction in intensity was seen, making determinations of peak position less accurate. All pellet signals were weaker after exposure. The C $1s$ peak intensities were higher than in those spectra recorded prior to exposure and their was growth, in particular, of the lower binding energy component. Figure 4.8.12 illustrates this for the $Fe_{0.5}Co_{0.5}Fe_2O_4$ oxide. The increase in the lower binding energy component after exposure at 650°C, in this case, is there, but leads just to an

increase in the shoulder on the peak. The spectrum recorded after exposure at 550°C, however, shows a clear, if overlapping, second peak.

Samples of the material found either side of the decomposed $NiFe_2O_4$ pellet exposed at 550°C were examined, in the form of powders pressed onto conducting copper adhesive tape. The nickel and iron signals were more apparent in these samples than in the intact exposed pellets, and the intense satellite features seen in the Ni *2p* region before exposure were, again, present. The lower binding energy C *1s* signal was dominant.

Sample	Exposure time /days	
	550°C	650°C
$CoFe_2O_4$ (Mn)	24	24
$Mn_{0.25}Co_{0.75}Fe_2O_4$	24	24
$Mn_{0.5}Co_{0.5}Fe_2O_4$	24	24
$Mn_{0.75}Co_{0.25}Fe_2O_4$	24	24
$MnFe_2O_4$	24	24
$CoFe_2O_4$ (Fe)	23	23
$Fe_{0.25}Co_{0.75}Fe_2O_4$	23	23
$Fe_{0.5}Co_{0.5}Fe_2O_4$	23	23
$Fe_{0.75}Co_{0.25}Fe_2O_4$	23	23
$FeFe_2O_4$	23	23
$CoFe_2O_4$ (Ni)	23	23
$Ni_{0.25}Co_{0.75}Fe_2O_4$	23	23
$Ni_{0.5}Co_{0.5}Fe_2O_4$	23	23
$Ni_{0.75}Co_{0.25}Fe_2O_4$	23	23
$NiFe_2O_4$	23	23
Deposit upstream of $NiFe_2O_4$	-----	-----
Deposit downstream of $NiFe_2O_4$	-----	-----

Table 4.8.1. Gamma cell exposure times for the spinels.

	C K peak area /counts.(100 s)$^{-1}$							
	550°C				650°C			
	Middle		Edge		Middle		Edge	
Sample	20 kV	10 kV	20 kV	10 kV	20 kV	10 kV	20 kV	10 kV
$CoFe_2O_4$ (Mn)	-----	-----	-----	-----	-----	-----	-----	-----
$Mn_{0.25}Co_{0.75}Fe_2O_4$	1066	3282	786	2208	987	1178	738	1153
$Mn_{0.5}Co_{0.5}Fe_2O_4$	1186	2888	703	2041	1422	1892	814	1007
$Mn_{0.75}Co_{0.25}Fe_2O_4$	1103	2857	961	2060	1588	3019	798	1260
$MnFe_2O_4$	1046	2582	769	1707	1679	2571	927	1230
$CoFe_2O_4$ (Fe)	1695	1683	1560	1272	2288	3430	1753	1931
$Fe_{0.25}Co_{0.75}Fe_2O_4$	1364	3467	1322	2858	2012	2410	1657	1802
$Fe_{0.5}Co_{0.5}Fe_2O_4$	1588	3701	1267	3295	1886	2335	1665	1735
$Fe_{0.75}Co_{0.25}Fe_2O_4$	1264	3884	1000	3027	2023	2529	1703	1920
$FeFe_2O_4$	1219	3025	1131	2099	2084	3567	1693	2951

Table 4.8.2. EDX carbon counts (counts.(100 s)$^{-1}$) off the exposed spinels.

	C K peak area /counts.(100 s)$^{-1}$							
	550°C				650°C			
	Middle		Edge		Middle		Edge	
Sample	20 kV	10 kV	20 kV	10 kV	20 kV	10 kV	20 kV	10 kV
$CoFe_2O_4$ (Ni)	----	----	----	----	----	-----	-----	-----
$Ni_{0.25}Co_{0.75}Fe_2O_4$	1096	3014	1013	2662	727	1179	827	942
$Ni_{0.5}Co_{0.5}Fe_2O_4$	1416	3667	1079	2479	897	1281	820	995
$Ni_{0.75}Co_{0.25}Fe_2O_4$	2453	4594	811	928	829	1210	663	992
$NiFe_2O_4$	-----	-----	-----	-----	1699	1840	1308	1089
Deposit upstream of $NiFe_2O_4$	5305	4025	-----	-----	-----	-----	-----	-----
Deposit downstream of $NiFe_2O_4$	11176	7820	-----	-----	-----	-----	-----	-----

Table 4.8.2 (continued). EDX carbon counts (counts.(100 s)$^{-1}$) off the exposed spinels.

168

	Carbon film thickness /nm							
	550°C				650°C			
	Middle		Edge		Middle		Edge	
Sample	20 kV	10 kV	20 kV	10 kV	20 kV	10 kV	20 kV	10 kV
$CoFe_2O_4$ (Mn)	-----	-----	-----	-----	-----	-----	-----	-----
$Mn_{0.25}Co_{0.75}Fe_2O_4$	35	19	26	13	32	7	24	7
$Mn_{0.5}Co_{0.5}Fe_2O_4$	39	17	23	12	46	11	27	6
$Mn_{0.75}Co_{0.25}Fe_2O_4$	36	17	31	12	52	18	26	7
$MnFe_2O_4$	34	15	25	10	55	15	30	7
$CoFe_2O_4$ (Fe)	55	10	51	7	75	20	57	11
$Fe_{0.25}Co_{0.75}Fe_2O_4$	44	20	43	17	66	14	54	11
$Fe_{0.5}Co_{0.5}Fe_2O_4$	52	22	41	19	62	14	54	10
$Fe_{0.75}Co_{0.25}Fe_2O_4$	41	23	33	18	66	15	56	11
$FeFe_2O_4$	40	18	37	12	68	21	55	17
$CoFe_2O_4$ (Ni)	-----	-----	-----	-----	-----	-----	-----	-----
$Ni_{0.25}Co_{0.75}Fe_2O_4$	36	18	33	16	24	7	27	5
$Ni_{0.5}Co_{0.5}Fe_2O_4$	46	21	35	14	29	7	27	6
$Ni_{0.75}Co_{0.25}Fe_2O_4$	80	26	26	5	27	7	22	6
$NiFe_2O_4$	-----	-----	-----	-----	55	11	43	6

Table 4.8.3. Carbon film thickness, as determined from EDX carbon counts, on the exposed spinels.

Sample	a_0 lattice parameter /Å		
	Before	After 550°C	After 650°C
$CoFe_2O_4$ (Mn)	8.391	8.393	8.395
$Mn_{0.25}Co_{0.75}Fe_2O_4$	8.425	8.413	8.421
$Mn_{0.5}Co_{0.5}Fe_2O_4$	8.466	8.461	8.468
$Mn_{0.75}Co_{0.25}Fe_2O_4$	8.488	8.487	8.490
$MnFe_2O_4$	8.507	8.510	8.523
$CoFe_2O_4$ (Fe)	8.392	8.394	8.392
$Fe_{0.25}Co_{0.75}Fe_2O_4$	8.391	8.392	8.389
$Fe_{0.5}Co_{0.5}Fe_2O_4$	8.392	8.388	8.396
$Fe_{0.75}Co_{0.25}Fe_2O_4$	8.389	8.394	8.400
$FeFe_2O_4$	8.400	8.392	8.401
$CoFe_2O_4$ (Ni)	8.393	8.390	8.397
$Ni_{0.25}Co_{0.75}Fe_2O_4$	8.379	8.381	8.385
$Ni_{0.5}Co_{0.5}Fe_2O_4$	8.368	8.364	8.380
$Ni_{0.75}Co_{0.25}Fe_2O_4$	8.353	8.351	8.362
$NiFe_2O_4$	8.345	-----	8.348

Table 4.8.4. a_0 lattice parameter values for the spinels.

Sample	Mn $2p_{3/2}$		Fe $2p_{3/2}$		Co $2p_{3/2}$		Ni $2p_{3/2}$		O $1s$	
	Al	Mg	Al	Mg	Al	Mg	Al	Mg	Al	Mg
$CoFe_2O_4$ (Mn)	-----	-----	-----	-----	-----	-----	-----	-----	-----	-----
$Mn_{0.25}Co_{0.75}Fe_2O_4$	-----	-----	-----	-----	-----	-----	-----	-----	532.3	532.4
$Mn_{0.5}Co_{0.5}Fe_2O_4$	-----	-----	-----	-----	-----	-----	-----	-----	531.7	531.9
$Mn_{0.75}Co_{0.25}Fe_2O_4$	-----	-----	-----	-----	-----	-----	-----	-----	532.4	532.5
$MnFe_2O_4$	-----	-----	-----	-----	-----	-----	-----	-----	531.9	532.0
$CoFe_2O_4$ (Fe)	-----	-----	709.8	709.6	779.2	780.2	-----	-----	531.9	532.1
$Fe_{0.25}Co_{0.75}Fe_2O_4$	-----	-----	710.2	710.0	779.7	780.0	-----	-----	531.9	531.9
$Fe_{0.5}Co_{0.5}Fe_2O_4$	-----	-----	710.2	710.2	779.8	780.1	-----	-----	531.8	531.9
$Fe_{0.75}Co_{0.25}Fe_2O_4$	-----	-----	709.7	709.8	780.4	-----	-----	-----	531.9	532.1
$FeFe_2O_4$	-----	-----	709.9	710.3	-----	-----	-----	-----	532.0	532.1

Table 4.8.5. Binding energies in the spinels exposed at 550°C.

	Binding energy /eV									
	Mn $2p_{3/2}$		Fe $2p_{3/2}$		Co $2p_{3/2}$		Ni $2p_{3/2}$		O $1s$	
Sample	Al	Mg	Al	Mg	Al	Mg	Al	Mg	Al	Mg
$CoFe_2O_4$ (Ni)	-----	-----	710.7	710.9	779.8	780.2	-----	-----	531.9	532.0
$Ni_{0.25}Co_{0.75}Fe_2O_4$	-----	-----	710.9	710.5	780.1	780.0	855.1	854.7	532.0	532.0
$Ni_{0.5}Co_{0.5}Fe_2O_4$	-----	-----	710.5	710.8	779.9	780.0	854.7	854.6	532.0	532.1
$Ni_{0.75}Co_{0.25}Fe_2O_4$	-----	-----	710.6	710.8	781.3	-----	854.7	854.4	532.1	532.1
$NiFe_2O_4$	-----	-----	-----	-----	-----	-----	-----	-----	-----	-----
Deposit upstream of $NiFe_2O_4$	-----	-----	713.0	-----	-----	-----	856.6	-----	531.3	-----
Deposit downstream of $NiFe_2O_4$	-----	-----	712.3	-----	-----	-----	856.4	-----	531.1	-----

Table 4.8.5 (continued). Binding energies in the spinels exposed at 550°C.

Sample	Mn $2p_{3/2}$		Fe $2p_{3/2}$		Co $2p_{3/2}$		Ni $2p_{3/2}$		O $1s$	
	Al	Mg	Al	Mg	Al	Mg	Al	Mg	Al	Mg
$CoFe_2O_4$ (Mn)	-----	-----	-----	-----	-----	-----	-----	-----	-----	-----
$Mn_{0.25}Co_{0.75}Fe_2O_4$	640.5	640.6	710.6	710.7	780.0	779.7	-----	-----	531.8	531.8
$Mn_{0.5}Co_{0.5}Fe_2O_4$	640.8	640.5	710.3	711.0	-----	-----	-----	-----	531.9	532.1
$Mn_{0.75}Co_{0.25}Fe_2O_4$	-----	-----	-----	-----	-----	-----	-----	-----	532.3	532.2
$MnFe_2O_4$	-----	-----	-----	-----	-----	-----	-----	-----	532.2	532.2
$CoFe_2O_4$ (Fe)	-----	-----	710.5	710.7	-----	-----	-----	-----	531.8	531.9
$Fe_{0.25}Co_{0.75}Fe_2O_4$	-----	-----	710.4	710.4	779.9	779.8	-----	-----	532.0	532.3
$Fe_{0.5}Co_{0.5}Fe_2O_4$	-----	-----	710.2	710.6	780.2	779.7	-----	-----	532.1	532.3
$Fe_{0.75}Co_{0.25}Fe_2O_4$	-----	-----	709.9	710.2	-----	-----	-----	-----	532.1	532.3
$FeFe_2O_4$	-----	-----	710.2	710.1	-----	-----	-----	-----	532.3	532.4
$CoFe_2O_4$ (Ni)	-----	-----	-----	-----	-----	-----	-----	-----	-----	-----
$Ni_{0.25}Co_{0.75}Fe_2O_4$	-----	-----	710.8	710.4	780.3	780.2	855.0	-----	532.1	532.0
$Ni_{0.5}Co_{0.5}Fe_2O_4$	-----	-----	709.8	709.8	780.3	779.8	854.9	853.9	532.2	532.3
$Ni_{0.75}Co_{0.25}Fe_2O_4$	-----	-----	710.9	710.9	781.0	-----	854.9	-----	532.1	532.2
$NiFe_2O_4$	-----	-----	710.4	710.7	-----	-----	854.8	854.1	532.0	532.1

Table 4.8.6. Binding energies in the spinels exposed at 650°C.
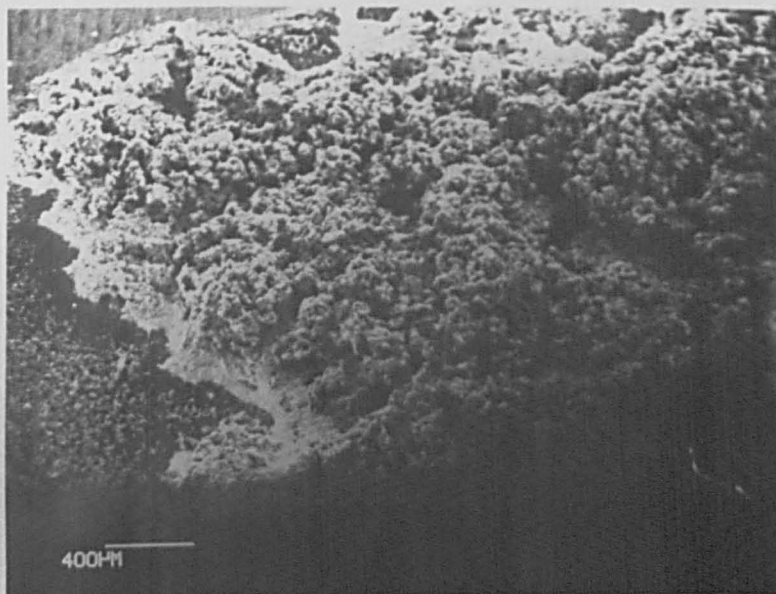
Figure 4.8.1. SEI of deposit formed after exposure of $NiFe_2O_4$ pellet at 550°C for 23 days: a) upstream; and b) downstream.

174
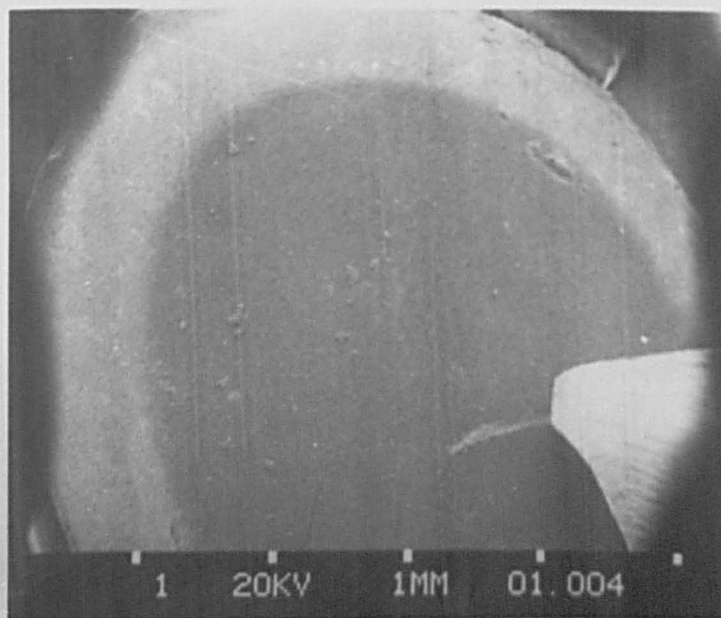
Figure 4.8.2. SEI of $Mn_{0.75}Co_{0.25}Fe_2O_4$ pellet after 24 days at 650°C.
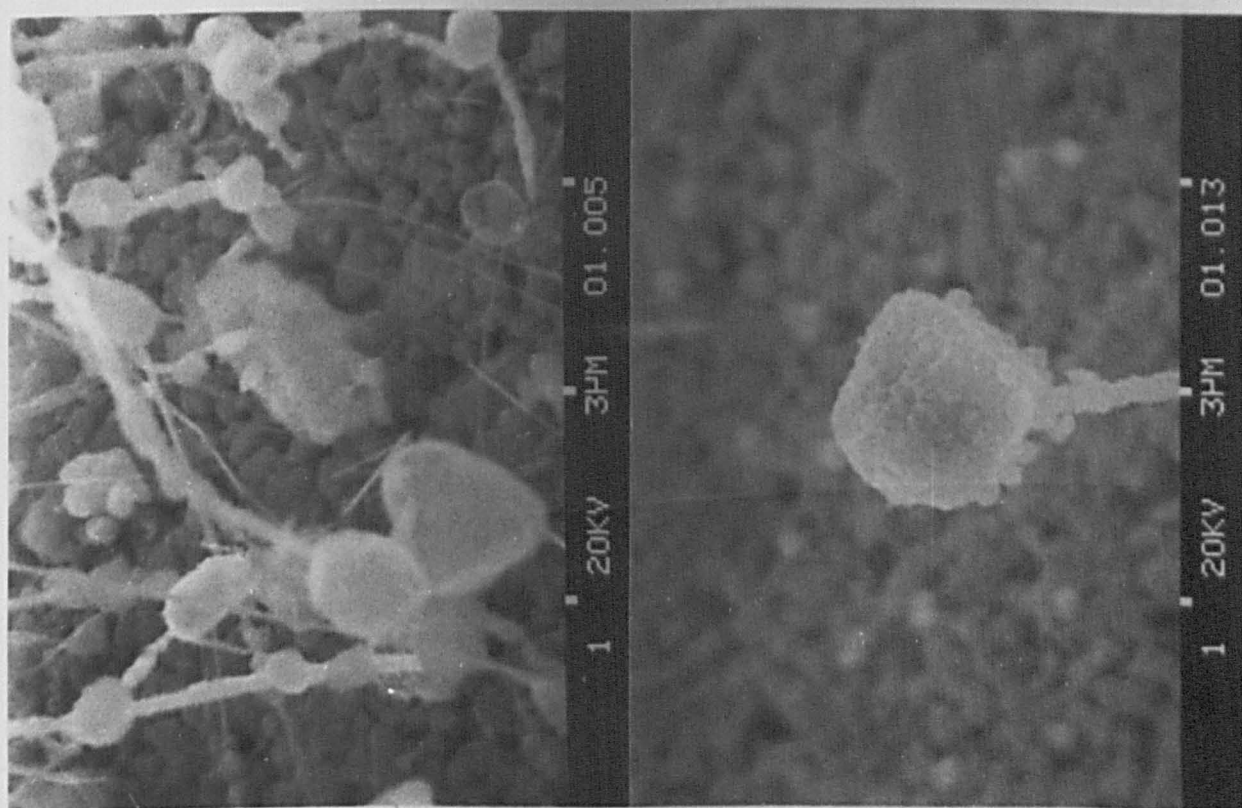
Figure 4.8.3. SEI of $Mn_{0.75}Co_{0.25}Fe_2O_4$ pellet after 24 days at 650°C - whiskers and nodules.
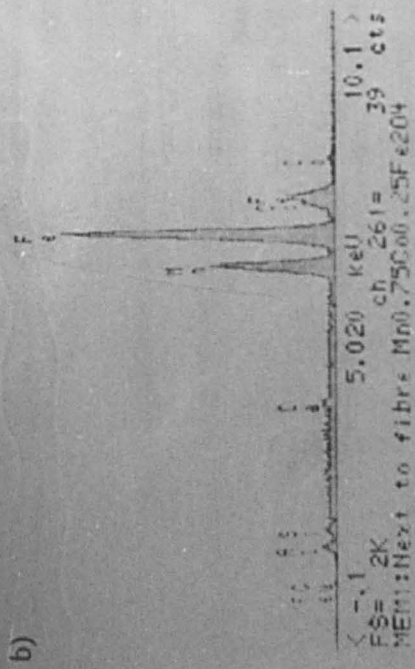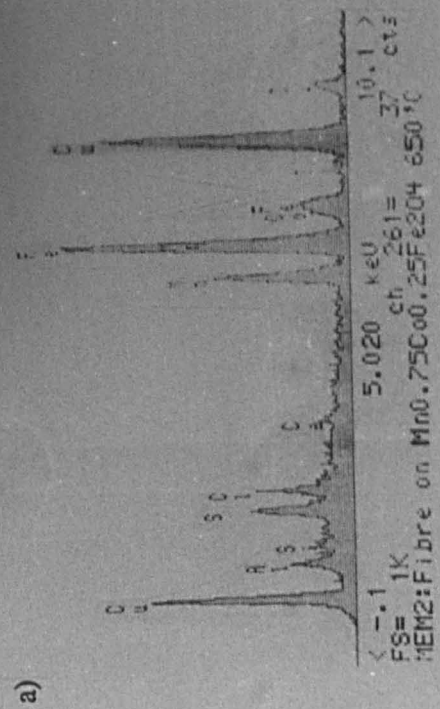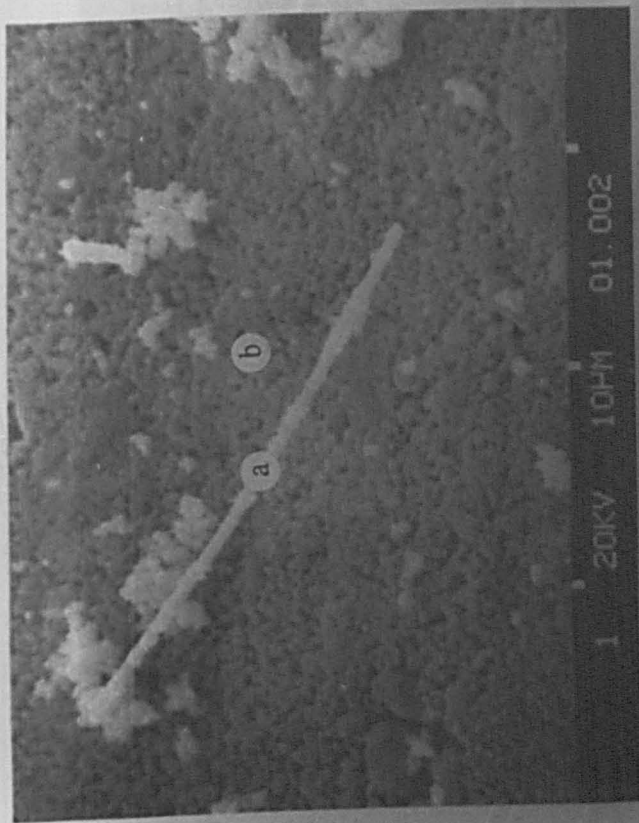
Figure 4.8.4. EDX spectra of $Mn_{0.75}Co_{0.25}Fe_2O_4$ pellet after 24 days at 650°C: a) fibre; and b) adjacent to fibre.

Figure 4.8.5. Carbon deposition on the spinels $Mn_xCo_{1-x}Fe_2O_4$ after 24 days in the gamma cell: a) 550°C, 20 kV; b) 550°C, 10 kV; c) 650°C, 20 kV; and d) 650°C, 10 kV.

177
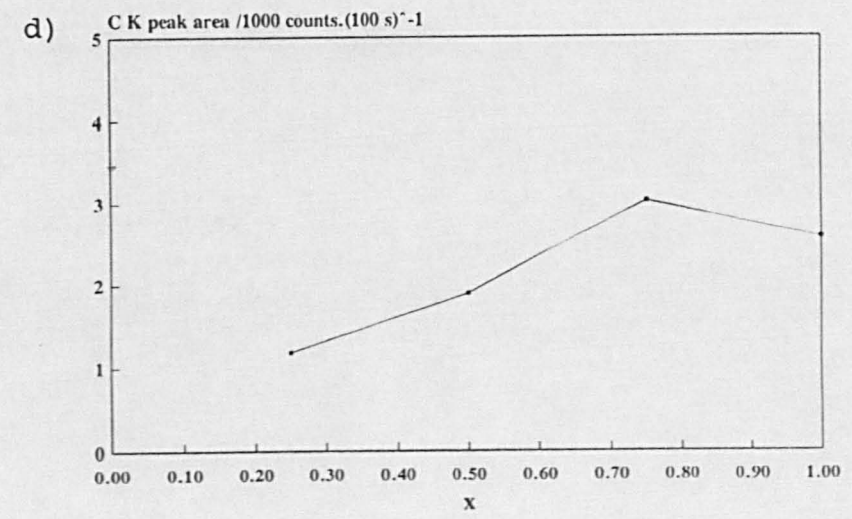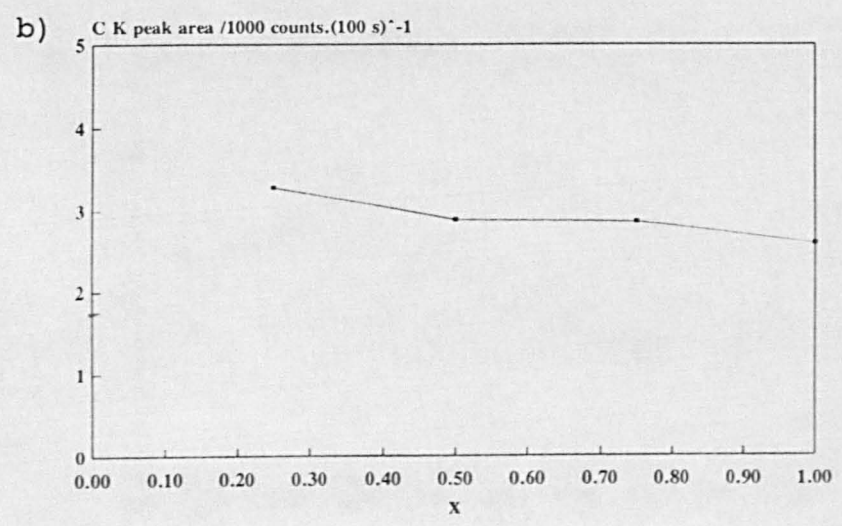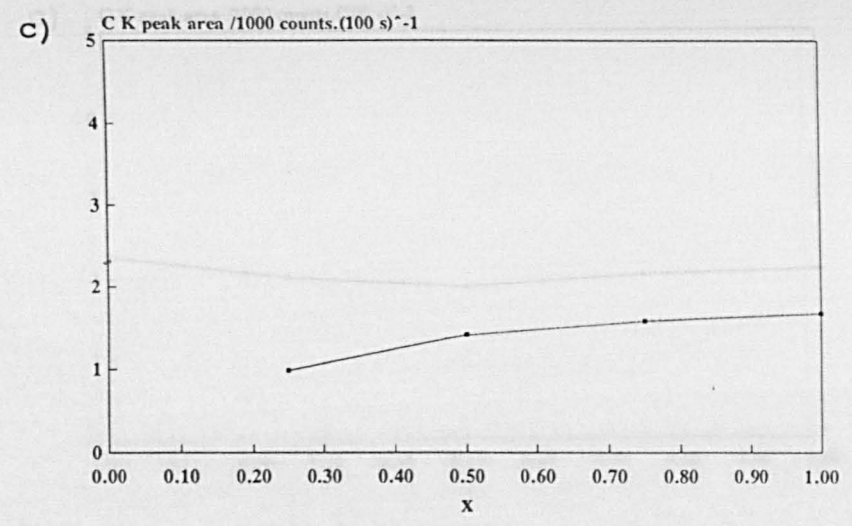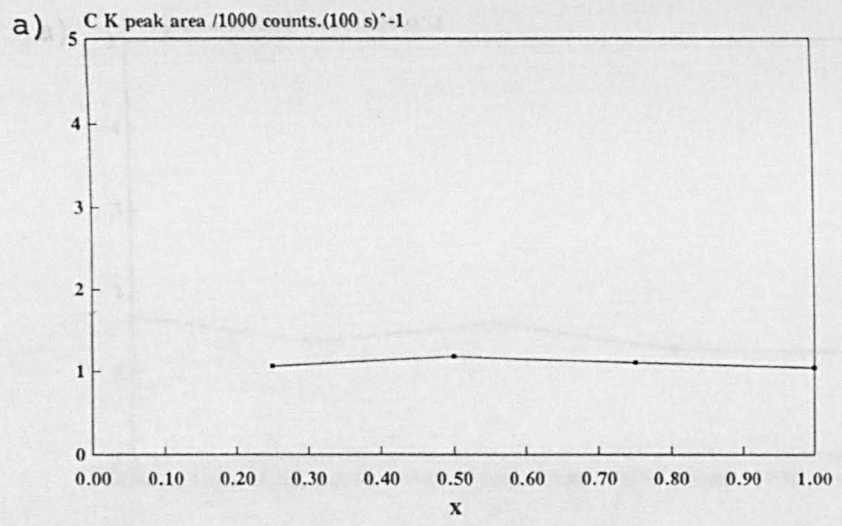
Figure 4.8.6. Carbon deposition on the spinels Fe$_x$Co$_{1-x}$Fe$_2$O$_4$ after 23 days in the gamma cell: a) 550°C, 20 kV; b) 550°C, 10 kV; c) 650°C, 20 kV; and d) 650°C, 10 kV.

178
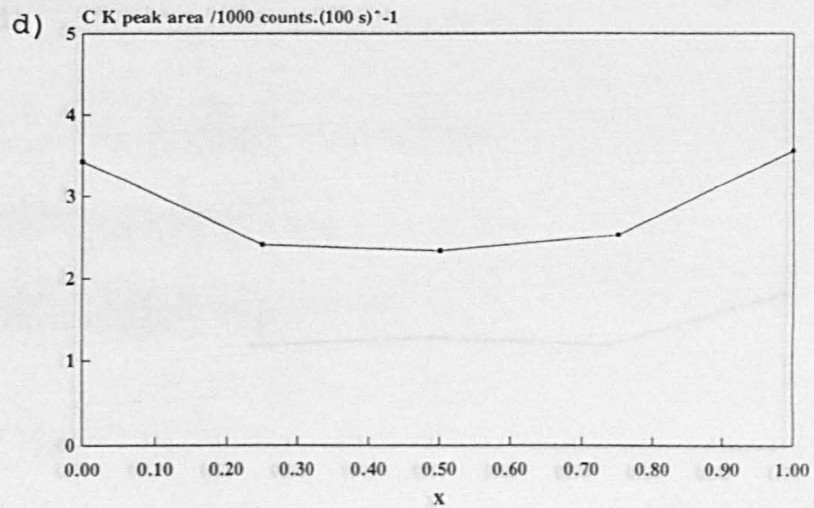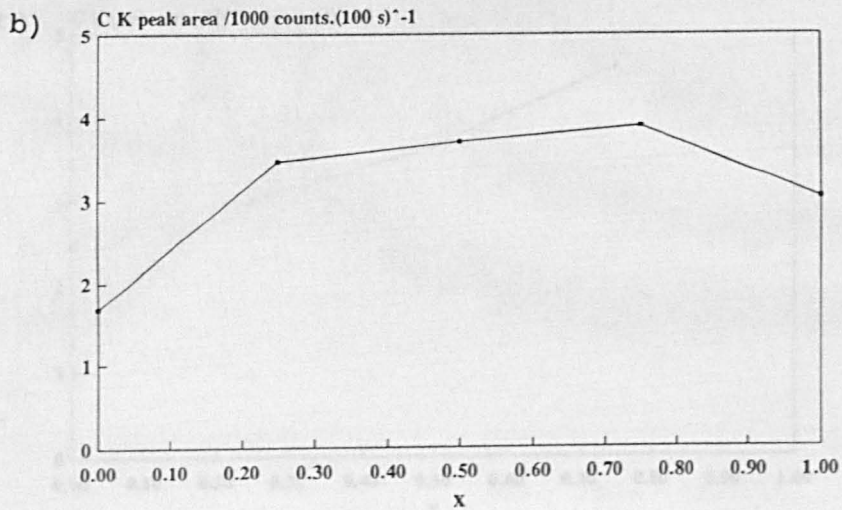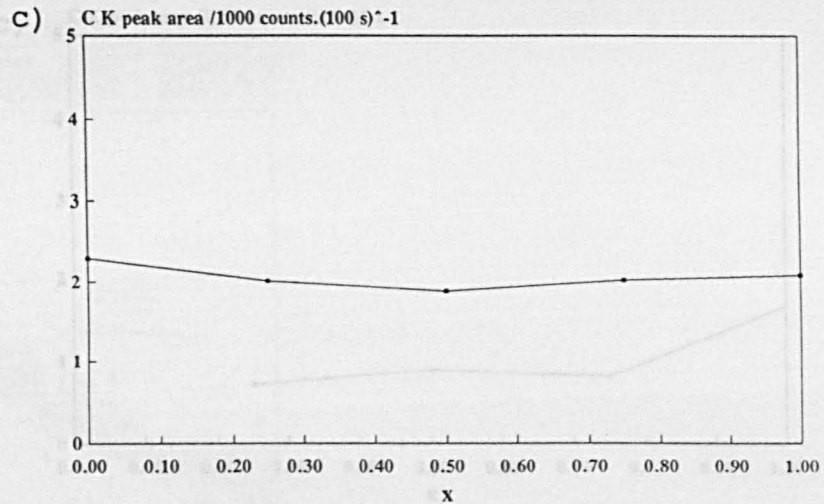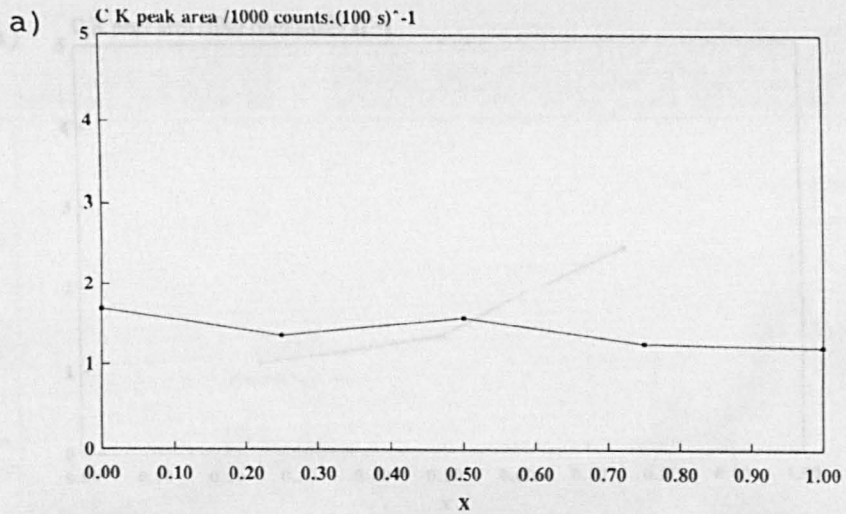
Figure 4.8.7. Carbon deposition on the spinels $Ni_xCo_{1-x}Fe_2O_4$ after 23 days in the gamma cell: a) 550°C, 20 kV; b) 550°C, 10 kV; c) 650°C, 20 kV; and d) 650°C, 10 kV.

179

a)

KH36F.RAW   CoFe2O4 (MnxCo1-xFe2O4) pellet after 24 days g-cell 550'C exSERIES: 1   OFFSET: 3.20
KH40D.RAW   Mn0.25Co0.75Fe2O4 pellet after 24 days g-cell 550'C expandedSERIES: 1   OFFSET: 2.40
KH37F.RAW   Mn0.5Co0.5Fe2O4 pellet after 24 days g-cell 550'C expended SERIES: 1   OFFSET: 1.60
KH38F.RAW   Mn0.75Co0.25Fe2O4 pellet after 24 days g-cell 550'C expandedSERIES: 1   OFFSET: 0.80
KH39F.RAW   MnFe2O4 pellet after 24 day g-cell 550'C expanded 19-12-89 KRSERIES: 1   OFFSET: 0.00

[1020]

[951]

[1022]

INTENSITY (CPS)

$CoFe_2O_4$

$Mn_{0.25}Co_{0.75}Fe_2O_4$

$Mn_{0.5}Co_{0.5}Fe_2O_4$

$Mn_{0.75}Co_{0.25}Fe_2O_4$

$MnFe_2O_4$

TWO – THETA (DEGREES)

Figure 4.8.8. [1020], [951] and [1022] regional XRD spectra of the $Mn_xCo_{1-x}Fe_2O_4$ ($0 \leq x \leq 1$) series after exposure at: a) 550°C; and b) 650°C.

180
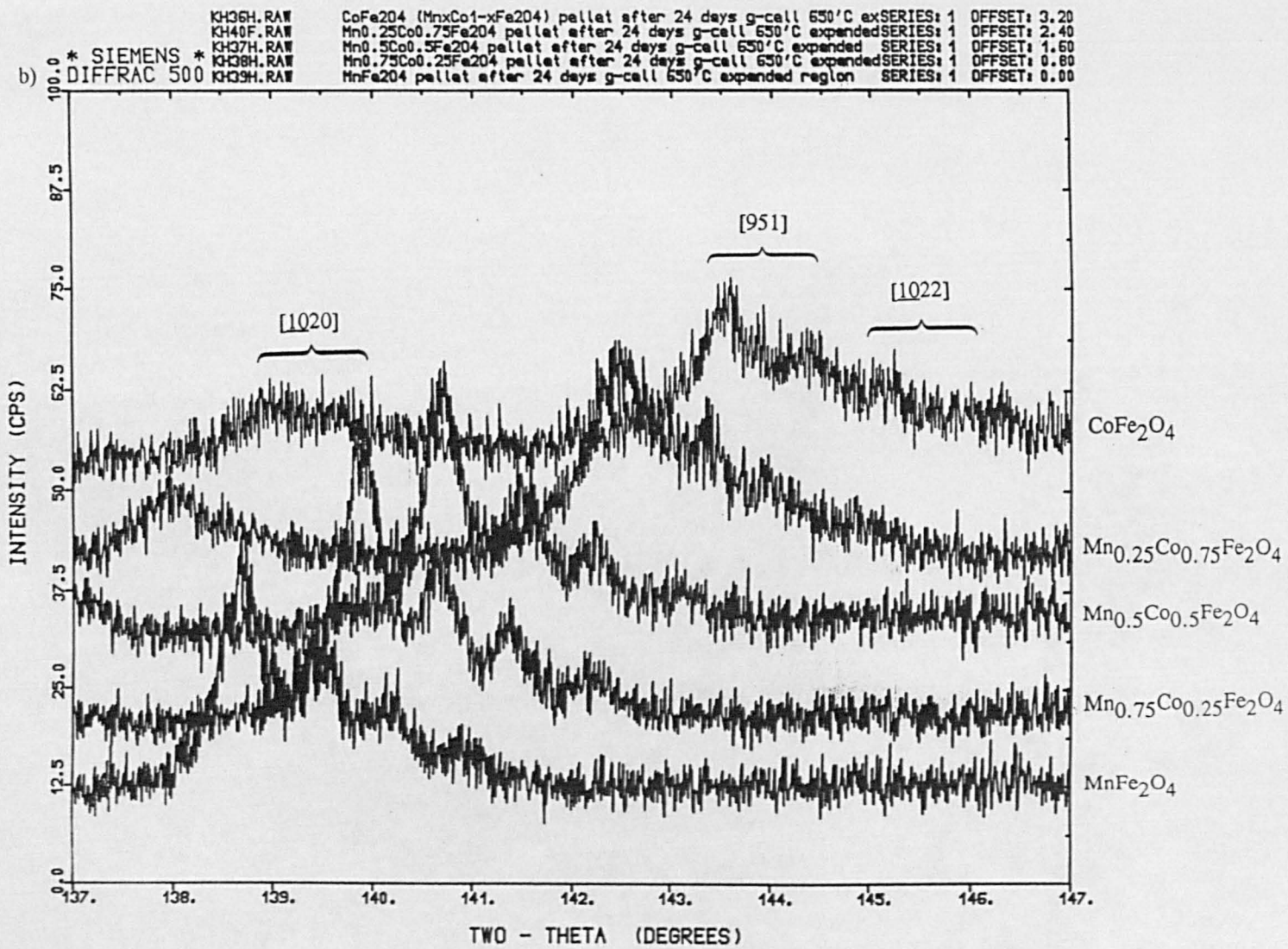
Figure 4.8.8 (continued). [1020], [951] and [1022] regional XRD spectra of the $Mn_xCo_{1-x}Fe_2O_4$ ($0 \leq x \leq 1$) series after exposure at: a) 550°C; and b) 650°C.

b)

[951]

[1020]

[1022]

INTENSITY (CPS)

100.0
87.5
75.0
62.5
50.0
37.5
25.0
12.5
0.0

$CoFe_2O_4$

$Mn_{0.25}Co_{0.75}Fe_2O_4$

$Mn_{0.5}Co_{0.5}Fe_2O_4$

$Mn_{0.75}Co_{0.25}Fe_2O_4$

$MnFe_2O_4$

137. 138. 139. 140. 141. 142. 143. 144. 145. 146. 147.

TWO - THETA (DEGREES)
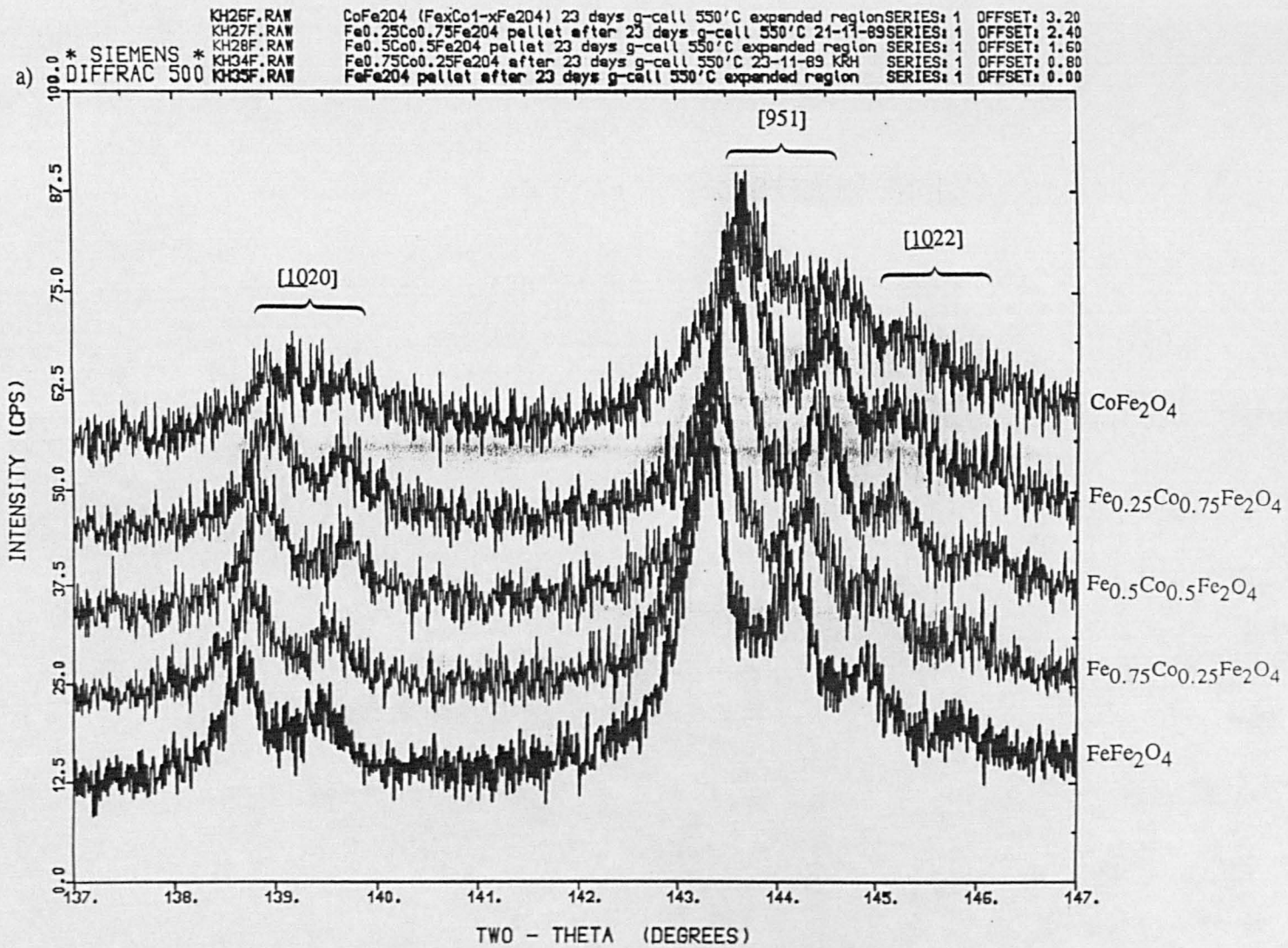
Figure 4.8.9. [1020], [951] and 1022] regional XRD spectra of the $Fe_xCo_{1-x}Fe_2O_4$ (0 ≤ x ≤ 1) series after exposure at: a) 550°C; and b) 650°C.

182
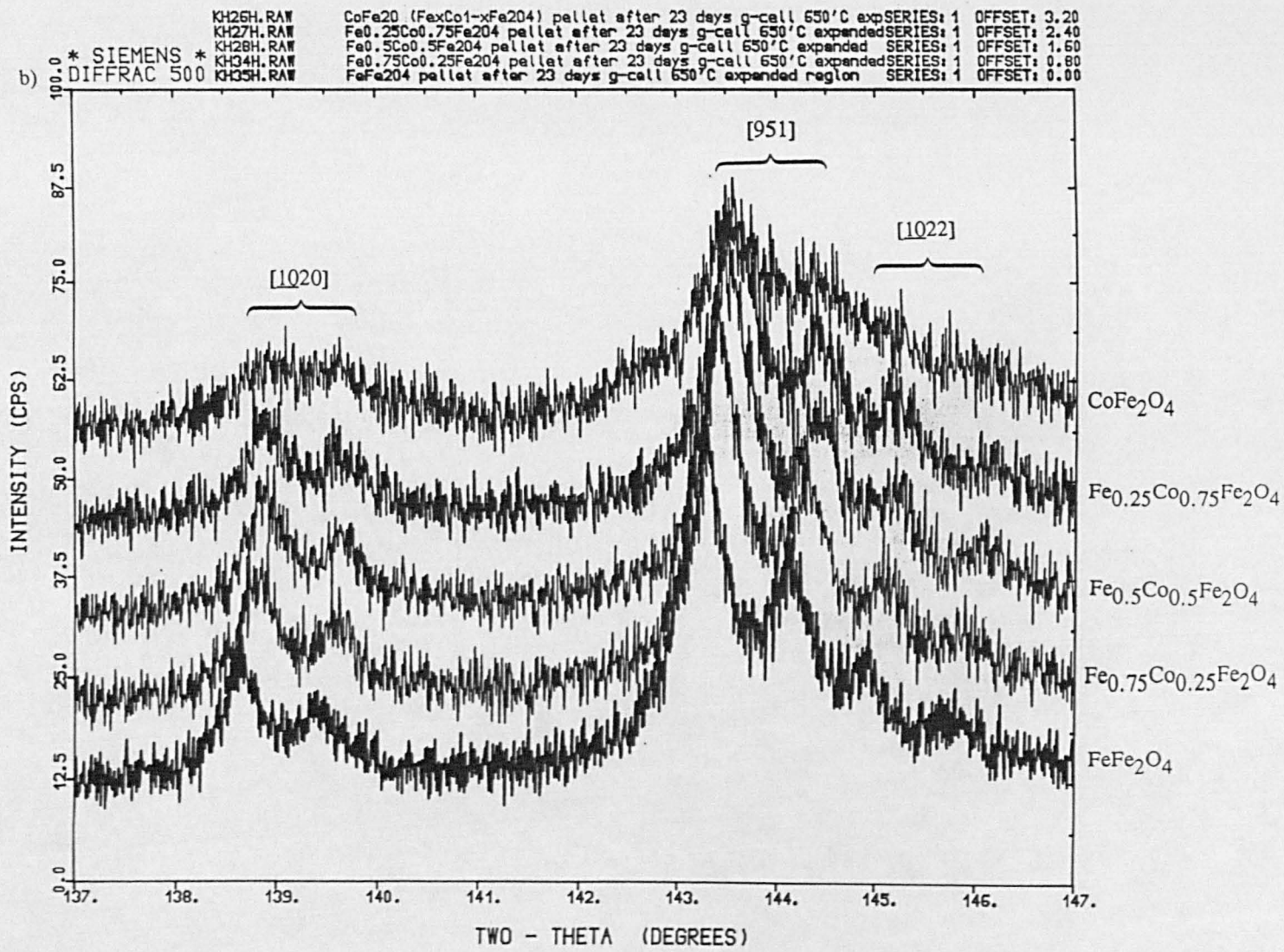
Figure 4.8.9 (continued). [1020], [951] and 1022] regional XRD spectra of the $Fe_xCo_{1-x}Fe_2O_4$ ($0 \leq x \leq 1$) series after exposure at: a) 550°C; and b) 650°C.
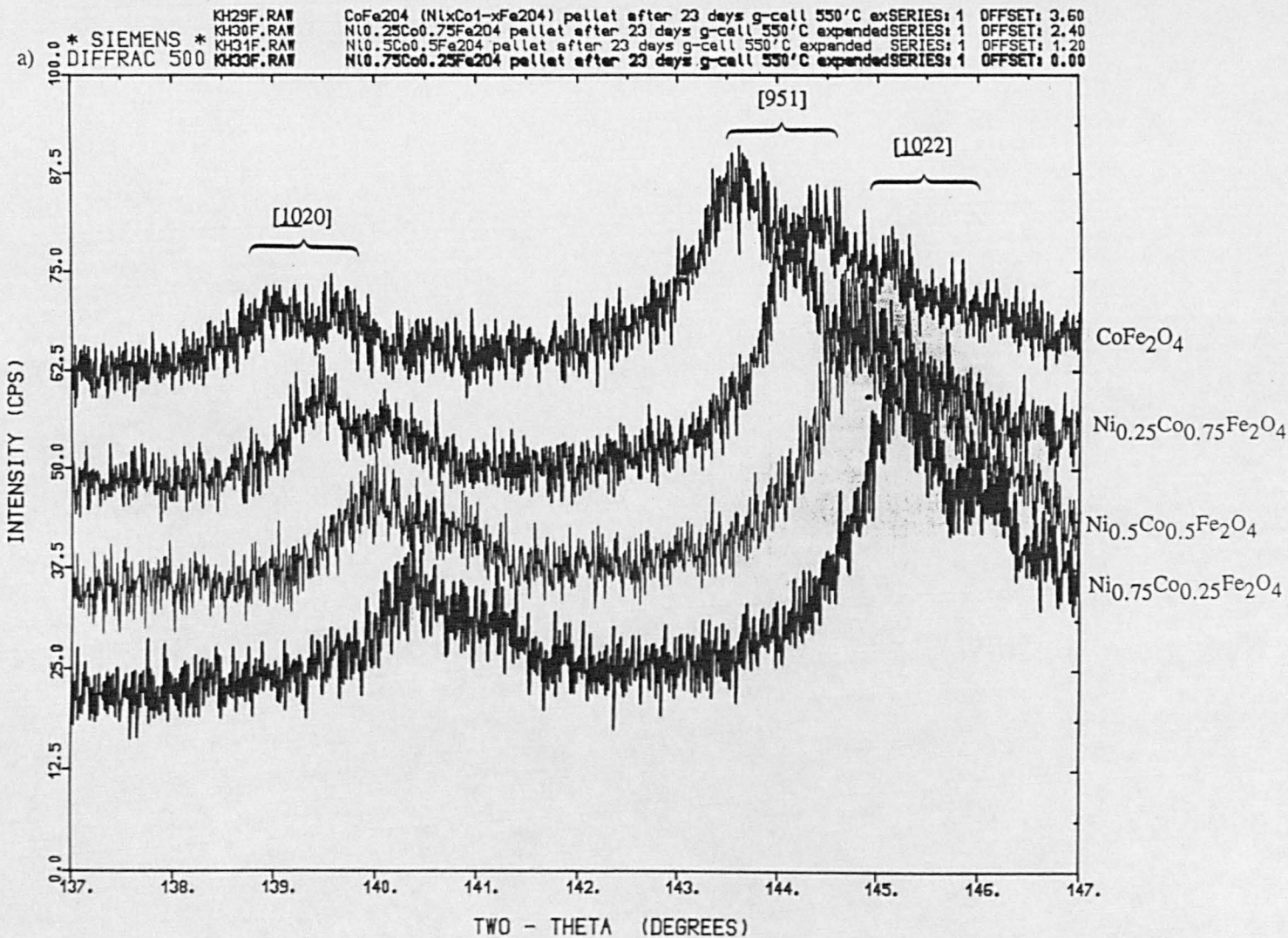
Figure 4.8.10. [1020], [951] and [1022] regional XRD spectra of the $Ni_xCo_{1-x}Fe_2O_4$ ($0 \leq x \leq 1$) series after exposure at: a) 550°C; and b) 650°C.
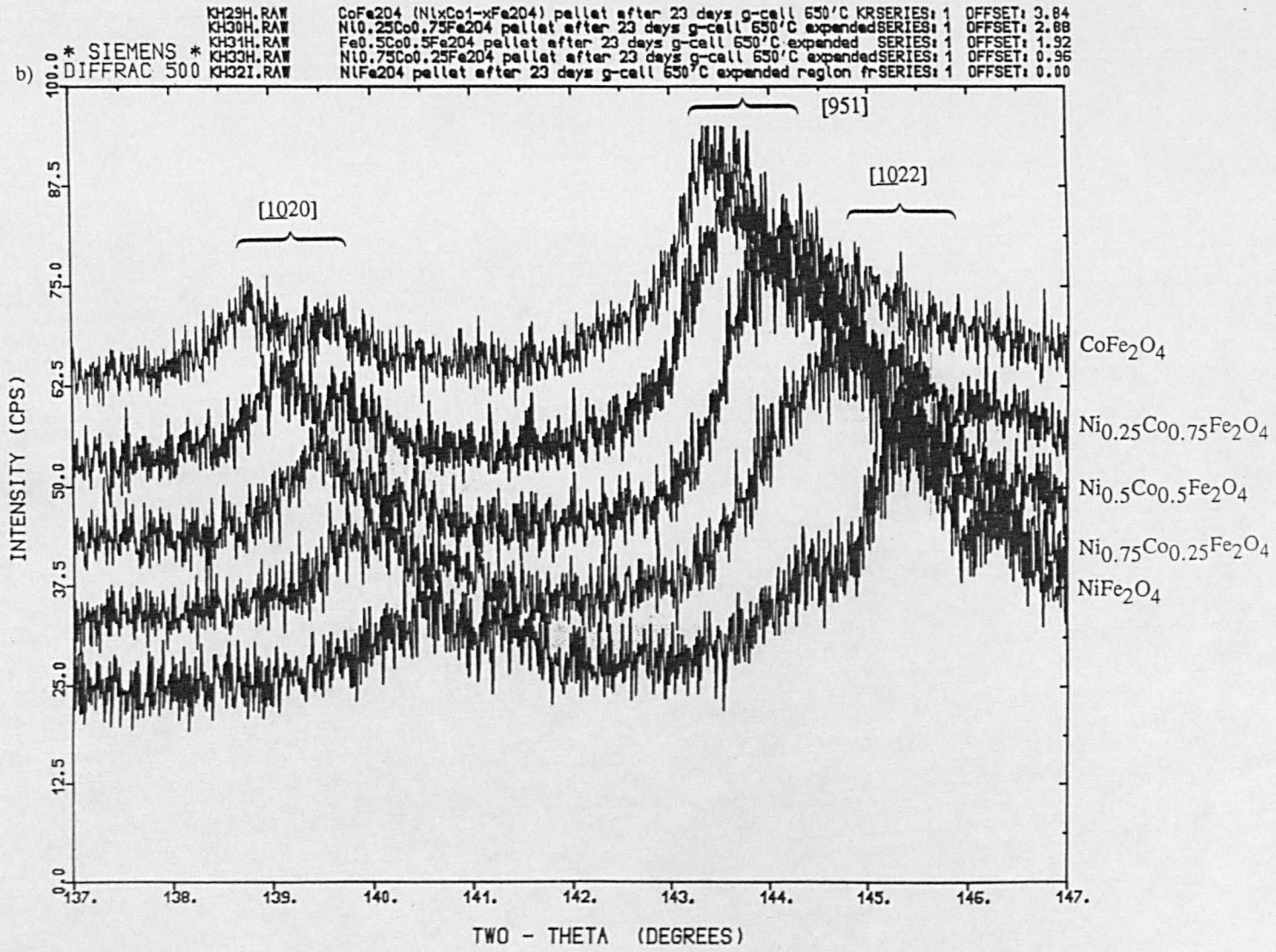
Figure 4.8.10 (continued). [$\overline{10}20$], [951] and [$\overline{10}22$] regional XRD spectra of the $Ni_xCo_{1-x}Fe_2O_4$ ($0 \leq x \leq 1$) series after exposure at: a) 550°C; and b) 650°C.

185
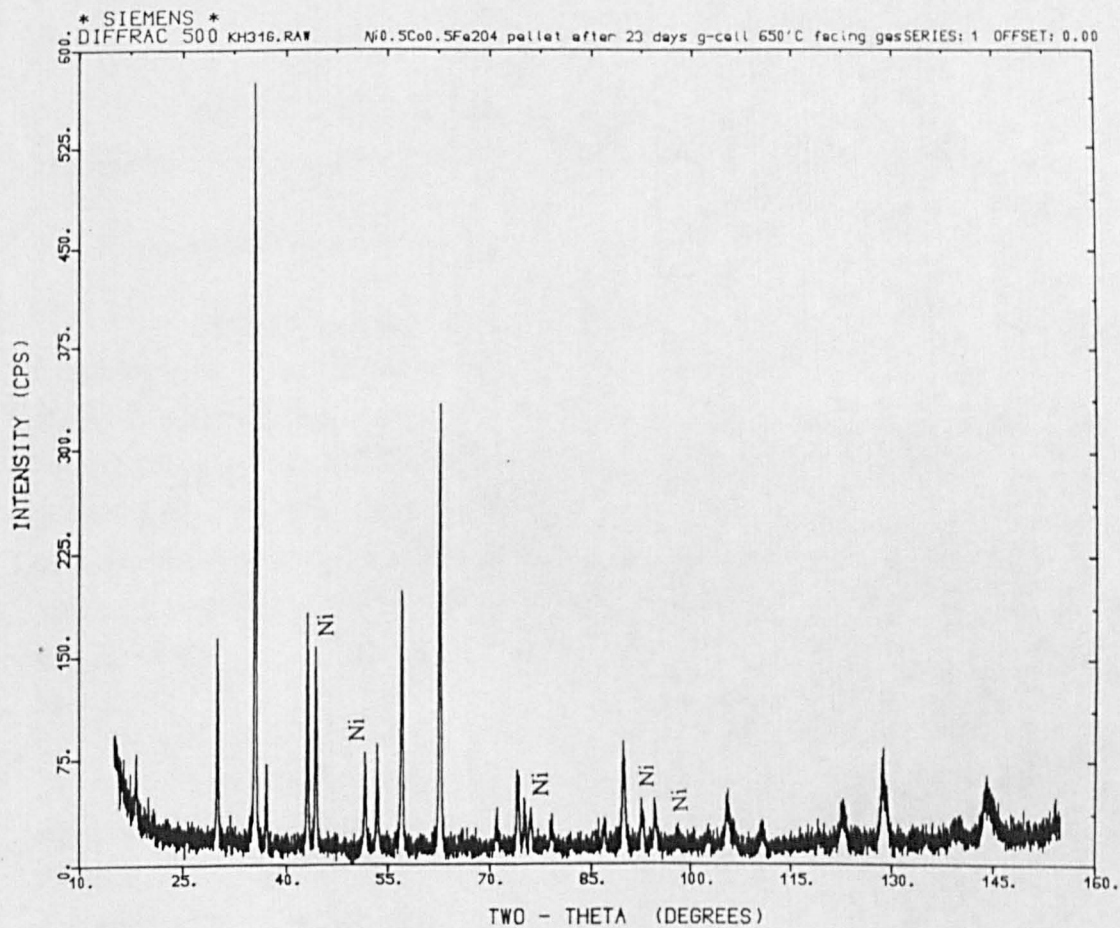
Figure 4.8.11. XRD spectrum of $Ni_{0.5}Co_{0.5}Fe_2O_4$ after exposure at 650°C.
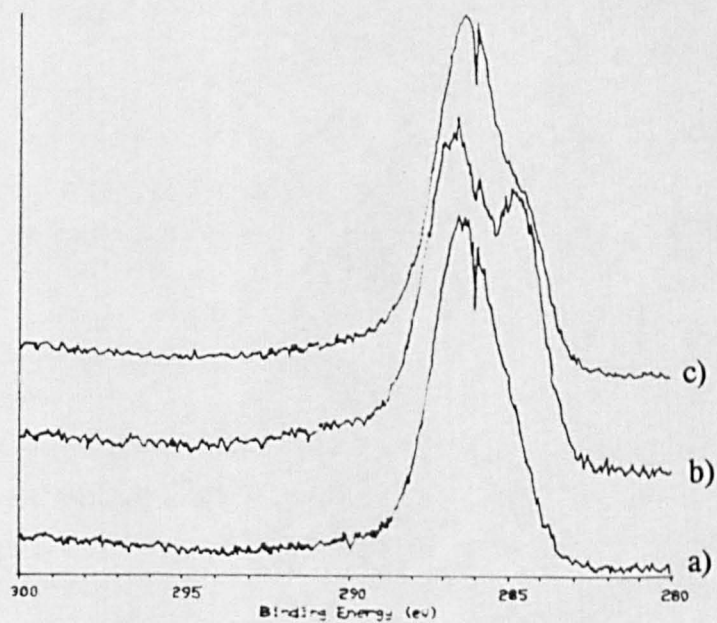
Figure 4.8.12. XP spectra of $Fe_{0.5}Co_{0.5}Fe_2O_4$ pellet: a) before exposure; b) after 23 days at 550°C; and c) after 23 days at 650°C.

4.9 Characterisation of Manganese Oxides after Exposure

4.9.1 Introduction

Table 4.9.1 gives the gamma cell exposure times for the manganese oxides. Pellets made out of the three oxides were exposed at both 550 and 650°C.

4.9.2 Optical Observations

All the manganese pellets after exposure were still strong and not readily breakable. All three oxides at both temperatures were green in colour, indicative of them all being MnO, the most reduced of the three manganese oxides examined. The higher oxidation state pellets had been reduced by the exposure conditions. When the pellets were split, they were found to be green in their interiors too. The reduction process had penetrated the 0.5 mm from the surface required to fully reduce the oxides. The edge regions of the Mn_3O_4 and Mn_2O_3 pellets, shielded from the direct effects of the gas mixture in the gamma cell, were, nevertheless, also reduced to MnO.

The 550°C MnO pellet had a mottled black surface (overlaying its green bulk) where the gas mixture had been able to contact with the pellet (i.e. the edges shielded by the spacers were still green). Likewise, the Mn_3O_4 and Mn_2O_3 pellets had green edges surrounding blackened centres.

The 650°C pellets also had darker centres to their faces and green edges, though not as prominent as with the 550°C samples. Both faces of the pellets, that facing the gas inlet end of the capsule and that facing the outlet, had similar appearances.

There was no evidence for any filamentary or fluffy carbon deposition on any of the samples when examined by scanning electron microscopy. Neither were there any major differences between the appearance of the middle and edges of the pellets.

4.9.3 Energy Dispersive X-Ray Analysis

Tables 4.9.2 and 4.9.3 list the carbon EDX counts and estimated carbon film thicknesses for the pellets after exposure. No data are available for the covered edge of the Mn_3O_4 pellet exposed at 550°C as, upon removal from the capsule, it was found to have been sideways on to the gas flow. Therefore, there was no covering of the edge by the silica spacers.

Figures 4.9.1 and 4.9.3 compare the spectra recorded at the middle and

edges of the MnO and Mn_2O_3 samples. Figure 4.9.2 shows the 650°C results for Mn_3O_4. These figures particularly highlight any increase in intensity of the C K signal in going from the shielded edge region of the pellets to the exposed central zones. The large peak to the higher keV side of the carbon signals is the O K signal (truncated by the expansion in the y direction imposed to show the carbon peak). The Mn $L\alpha_1$ signal can also be seen, giving a shoulder to the high energy side of the oxygen peak.

The MnO pellets show increased carbon in their middles compared to their edge regions. The 650°C sample has a less intense carbon signal (in both the 10 and 20 kV spectra, though, of course, the contribution from the surface carbon is enhanced in the lower energy spectrum, with its shallower average sampling depth), in agreement with the visual observations of the surface being less dark compared to the 550°C pellet. These results also manifest themselves in the C K peak area count rates, given in Table 4.9.2.

The 10 kV results from the Mn_3O_4 pellets show the expected enhanced carbon signal, compared to that obtained from the 20 kV spectra. As stated earlier, mispositioning of the sample in the gamma cell capsule liner prevented any "edge" information being obtained from the 550°C pellet. The spectra recorded from the pellet did, though, contain a clear carbon peak, above the expected background of the spectrum. The intensity was not as great as from any of the MnO pellets, but carbon was definitely present. The pellet exposed at 650°C gave higher carbon count rates at the edge than in the middle. However, it can be seen in Figure 4.9.2 that this must have been the result of noise in the spectra affecting the position of the baseline calculated by the software. The 10 kV spectra show slightly enhanced signals compared to the 20 kV ones, for both the middle and edge regions. There is no apparent difference in carbon peak intensity in the 20 kV spectra (there is no C K signal to be seen), but the 10 kV spectra might just indicate additional carbon to be present in the middle of the pellet. However, the evidence for any carbon deposition on the Mn_3O_4 pellet exposed at 650°C is not strong.

As with the MnO and Mn_3O_4 results, use of a 10 kV electron beam on the Mn_2O_3 samples increases the C K signal above that seen with a 20 kV accelerating potential. There are also enhanced carbon count rates in the central regions of the pellets, compared to their edges, though this is less pronounced than with the MnO pellets. The 650°C sample, as can be seen both from the figures given in Table 4.9.2 and in Figure 4.9.3, showed no additional carbon in the middle. The 550°C pellet did show enhanced carbon in its centre, particularly in the 10 kV spectrum.

As was seen with the spinel oxides (Table 4.8.3), the carbon film

thicknesses calculated from the 10 kV spectra, and given in Table 4.9.3, were all smaller than those obtained from the 20 kV results. The edge results were all similar, readily allowing the increased carbon signals, and, thus, deposition, on the MnO pellet exposed at 650°C and all three oxides exposed at 550°C to show through. It would appear from these results that only MnO brings about carbon deposition from the gas mixture at both temperatures, 550 and 650°C. The other two oxides, Mn_3O_4 and Mn_3O_3, only catalyse deposition at 550°C. At the lower temperature, the deposition rates on the two higher oxides, Mn_3O_4 and Mn_2O_3, were similar while MnO brought about carbon deposition at a rate some 2½ times greater.

The lack of any obvious structural carbon deposits on the pellet faces, but the presence of carbon signals in the EDX spectra, particularly in the 10 kV results, suggests that the carbon has been deposited as a thin film, covering the whole of the exposed pellet surface more or less evenly.

4.9.4   X-Ray Diffraction

All of the pellets, after exposure at both 550 and 650°C, gave only an MnO XRD spectrum, in good agreement with the JCPDS 7-230 manganese oxide / manganosite spectrum. No other peaks were seen. Figure 4.9.4 compares the spectra off an Mn_2O_3 pellet before and after exposure at 550°C.

4.9.5   X-Ray Photoelectron Spectroscopy

Table 4.9.4 lists the Mn $2p_{3/2}$ binding energy values obtained off the pellets after exposure. The Mn_2O_3 pellet exposed at 550°C gave a weak Mn $2p_{3/2}$ signal. The Mn_3O_4 pellet exposed at 550°C, likewise, gave an extremely weak response (both of these weak Mn $2p_{3/2}$ peaks were also broad) while that for MnO was nonexistent. These are signs in agreement with the EDX results, suggesting the presence of deposited carbon layers covering the pellets. The Mn $2p_{3/2}$ peak positions show a degree of scatter. Complex C $1s$ spectra made it difficult to accurately determine the degree of charging for each sample, and, of course, any carbon deposits present need not necessarily charge to the same extent as the underlying manganese oxide. In this respect, the XRD results provide a more reliable determination of the oxidation state of the manganese in the exposed samples.

| | Exposure time /days | |
Sample	550°C	650°C
MnO	24	24
Mn_3O_4	24	24
Mn_2O_3	24	24

Table 4.9.1. Gamma cell exposure times for the manganese oxides.

	C K peak area /counts.$(100\ s)^{-1}$							
	550°C				650°C			
	Middle		Edge		Middle		Edge	
Sample	20 kV	10 kV	20 kV	10 kV	20 kV	10 kV	20 kV	10 kV
MnO	5801	10103	2319	3077	2352	4455	1691	2188
Mn_3O_4	2358	3615	----	----	1498	1725	1608	1878
Mn_2O_3	2469	3307	1966	2598	1631	2009	1620	1954

Table 4.9.2. EDX carbon counts (counts.$(100\ s)^{-1}$) off the exposed manganese oxides.

Carbon film thickness /nm							
550°C				650°C			
Middle		Edge		Middle		Edge	
20 kV	10 kV	20 kV	10 kV	20 kV	10 kV	20 kV	10 kV
Sample							
MnO — 189	59	76	18	77	26	55	13
Mn_3O_4 — 77	21	----	----	49	10	52	11
Mn_2O_3 — 81	19	64	15	53	12	53	11

Table 4.9.3. Carbon film thickness, as determined from EDX carbon counts, on the exposed manganese oxides.

| Sample | 550°C | | 650°C | |
	BE /eV	FWHM /eV	BE /eV	FWHM /eV
MnO	-----	-----	639.9	3.2
Mn_3O_4	639.2	5.0	643.3	2.9
Mn_2O_3	640.5	3.9	642.6	3.3

Table 4.9.4. Mn $2p_{3/2}$ binding energy values for the manganese oxides after exposure.
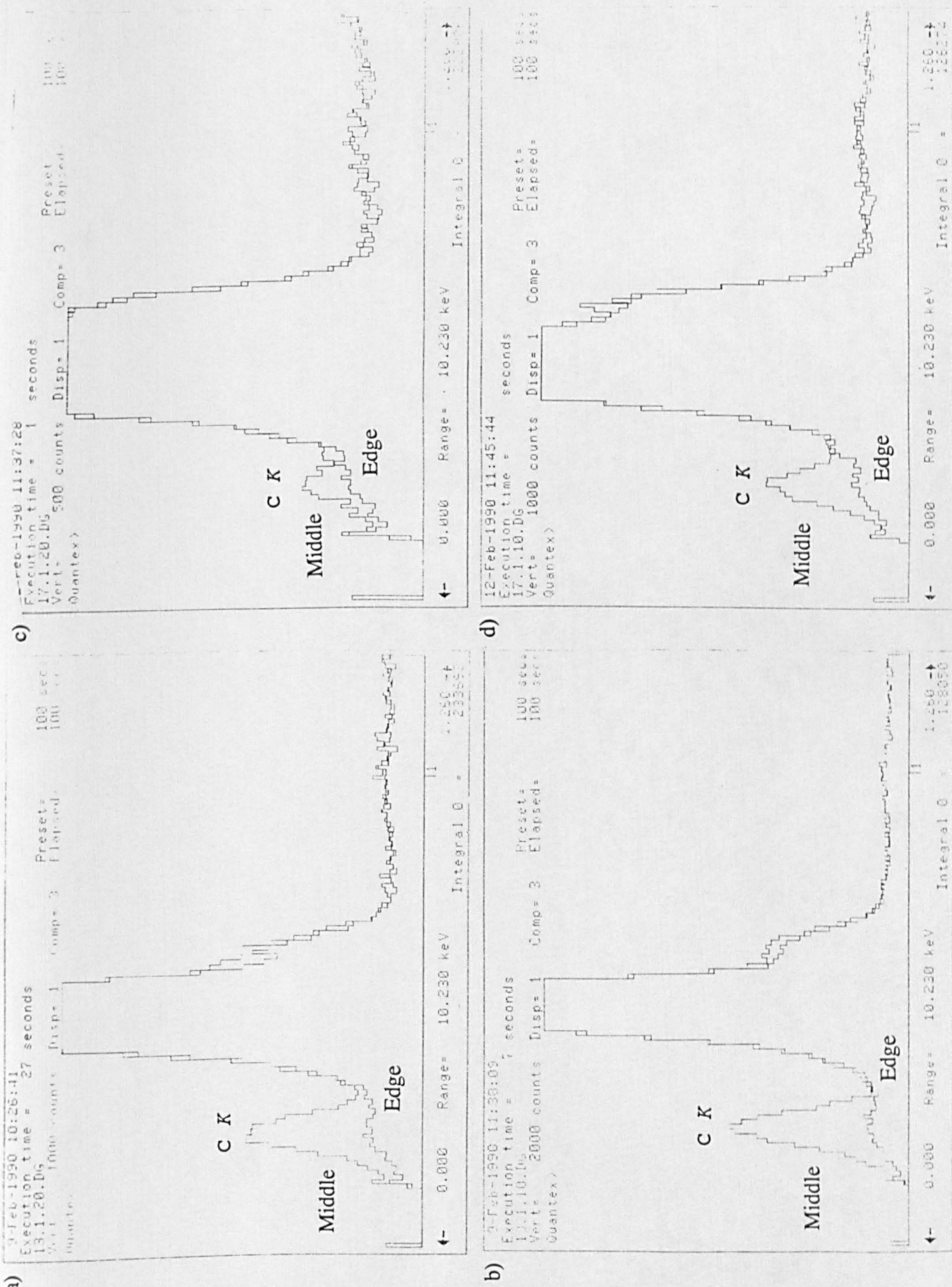
Figure 4.9.1. Comparison of edge and middle EDX spectra for MnO: a) 550°C, 20 kV; b) 550°C, 10 kV; c) 650°C, 20 kV; and d) 650°C, 10 kV.

a)
```
12-Feb-1990 11:41:24
Execution time =    1. seconds
18.1.20.DG                                    Preset=      100 secs
Vert=      500 counts   Disp= 1   Comp= 3   Elapsed=     100 secs
Quantex>
```

Middle

C K

Edge

```
<-   0.000    Range=  10.230 keV
                                    Integral 0  =
```

b)
```
12-Feb-1990 11:47:05
Execution time =       seconds
18.1.10.DG                                    Preset=      100 secs
Vert=      500 counts   Disp= 1   Comp= 3   Elapsed=     100 secs
Quantex>
```

C K

Middle

Edge

```
<-   0.000    Range=  10.230 keV
                                    Integral 0  =
```
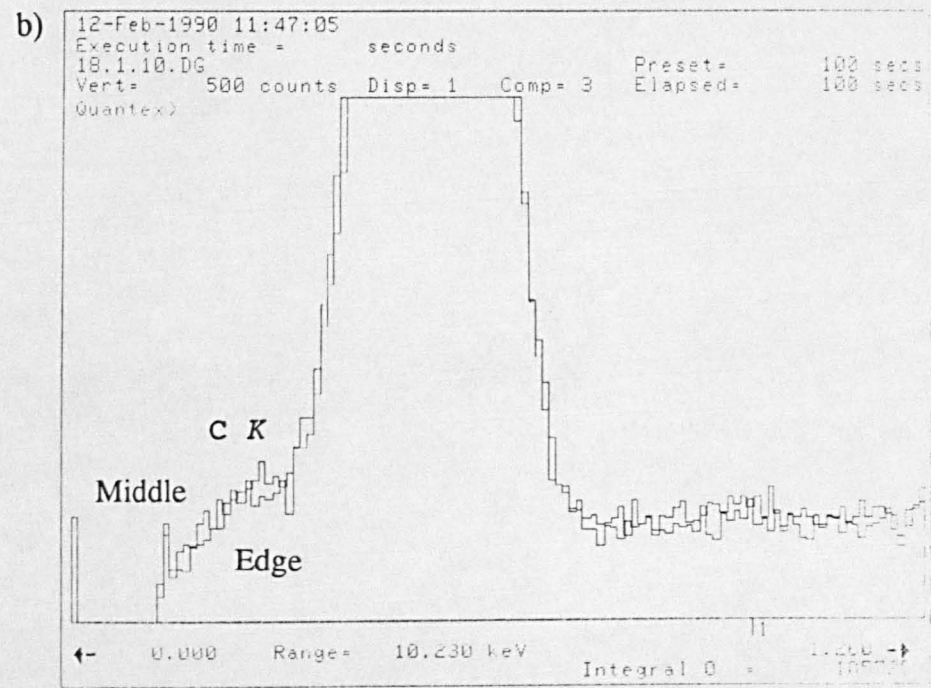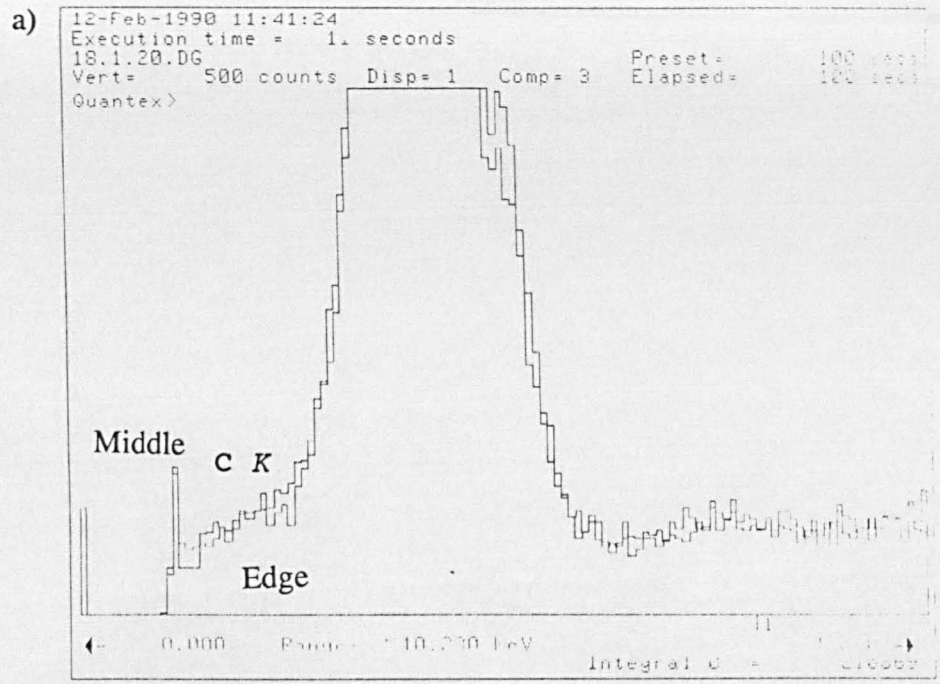
Figure 4.9.2. Comparison of edge and middle EDX spectra for Mn_3O_4: a) 650°C, 20 kV; and b) 650°C, 10 kV.

193

Figure 4.9.3. Comparison of edge and middle EDX spectra for Mn_2O_3: a) 550°C, 20 kV; b) 550°C, 10 kV; c) 650°C, 20 kV; and d) 650°C, 10 kV.

194

a)

b)
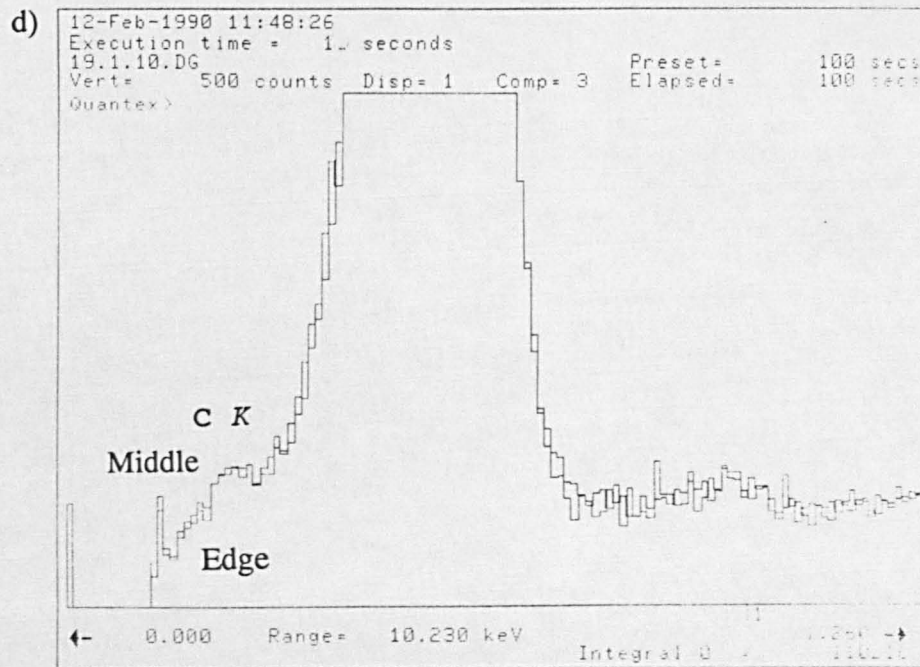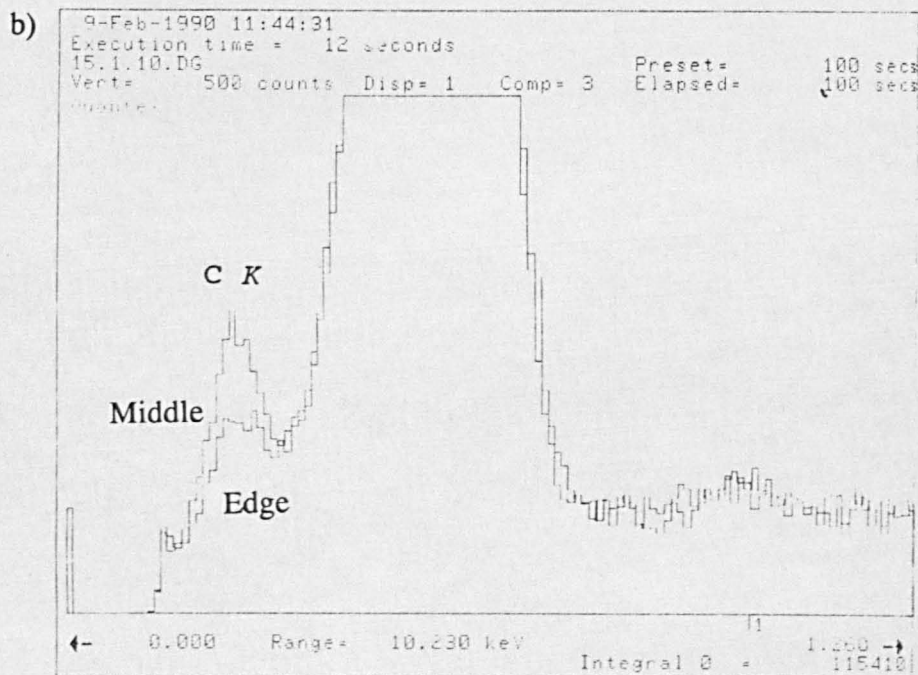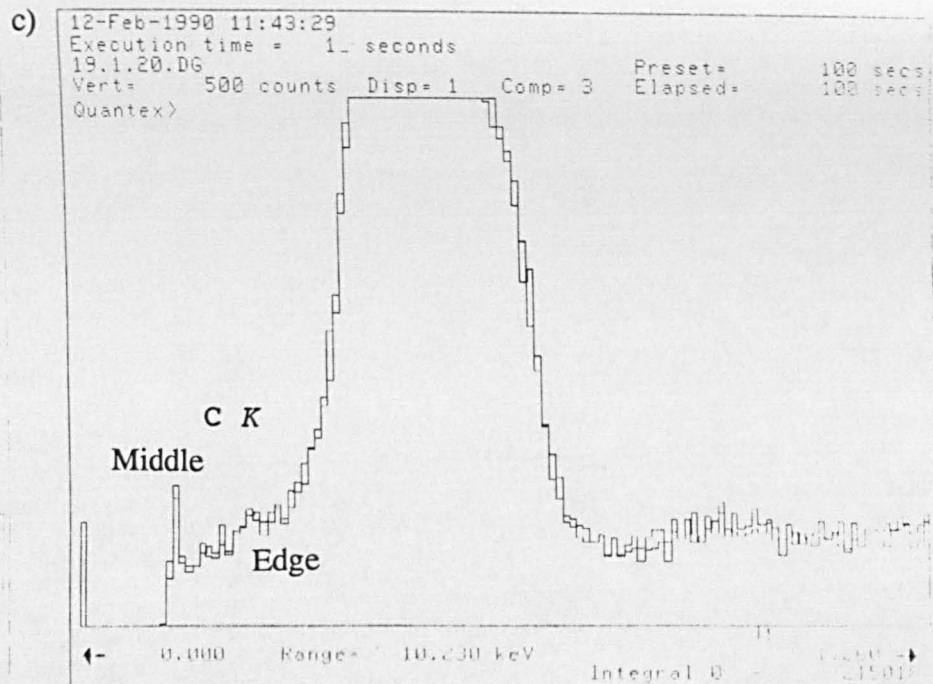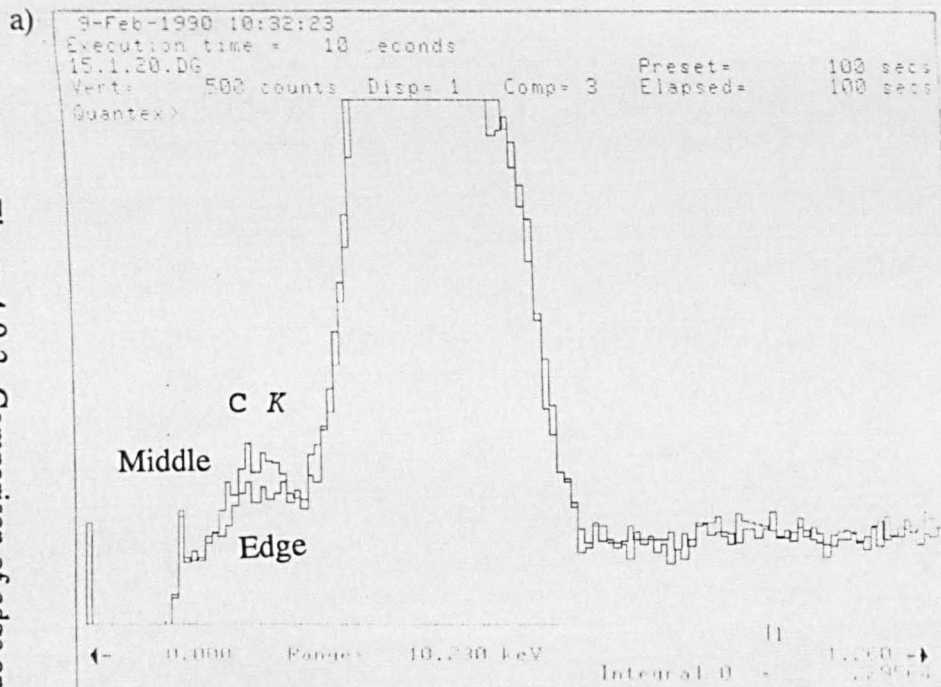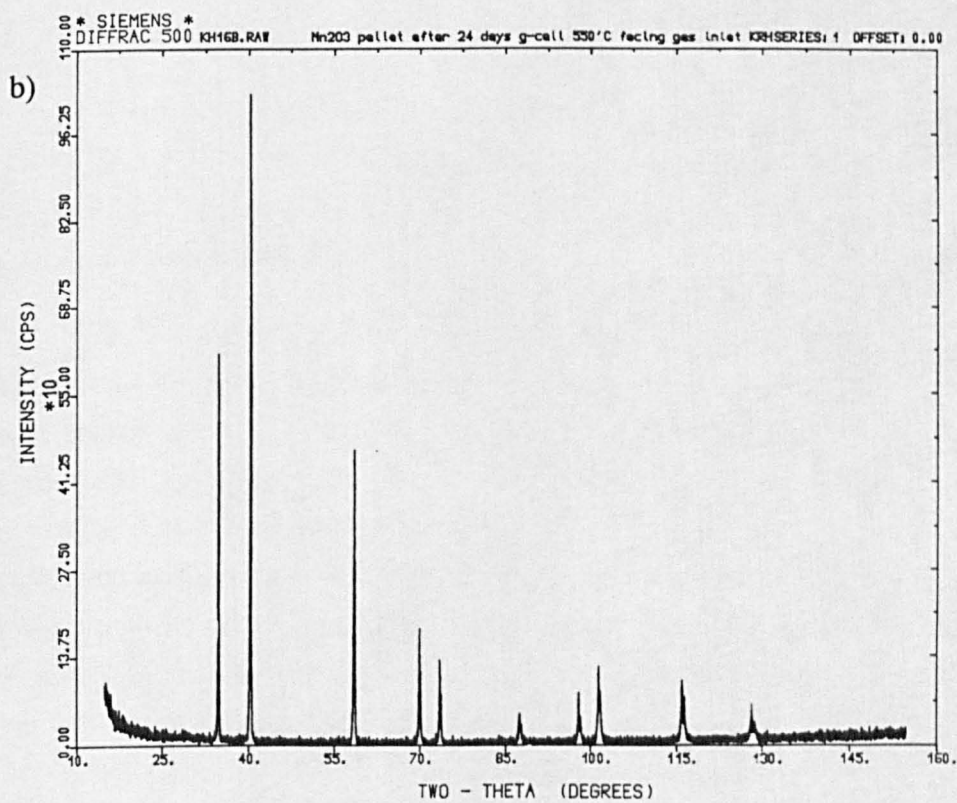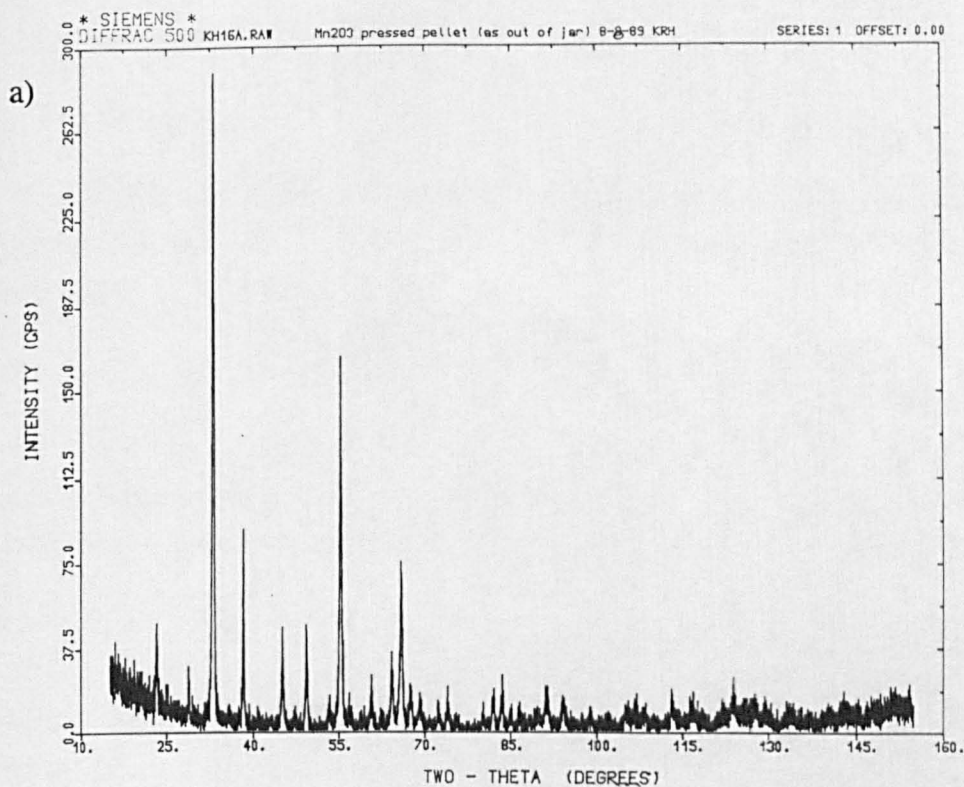
Figure 4.9.4. XRD spectra of an Mn_2O_3 pellet: a) before; and b) after exposure at 550°C.

4.10   Characterisation of Uranium Oxides after Exposure

4.10.1   Introduction

Pellets of the three oxides were mounted in the silica holder, installed into the gamma cell and exposed at temperatures of 550°C and 650°C for 22 days (Table 4.10.1).

4.10.2   Optical Observations

After exposure in the gamma cell at 550°C, the UO_2 pellet was a shiny grey colour and no longer flat but, instead, curved. The α-U_3O_8 became a matt grey in colour, but remained flat. The γ-UO_3 had changed to shiny grey and was a little curved.

The 650°C UO_2 pellet was grey in the middle, but had brown regions at the edges. The α-U_3O_8 pellet was curved and grey in colour. The γ-UO_3 had also become grey.

All of the pellets were brittle and required careful handling. Cracks were present in all the pellets.

4.10.3   Energy Dispersive X-Ray Analysis

The only signs of possible carbon deposition seen in the SEI micrographs recorded of the uranium oxide pellets after exposure were the dividing lines between the edge and middle regions of the pellets. Figure 4.10.1 is an image taken from the U_3O_8 pellet after exposure at 550°C.

EDX spectra were recorded at 10 and 20 kV accelerating voltages using the windowless detector. In addition to the uranium M and oxygen K lines, large carbon K signals were seen off all the samples. Table 4.10.2 summarises the carbon count rates for the oxides and Table 4.10.3 the estimated carbon film thicknesses. Figure 4.10.2 shows the spectrum obtained off UO_2 after exposure at 550°C. The spectrum was recorded from a 3000x magnification area in the central region of the pellet using a 10 kV beam. The lowest energy peak on the left of Figure 4.10.2 is the carbon signal. As explained in Section 3.2.3, the lower the energy of the primary electron beam, the shallower is the depth into the sample from which the analysed x-rays originate. Since the surface of the pellets is relatively rich in carbon compared to the bulk, in all cases the use of a 10 kV electron beam increased the intensity of the C *1s* signal. In contrast to the situation with the manganese oxides, there were no major differences in the carbon intensities recorded from the edges and centres of the exposed uranium oxide pellets. This was surprising in view of the clear distinctions

that could be made between the two regions visually and in secondary electron images. The C K peaks in all spectra were of much greater intensity than from either the spinel oxides or the manganese oxides. The three oxides gave similarly high carbon count rates, but in the descending orders UO_2 > γ-UO_3 > α-U_3O_8, for the 20 kV results, and γ-UO_3 > UO_2 > α-U_3O_8, for the 10 kV ones. The switching in order of the UO_2 and γ-UO_3 with changing primary electron beam energy suggests that carbon may have diffused more into the bulk of the UO_2 samples than into that of the γ-UO_3. γ-UO_3 shows a higher near-surface concentration of carbon, but with less penetration of carbon into the bulk.

4.10.4 X-Ray Diffraction

After exposure in the gamma cell, all the samples (obviously, still in pellet form), from both of the temperatures, gave spectra similar to the 5-550 JCPDS reference spectrum for UO_2, uranium oxide / uraninite. No other peaks were identified in the spectra apart from some calcium carbonate signals derived from the BluTack used to locate the pellets in place on the sample holder. The conditions present in the gamma cell had reduced the α-U_3O_8 and γ-UO_3 samples. This explains the colour change that occurred for the γ-UO_3.

4.10.5 X-Ray Photoelectron Spectroscopy

The U $4f_{7/2}$ peak positions for the six samples are given in Table 4.10.4. The low values obtained are all indicative of reduction of the α-U_3O_8 and γ-UO_3 samples, in agreement with the XRD data. In all cases, the intensity of the uranium signals above the spectrum background was reduced in comparison with the spectra recorded before exposure. As with the manganese oxides, this is indicative of a carpeting layer of carbon being present on the surface of the samples.

Sample	Exposure time /days	
	550°C	650°C
UO_2	22	22
$\alpha\text{-}U_3O_8$	22	22
$\gamma\text{-}UO_3$	22	22

Table 4.10.1. Gamma cell exposure times for the uranium oxides.

Sample	C K peak area /counts.(100 s)$^{-1}$							
	550°C				650°C			
	Middle		Edge		Middle		Edge	
	20 kV	10 kV	20 kV	10 kV	20 kV	10 kV	20 kV	10 kV
UO_2	11914	19336	11027	19167	12249	20291	12492	18946
$\alpha\text{-}U_3O_8$	11295	18386	11407	17753	9206	14961	10233	16266
$\gamma\text{-}UO_3$	11487	19496	11435	18099	11544	21399	11788	19968

Table 4.10.2 EDX carbon counts (counts.(100 s)$^{-1}$) off the exposed uranium oxides.

Sample	Carbon film thickness /nm							
	550°C				650°C			
	Middle		Edge		Middle		Edge	
	20 kV	10 kV	20 kV	10 kV	20 kV	10 kV	20 kV	10 kV
UO_2	389	113	360	112	399	118	407	111
α-U_3O_8	368	107	372	104	300	87	334	95
γ-UO_3	375	114	373	106	376	125	384	116

Table 4.10.3 Carbon film thickness, as determined from EDX carbon counts, on the exposed uranium oxides.

Sample	Binding Energy /eV	
	550°C	650°C
UO_2	378.5	379.2
α-U_3O_8	379.1	379.1
γ-UO_3	378.7	378.6

Table 4.10.4. U $4f_{7/2}$ binding energies for the uranium oxides after exposure.
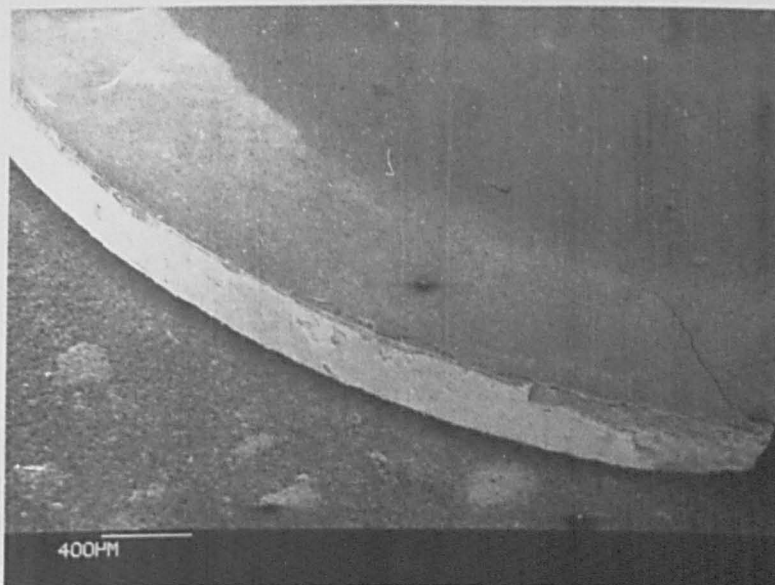
Figure 4.10.1. SEI of U_3O_8 after 22 days at 550°C.

1990 13:08:11
time =   11 seconds
2707 counts   Disp= 1

Preset=   100 secs
Elapsed=   100 secs

Range=   10.230 keV

Integral 0   =
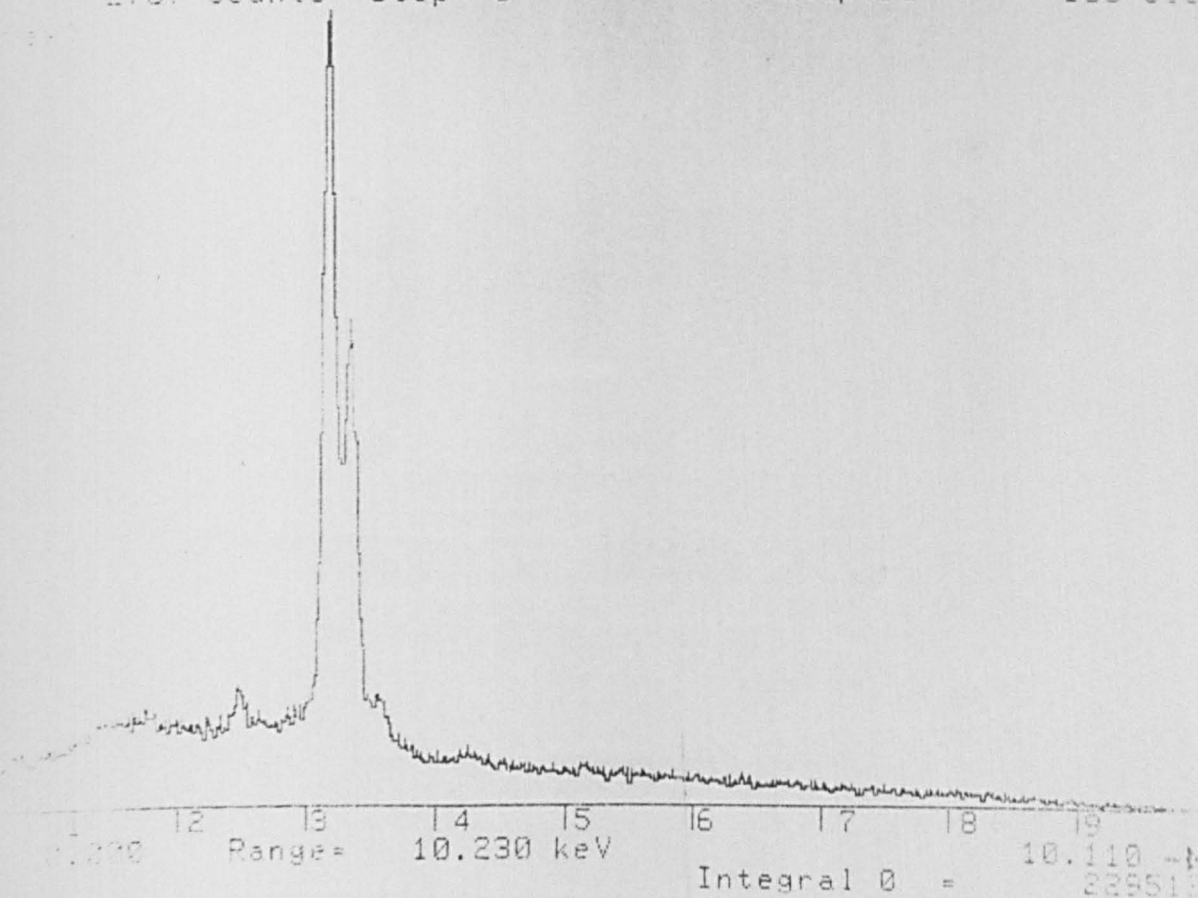
Figure 4.10.2. EDX spectrum of UO_2 after 22 days at 550°C.

200

4.11   Characterisation of Magnetite after Exposure

4.11.1   Introduction

Slices of the single crystal magnetite were prepared as described in Section 4.6. These were placed into the silica holder and exposed in the gamma cell. Table 4.11.1 summarises the samples and conditions used.

4.11.2   Optical Observations

The Fe_3O_4 slices 9.3 ([110], polished and etched for 2½ min in 12 M $HCl_{(aq)}$, exposed at 650°C for 22 days) and 14.3 ([110], polished and etched for 2½ min in 12 M $HCl_{(aq)}$, exposed at 650°C for 22 days) had noticeably darker central regions compared to their edges.

Slice 6.3 ([111], polished, 550°C, 18 + 28 days) showed the exposed and unexposed areas well in secondary electron images. Figure 4.11.1 contains secondary electron images both as acquired and after processing to contain just two grey levels, to enhance the distinction between the two regions.

Figure 4.11.2 shows a region on one [111] slice, that had been etched for 2½ min in 12 M $HCl_{(aq)}$ prior to exposure at 650°C. The smooth patch in the middle of one of the textured regions, towards the centre of the image, was produced by the electron beam during acquisition of an EDX spectrum. Both 10 and 20 kV beams were used, in the spot mode, to acquire 100 s spectra. The texture was present over the whole of the flat areas of the sample before this analysis. It appears that the energy of the beam has caused the material creating the texture to be removed from the surface of the specimen, or to withdraw back from the point of impact of the electron beam. This sample (10.3) didn't produce a prominent carbon peak. Surface texture like this was also found on a [110] slice, similarly prepared and, likewise, exposed at 650°C for 22 days (Figure 4.11.3). No other magnetite samples exhibited such features.

4.11.3   Energy Dispersive X-Ray Analysis

[100] slice 5.3 was examined using the beryllium window EDX analyser after 18 days in the gamma cell at 550°C. Obviously, it was nor possible to directly analyse for carbon and oxygen. However, when the oxygen concentration was calculated by difference, a stoichiometric formula was obtained ($Fe_{3.02}O_{3.98}$) that was closer to that expected than the one calculated prior to exposure ($Fe_{3.31}O_{3.69}$). A similar effect of exposure was seen on the [111] slice, 6.3.

The magnetite slices, when examined using the windowless EDX detector,

usually showed greater carbon signals in the middle compared to the edges, where the silica spacers shielded the surface from the gas mixture. This was particularly apparent when using the more surface specific 10 kV accelerating potential. In contrast, the oxygen count rates were usually greater in spectra recorded at the edges of the samples. This will have been because of the effect of carbon on the central regions acting to absorb oxygen x-rays, reducing the signal intensity.

Because of the difficulty in obtaining flat specimens when using etched magnetite, there was always a choice in the area to analyse for carbon. The results given in Tables 4.11.2 and 4.11.3 relate to analyses taken off areas chosen to be as flat as possible, with respect to the intended orientation of the slice. However, spectra were recorded off different areas of many of the samples. The analyses will have been affected by the orientation of the area selected with respect to the x-ray detector, and on whether or not there was a direct line-of-sight path from the analysis area to the detector. When looking at faces with a ready line-of-sight to the detector the carbon and oxygen signals were enhanced in comparison to spectra recorded off, for instance, inner walls of etch pits or large areas covering a range of surface topography. Figure 4.11.4 compares the spectra recorded from the two locations indicated on the electron micrograph. The low energy signals are much reduced in intensity in the spectrum recorded off the face away from the detector. Because of such topographical influences on the EDX spectra acquired, it is not possible to make any comments on the relative deposition rates of the different samples from the results obtained. The polished samples giving much greater carbon count rates than the etched slices is another indication of the effect of topography on the spectra acquired.

4.11.4   X-Ray Diffraction

After exposure in the gamma cell, magnetite samples yielded spectra with narrower peaks. Figure 4.11.5 illustrates this in the case of a [111] slice, 6.3 (here, looking at the side facing away from the gas inlet). Figure 4.11.6 is the spectrum recorded off the other (facing gas inlet) side of this magnetite slice. The higher order reflections ([444], [555] and [666]) are more intense on the side of the slice that was mounted facing away from the gas inlet. The only difference in the XRD spectrum recorded off the [111] slice 57.7.2 after 23 days exposure in the gamma cell at 550°C, compared to that recorded before exposure, was the absence of Fe_2O_3 peaks, following reduction of haematite to magnetite in the gas conditions used. No peaks other than those due to Fe_3O_4, magnetite, were identified in the XRD spectra.

4.11.5   X-Ray Photoelectron Spectroscopy

All XP spectra recorded after exposure of a sample in the gamma cell showed much reduced Fe $2p_{3/2}$ peak intensities, presumably due to covering of the

sample surfaces with carbon. C *1s* signals show an increase. The gas and temperature conditions present in the gamma cell would be expected to cause magnetite to be the iron oxide produced / retained. Table 4.11.4 lists the Fe $2p_{3/2}$ spectra details obtained off exposed samples, with two peaks being fitted, for the two oxidation states present in magnetite. Where data are given only for the Fe(III) state, the low intensity of the Fe $2p_{3/2}$ peak prevented fitting of more than one contributor to the experimental data. Where no data are given, there was no Fe $2p_{3/2}$ peak visible in the spectra. The peaks, due to their reduced intensity, are all broader than before exposure in the gamma cell and more difficult to accurately fit, but their positions appear to be little changed from before exposure. Figure 4.11.7 compares the wide scan spectra recorded off sample 6.3 before and after exposure for 18 days at 550°C.

There were changes in the C *1s* regional XP spectra on exposure of the samples in the gamma cell. For the polished samples, 5.3 and 6.3, the spectra recorded after exposure contained a C *1s* peak that was narrower than the "before" adventitious carbon signal, and centred at 284.6 eV. These samples both gave high carbon EDX count rates. For most of the other samples, which did not give so high carbon EDX count rates, exposure brought about the appearance of a higher binding energy carbon component. Figure 4.11.8 illustrates this for slices 5.3, 6.3, 9.4 and 10.3.

Sample	Orientation	Treatment (Polishing +)	Temperature /°C	Time /days
1.2.1[a]	[110]	None	550	18 + 28
1.2.2[a]	[110]	None	550	18 + 28
1.3[a]	[110]	None	550	18 + 28
1.4[a]	[110]	None	550	18 + 28
5.2	[100]	None	550	18 + 28
5.3	[100]	None	550	18 + 28
5.4	[100]	None	550	18 + 28
5.5	[100]	None	550	18 + 28
6.3	[111]	None	550	18 + 28
6.4	[111]	None	550	18 + 28
6.5	[111]	None	550	18 + 28
6.6	[111]	None	550	18 + 28
9.1	[100]	2½ min 12 M $HCl_{(aq)}$	550	22
9.2	[100]	5 min 12 M $HCl_{(aq)}$	550	22
9.3	[100]	2½ min 12 M $HCl_{(aq)}$	650	22
9.4	[100]	5 min 12 M $HCl_{(aq)}$	650	22
10.1	[111]	2½ min 12 M $HCl_{(aq)}$	550	22

a) Crystal number 1 contained Fe_2O_3 regions.

Table 4.11.1. Magnetite samples exposed in the gamma cell.

Sample	Orientation	Treatment (Polishing +)	Temperature /°C	Time /days
10.2	[111]	5 min 12 M $HCl_{(aq)}$	550	22
10.3	[111]	2½ min 12 M $HCl_{(aq)}$	650	22
10.4	[111]	5 min 12 M $HCl_{(aq)}$	650	22
14.1	[110]	2½ min 12 M $HCl_{(aq)}$	550	22
14.2	[110]	5 min 12 M $HCl_{(aq)}$	550	22
14.3	[110]	2½ min 12 M $HCl_{(aq)}$	650	22
14.4	[110]	5 min 12 M $HCl_{(aq)}$	650	22
15.2	[110]	Unpolished	650	24
15.3	[110]	Unpolished	550	24
15.4.2	[110]	Unpolished	550	24
15.5	[110]	Unpolished	650	24
57.2	[111]	Unpolished	550	23
57.5	[111]	Unpolished	650	23
57.7.2	[111]	Unpolished	550	23
57.8	[111]	Unpolished	650	23

Table 4.11.1 (continued). Magnetite samples exposed in the gamma cell.

Sample	C K peak area /counts.$(100 \text{ s})^{-1}$							
	550°C				650°C			
	Middle		Edge		Middle		Edge	
	20 kV	10 kV	20 kV	10 kV	20 kV	10 kV	20 kV	10 kV
1.2.1 [110][a]	-----	-----	-----	-----	-----	-----	-----	-----
1.2.2 [110][a]	4102	32255	1745	19671	-----	-----	-----	-----
1.3 [110][a]	4683	30530	3347	11158	-----	-----	-----	-----
1.4 [110][a]	-----	-----	-----	-----	-----	-----	-----	-----
5.2 [100]	-----	-----	-----	-----	-----	-----	-----	-----
5.3 [100]	4233	33424	261	1125	-----	-----	-----	-----
5.4 [100]	6058	28380	921	2505	-----	-----	-----	-----
5.5 [100]	-----	-----	-----	-----	-----	-----	-----	-----
6.3 [111]	-----	-----	-----	-----	-----	-----	-----	-----
6.4 [111]	5025	33821	452	306	-----	-----	-----	-----
6.5 [111]	6273	25643	403	1970	-----	-----	-----	-----
6.6 [111]	-----	-----	-----	-----	-----	-----	-----	-----
9.1 [100]	3079	5564	-----	-----	-----	-----	-----	-----
9.2 [100]	225	262	-----	-----	-----	-----	-----	-----
9.3 [100]	-----	-----	-----	-----	1542	2199	2520	5604
9.4 [100]	-----	-----	-----	-----	1755	3280	-----	-----

a) Crystal number 1 contained Fe_2O_3 regions.

Table 4.11.2. EDX carbon counts (counts.$(100 \text{ s})^{-1}$) off the exposed magnetite slices.

Sample	C K peak area /counts.(100 s)$^{-1}$							
	550°C				650°C			
	Middle		Edge		Middle		Edge	
	20 kV	10 kV	20 kV	10 kV	20 kV	10 kV	20 kV	10 kV
10.1 [111]	-----	-----	-----	-----	-----	-----	-----	-----
10.2 [111]	3987	5888	-----	-----	-----	-----	-----	-----
10.3 [111]	-----	-----	-----	-----	1955	4175	-----	-----
10.4 [111]	-----	-----	-----	-----	1550	2613	-----	-----
14.1 [110]	2214	5238	-----	-----	-----	-----	-----	-----
14.2 [110]	510	4036	-----	-----	-----	-----	-----	-----
14.3 [110]	-----	-----	-----	-----	4191	8675	-----	-----
14.4 [110]	-----	-----	-----	-----	1771	2990	-----	-----
15.2 [110]	-----	-----	-----	-----	1624	2364	-----	-----
15.3 [110]	3650	6468	-----	-----	-----	-----	-----	-----
15.4.2 [110]	-----	-----	-----	-----	-----	-----	-----	-----
15.5 [110]	-----	-----	-----	-----	-----	-----	-----	-----
57.2 [111]	-----	-----	-----	-----	-----	-----	-----	-----
57.5 [111]	-----	-----	-----	-----	-----	-----	-----	-----
57.7.2 [111]	2513	2923	-----	-----	-----	-----	-----	-----
57.8 [111]	-----	-----	-----	-----	5382	7275	-----	-----

Table 4.11.2 (continued). EDX carbon counts (counts.(100 s)$^{-1}$) off the exposed magnetite slices.

Sample	Carbon film thickness /nm							
	550°C				650°C			
	Middle		Edge		Middle		Edge	
	20 kV	10 kV	20 kV	10 kV	20 kV	10 kV	20 kV	10 kV
1.2.1 [110][a)	-----	-----	-----	-----	-----	-----	-----	-----
1.2.2 [110][a)	134	188	57	115	-----	-----	-----	-----
1.3 [110][a)	153	178	109	65	-----	-----	-----	-----
1.4 [110][a)	-----	-----	-----	-----	-----	-----	-----	-----
5.2 [100]	-----	-----	-----	-----	-----	-----	-----	-----
5.3 [100]	138	195	9	7	-----	-----	-----	-----
5.4 [100]	198	166	30	15	-----	-----	-----	-----
5.5 [100]	-----	-----	-----	-----	-----	-----	-----	-----
6.3 [111]	-----	-----	-----	-----	-----	-----	-----	-----
6.4 [111]	164	197	15	2	-----	-----	-----	-----
6.5 [111]	205	150	13	11	-----	-----	-----	-----
6.6 [111]	-----	-----	-----	-----	-----	-----	-----	-----
9.1 [100]	101	32	-----	-----	-----	-----	-----	-----
9.2 [100]	7	2	-----	-----	-----	-----	-----	-----
9.3 [100]	-----	-----	-----	-----	50	13	82	33
9.4 [100]	-----	-----	-----	-----	57	19	-----	-----

a) Crystal number 1 contained Fe_2O_3 regions.

Table 4.11.3. Carbon film thickness, as determined from EDX carbon counts, on the exposed magnetite slices.

Sample	550°C Middle 20 kV	550°C Middle 10 kV	550°C Edge 20 kV	550°C Edge 10 kV	650°C Middle 20 kV	650°C Middle 10 kV	650°C Edge 20 kV	650°C Edge 10 kV
10.1 [111]	-----	-----	-----	-----	-----	-----	-----	-----
10.2 [111]	130	34	-----	-----	-----	-----	-----	-----
10.3 [111]	-----	-----	-----	-----	64	24	-----	-----
10.4 [111]	-----	-----	-----	-----	51	15	-----	-----
14.1 [110]	72	31	-----	-----	-----	-----	-----	-----
14.2 [110]	17	24	-----	-----	-----	-----	-----	-----
14.3 [110]	-----	-----	-----	-----	137	51	-----	-----
14.4 [110]	-----	-----	-----	-----	58	17.4	-----	-----
15.2 [110]	-----	-----	-----	-----	53	14	-----	-----
15.3 [110]	119	38	-----	-----	-----	-----	-----	-----
15.4.2 [110]	-----	-----	-----	-----	-----	-----	-----	-----
15.5 [110]	-----	-----	-----	-----	-----	-----	-----	-----
57.2 [111]	-----	-----	-----	-----	-----	-----	-----	-----
57.5 [111]	-----	-----	-----	-----	-----	-----	-----	-----
57.7.2 [111]	82	17	-----	-----	-----	-----	-----	-----
57.8 [111]	-----	-----	-----	-----	176	42	-----	-----

Table 4.11.3 (continued). Carbon film thickness, as determined from EDX carbon counts, on the exposed magnetite slices.

	Binding energy /eV		FWHM /eV		Area ratio Fe(II) : Fe(III)
Sample	Fe(II) $2p_{3/2}$	Fe(III) $2p_{3/2}$	Fe(II) $2p_{3/2}$	Fe(III) $2p_{3/2}$	
5.3 [100]	709.5	711.3	4.4	4.5	1:1.46
6.3 [111]	709.7	711.6	3.8	4.4	1:1.30
9.1 [100]	-----	-----	-----	-----	-----
9.2 [100]	-----	-----	-----	-----	-----
9.3 [100]	709.9	711.6	4.1	5.0	2.24
9.4 [100]	-----	710.1	-----	5.1	-----
10.1 [111]	-----	-----	-----	-----	-----
10.2 [111]	-----	-----	-----	-----	-----
10.3 [111]	-----	712.0	-----	5.1	-----
10.4 [111]	-----	711.6	-----	6.2	-----
14.1 [110]	-----	-----	-----	-----	-----
14.2 [110]	-----	-----	-----	-----	-----
14.3 [110]	-----	711.0	-----	5.0	-----
14.4 [110]	-----	711.7	-----	5.8	-----
15.2 [110]	-----	711.5	-----	5.1	-----
15.3 [110]	-----	-----	-----	-----	-----
57.7.2 [111]	-----	-----	-----	-----	-----
57.8 [111]	-----	-----	-----	-----	-----

Table 4.11.4. Fe $2p_{3/2}$ XPS binding energy values obtained off Fe_3O_4 slices after gamma cell exposure.
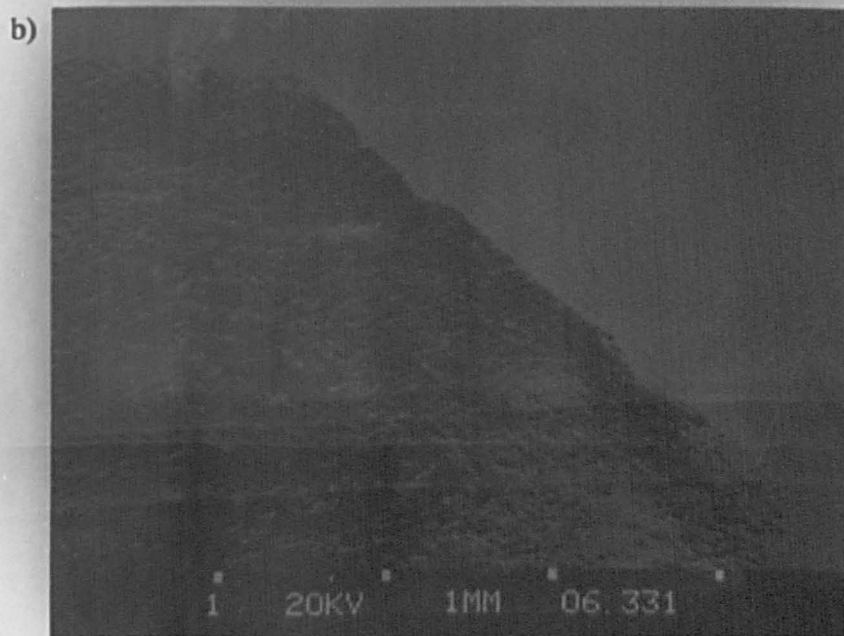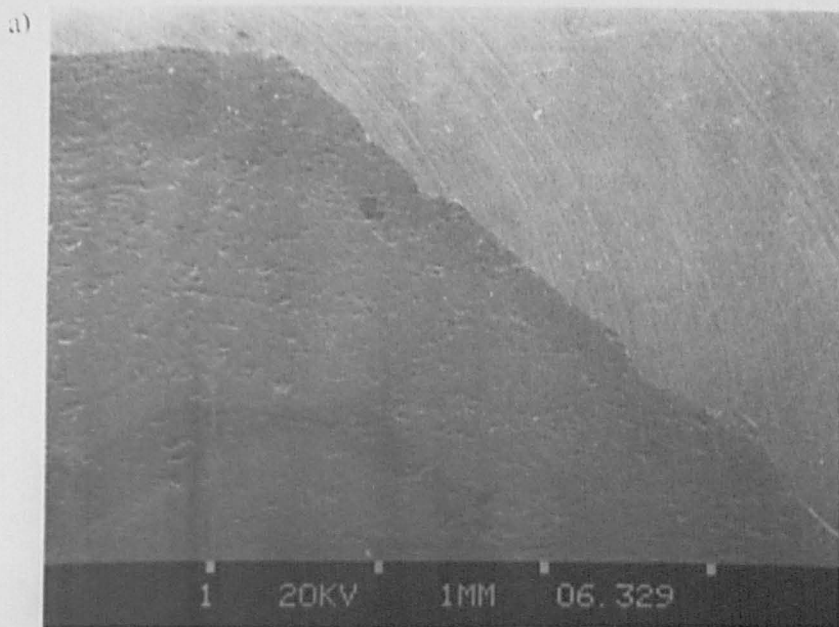
Figure 4.11.1. SEI of [111] magnetite slice 6.3 after 46 days at 550°C: a) as
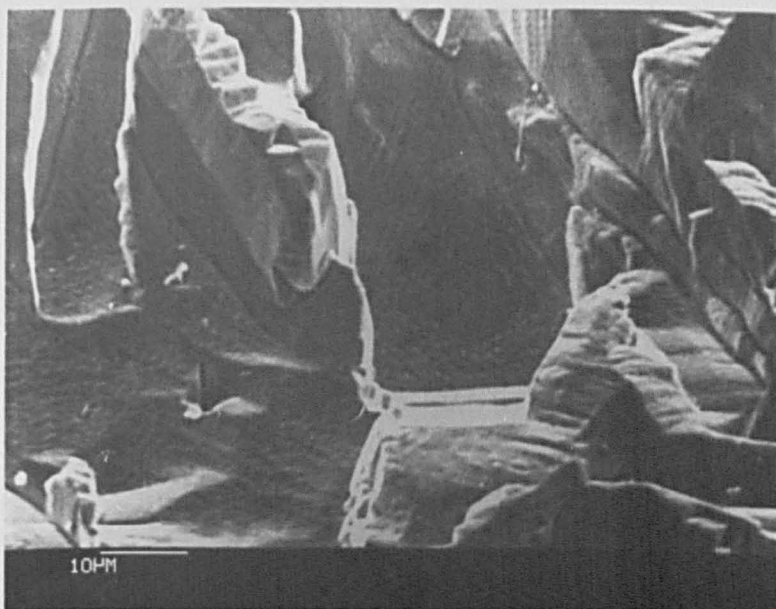acquired; and b) processed to two grey levels.

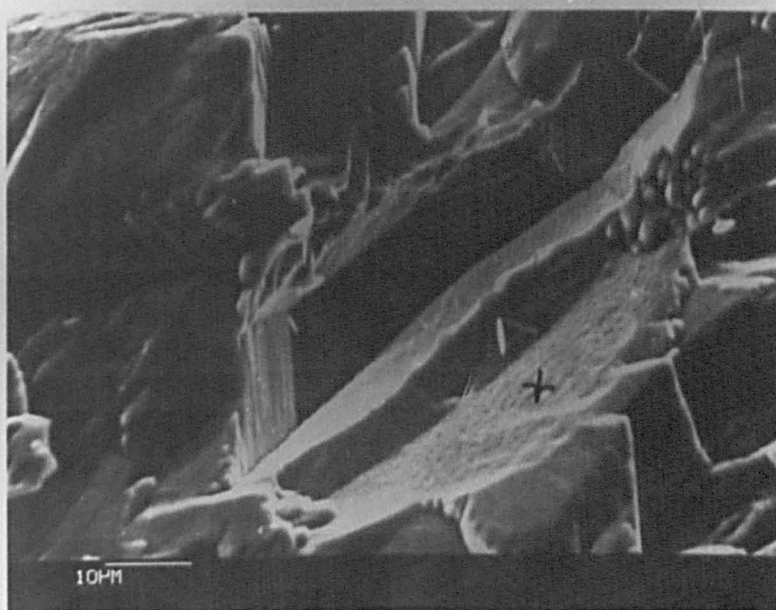Figure 4.11.2. SEI of [111] magnetite slice (2½ min 12 M HCl$_{(aq)}$) 10.3 after 22 days at 650°C.

Figure 4.11.3. SEI of [110] magnetite slice (2½ min 12 M HCl$_{(aq)}$) 14.3 after 22 days at 650°C.

212
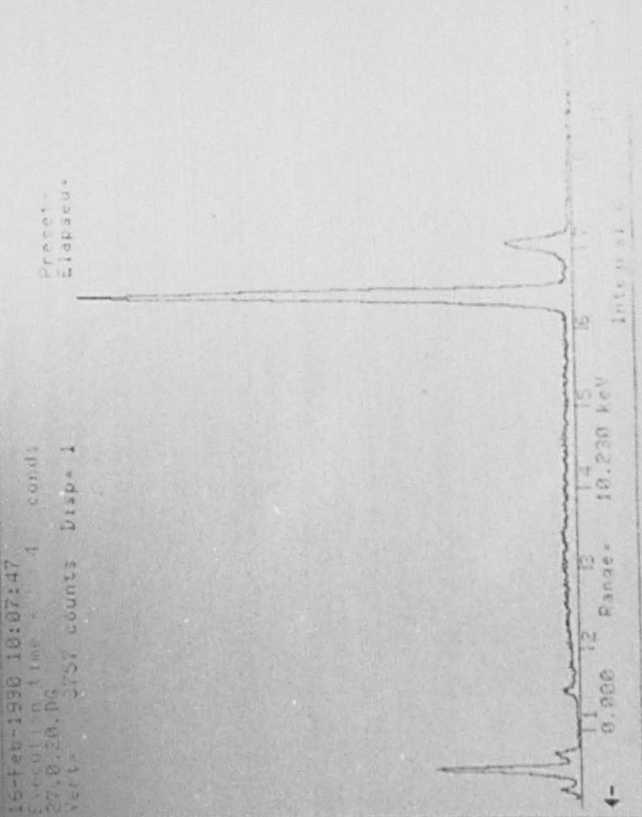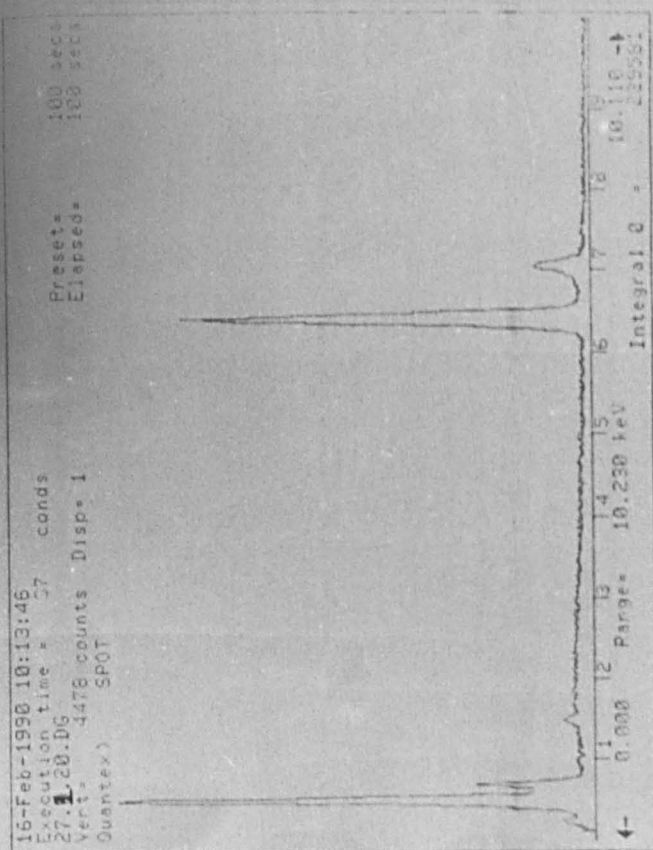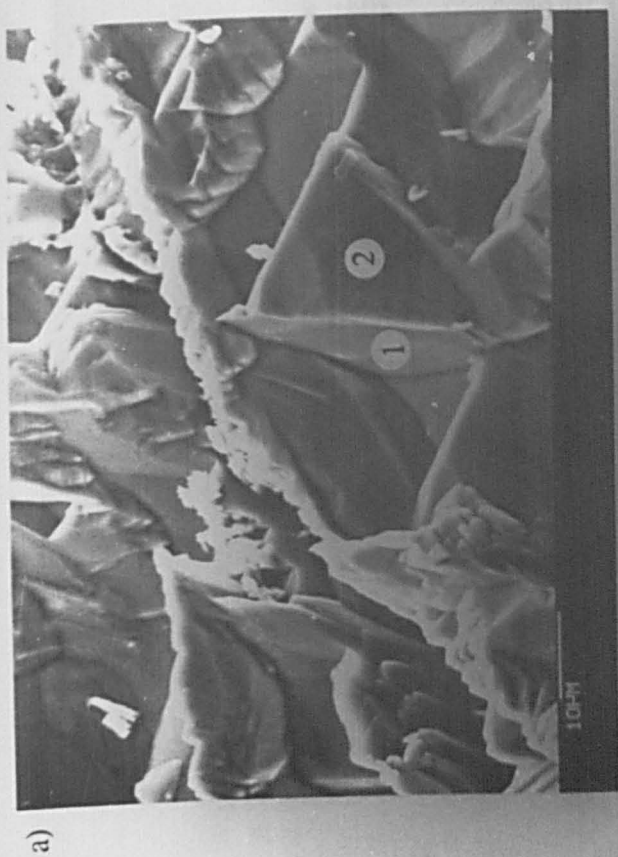
Figure 4.11.4. EDX spectra and SEI of [111] magnetite slice (2½ min 12 M HCl$_{(aq)}$) 10.1 after 22 days at 550°C: a) SEI; b) EDX spectrum from point 1; and c) EDX spectrum from point 2.

213

a)

```
375.00  * SIEMENS *
        DIFFRAC 500 KH1A.RAW    Fe3O4 MAGNETITE 6.3a POLISHED              SERIES: 1  OFFSET: 0.00
```

b)

```
599.00  * SIEMENS *
        DIFFRAC 500 KH4C.RAW    Fe3O4 magnetite 6.3a after 3 weeks in g-cell 28-9-88 KRH   SERIES: 1  OFFSET: 0.00
```

Figure 4.11.5. XRD spectra of [111] magnetite slice 6.3: a) before; and b) after 18 days at 650°C.

214
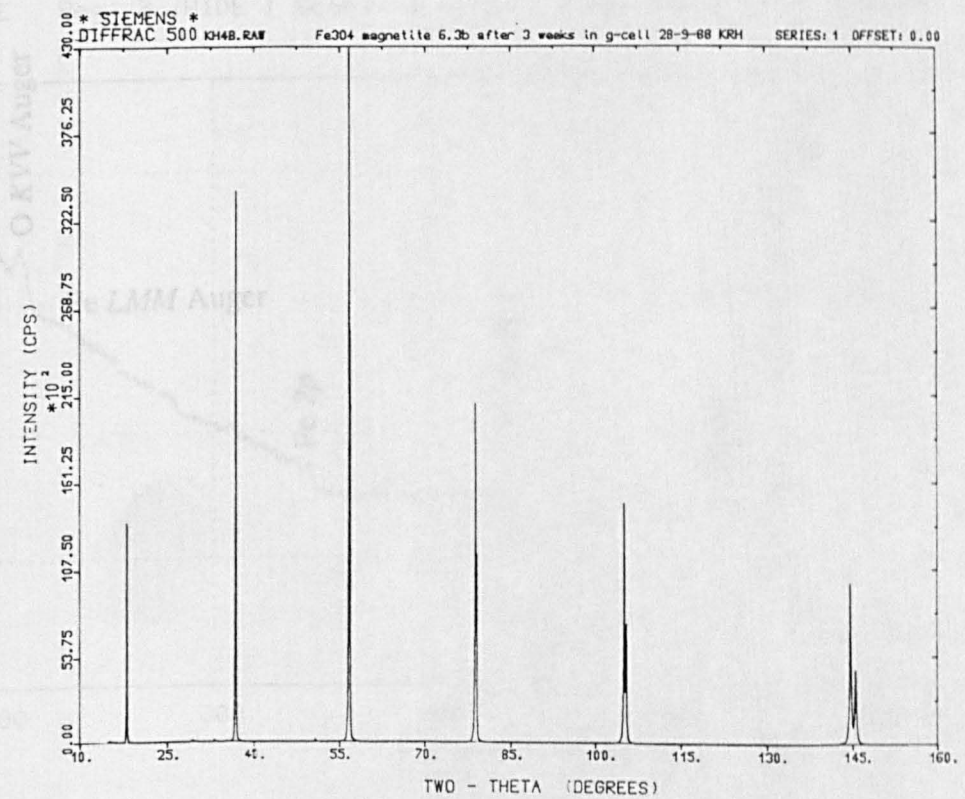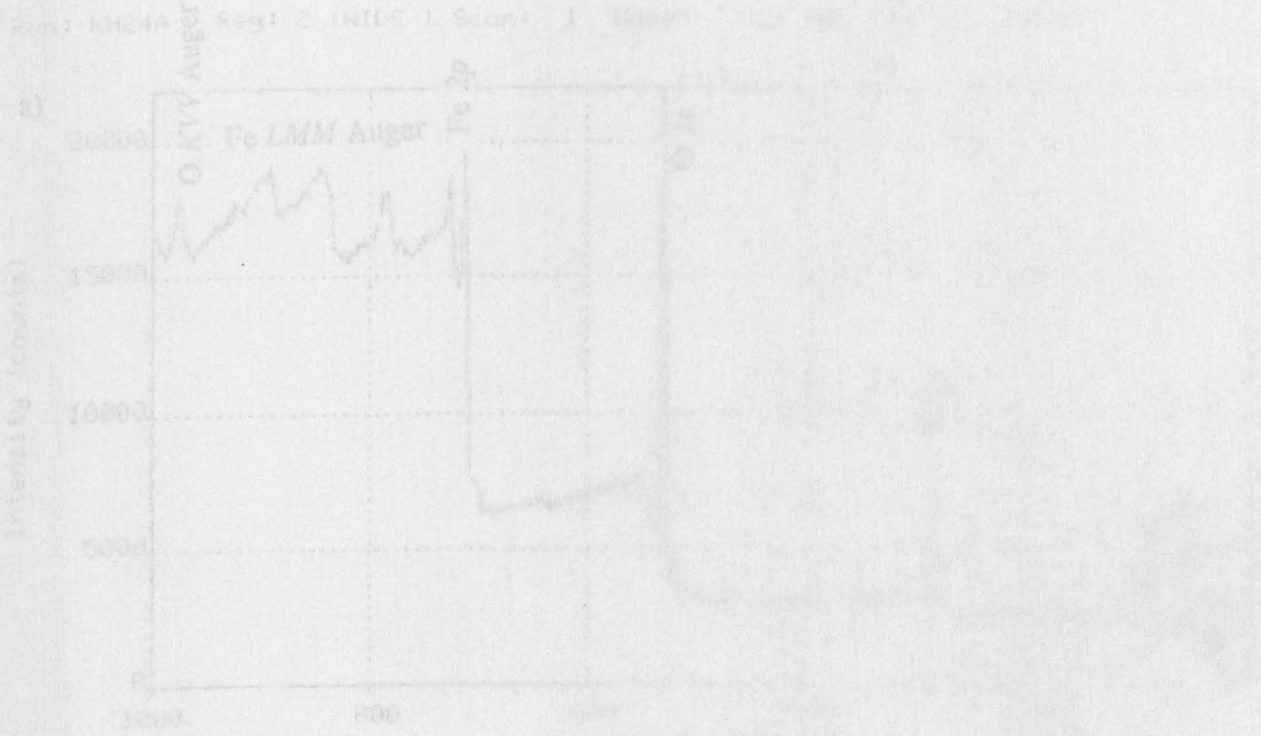
Figure 4.11.6. XRD spectrum of [111] magnetite slice 6.3 after 18 days at 650°C, side facing gas inlet.

215

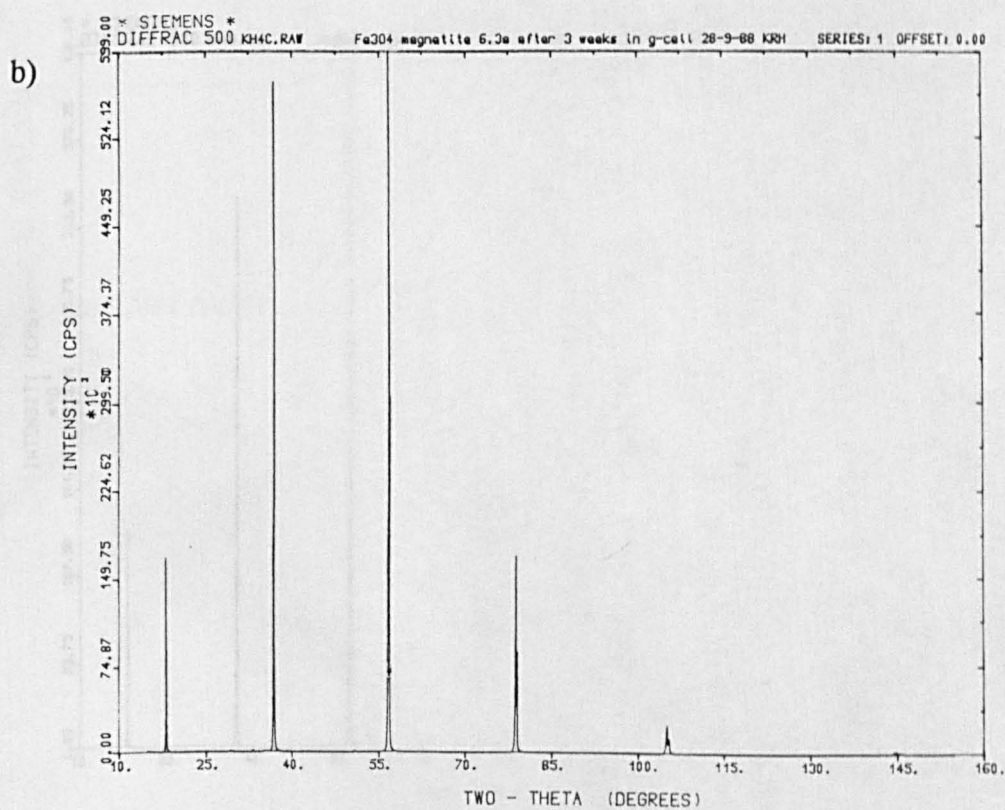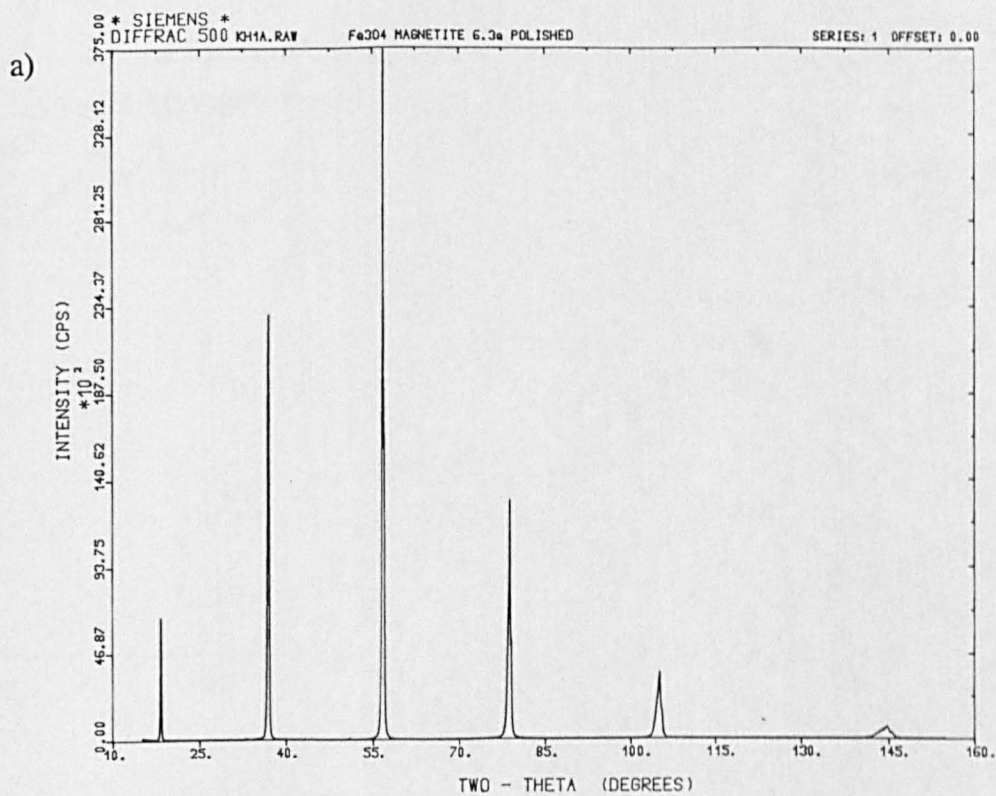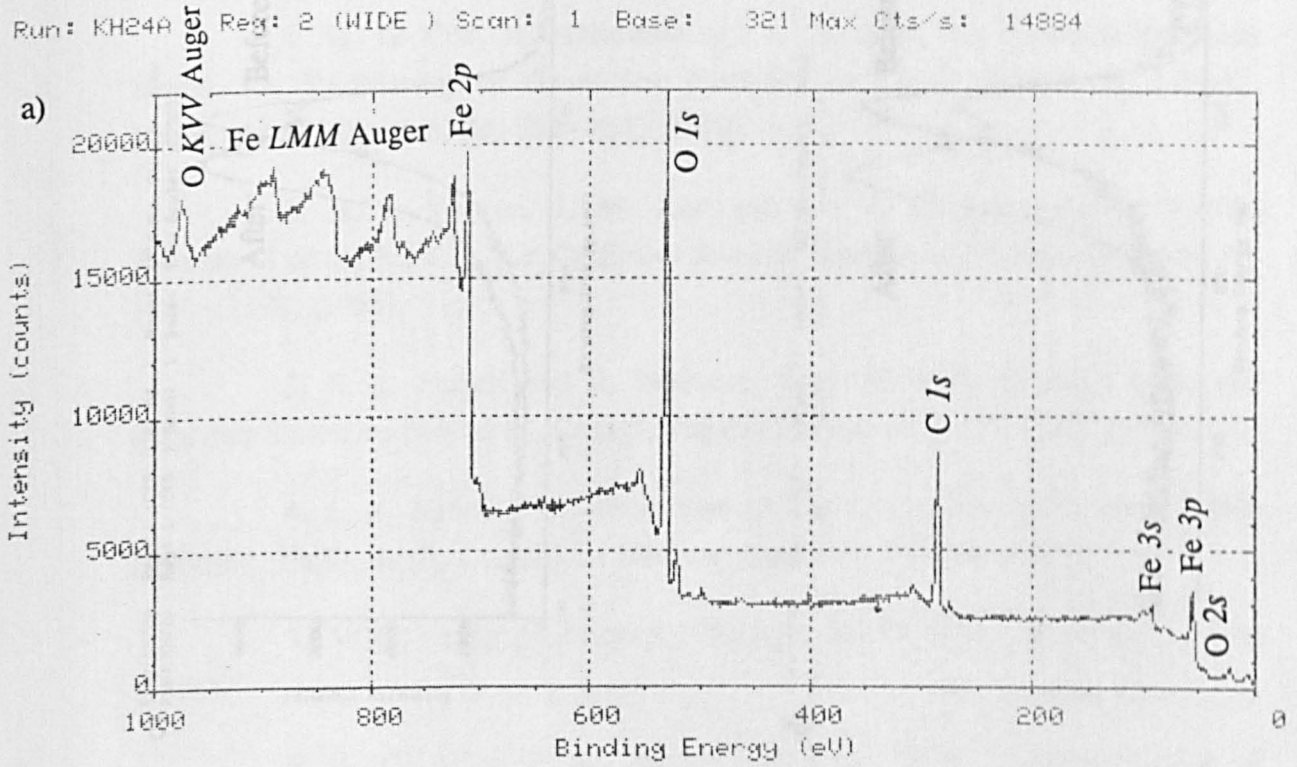Figure 4.11.7. XP spectra of [111] magnetite slice 6.3: a) before; and b) after 18 days at 650°C.

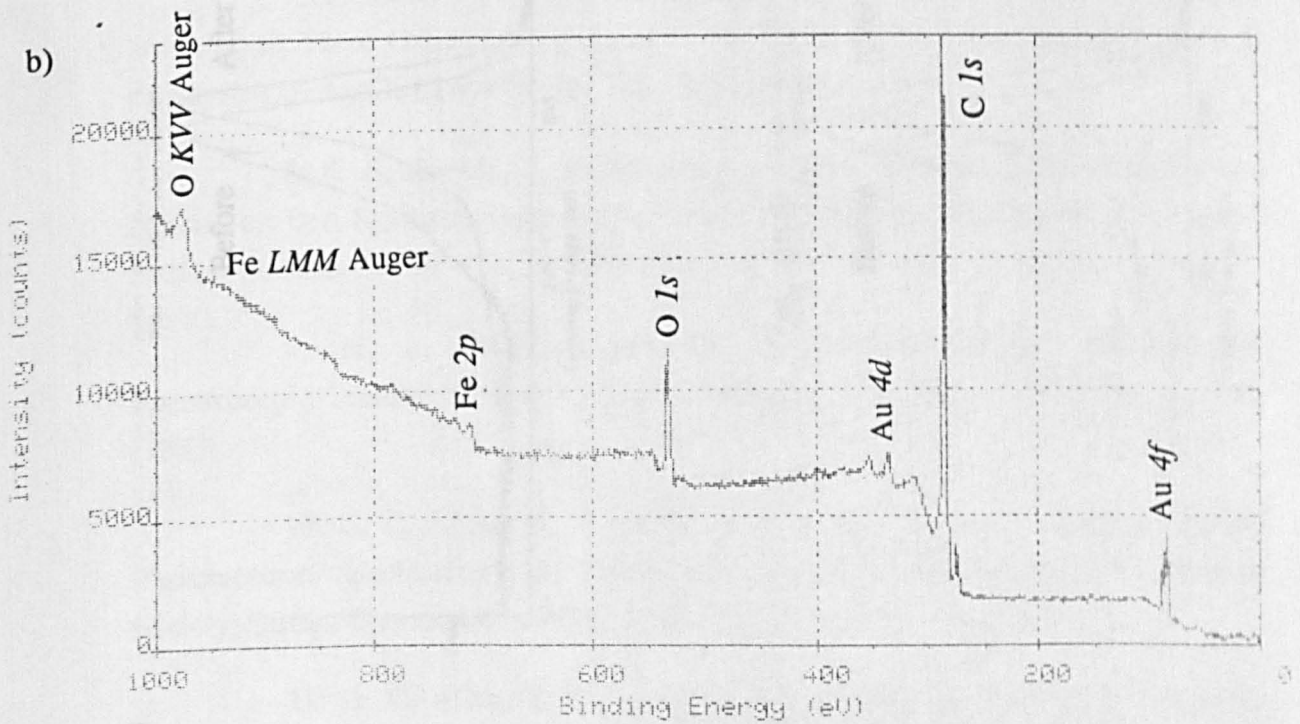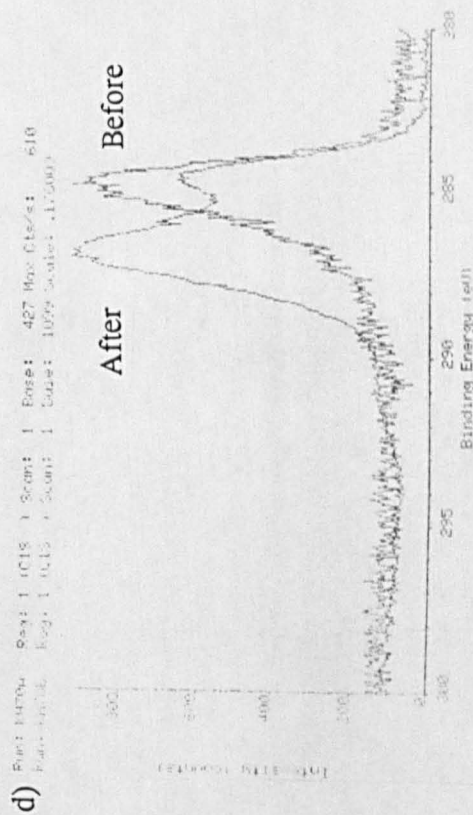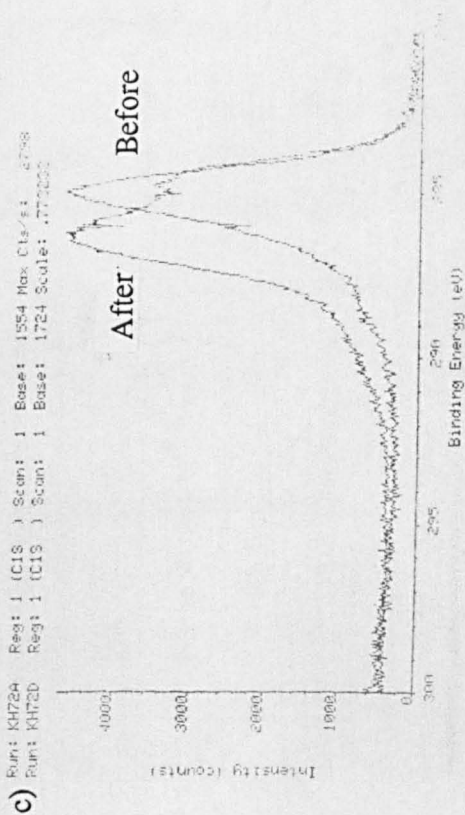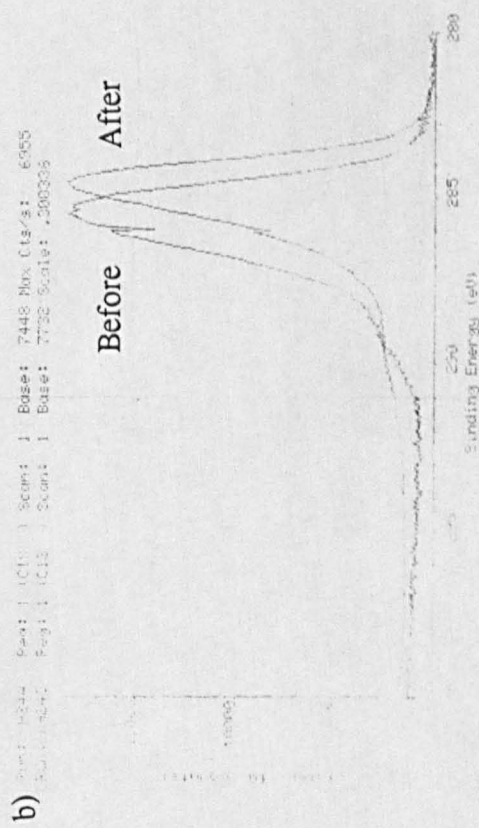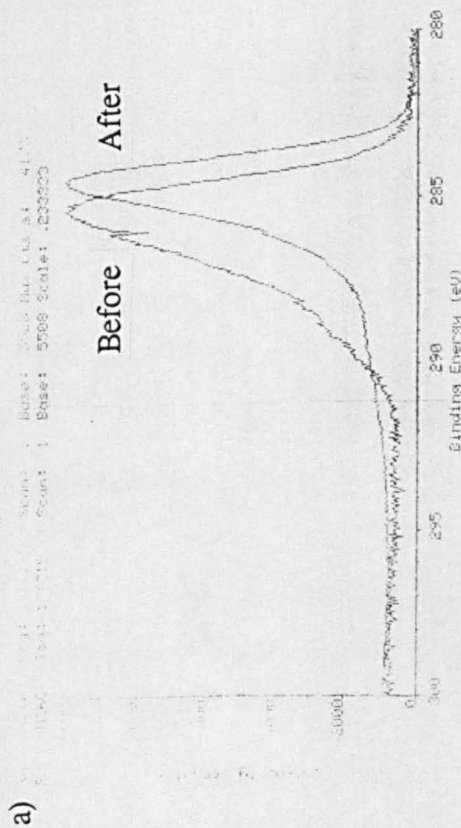Figure 4.11.8. C *1s* XP spectra before and after gamma cell exposure: a) sample 5.3; b) sample 6.3; c) sample 9.4; and d) sample 10.3.

4.12   References

1. M. G. Cox, B. McEnaney and V. D. Scott, "A Chemical Diffusion Model for Partitioning of Transition Elements in Oxide Scales on Alloys", Philosophical Magazine, *26*, 839 - 851, (1972).

2. H. J. Yearian, J. M. Kortright and R. H. Langenheim, "Lattice Parameters of the $FeFe_{(2-x)}Cr_xO_4$ Spinel System", Journal of Chemical Physics, *22*, 1196 - 1198, (1954).

3. S. J. Pickart and R. Nathans, "Neutron Study of the Crystal and Magnetic Structures of $MnFe_{2-t}Cr_tO_4$", Physics Review, *116*, 317 - 322, (1959).

4. J. A. Jutson, "The Deposition of Carbon on Transition Metal Oxide Surfaces", Ph.D. thesis, Council for National Academic Awards, (1989).

5. VCH Verlagsgesellschaft, "Periodic Table of the Elements", chart, (1986).

6. G. C. Allen, P. M. Tucker and R. K. Wild, "Characterisation of Iron/Oxygen Surface Reactions by X-Ray Photoelectron Spectroscopy", Philosophical Magazine B, *46*, 411 - 421, (1982).

7. P. Mills and J. L. Sullivan, "A Study of the Core Level Electrons in Iron and its Three Oxides by Means of X-Ray Photoelectron Spectroscopy", Journal of Physics D: Applied Physics, *16*, 723 - 732, (1983).

8. C. S. Kuivila, J. B. Butt and P. C. Stair, "Characterisation of Surface Species on Iron Synthesis Catalysts by X-Ray Photoelectron Spectroscopy", Applied Surface Science, *32*, 99 - 121, (1988).

9. N. S. McIntyre and D. G. Zetaruk, "X-Ray Photoelectron Spectroscopic Studies of Iron Oxides", Analytical Chemistry, *49*, 1521 - 1529, (1977).

10. G. C. Allen, M. T. Curtis, A. J. Hooper and P. M. Tucker, "X-Ray Photoelectron Spectroscopy of Iron-Oxygen Systems", Journal of the Chemical Society, Dalton Transactions, 1525 - 1530, (1974).

11. G. C. Allen, S. J. Harris, J. Jutson and J. M. Dyke, "A Study of a Number of Mixed Transition Metal Oxide Spinels Using X-Ray Photoelectron Spectroscopy", Applied Surface Science, *37*, 111 - 134, (1989).

12. M. Paul, "Spectroscopic Studies of the Oxidation of Pyrite and the

Composition of Spinel-Type Oxides", M.Sc thesis, University of Bristol, (1989).

13. K. Patel, "Determination of the Fe^{2+} Content of Spinels by Oxidative Titrimetry, Characterisation of Lanthanum Sulphides, Characterisation of Spinels", University of Bath / Central Electricity Generating Board industrial training report, (1988).

14. N. S. McIntyre and M. G. Cook, "X-Ray Photoelectron Studies on Some Oxides and Hydroxides of Cobalt, Nickel, and Copper", Analytical Chemistry, *47*, 2208 - 2213, (1975).

15. C. D. Wagner, W. M. Riggs, L. E. Davis, J. F. Moulder and G. E. Muilenberg (Editor), "Handbook of X-Ray Photoelectron Spectroscopy: A Reference Book of Standard Data for use in X-Ray Photoelectron Spectroscopy", Perkin Elmer Corporation, (1979).

16. N. G. Parr and H. J. Griesser, "XPS Excitation Dependence of Measured Cobalt $2p_{3/2}$ Peak Intensity due to Auger Peak Interference" Journal of Electron Spectroscopy and Related Phenomena, *49*, 293 - 302, (1989).

17. G. V. Samsonov, "The Oxide Handbook", IFI / Plenum, (1973).

18. J. S. Smart and S. Greenwald, "Crystal Structure Transitions in Antiferromagnetic Compounds at the Curie Temperature", Physical Review, *82*, 113 - 115, (1951).

19. D. M. Adams, "Inorganic Solids - An Introduction to Concepts in Solid-State Structural Chemistry", John Wiley and Sons, (1974).

20. A. F. Wells, "Structural Inorganic Chemistry, 5th. Edition", Clarendon Press, (1984).

21. J. S. Foord, R. B. Jackman and G. C. Allen, "An X-Ray Photoelectron Spectroscopic Investigation of the Oxidation of Manganese", Philosophical Magazine A, *49*, 657 - 663, (1984).

22. N. R. Holmes, "The Characterisation of Uranium Oxide Surfaces", Council for National Academic Awards Ph.D. thesis, (1988).

23. G. C. Allen and N. R. Holmes, "X-Ray Photoelectron Spectroscopy of the Uranium / Oxygen System Part XII - Surface Characterisation of α-UO_3, β-UO_3, γ-UO_3 and δ-UO_3", Central Electricity Generating Board report TPRD/B/0875/R86, (1986).

24. T. R. Griffiths, H. V.St.A. Hubbard, G. C. Allen and P. A. Tempest, "A New Method for the Determination of x in UO_{2+x}: Optical Absorption Spectroscopy Measurements", Journal of Nuclear Materials, *151*, 307 - 312, (1988).

25. D. W. Shoesmith, T. E. Rummery, W. Lee and D. G. Owen, "Dissolution of Oxide Films on Iron in Aqueous Solutions Containing Complexing Anions I - Magnetite in Citrate and Ethylenediaminetetraacetate", Power Industry Research, *1*, 43 - 63, (1981).

26. D. W. Shoesmith, D. S. Mancey, D. C. Doern and M. G. Bailey, "Characterisation and Dissolution of Deposited Magnetite Films on AISI 304 Stainless Steel Surfaces in EDTA and EDTA / Oxalate Solutions", Corrosion Science, *45*, 149 - 159, (1989).

27. E. Baumgartner, M. A. Blesa, H. A. Marinovich and A. J. G. Maroto, "Heterogeneous Electron Transfer as a Pathway in the Dissolution of Magnetite in Oxalic Acid Solutions", Inorganic Chemistry, *22*, 2224 - 2226, (1983).

28. G. C. Allen, R. M. Sellers and P. M. Tucker, "Surface Composition and Morphology of Magnetite Crystals During Dissolution", Philosophical Magazine B, *48*, L4 - L9, (1983).

29. G. C. Allen, C. Kirby and R. M. Sellers, "The Effect of the Low-Oxidation-State Metal Ion Reagent Tris-picolinatovanadium(II) Formate on the Surface Morphology and Composition of Crystalline Iron Oxides", Journal of the Chemical Society, Faraday Transactions I, *84*, 355 - 364, (1988).

30. C. S. Hurlbut, Jr., "Dana's Manual of Mineralogy, 18th. Edition", John Wiley and Sons.

31. R. Bauminger, S. G. Cohen, A. Marinov, S. Ofer and E. Segal, "Study of the Low-Temperature Transition in Magnetite and the Internal Fields Acting on Iron Nuclei in Some Spinel Ferrites, Using Mössbauer Absorption", Physical Review, *122*, 1447 - 1450, (1961).

32. K. Hirokawa and M. Oku, "Application of ESCA to Semi-Quantitative Surface and State Analysis of Iron Oxides", Talanta, *26*, 855 - 859, (1979).

33. K. Asami, K. Hashimoto and S. Shimodaira, "X-Ray Photoelectron Spectrum of Fe^{2+} State in Iron Oxides", Corrosion Science, *16*, 35 - 45, (1976).

34. C. R. Brundle, T. J. Chuang and K. Wandelt, "Core and Valence Level Photoemission Studies of Iron Oxide Surfaces and the Oxidation of Iron", Surface Science, *68*, 459 - 468, (1977).

35. K. Wandelt, "Photoemission Studies of Adsorbed Oxygen and Oxide Layers", Surface Science Reports, *2*, 1 - 121, (1982).

5   DISCUSSION

5.1   Spinels

The carefully prepared spinels proved to be the stable oxides produced in the CO_2 or CO_2 / 2% CO gas passing through the preparation furnaces. They were also, in the main, stable in the gamma cell reaction gas mixture. The $Ni_xCo_{1-x}Fe_2O_4$ spinels, however, showed some reduction of Ni^{2+} to nickel metal. XRD spectra from the nickel spinels after exposure, at both 550 and 650°C, showed the presence of both spinel oxide and nickel metal phases. Table 5.1.1 gives the height ratios of the most intense nickel XRD peak ([111]) to the spinel [311] signal (also, the most intense peak from its phase). It can be seen that, in all cases, a greater quantity of nickel was produced at the higher, 650°C, temperature and that the greater the initial concentration of nickel in the spinel, the greater the nickel : spinel ratio in the XRD spectra after exposure in the gamma cell.

Increased formation of carbon would be expected on metallic nickel rich regions of the samples. The x-ray photoelectron spectroscopy results provide evidence for this. Owing to the surface coverage of carbon on the pellets, nickel XPS peaks were weak, or non existent, after exposure. However, as can be seen from Tables 4.3.5, 4.8.5 and 4.8.6, there has been little apparent reduction in the Ni $2p_{3/2}$ binding energies of the $Ni_xCo_{1-x}Fe_2O_4$ spinels. There is no evidence in the XP spectra for the presence of metallic nickel on the sample surfaces. Since the XRD results show metallic nickel to be present in the pellets, the lack of nickel metal peaks in the XPS spectra must be explained by it being covered by carbon to a depth greater than the analysis depth of the technique.

The EDX results show that the formation of nickel metal coincides with an increase in carbon deposition. The increased carbon deposition arising from the presence of metallic nickel is less noticeable in the 650°C results. Nickel is known to catalyse the formation of carbon deposits from gas mixtures such as that used here (see Chapter 2), particularly when present in a finely divided form, like that produced from the spinel pellets. A catastrophic change to the $NiFe_2O_4$ pellet occurred on exposure at 550°C, where the nickel produced on reduction catalysed carbon formation to the point where the pellet disintegrated. Even with this sample, there was no evidence in the secondary electron micrographs of the presence of filamentary carbon formation. At 650°C, however, the pellet remained intact. The results show that deposition on the nickel spinels was greater at 550°C than at 650°C, despite the fact that the 650°C samples produced a greater quantity of metallic nickel during their gamma cell exposure. The increase in deposition on $Ni_xCo_{1-x}Fe_2O_4$ with increasing x may have been due to the changing spinel composition, the increasing formation of

metallic nickel on the surface of the pellets or a combination of both factors. The increasing metallic nickel effect would, certainly, operate, but that does not mean that the spinel composition may not, also, play a rôle. However, consideration of the energies required for electron transfer to occur between the octahedral metal ions (see below) indicates that $NiFe_2O_4$ ought to deposit less readily than $CoFe_2O_4$. Therefore, carbon deposition should decrease with increasing nickel substitution, in place of cobalt. The fact that the opposite was observed showed that the enhanced deposition was due to the metallic nickel, produced via reduction of a portion of the spinel phase, more than countering the effect of decreasing cobalt content. Also, Ni^{2+} had previously been ruled out as a catalytic species for carbon deposition on spinels[1]. Temperature had a large effect, though, bringing about greater deposition on the 550°C samples, despite their lower metallic nickel production. The deposition trend results obtained are similar to those obtained from a series of $Ni_xFe_{1-x}Fe_2O_4$ spinel oxides exposed in the gamma cell[1]. Here, too, metallic nickel was produced upon exposure and deposition at 550°C was greater than at 650°C. The reduced deposition at the higher temperature was also in agreement with the results of an investigation into the radiolytically induced reactions in AGR gas mixtures, which showed a dramatic fall off in deposition rate at temperatures above 630°C, when thermal oxidation of previously deposited material became significant[2].

Earlier work on the deposition of carbon on transition metal oxide surfaces has put forward arguments in favour of the octahedrally coordinated Fe^{2+} / Fe^{3+} couple, in materials such as magnetite, being a catalytic site[1, 3, 4]. The mobile electron in this couple (present at temperatures above the Verwey transition temperature of 120 K [5]) was said to be able to readily bond with ethyl radicals in the gas mixture. A mechanism was proposed where the lone electron of an ethyl, or similar, radical bonds with the Fe^{2+} / Fe^{3+} site delocalised electron, in either a σ (Figure 5.1.1) or π (Figure 5.1.2) fashion. The extraction of hydrogen from the resulting surface complex by a positive ion present in the gas, such as $CO_2CO_2^{2+}$, allows propagation to occur. The catalytic site would be expected to remain bound into the oxide surface, and this mechanism was said to be particularly relevant to the formation of dense layers of carbon deposit. Such deposits, with the notable exception of the 550°C $NiFe_2O_4$ sample, were the only kind identified in the present study. It was possible to see, by eye, darker regions in the centres of pellets. No filamentary growths were identified when the samples were studied by scanning electron microscopy, suggesting that the catalytic species remained embedded in the surface of the oxides. The non radiation dependent Boudouard reaction is suppressed in the low CO gas mixtures used here by the high CO_2 content of the gas phase and will not play a significant part in the formation of the observed carbon deposits. CO : CO_2 ratios greater than 3 : 1 are required for the Boudouard reaction to occur at temperatures

around 600°C [6].

In previous work, the extent of blanket deposition decreased as the number of Fe^{2+} / Fe^{3+} sites decreased in the spinel oxides examined[1,7]. Filamentary deposition was only observed on Fe_3O_4 pressed powder pellets exposed at 650°C. All other reacting samples produced thin carbon deposits. The present work produced, as mentioned earlier, purely dense blanket carbon deposition and no fluffy or filamentous growth, with the exception of the, already discussed, 550°C $NiFe_2O_4$ sample. None of the spinel series gave any change in the type of deposition produced at some particular value of x.
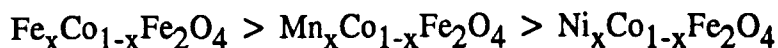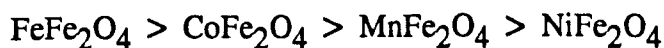
For the $Fe_xCo_{1-x}Fe_2O_4$ spinels studied here, there was no clear trend in deposition with changing value of x. In the inverse spinel structure adopted by the $Fe_xCo_{1-x}Fe_2O_4$ spinels, both the Co^{2+} and Fe^{2+} ions occupy the octahedral lattice sites. Substitution of Co^{2+} by Fe^{2+} maintains the total ion content of the octahedral lattice, but increases the number of Fe^{2+} / Fe^{3+} couples. The Fe^{3+} content remains constant. No filamentary growth was observed on $FeFe_2O_4$, after exposure at either 550 or 650°C. Magnetite pressed pellet samples have previously produced filamentary deposition at 650°C [1]. The manganese spinels showed decreasing carbon deposition as x increased at 550°C, but the opposite at 650°C, carbon intensity increasing with increasing x.

The XRD spectra of the $MnFe_2O_4$ pellets exposed at both 550 and 650°C showed only signals originating from the spinel phase. $MnFe_2O_4$ was stable in the CO_2 / CO / CH_4 / C_2H_6 reaction gas mixture. A previous study noted that $MnFe_2O_4$ decomposed in the gamma cell, forming MnO and an iron enriched spinel[1]. The spinel was, then, also found to be unstable in a CO_2 / 2% CO preparation gas mixture, necessitating the use of pure CO_2, as used for the present work. This sample showed an initially high deposition rate, attributed to the presence of the MnO. This effect was not observed in the present study. The $MnFe_2O_4$ was still present as a single phase after exposure at both of the temperatures. MnO was, however, shown separately to act on its own as a catalyst for the formation of dense carbon deposits (see Section 5.2).

One approach to an estimation of the expected relative carbon deposition rates off the exposed spinels is to look at the energies involved in the electron transfer reactions. Ionisation potentials for the ions concerned give us this information. Table 5.1.2 lists the ionisation potentials required while Table 5.1.3 lists the energies determined for the various spinels. The values listed are the ionisation potentials and energies for the ions in the gaseous state. The energy required for electron transfer will be less in a solid, compared to the gaseous state, as a result of reduced ionicity

and electron correlation[7]. The energy determined for the $Fe^{2+} + Fe^{3+} \rightleftarrows Fe^{3+} + Fe^{2+}$ case, 0 eV, clearly shows that something has been ignored. The electron hopping only occurs above 120 K [5], and, so, some energy is, obviously, required. Taking the simple approach of using ionisation potentials ignores the effect of creating, say, an Fe^{3+} ion in a site previously occupied by an Fe^{2+}, with Fe^{2+} type interatomic separations, between the metal ion and its neighbours. Energy will be required to create the ions in sites with different Madelung constants. An activation energy barrier to the electron transfer will also exist, but the free energy values determined from the ionisation potentials should provide an indication of the relative ease of electron transfer between the various transition metal ions present in the spinel oxides studied here. Figure 5.1.3 (taken from Reference 8) illustrates the situation where electron exchange between two different valency ions of the same element (e.g. Fe^{2+} and Fe^{3+}) causes ions to be created in the incorrect environments. If the resonance interaction, H_{res}, between the two states, X, before exchange, and Y, after electron exchange, is greater than E_{Ad}, the trapping energy, then the mixed valence compound will exhibit class III [5] behaviour. On the other hand, if $H_{res} < E_{Ad}$ then valence trapping will exist (there will be no delocalised electron) and a class II mixed valence compound will result.

To a first approximation, we would expect deposition to be present in the order:

$$FeFe_2O_4 > CoFe_2O_4 > MnFe_2O_4 > NiFe_2O_4$$

$$Fe_xCo_{1-x}Fe_2O_4 > Mn_xCo_{1-x}Fe_2O_4 > Ni_xCo_{1-x}Fe_2O_4$$

Looking at the results obtained using EDX (Table 4.8.2 and Figures 4.8.5, 4.8.6 and 4.8.7), we can see that the spinels do indeed give carbon count rates in this expected order. The 20 kV, 650°C results for the spinels, over all values of x, give the expected order. The 10 kV results do likewise, with the exception of $Mn_{0.75}Co_{0.25}Fe_2O_4$, which gives a high value. The $Mn_{0.75}Co_{0.25}Fe_2O_4$ result, like the other $Mn_xCo_{1-x}Fe_2O_4$ carbon deposition values after exposure at 650°C, which are discussed below, may show that the Mn^{2+} / Fe^{3+} couple, given sufficient energy (in the form of the higher, 650°C, temperature), is efficient at the formation of laminar carbon deposits, more so, even, than the Fe^{2+} / Fe^{3+} one. $Mn_{0.75}Co_{0.25}Fe_2O_4$ takes the deposition versus degree of substitution plot for the manganese spinels above that of the $Fe_xCo_{1-x}Fe_2O_4$ oxides. The $Fe_xCo_{1-x}Fe_2O_4$ and $Mn_xCo_{1-x}Fe_2O_4$ spinels exposed at 550°C show the expected results, with the manganese spinels producing less carbon deposition. The nickel spinels gave higher than expected carbon count rates, due, as discussed above, to the reduction of Ni^{2+} to metallic nickel, and, so, do not fit this trend. It

can, therefore, be seen that the spinels, with the exception of the nickel spinels exposed at 550°C, do indeed produce carbon in the expected relative quantities, based on the relative ease of electron transfer between their octahedrally coordinated mixed valence state metal ions.

The trends across the particular spinel series, as x varies, are not, however, in such good agreement with the expected results. We might expect to see that, for $Fe_xCo_{1-x}Fe_2O_4$, as x increases, deposition increases, while, for $Mn_xCo_{1-x}Fe_2O_4$ and $Ni_xCo_{1-x}Fe_2O_4$, deposition decreases as x increases. In the case of the nickel spinels, the expected drop in deposition as x increases has been exceeded by the increase in carbon formation due to the production of metallic nickel in the sample. The increase in deposition with increasing x follows the increase in metallic nickel content of the spinels after exposure.

The $Mn_xCo_{1-x}Fe_2O_4$ spinels show the expected drop in carbon deposition with increasing manganese content (and consequential drop in cobalt content) when exposed at the lower temperature of 550°C. As the Co^{2+} / Fe^{3+} octahedrally coordinated couples are replaced by Mn^{2+} / Fe^{3+} ones, which require more energy for their electron transfer to occur, there is a reduction in carbon deposition on the spinels as the total number of sites available on the surface of the pellets, for reaction with gas phase radical species, reduces. At the higher temperature of 650°C, there is more thermal energy available in the system, and the Mn^{2+} / Fe^{3+} couple electron exchange can more readily occur. The octahedral Co^{2+} / Fe^{3+} couple is still present in the $Mn_xCo_{1-x}Fe_2O_4$ samples (unless x = 1) and is available for interaction with gas phase radical species alongside the Mn^{2+} / Fe^{3+} one. The observed increase in carbon deposition with increasing substitution of cobalt by manganese implies that the Mn^{2+} / Fe^{3+} couple is inherently more favourable for the deposition of carbon than the Co^{2+} / Fe^{3+} one, given sufficient energy in the system. The drop in carbon deposition for the $MnFe_2O_4$ pellet exposed at 650°C (10 kV results), compared to that for $Mn_{0.75}Co_{0.25}Fe_2O_4$, will be due to the change away from a pure inverse structure. The Mn^{2+} content of the octahedral lattice in $MnFe_2O_4$ is low (the ground state formula is $Mn_{0.8}^{2+}Fe_{0.2}^{3+}(Mn_{0.2}^{2+}Fe_{1.8}^{3+})O_4$, with the octahedral ions in brackets[1]) compared to the previous member of the manganese spinel series, $Mn_{0.75}Co_{0.25}Fe_2O_4$, which adopts the inverse structure with all manganese ions in the octahedral lattice. Therefore, there is a much reduced possibility of rapid electron exchange occurring between octahedrally coordinated metal ions, in different oxidation states. The majority of the octahedral sites in the spinel lattice are occupied by Fe^{3+} ions. The reducing conditions present in the gamma cell during exposure, together with the presence of manganese in the spinel, may cause some enhancement in Fe^{2+} occupancy of octahedral sites, and, thus, allow Fe^{2+} / Fe^{3+} couples to operate[9], but this did not prove to have a major effect on the carbon deposition

observed.

The surface compositions of the spinels, prior to exposure, were not necessarily equal to their bulk stoichiometries. For instance, as discussed in Section 4.3.5, the manganese and iron spinels appeared, in the x-ray photoelectron spectra, to be surface enriched in cobalt and depleted in iron. The overlayers of carbon present on the pellets after exposure, however, prevent accurate determination of the relative concentrations of the metal ion species on the surfaces of the exposed spinels. As an example, no identifiable metal $2p$ peaks were seen in the spectra recorded from the $Mn_xCo_{1-x}Fe_2O_4$ pellets after exposure at 550°C. The conditions present within the gamma cell during exposure will affect the surface presented by the spinel pellets to the gas phase. The two temperatures used for the experiments, 550 and 650°C, may be expected to bring about different surface elemental and chemical state compositions. As an example, FeO is stable at temperatures greater than 570°C, but disproportionates, to give metallic iron and Fe_3O_4, at lower temperatures[4, 10]. No FeO will be present on the pellet surfaces at the 550°C but may be there during exposure at the higher temperature. The XPS peak position results detailed in Tables 4.8.5 and 4.8.6, recorded off the spinels after exposure, when compared to those given in Table 4.3.5, recorded prior to placement in the gamma cell, show that, indeed, reduction of the surfaces of the spinels, or, rather, those spinels for which XP peak position data were obtainable, has occurred. The $Fe_xCo_{1-x}Fe_2O_4$ spinels, prepared in gas mixtures contained carbon monoxide and similar in reducing potential to those used for the deposition runs, have suffered reduction, as have the $Mn_xCo_{1-x}Fe_2O_4$ and $Ni_xCo_{1-x}Fe_2O_4$ spinels, prepared in pure CO_2. The possibility exists that, for instance, FeO is formed in areas on the surfaces of pellets, after reduction of Fe^{3+} to Fe^{2+} (at least, at temperatures above 570°C). An experimental difficulty that arises is the inability to monitor the actual surface elemental and chemical state compositions *in situ* in the gamma cell. X-ray photoelectron spectra may be recorded under ultra high vacuum conditions at elevated temperatures but not at high pressures of the gas mixtures used in the gamma cell. Any reduction of the spinel surfaces that occurred during exposure in the gamma cell did not, however, extend to the bulk of the pellets, as evidenced by the typical spinel XRD spectra obtained off the exposed samples. The only non spinel peaks seen in the sample XRD spectra were of metallic nickel in the $Ni_xCo_{1-x}Fe_2O_4$ results.

5.2   Manganese Oxides

The manganese oxides were examined in this study in an attempt to throw further light on the Fe^{2+} / Fe^{3+} couple effect, shown previously to enhance carbon deposition from the gas phase[1]. Mn_3O_4, unlike magnetite, Fe_3O_4, adopts the normal spinel structure. This means that the 2+ and 3+ manganese ions occupy separate

227

lattices. In magnetite, there are both Fe^{2+} and Fe^{3+} ions present in the octahedral sites, and rapid electron exchange is possible between them at the temperatures involved in this study. This is not the case with Mn_3O_4. The Mn^{3+} ions are to be found in octahedral sites, but the Mn^{2+} ions are only present in tetrahedral locations. The lack of electron exchange makes Mn_3O_4 a much less intense colour compared to Fe_3O_4, with, above 120 K [5], its delocalised electron (light brown compared to black). If the electron exchange that is possible in Fe_3O_4 is a cause of carbon deposition, then its absence in Mn_3O_4 would be expected to diminish the extent of deposition on the latter. MnO (Mn^{2+}) and Mn_2O_3 (Mn^{3+}) were chosen to provide the opportunity to compare the mixed valence oxide, Mn_3O_4, with two single oxidation state manganese oxides, each with one of the manganese oxidation states present in the mixed valence compound.

X-ray diffraction analysis of the samples after exposure in the gamma cell showed that the Mn_2O_3 and Mn_3O_4 oxides had, during their time in the gamma cell, converted to MnO. They had been reduced by their treatment. This complicates comparisons made between the rates of carbon deposition on the different manganese oxides and of the effect of the presence or absence of the non interacting Mn^{2+} / Mn^{3+} mixed valency.

None of the samples gave any filamentary deposition. Carbon was seen to be deposited on the surfaces, evidenced by the increased carbon signals in the EDX and XP spectra. Dark regions were also optically visible on the pellets (which had all become green in colour, throughout their bulk, due to their being MnO). It would, therefore, appear that the carbon deposited in the form of a dense layer, evenly covering the pellet surfaces. The EDX results suggest that MnO is the most effective catalyst of the three manganese oxides examined, and the only one to operate at both temperatures. The other two oxides only catalysed carbon deposition at the lower temperature. Since the MnO pellets gave more carbon deposition than did the Mn_3O_4 and Mn_2O_3 ones (which gave roughly similar results), and, yet, the latter two oxides had, by the end of the exposure, reduced to MnO, it is clear that MnO is a more effective catalyst than either of the other two materials. The time taken for the conversion to MnO was such that the converted pellets had insufficient time remaining to accumulate as much deposition as the original MnO samples. In all cases, the MnO carbon deposition was greater than on the other oxides. The Mn_3O_4 did not give large amounts of deposition. The non interacting Mn^{2+} / Mn^{3+} mixed valency present did not enhance the deposition rate compared to the single valency oxide cases.

MnO has been produced upon exposure of $MnFe_2O_4$ in the BNL gamma cell under similar (reducing) conditions to those used for this work[4]. In that study, the MnO produced was said to be the cause of the increased carbon deposition seen on

the manganese ferrite end members of the spinel series $Mn_xFe_{1-x}Fe_2O_4$ and $MnFe_xCr_{2-x}O_4$. In that case, MnO was believed to be acting as a promoter, a rôle it is known to play in iron containing systems[11, 12].

The efficiency of MnO as a carbon coupling catalyst in its own right has been demonstrated to be affected by the gas mixtures used[13]. With a pure CH_4 gas phase, MnO gave no conversion of CH_4 to higher hydrocarbons, while Mn_3O_4 gave significant conversion. However, with a 50% CH_4 / 2.5% O_2 / 47.5% N_2 gas mixture, both oxides showed activity, with MnO giving a conversion rate approximately a third that of Mn_3O_4. (The use of single pulses of gas prevented significant reduction of the Mn_3O_4 to MnO from occurring during the time of the experiment.) For the present work, it is significant that the study described in Reference 12 found that MnO in the CH_4 / O_2 / N_2 gas showed a higher selectivity (almost twice so) for the formation of C_2 derivatives than did Mn_3O_4. This indicates that MnO, if less effective in reacting with CH_4 overall, is more efficient in the coupling of carbon species and, thus, more susceptible to the formation of carbon deposits, as opposed to gas phase products. Carbon deposits are the important product for the present work. This study has shown that for gas mixtures akin to those found in AGRs, MnO is the most effective catalyst for the formation of carbon deposits. FeO has, as was discussed in Section 2.3, been shown to be an effective catalyst for the formation of filamentous carbon from hydrocarbons[14, 15]. It is more effective than pure iron metal. However, the increased catalytic activity is said to arise not from any intrinsic catalytic capability of the oxide but, instead, from the formation of a high surface area, porous iron structure when the oxide is reduced in the gas conditions present. It should be remembered, though, that FeO is a non stoichiometric compound. It is cation deficient and is usually represented as $Fe_{1-x}O$. x typically takes on values between 0.04 and 0.12 [16]. In order to maintain overall charge neutrality, Fe^{3+} ions are present, in addition to Fe^{2+}. More than 25% of the iron in FeO, wüstite, may be in the 3+ oxidation state. FeO is, therefore, a mixed valence compound, and one in which the two types of metal ions are located in the same sites. Rapid electron exchange is possible between the Fe^{2+} and Fe^{3+} ions. The small size of the Fe^{3+} ion allows it to occupy not only rock salt lattice sites but, also, interstitial locations, but the lattice ions are still able to house delocalised electrons. The electron exchange will be expected to play a rôle in promoting carbon deposition out of the gas phase in systems such as that studied here.

Nickel has been shown to only produce deposits when present in the metallic state, and not as an Ni^{2+} oxide[1, 3]. Nickel spinels were shown in this study to readily reduce to produce metallic nickel and produce carbon deposits. The type of metallic phase produced on reduction of, say, nickel spinels or FeO will be highly dispersed and well suited to the formation of deposits.

MnO, like FeO, is a non stoichiometric compound. Represented as $Mn_{1-x}O$, x typically ranges between 0.001 and 0.15 [17, 18]. Therefore, MnO is a mixed valence compound, with both Mn^{2+} and Mn^{3+} ions located on the same, rock salt type, lattice. As with $Fe_{1-x}O$, there will also be a proportion of the manganese ions located in interstitial sites. Unlike Mn_3O_4, the mixed valency is present on the same lattice, and rapid electron exchange will be possible between the two types of manganese ions. The ions are located in very similar environments, with regards to their neighbouring ions, so the energy required for the electron exchange will be low, as it is in magnetite, Fe_3O_4. This type of mixed valency is believed to account for the observation that, of the three manganese oxides studied, MnO gave the greatest extent of carbon deposition upon exposure in the gamma cell.

In order to study better the differences in carbon deposition behaviour on the three manganese oxides it will be necessary to expose them for much shorter times in the gamma cell. Over very short exposure times, the different oxidation states will be able to impose themselves more uniquely on the deposition rate. In order for the heating up and cooling down sections of the gamma cell exposure profile not to then become dominant, it may be desirable to have an inert gas flowing through the system during these times, and to have the reaction gas only on stream when the capsule is at temperature. Normally, the gas mixture is allowed to flow through the capsule as the furnace temperature is increased. It is necessary to purge the capsule, and gas lines, of any residual air before exposing the samples at elevated temperatures.

5.3 Uranium Oxides

As with the manganese oxides, the uranium oxides examined in this study were selected to allow comparisons to be made between two compounds with single metal oxidation states and a mixed valence oxide containing both oxidation states. UO_2 and γ-UO_3 contain uranium in the single oxidation states +4 and +6, respectively. α-U_3O_8 is a class 1 (in the Robin and Day classification scheme[5]) mixed valence, U(IV) and U(VI), uranium oxide, where the U^{4+} and U^{6+} ions are relatively non interacting[19, 20], unlike the Fe^{2+} and Fe^{3+} ions in magnetite. If a delocalised mixed valence system is required for enhanced carbon deposition rates, then we ought not to see such an enhancement when α-U_3O_8 is exposed, in the same way as the non interacting mixed valence Mn_3O_4 was shown not to enhance deposition.

As was noted in Section 4.10.2, several of the uranium oxide pellets had deformed during their exposure in the gamma cell. This is presumably due to carbon preferentially diffusing into the body of the pellets from one side. The consequent expansion of the oxide lattice would bring about the observed curvature in the

exposed pellets.

As with the manganese oxides, exposure of these uranium oxides resulted in them all converting to the same oxidation state. All three oxides, after exposure, gave XRD spectra similar to that of UO_2. The γ-UO_3 and α-U_3O_8 had been reduced by their exposure in the gamma cell. Again, this prevents any conclusions to be readily drawn with regards to the effect of the mixed valency on carbon deposition, since the observed deposits will be due to all oxide forms that the pellets have been during their exposure. It, as for the manganese oxides, points towards the need for exposures of shorter duration if the effect of mixed valency is to be firmly defined. Along with the chemical changes in the pellets, some became physically distorted too during their exposure.

No filamentary carbon deposition was observed, though the laying down of deposits was seen to be happening by the increase in carbon signals in the EDX and XP spectra and the optically observable differences between the centres and edges of the pellets. As with the manganese and spinel oxide samples, this implies the formation of dense, laminar carbon deposits on the pellet surfaces. The reduction in intensity of the U $4f_{7/2}$ XP signals also points this way. There was no evidence for increased deposition on the class 1 (non interacting[19, 20]) mixed valence α-U_3O_8 pellet. In fact, this material gave the lowest carbon signals in EDX spectra.

The XRD spectrum of UO_2 is very similar to that of U_4O_9 [21]. Table 5.3.1 compares literature UO_2 and U_4O_9 XRD 2Θ values with those obtained experimentally off the exposed uranium oxide pellets. All six samples (three oxides each exposed at two temperatures) gave 2Θ values closer to those expected off U_4O_9 than off UO_2. It is, therefore, clear that the samples had not, as originally supposed, converted to UO_2 but had, instead, converged on the U_4O_9 phase. The conditions present in the gamma cell during exposure had reduced the α-U_3O_8 and γ-UO_3, while oxidising the UO_2, to U_4O_9. Like uranium oxides with the stoichiometry UO_{2+x} ($0 < x < 0.3$), U_4O_9 is a class II mixed valence compound[5]. Thus, it exhibits rapid electron exchange between the U^{4+} and U^{5+} ions present in its lattice[20].

U_4O_9 has an infrared absorption edge which starts at $850\,cm^{-1}$ [21]. This corresponds to the electron transfer between U^{4+} and U^{5+} and an energy of 0.1 eV. In general, the energy of electronic transitions is much greater than this and the low value is attributed to the mixed valency of this compound. The crystal environments of the U^{4+} and U^{5+} sites in U_4O_9 are almost identical. Thus, the energy required to bring about the electron transfer is small. As with Fe_3O_4, there is an activation energy barrier to this transfer. This has been estimated from high temperature

231

conductivity measurements to be 0.3 eV, corresponding to an absorption of 2000 cm^{-1} [21]. The 850 cm^{-1} absorption edge probably represents the mixed valence absorption of U_4O_9. Magnetite, Fe_3O_4, also shows a broad infrared absorption, extending down to 500 cm^{-1}. Fe_3O_4 is, like U_4O_9, a class II mixed valence compound and has been compared previously with U_4O_9 in connection with several of its physical and chemical properties[22].

As all three oxides (at both temperatures) converted, ultimately, to the same uranium oxide, any differences in deposition behaviour will be due to the initial oxides present, and the time taken for the oxidation or reduction to occur. The high carbon signals obtained off all three samples point to the fact that U_4O_9, an electron exchanging mixed valence compound, is a good catalyst for the deposition of carbon from gas phase species, and that conversion to this oxide was rapid in comparison to the total exposure time in the gamma cell for the samples.

5.4 Magnetite

Magnetite, in the form of a pressed powder pellet, was shown in an earlier study to produce filamentous carbon deposition when exposed in the gamma cell at 650°C [1]. We set out in this work to see if it was possible to detect any differences in deposition rate on different crystallographic faces of magnetite single crystals.

The difficult task of preparing the desired crystallographically smooth magnetite surfaces was not achieved with complete success. Therefore, comparisons could not be made between the deposition rates on the three chosen Fe_3O_4 planes. However, some smooth surfaces and regular etch patterns were obtained, although these did not continue across the whole face of a slice. To compound the problem, topographical influences on the relative intensities of the detected EDX signals were significant. Therefore, our efforts were concentrated on the topographically smooth and oriented regions on the various slices exposed.

No filamentary carbon deposition was identified on any of the magnetite samples exposed in the gamma cell. Edge (shielded from the gas phase by the silica spacers) and centre regions of the slices could be identified, either visually or using a scanning electron microscope. This, together with the presence of carbon signals in the EDX and XP spectra, suggests that the carbon was laid down in the form of smooth sheets across the faces of the slices, the catalytic sites remaining embedded in the slice. Two samples, etched and exposed at 650°C, did show some regions where structure was present in a material laying on the surface. The SEM electron beam was able to interfere with this surface appearance. This surface structure was observed on two of the samples. One of these samples was a [111] slice (see Figure 4.11.2), and the structure was apparent on a flat etched face approximately parallel to the [111]

plane. The other slice showing such a surface feature was originally cut parallel to the [110] direction, but the deposit was present on a face at an angle to this (Figure 4.11.3). The [111] plane of magnetite has previously been shown to be the most rapidly etched, out of the [100], [110] and [111] planes[23], and it was expected that this face would give the greater amount of carbon deposition. It is able to present to the gas phase large arrays of octahedrally coordinated Fe^{2+} and Fe^{3+} ions, electronically coupled and able to interact with gas phase hydrocarbon radicals. The appearance of this structure on faces of approximately [111] orientation shows that we have identified preferential deposition on the [111] face of the single crystal magnetite. The preparation of larger surfaces of uniform orientation would allow this deposition effect to be better examined.

5.5   References

1. J. A. Jutson, "The Deposition of Carbon on Transition Metal Oxide Surfaces", Council for National Academic Awards, Ph.D. thesis, (1989).

2. D. J. Norfolk, R. F. Skinner and W. J. Williams, "Mechanisms Involved in Radiolytic Carbon Deposition from $CO_2/CO/CH_4$", in "Gas Chemistry in Nuclear Reactors and Large Industrial Plant" edited by A. Dyer, Heyden, 67 - 74, (1980).

3. G. C. Allen and J. A. Jutson, "Carbon Deposition on Nickel Ferrites and Nickel - Magnetite Surfaces", Journal of the Chemical Society, Faraday Transactions, *86*, 867 - 873, (1990).

4. G. C. Allen and J. A. Jutson, "Carbon Deposition on Iron - Manganese - Chromium Spinels", Journal of Materials Chemistry, *1*, 73 - 78, (1991).

5. M. B. Robin and P. Day, "Mixed Valence Chemistry - A Survey and Classification", Advances in Inorganic Chemistry and Radiochemistry, *10*, 247 - 422, (1967).

6. M. J. Bennett, G. H. Chaffey, A. J. Langford and D. R. V. Silvester, "The Heterogeneous Decomposition of Acetone by a 20% Cr / 25% Ni / Nb Stabilised Austenitic Stainless Steel and Other Materials", United Kingdom Atomic Energy Authority report AERE R7407, (1973).

7. K. Prassides and P. Day, "Estimation of the Effective On-Site One-Centre Coulomb Repulsion Energy U in Mixed-Valence Cs_2SbCl_6", Inorganic Chemistry, *24*, 1109 - 1110, (1985).

8. B. Mayoh and P. Day, "Trapping of Valence States in a Ruthenium(II,III)-Pyrazine Complex", Journal of the American Chemical Society, *94*, 2885 - 2886, (1972).

9. G. C. Allen and J. A. Jutson, "Effect of Spinel Oxide Composition on Rate of Carbon Deposition", Journal of the Chemical Society, Faraday Transactions I, *85*, 55 - 64, (1989).

10. S. Iida, K. Mizushima, M. Mizoguchi, K. Kato, K. Yanai, N. Goto and S. Yumoto, "Details of the Electronic Superstructure of Fe_3O_4", Journal of Applied Physics, *53*, 2164 - 2166, (1982).

11. K. M. Kreitman, M. Baerns and J. B. Butt, "Manganese-Oxide-Supported Iron Fischer-Tropsch Synthesis Catalysts: Physical and Catalytic Characterisation", Journal of Catalysis, *105*, 319 - 334, (1987).

12. J. Venter, M. Kaminsky, G. L. Geoffroy and M. A. Vannice, "Carbon-Supported Fe-Mn and K-Fe-Mn Clusters for the Synthesis of C_2-C_4 Olefins from CO and H_2 I - Chemisorption and Catalytic Behaviour", Journal of Catalysis, *103*, 450 - 465, (1987).

13. R. Burch, S. Chalker, G. D. Squire and S. C. Tsang, "Oxidative Coupling of Methane over Manganese Oxide Catalysts", Journal of the Chemical Society, Faraday Transactions, *86*, 1607 - 1614, (1990).

14. R. T. K. Baker, J. R. Alonzo, J. A. Dumesic and D. J. C. Yates, "Effect of the Surface State of Iron on Filamentous Carbon Formation", Journal of Catalysis, *77*, 74 - 84, (1982).

15. D. J. C. Yates and J. A. McHenry, "Studies on the Low-Temperature Synthesis and Surface Chemistry of Iron Monoxide", Inorganic Chemistry, *26*, 3193 - 3201, (1987).

16. G. J. Long and F. Grandjean, "Mössbauer Effect, Magnetic and Structural Studies of Wüstite", in "Advances in Solid-State Chemistry", edited by C. R. A. Catlow, *2*, 187 - 221, (1991).

17. P. K. Khowash and D. E. Ellis, "Electronic Defect Structure in TiO and MnO", Journal of Applied Physics, *65*, 4815 - 4817, (1989).

18. A. Fujimori, N. Kimizuka, T. Akahane, T. Chiba, S. Kimura, F. Minami, K. Siratori, M. Taniguchi, S. Ogawa and S. Suga, "Electronic Structure of MnO", Physical Review B, *42*, 7580 - 7586, (1990).

19. P. A. Cox, R. G. Egdell and A. F. Orchard, "Photoelectron Spectroscopy of Mixed-Valence Compounds", in "Mixed-Valence Compounds - Theory and Applications in Chemistry, Physics, Geology and Biology", edited by D. B. Brown, D. Reidel, 475 - 502, (1980).

20. G. C. Allen, P. M. Tucker and J. W. Tyler, "The Behaviour of Uranium Oxides in Low Partial Pressures of O_2 Studied Using X-Ray Photoelectron Spectroscopy", Vacuum, *32*, 481 - 486, (1982).

21. N. R. Holmes, "The Characterisation of Uranium Oxide Surfaces", Ph.D. thesis, Council for National Academic Awards, (1988).

22. J. Tateno, "On the Phase Transition in Mixed Valence Type Oxides", Journal of Physics and Chemistry of Solids, *30*, 1321 - 1326, (1969).

23. G. C. Allen, C. Kirby and R. M. Sellers, "The Effect of the Low-Oxidation-State Metal Ion Reagent Tris-picolinatovanadium(II) Formate on the Surface Morphology and Composition of Crystalline Iron Oxides", Journal of the Chemical Society, Faraday Transactions I, *84*, 355 - 365, (1988).

24. "Handbook of Chemistry and Physics, 51st. Edition", Chemical Rubber Company, (1970).

Sample	550°C	650°C
$CoFe_2O_4$	-----	-----
$Ni_{0.25}Co_{0.75}Fe_2O_4$	0.02	0.21
$Ni_{0.5}Co_{0.5}Fe_2O_4$	0.04	0.25
$Ni_{0.75}Co_{0.25}Fe_2O_4$	0.08	0.28
$NiFe_2O_4$	-----	-----

Table 5.1.1. Nickel [111] : spinel [311] XRD peak ratios for the exposed $Ni_xCo_{1-x}Fe_2O_4$ spinels.

Ionisation	Potential /V [24]
$Mn^{2+} \rightarrow Mn^{3+} + e^-$	33.69
$Fe^{2+} \rightarrow Fe^{3+} + e^-$	30.64
$Co^{2+} \rightarrow Co^{3+} + e^-$	33.49
$Ni^{2+} \rightarrow Ni^{3+} + e^-$	35.16

Table 5.1.2. Second ionisation potentials for the spinel metal ions.

Electron transfer reaction	Energy /eV
$Mn^{2+} + Fe^{3+} \rightleftarrows Mn^{3+} + Fe^{2+}$	3.05
$Fe^{2+} + Fe^{3+} \rightleftarrows Fe^{3+} + Fe^{2+}$	0
$Co^{2+} + Fe^{3+} \rightleftarrows Co^{3+} + Fe^{2+}$	2.85
$Ni^{2+} + Fe^{3+} \rightleftarrows Ni^{3+} + Fe^{2+}$	4.52

Table 5.1.3. Calculated electron hopping energies for the spinels.

Sample	Reflection peak /[hkl]					
	[111]	[200]	[220]	[311]	[222]	[400]
UO_2 [12]	28.234°	32.718°	46.962°	55.702°	58.401°	68.559°
U_4O_9 [12]	28.373°	32.884°	47.193°	55.990°	58.710°	68.959°
UO_2 550°C	28.459°	32.928°	47.149°	55.891°	58.607°	68.778°
UO_2 650°C	28.557°	33.061°	47.321°	56.068°	58.777°	68.940°
α-U_3O_8 550°C	28.441°	32.923°	47.163°	55.909°	58.625°	68.794°
α-U_3O_8 650°C	28.695°	33.181°	47.467°	56.218°	58.915°	69.093°
γ-UO_3 550°C	28.739°	33.215°	47.461°	56.195°	58.906°	69.056°
γ-UO_3 650°C	28.447°	32.935°	47.183°	55.937°	58.653°	68.839°

Table 5.3.1. Comparison between literature UO_2 and U_4O_9 XRD 2Θ values and those obtained experimentally off the exposed uranium oxides.
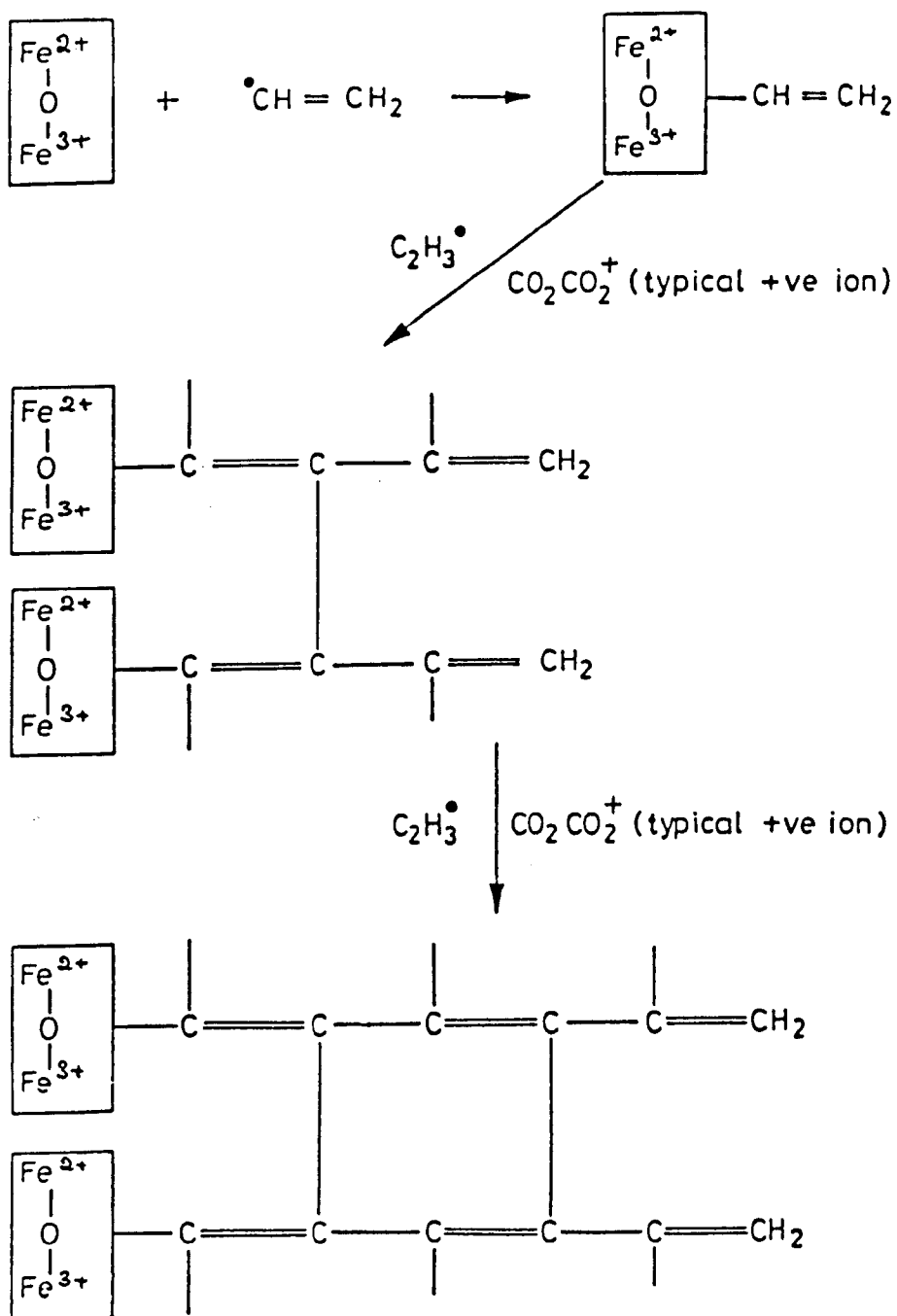
Figure 5.1.1. Carbon filamentary growth initiated at Fe^{2+} / Fe^{3+} sites by σ bonding with hydrocarbon radicals (typically $\cdot C_2H_3$).

238
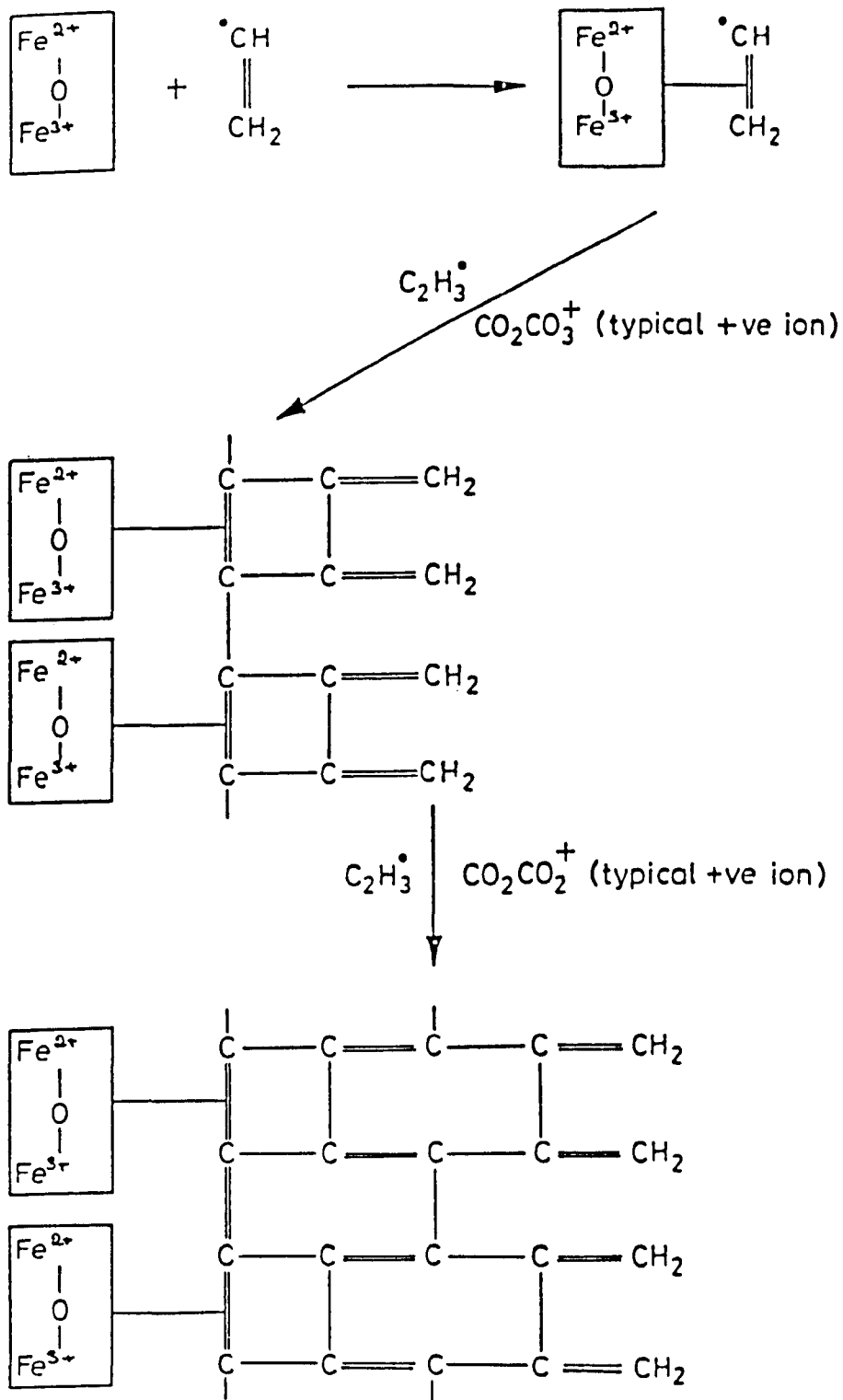
Figure 5.1.2. Carbon filamentary growth initiated at Fe^{2+} / Fe^{3+} sites by π bonding with hydrocarbon radicals (typically $\cdot C_2H_3$).
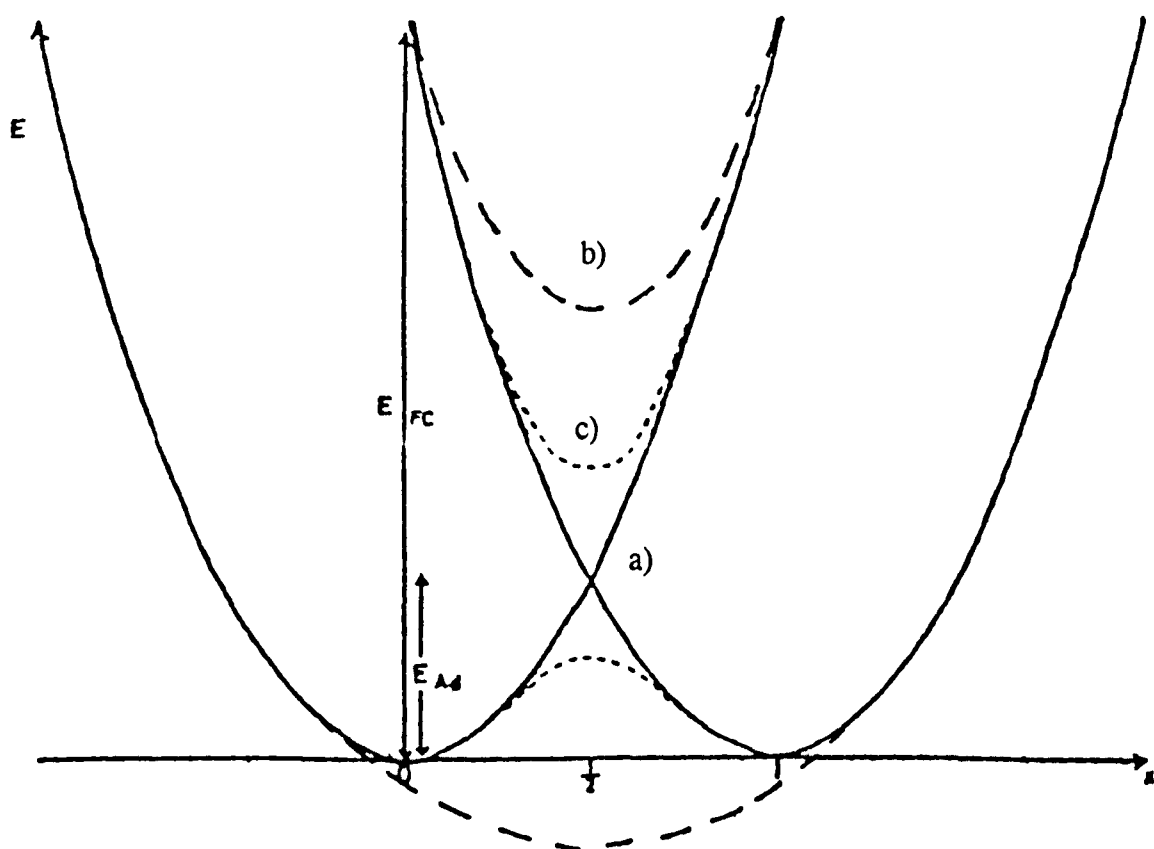
239

Figure 5.1.3. Reaction coordinates for valence interchange $(X,Y) \rightleftarrows (Y,X)$: a) (——) energy surface for (X,Y), (Y,X) in the absence of resonance interaction between the sites; b) (- - -) energy surface with $H_{res} > E_{Ad}$; and c) ($\cdots\cdots$) energy surface with $H_{res} < E_{Ad}$.

6 <u>CONCLUSIONS</u>

1. The intended $Mn_xCo_{1-x}Fe_2O_4$, $Fe_xCo_{1-x}Fe_2O_4$ and $Ni_xCo_{1-x}Fe_2O_4$ ($0 \leq x \leq 1$) spinels were successfully prepared by solid state reaction of the relevant oxides, oxalates and / or carbonates.

2. The $Mn_xCo_{1-x}Fe_2O_4$ and $Fe_xCo_{1-x}Fe_2O_4$ spinels were stable in the conditions present within the gamma cell during exposure.

3. The $Ni_xCo_{1-x}Fe_2O_4$ spinels suffered some reduction upon exposure in the gamma cell, producing quantities of metallic nickel.

4. At 650°C, the spinels gave deposition in the order expected after consideration of the relative ease of electron transfer between the octahedrally coordinated metal ions:

$$Fe_xCo_{1-x}Fe_2O_4 > Mn_xCo_{1-x}Fe_2O_4 > Ni_xCo_{1-x}Fe_2O_4$$
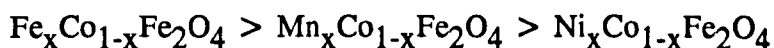
At 550°C, the iron spinels gave greater deposits than the manganese spinels, also as expected. (The $Ni_xCo_{1-x}Fe_2O_4$ spinels gave enhanced deposition due to their formation of metallic nickel.)

5. With the $Mn_xCo_{1-x}Fe_2O_4$ spinels, at 550°C, carbon deposition decreased as the substitution of cobalt by manganese increased, reducing the availability of octahedrally coordinated Co^{2+} / Fe^{3+} couples for interaction with gas phase radical species and subsequent deposition of carbon.

6. With the $Mn_xCo_{1-x}Fe_2O_4$ spinels, for $x \leq 0.75$, at 650°C, carbon deposition increased as the substitution of cobalt by manganese increased.

7. $MnFe_2O_4$ exhibited reduced carbon deposition compared to $Mn_{0.75}Co_{0.25}Fe_2O_4$, owing to the change in structure, from inverse spinel to intermediate spinel, with increasing manganese content.

8. There were no regular trends of increasing or decreasing carbon deposition behaviour with changing value of x for the $Fe_xCo_{1-x}Fe_2O_4$ spinels.

9. At both 550 and 650°C, the $Ni_xCo_{1-x}Fe_2O_4$ spinels showed increasing deposition with increasing x. The deposition was greater at 550°C than at 650°C. This deposition was due to the formation of metallic nickel, counteracting the expected drop in carbon formation with increasing nickel content of the spinels.

10. At 550°C, the $NiFe_2O_4$ pellet suffered catastrophic deposition, breaking up and forming a large mass of deposit material.

11. The manganese oxides gave relative carbon deposition rates in the order:

$$MnO > Mn_3O_4 \approx Mn_2O_3$$
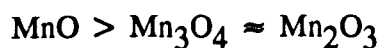
The non interacting metal ions present in Mn_3O_4 did not yield enhanced deposition.

12. At both 550 and 650°C, Mn_3O_4 and Mn_2O_3 reduced to MnO during the time of exposure.

13. The interacting mixed valency present in MnO is believed to have brought about the enhanced carbon deposition seen on this oxide.

14. The uranium oxides all converted to U_4O_9 under the conditions present within the gamma cell during exposure, at both 550 and 650°C.

15. The 10 kV EDX spectra yielded uranium oxide relative carbon deposition rates in the order γ-UO_3 > UO_2 > α-U_3O_8, while the 20 kV results gave UO_2 > γ-UO_3 > α-U_3O_8. The non interacting metal ions present in α-U_3O_8 did not yield enhanced deposition.

16. For both the manganese and uranium oxides, it would be desirable to expose the samples for shorter periods of time to more clearly study the effect of the different oxidation states on the rates of carbon deposition.

17. Selected Fe_3O_4 crystallographic planes could not be systematically prepared as wanted.

18. No filamentary deposition was observed on the magnetite slices. Instead, a thin, dense carbon deposit was formed on the samples.

19. Structured deposit was seen on two smooth magnetite faces, including one oriented approximately parallel to the [111] direction. The [111] plane was previously expected to give the highest deposition rate of the three faces studied.